

This file is part of the following work:

**Garland, Nathan Ashley (2018) *Electron transport modeling in gas and liquid media for application in plasma medicine*. PhD Thesis, James Cook University.**

Access to this file is available from:

<https://doi.org/10.25903/5bf38aee6e2a4>

Copyright © 2018 Nathan Ashley Garland

The author has certified to JCU that they have made a reasonable effort to gain permission and acknowledge the owners of any third party copyright material included in this document. If you believe that this is not the case, please email

[researchonline@jcu.edu.au](mailto:researchonline@jcu.edu.au)

# Electron transport modeling in gas and liquid media for application in plasma medicine

Thesis submitted by

**Nathan Ashley Garland BEng(Hons)-BSc**

on 13th July 2018

for the degree of Doctor of Philosophy  
in the College of Science and Engineering

**James Cook University**



COPYRIGHT © NATHAN GARLAND, 2018.

Some rights reserved.

This work is licensed under Creative Commons  
Attribution–Noncommercial–No Derivative Works license.

<http://creativecommons.org/licenses/by-nc-nd/3.0/au/>

# Statement of Access

I, the undersigned, the author of this thesis, understand the James Cook University will make it available for use within the University Library and, by microfilm or other means, allow access to users in other approved libraries. All users consulting with this thesis will have to sign the following statement:

In consulting this thesis I agree not to copy or closely paraphrase it in whole or in part without the written consent of the author; and to make proper written acknowledgement for any assistance which I have obtained from it.

Beyond this, I do not wish to place any restriction on access to this thesis.

---

Nathan Garland

---

13th July 2018  
Date

# Sources Declaration

I declare that this thesis is my own work and has not been submitted in any form for another degree or diploma at any university or other institute of tertiary education. Information derived from the published and unpublished work of others has been acknowledged in the text and a list of references is given.

---

Nathan Garland

---

13th July 2018

Date

# Statement of the contribution of others

I gratefully acknowledge the contributions detailed below.

Editorial assistance for the overall thesis was provided by Prof. Ronald White of James Cook University. Chapters 2-5 are each based on published, or submitted, manuscripts, and editorial assistance was provided by all of the listed coauthors.

Contributions to co-authored publications that feature in this work are detailed as follows. Chapters 2-4 are taken from first authored publications, where input data to the simulations was provided by Daniel Cocks, Gregory Boyle, and Madalyn Casey. To compare against my simulation results, results obtained from Gregory Boyle via solution of the Boltzmann equation, and Daniel Cocks via Monte Carlo simulations, were used. Chapter 5 is largely based on a first authored publication, where the listed co-authors provided advice and feedback on the featured data and analysis. Using the data generated in that study the FORTRAN code of Ronald White was used to calculate transport coefficients, which was then analysed by myself. Experimental measurements and considerations were contributed by Jaime de Urquijo. Transport data for ionisation front simulations in Chapter 5 was provided by Madalyn Casey.

# Abstract

Emerging plasma technologies, such as plasma medicine, rely on the transport of plasma species across gas-liquid interfaces to achieve their function. Recent studies have identified that, while poorly understood at present, electron transport through the interface is an important driver of plasma chemistry in plasma medicine. In order to understand this fundamental transport, so to facilitate understanding and future optimisation of plasma technologies, a modeling framework for electron transport simulations across gas-liquid interfaces has been developed. This modeling framework has been applied to noble liquids, such as argon and xenon, and the first steps have been made towards application to a biomolecule system involving tetrahydrofuran.

This research has extended previous approaches to electron fluid modeling in the gas phase to propose a fluid model for electron transport in gas and liquid media based on four moments of the Boltzmann kinetic equation. The model was benchmarked against kinetic solutions of electron transport to validate the applicability of the model to describe non-local electron transport phenomena in both gas and liquids, given that appropriate and accurate input data is available. To assess the impact of employing steady-state collision and closure input data in electron fluid models, non-equilibrium velocity distribution functions, computed via multi-term solution of the Boltzmann equation for benchmark calculations, were studied.

The dependence of the proposed model's input transport data on the background medium density was examined in this research. By examining how electron momentum and energy transfer occurs due to collisions in gas and liquid extremes, an approximation method was proposed to generate input transport data at intermediate densities for which data is required, but not available, for modeling interfacial transport. The proposed approximation was benchmarked against analytic simple liquids and experimental data measured in cryogenic argon and xenon to verify the applicability of the proposed approach.

Simulations of electron transport between gas and liquid argon, and vice versa, was performed by applying both the proposed fluid model and input data approximation method. Comparisons of the abilities of modeling methods to resolve realistic non-local transport were studied, and the stark differences between using electron-liquid transport data compared to simply scaling up electron-gas transport data were discussed. Application of this modeling framework to dual-phase simple liquid particle detector apparatus was demonstrated.

Finally, application of the developed modeling framework was made to electron transport in tetrahydrofuran. To do so, a complete gas phase electron scattering cross section set was assembled and analysed using available experimental and theoretical data. Modifications of gas phase scattering to a simulated liquid phase were made using available experimental data. Comparison of streamer formation and propagation in both gaseous and simulated liquid tetrahydrofuran was studied to demonstrate applicability of the framework developed in this research to electron transport in biologically relevant soft-condensed matter.

# Acknowledgements

Without the help and support of countless people I would not have been able to finish this project. No doubt I will forget to include some people in this acknowledgement, my apologies in advance.

First thanks goes to my immediate supervisors Ron and Danny, for all the help and belief over the years. Things weren't always easy during the project, so I'm eternally grateful for the guidance and patience along the way.

Infinite thanks go to my family Debbie, Colin, Paul, and Kirsha for the constant love and belief in whatever crazy things I have been doing at university over the years. I know I've never made it easy to understand me, or what I've been working on, so thank you for always believing in me, even when I didn't.

Many thanks to my colleagues and collaborators through the various stages of my work. The excellent group of students and staff at JCU, as well as those abroad who have provided great advice or input data over the years. Your help was instrumental in allowing me to get somewhere with this work, thank you.

Thanks goes to all of my friends, old, new, local, and afar, for sticking with me during the last few years. Without the fun times, bad jokes, beers, cricket, football, video games, chats, arguments, and countless other things life would be very boring indeed.

I'd like to thank the long list of people who have supported me at JCU over the years, as both a student and staff member. The name of the department might change, regimes of management might come and go, buildings will rise and fall, but the people here are what makes this place great - thank you for including me and giving me an opportunity to learn.

Though she will have no way of ever knowing, thanks goes to my dog, Jersey, for bringing boundless energy and happy memories after even the worst days at the office.

Finally, the last thanks goes to my dear Erin. Without your constant love and support I would be nothing. In the darkest times, you provided the spark that enabled me to see the light at the end of the tunnel. We finally made it - now onto the next adventure!

## Acknowledgement of financial support

I wish to acknowledge the financial support of:

- the Australian Government through the Australian Postgraduate Award scheme, which supported me through the bulk of my studies, and
- James Cook University through the HDR enhancement and write-up grant schemes, which enabled me to participate in conferences and finish the write-up of this thesis.

# Research Output

## Peer reviewed publications

---

The research undertaken during the PhD program, detailed in this document, has been published in the following first-authored journal articles:

[1] **NA Garland**, MJ Brunger, G Garcia, J de Urquijo, and RD White. Transport properties of electron swarms in tetrahydrofuran under the influence of an applied electric field. *Physical Review A*, 88 062712 (2013). Available online at doi:10.1103/PhysRevA.88.062712

[2] **NA Garland**, DG Cocks, GJ Boyle, S Dujko and RD White. Unified fluid model analysis and benchmark study for electron transport in gas and liquid analogs. *Plasma Sources Science and Technology*, 26 075003 (2017). Available online at doi:10.1088/1361-6595/aa73c6

[3] **NA Garland**, GJ Boyle, DG Cocks and RD White. Approximating the nonlinear density dependence of electron transport coefficients and scattering rates across the gas-liquid interface. *Plasma Sources Science and Technology*, 27 024002 (2018). Available online at doi:10.1088/1361-6595/aaa0c

The following publication has been submitted to *Plasma Sources Science and Technology* for peer-review:

**NA Garland**, I. Simonović, GJ Boyle, DG Cocks, S Dujko, RD White. Electron swarm and streamer transport across the gas-liquid interface: a comparative fluid model study. Submitted to *Plasma Sources Science and Technology* on the 29 of April 2018.

In addition, the co-authored publications below were produced, but do not directly form part of this thesis document:

[4] RD White, MJ Brunger, **NA Garland**, RE Robson, KF Ness, G Garcia, J de Urquijo, S Dujko, Z Lj Petrovic. Electron swarm transport in THF and water mixtures. *The European Physical Journal D* 68 (5), 125 19 (2014). Available online at doi:10.1140/epjd/e2014-50085-7

[5] RD White, DG Cocks, GJ Boyle, MJE Casey, **NA Garland**, D Konovalov, B Philippa, P Stokes, J de Urquijo, O González-Magaña, RP McEachran, SJ Buckman, MJ Brunger, G Garcia, S Dujko, and Z Lj Petrovic. Non-equilibrium electron transport in biomolecular gaseous and liquid systems: Theory, experiment and self-consistent cross-sections. *Plasma Sources Science and Technology*, 27 053001 (2018). Available online at doi:10.1088/1361-6595/aabdd7

## Conference presentations

---

The following conference presentations were made during the PhD program:

A framework for fluid modelling of continuous electron transport across the gas-liquid interface. Presented at XX International Symposium on Electron-Molecule Collisions and Swarms (POSMOL) 2017, Magnetic Island, Australia

Transport properties of electron swarms in simulated biological matter under the influence of an applied electric field. Presented at Gaseous Electronics Meeting (GEM) 2014, Victor Harbour, Australia.

In addition, the following posters were presented at conferences:

Towards a continuum model of electron transport across a gas-liquid interface. Presented at the 10th EU-Japan Joint Symposium on Plasma Processing (JSPP2017), Okinawa, Japan

A framework for fluid modelling of continuous electron transport across the gas-liquid interface. Presented at XX International Symposium on Electron-Molecule Collisions and Swarms (POSMOL) 2017, Magnetic Island, Australia

Higher order moment models of electron transport in gases and liquids. Presented at Gaseous Electronics Conference (GEC) 2016, Bochum, Germany.

Electronic versions of the manuscripts and conference presentations produced during the PhD program are available online at [ngarland.info/research](http://ngarland.info/research).

# Contents

<b>1</b>	<b>Introduction</b>	<b>1</b>
1.1	Scope, motivation, and applications . . . . .	1
1.2	Liquid transport modeling studies . . . . .	5
1.3	Kinetic theory and the Boltzmann equation . . . . .	5
1.3.1	The Boltzmann equation . . . . .	5
1.3.2	Collision term and scattering cross sections . . . . .	7
1.3.3	Electron scattering in liquids . . . . .	8
1.3.4	Alternative stochastic modeling methods . . . . .	11
1.4	Fluid modeling of low-temperature discharges . . . . .	12
1.4.1	Field dependent drift-diffusion models . . . . .	14
1.4.2	Energy dependent drift-diffusion models . . . . .	15
1.4.3	Higher order models . . . . .	16
1.4.4	Coupling electromagnetic fields . . . . .	17
1.5	Modeling packages . . . . .	17
1.6	Benchmark methods . . . . .	18
1.6.1	Experimental validation . . . . .	18
1.6.2	Validation against kinetic solutions . . . . .	18
1.6.3	Analytic time of flight solution . . . . .	19
1.7	Use of swarm experiments towards low-temperature plasma modeling . .	19
1.8	Electron transport data in biomolecules . . . . .	21
1.9	Research goals of this study . . . . .	22
1.10	Structure of this document . . . . .	23
<b>2</b>	<b>Fluid modeling of electrons in gas and liquid</b>	<b>25</b>
2.1	Chapter Introduction . . . . .	25
2.2	Theory . . . . .	26
2.2.1	Fluid Modeling . . . . .	26
2.2.2	Four Moment Electron Fluid Model . . . . .	29
2.2.3	Other Fluid Models . . . . .	32
2.3	Benchmark Results and Discussion . . . . .	34
2.3.1	Gas Phase Collision Model . . . . .	34
2.3.2	Liquid Phase Modification . . . . .	35
2.3.3	Input Data . . . . .	35
2.3.4	Hat Field Benchmarks . . . . .	40
2.3.5	Spatiotemporal Pulse Evolution . . . . .	47
2.3.6	Distribution effects and implications for fluid modeling . . . . .	51
2.4	Chapter Summary . . . . .	54
<b>3</b>	<b>Density dependence of electron transport data</b>	<b>56</b>
3.1	Chapter Introduction . . . . .	56
3.2	Theory . . . . .	57
3.2.1	Moment modeling for electron transport in gases and liquids . .	57

3.2.2	Interfacial density properties . . . . .	60
3.2.3	Simple model for benchmarking collisions in liquids . . . . .	61
3.3	Approximating electron transport at associated intermediate densities . . . . .	62
3.3.1	Momentum balance method . . . . .	63
3.3.2	Energy balance method . . . . .	66
3.3.3	Modified momentum balance method . . . . .	68
3.3.4	Practical implementation for plasma modeling . . . . .	72
3.3.5	Approximating collision frequencies across an interface . . . . .	73
3.4	Application to noble gas-liquid systems . . . . .	74
3.5	Chapter Summary . . . . .	77
<b>4</b>	<b>Electron swarm and streamer transport at the gas-liquid interface</b>	<b>81</b>
4.1	Chapter Introduction . . . . .	81
4.2	Fluid modeling in gases and liquids . . . . .	82
4.2.1	Fluid models for electron transport . . . . .	82
4.2.2	Transport data in gaseous and liquid argon . . . . .	85
4.3	Modeling at the gas-liquid interface . . . . .	89
4.3.1	Density profile variations . . . . .	90
4.3.2	Fluid model input data for continuum models between gas and liquid phases . . . . .	91
4.3.3	Space-charge field & spatially varying permittivity . . . . .	92
4.3.4	Accommodating spatial variation of $V_0$ across the interface . . . . .	93
4.4	Numerical solution of system of hyperbolic PDEs . . . . .	93
4.5	Results and discussion . . . . .	94
4.5.1	Simulation conditions . . . . .	94
4.5.2	Electron transport from liquid argon into gaseous argon . . . . .	95
4.5.3	Electron ionisation front transport from gaseous argon into liquid argon . . . . .	102
4.5.4	Impact of step function input data . . . . .	110
4.5.5	Use of gas phase data to simulate liquid transport . . . . .	116
4.6	Chapter Summary . . . . .	121
<b>5</b>	<b>Scattering, transport, and simulation of electron transport in THF</b>	<b>130</b>
5.1	Chapter Introduction . . . . .	130
5.2	cross sections in THF . . . . .	131
5.2.1	Grand total cross section set . . . . .	131
5.2.2	Elastic cross section set . . . . .	132
5.2.3	Vibrational excitation and ionisation cross section sets . . . . .	133
5.2.4	Electronic-state excitation cross section sets . . . . .	135
5.2.5	Unknown cross sections: rotations and neutral dissociation . . . . .	136
5.3	Transport properties of electrons in gaseous THF . . . . .	137
5.3.1	Swarm transport coefficients . . . . .	138
5.3.2	Boltzmann equation and its solution . . . . .	140
5.3.3	Electron transport in THF . . . . .	142
5.3.4	Swarm experiment considerations in THF using the pulsed-Townsend technique . . . . .	146
5.4	Modifications for transport in liquid THF . . . . .	146
5.5	Modeling of electron ionisation fronts in gaseous and structured THF . . . . .	148
5.6	Chapter Summary . . . . .	151

<b>6 Conclusion</b>	<b>155</b>
6.1 Summary of results . . . . .	155
6.2 Future research directions . . . . .	156
<b>References</b>	<b>158</b>
<b>A Flux-corrected transport methods for hyperbolic PDEs</b>	<b>175</b>
A.1 Introduction . . . . .	175
A.1.1 Finite difference methods . . . . .	176
A.2 Flux-Corrected Transport schemes . . . . .	176
A.2.1 FCT algorithm . . . . .	177
A.2.2 Explicit versus implicit discretisation . . . . .	179
A.2.3 Spatial discretisation . . . . .	180
A.2.4 Time discretisation . . . . .	182
A.3 Unit testing and validation . . . . .	182
A.3.1 Square wave advection and advection-diffusion of a Gaussian pulse	182
A.3.2 Sod's shock tube . . . . .	185
A.4 Poisson equation solution . . . . .	187
A.5 Treating zero density regions . . . . .	188
A.6 Scaling variables . . . . .	188

# List of Figures

1.1	Electron temperature versus density landscape of typical natural and man-made plasmas . . . . .	1
1.2	Lightning propagation demonstrating streamer filaments branching from the leader front . . . . .	2
1.3	Dual phase particle detector schematic diagram. . . . .	3
1.4	As an example of experimental plasma medicine apparatus (Left) APPJ plasma jet source, and (Right) kINPen prototype presented by Höntsch <i>et al.</i> [6] . . . . .	4
1.5	Plasma medicine schematic diagram demonstrating the array of physical processes that can occur throughout a typical plasma medicine treatment . . . . .	4
1.6	Schematic interaction of an incoming electron wave packet coherently scattering from multiple scattering centres, instead of a fixed centre, to an outgoing wave packet. . . . .	9
1.7	Typical static structure factors for gas, liquid, and solid (crystal) states of matter, where $d$ is the crystal interatomic distance. . . . .	10
1.8	Computational flow diagram for a PIC-MC scheme. . . . .	12
1.9	Summary of the ultimate goal of a tissue analogue input data for simulations . . . . .	21
2.1	Hydrodynamic transport input data for gas and liquid phase transport for collision model in Table 2.1. <b>(a)</b> Reduced electron mobility coefficient; <b>(b)</b> Reduced electron longitudinal diffusion coefficient . . . . .	36
2.2	Electron collision rate input data for gas and liquid phase transport for collision model in Table 2.1. <b>(a)</b> Effective reduced energy transfer collision rate, $\frac{\nu_e}{n_0}$ ; <b>(b)</b> Effective reduced momentum transfer, $\frac{\nu_m}{n_0}$ , and energy flux transfer, $\frac{\nu_\xi}{n_0}$ , collision rates. . . . .	37
2.3	Higher order closure input for gas and liquid media according to collision model in Table 2.1: <b>(a)</b> Momentum balance term, $\theta_m^{ss}$ ; <b>(b)</b> energy flux balance term, $\theta_\xi^{ss}$ . . . . .	39
2.4	Hat and inverse hat field benchmark problem geometry . . . . .	40
2.5	Gas phase hat field perturbation benchmark as per Figure 2.4 where $\tilde{L}_{\text{HAT}} = 30$ , $\frac{\mathbf{E}}{n_0} = -1 \text{ Td} : -10 \text{ Td} : -1 \text{ Td}$ . . . . .	43
2.6	Liquid phase hat field perturbation benchmark as per Figure 2.4 where $\tilde{L}_{\text{HAT}} = 50$ , $\frac{\mathbf{E}}{n_0} = -1 \text{ Td} : -5 \text{ Td} : -1 \text{ Td}$ . . . . .	44
2.7	Gas phase inverse hat field perturbation benchmark as per Figure 2.4 where $\tilde{L}_{\text{HAT}} = 30$ , $\frac{\mathbf{E}}{n_0} = -1 \text{ Td} : -0.1 \text{ Td} : -1 \text{ Td}$ . . . . .	46
2.8	Liquid phase inverse hat field perturbation benchmark as per Figure 2.4 where $\tilde{L}_{\text{HAT}} = 50$ , $\frac{\mathbf{E}}{n_0} = -1 \text{ Td} : -0.2 \text{ Td} : -1 \text{ Td}$ . . . . .	47
2.9	Transient evolution of electron density from narrow Gaussian pulse. Gas phase media as per Table 2.1 with background $\frac{\mathbf{E}}{n_0} = -3 \text{ Td}$ . . . . .	49
2.10	Transient evolution of electron mean velocity from narrow Gaussian pulse. Gas phase media as per Table 2.1 with background $\frac{\mathbf{E}}{n_0} = -3 \text{ Td}$ . . . . .	51

2.11	Transient evolution of electron mean energy from narrow Gaussian pulse. Gas phase media as per Table 2.1 with background $\frac{\mathbf{E}}{n_0} = -3\text{Td}$ . . . . .	52
2.12	Transient mean energy evolution at $t_{\text{sample}} \approx 5\tau_e$ indicating sample points coinciding with $\langle \epsilon \rangle_{\text{ss}} = 0.8337\text{ eV}$ . . . . .	53
2.13	Comparison of typical energy distribution functions, $U^{\frac{1}{2}}f_0(U)$ , for transient heating and cooling regimes. Steady state distribution and drifted Maxwellian shown for comparison. . . . .	54
3.1	Argon vapor-liquid equilibrium interface as determined by molecular dynamics simulations [7–9]. Labels <b>G</b> and <b>L</b> denote dilute gas and liquid extremities respectively. Labels <b>I1</b> , <b>I2</b> , <b>I3</b> denote densities at one-quarter, half-way, and three-quarters along the density transition which will be used for benchmarking in Section 3.3. . . . .	61
3.2	Comparison of electron drift velocities in model simple liquids for $\phi = 0.1, 0.2, 0.3$ . Solid lines: multi-term solution of the Boltzmann equation [10]. Dashed lines: computed via approximation (3.25) derived from momentum balance. . . . .	65
3.3	Comparison of electron drift velocities in model simple liquids for $\phi = 0.1, 0.2, 0.3$ . Solid lines - multi-term solution of the Boltzmann equation [10]. Dashed lines - computed via approximation (3.29) derived from energy balance. . . . .	68
3.4	Comparison of approximated angle-integrated structure factors for Percus-Yevick model liquids. Solid lines - exact values via (3.31). Dashed lines - approximated $s$ via equations (3.33) and (3.34). . . . .	70
3.5	Comparison of electron drift velocities in model simple liquids for $\phi = 0.1, 0.2, 0.3$ . Solid lines - multi-term solution of the Boltzmann equation [10]. Dashed lines - computed via approximation (3.35) derived from structure modified momentum balance. . . . .	71
3.6	Comparison of electron drift velocities in model simple liquids for $\phi = 0.1, 0.2, 0.3$ . Solid lines - multi-term solution of the Boltzmann equation [10]. Dashed lines - computed via the practical approximation (3.36). . . . .	73
3.7	Approximated $\tilde{\nu}_m^{\text{mix}}$ for multiple packing fractions of Percus Yevick model liquid. Solid line: exact via multi-term kinetic solution [10], --: approximation via (3.37). . . . .	74
3.8	Electron drift velocity in liquid argon at 130 K. Present approximation computed via equation (3.38) compared with experimental results of Gushchin <i>et al.</i> [11]. Reference data: Boyle <i>et al.</i> [10, 12], Miller <i>et al.</i> [13], Pack <i>et al.</i> [14]. . . . .	76
3.9	Electron drift velocity in liquid xenon at 230 K. Present approximation computed via equation (3.38) compared with experimental results of Gushchin <i>et al.</i> [11]. Reference data: Boyle <i>et al.</i> [10, 15], Huang and Freeman [16], Pack <i>et al.</i> [14]. . . . .	77
4.1	Gas and liquid argon electron scattering cross sections utilized in this study. Gas cross section data of Hayashi [17] via www.lxcat.net. Liquid cross section data of Boyle <i>et al.</i> [12] and necessary modifications of Hayashi set detailed in Section 4.2.2. . . . .	87

4.2	Input transport data of electrons in argon for local-field dependent electron fluid models. Dashed lines denote gas transport, dotted lines denote liquid transport. (Top-left) Drift velocity versus reduced field. (Top-right) Electron mean energy versus reduced field. (Bottom-left) Longitudinal reduced diffusion coefficient versus reduced field. (Bottom-right) Reduced ionisation collision rate versus reduced field. . . . .	88
4.3	Input collision rates of electrons in argon for mean energy dependent higher order fluid model. Dashed lines denote gas transport, dotted lines denote liquid transport. . . . .	89
4.4	Input closure terms for mean energy dependent higher order fluid model for electrons in argon. (Left axis) Momentum balance closure term $\theta_m = \langle v_z v_z \rangle$ . (Right axis) Energy flux balance closure term $\theta_\xi = \langle v^2 v_z v_z \rangle$ . Dashed lines denote gas transport, dotted lines denote liquid transport. . . . .	89
4.5	Equilibrium argon vapor-liquid interface as determined by molecular dynamics simulations [7–9]. The interface transition region is marked explicitly. . . . .	91
4.6	Reduced electric field profiles for applied and $V_0$ contributions for both simulation configurations presented. Note that zero is included on the $E/n_0$ logarithmic axis to reinforce the zero contribution via the $V_0$ potential far from the interface. . . . .	95
4.7	Electron density evolution for 4MM and LFA models at short, intermediate, and longer times as the electron swarm propagates from liquid to gaseous argon. Top view: Macroscopic results. Bottom view: Expanded view of interfacial results. Initial condition given by green dotted green line. Direction of field-driven propagation is from left to right. . . . .	96
4.8	Average electron velocity for 4MM and LFA models at short, intermediate, and longer times as the electron swarm propagates from liquid to gaseous argon. Top view: Macroscopic results. Bottom view: Expanded view of interfacial results. Initial condition given by green dotted green line. Direction of field-driven propagation is from left to right. . . . .	98
4.9	Total $E/n_0$ and space-charge (S.C.) contribution to $E/n_0$ for 4MM and LFA models at short, intermediate, and longer times as the electron swarm propagates from liquid to gaseous argon. Top view: Macroscopic results. Bottom view: Expanded view of interfacial results. . . . .	100
4.10	Electron mean energy for 4MM model at short, intermediate, and longer times as the electron swarm propagates from liquid to gaseous argon. Top view: Macroscopic results. Bottom view: Expanded view of interfacial results. Initial condition given by green dotted green line. Direction of field-driven propagation is from left to right. . . . .	102
4.11	Electron density evolution for 4MM and LFA models at short, intermediate, and longer times as the electron streamer tip propagates from gaseous to liquid argon. Top view: Macroscopic results. Bottom view: Expanded view of interfacial results. Initial condition given by green dotted green line. Direction of field-driven propagation is from right to left. . . . .	104
4.12	Average electron velocity for 4MM and LFA models at short, intermediate, and longer times as the electron streamer tip propagates from gaseous to liquid argon. Top view: Macroscopic results. Bottom view: Expanded view of interfacial results. Initial condition given by green dotted green line. Direction of field-driven propagation is from right to left. . . . .	106

4.13	Total $E/n_0$ and space-charge (S.C.) contribution to $E/n_0$ for 4MM and LFA models at short, intermediate, and longer times as the electron streamer tip propagates from gaseous to liquid argon. Top view: Macroscopic results. Bottom view: Expanded view of interfacial results. . . . .	108
4.14	Electron mean energy for 4MM model at short, intermediate, and longer times as the electron streamer tip propagates from gaseous to liquid argon. Top view: Macroscopic results. Bottom view: Expanded view of interfacial results. Initial condition given by green dotted green line. Direction of field-driven propagation is from right to left. . . . .	110
4.15	Effects of tanh or step-function interface on electron density evolution for 4MM and LFA models at short, intermediate, and longer times as the electron streamer tip propagates from gaseous to liquid argon. Top view: Macroscopic results. Bottom view: Expanded view of interfacial results. Initial condition given by green dotted green line. Direction of field-driven propagation is from right to left. . . . .	112
4.16	Effects of tanh or step-function interface on average electron velocity for 4MM and LFA models at short, intermediate, and longer times as the electron streamer tip propagates from gaseous to liquid argon. Top view: Macroscopic results. Bottom view: Expanded view of interfacial results. Initial condition given by green dotted green line. Direction of field-driven propagation is from right to left. . . . .	114
4.17	Effects of tanh or step-function interface on electron mean energy for 4MM model at short, intermediate, and longer times as the electron streamer tip propagates from gaseous to liquid argon. Top view: Macroscopic results. Bottom view: Expanded view of interfacial results. Initial condition given by green dotted green line. Direction of field-driven propagation is from right to left. . . . .	115
4.18	Electron propagation of electrons in a streamer front within liquid argon. Green dotted series denotes the initial condition. Evolution over time denotes major differences when using liquid data, compared to simply scaling gas phase data. . . . .	116
4.19	Electron density evolution for 4MM, LFA, and LFAG models at short, intermediate, and longer times as the electron swarm propagates from liquid to gaseous argon. Top view: Macroscopic results. Bottom view: Expanded view of interfacial results. Initial condition given by green dotted green line. Direction of field-driven propagation is from left to right. . . . .	118
4.20	Average electron velocity for 4MM, LFA, and LFAG models at short, intermediate, and longer times as the electron swarm propagates from liquid to gaseous argon. Top view: Macroscopic results. Bottom view: Expanded view of interfacial results. Initial condition given by green dotted green line. Direction of field-driven propagation is from left to right. . . . .	120
4.21	Drift velocity surface of electrons in argon as a function of $\frac{E}{n_0}$ and $n_0$ used to interpolate input data for LFA models. . . . .	124
4.22	Reduced longitudinal diffusion coefficient, $n_0 D_L$ , surface of electrons in argon computed via the GER (4.25) as a function of $\frac{E}{n_0}$ and $n_0$ used to interpolate input data for LFA models. . . . .	125

4.23	Reduced ionisation collision rate, $\nu_I/n_0$ , surface of electrons in argon computed via (4.28) as a function of $\frac{E}{n_0}$ and $n_0$ used to interpolate input data for LFA models. . . . .	126
4.24	Reduced momentum transfer collision frequency, $\frac{\nu_m}{n_0}$ , surface of electrons in argon computed via (4.29) as a function of $\langle\epsilon\rangle$ and $n_0$ used to interpolate input data for the 4MM model. . . . .	127
4.25	Reduced lumped energy transfer rate, $\frac{S_\epsilon}{n_0}$ , surface of electrons in argon computed via (4.31) as a function of $\langle\epsilon\rangle$ and $n_0$ used to interpolate input data for the 4MM model. . . . .	128
4.26	Reduced ionisation collision frequency, $\frac{\nu_I}{n_0}$ , surface of electrons in argon computed via (4.32) as a function of $\langle\epsilon\rangle$ and $n_0$ used to interpolate input data for the 4MM model. . . . .	129
5.1	Proposed grand total cross section for electron scattering in THF, as compared with existing GTCS data (Mozejko <i>et al.</i> [18]; Fuss <i>et al.</i> [19]; Zecca <i>et al.</i> [20]; Chiari <i>et al.</i> [21]; Baek <i>et al.</i> [22]). . . . .	132
5.2	Proposed elastic ICS for electron scattering in THF, compared with existing data from which the set was constructed (Fuss <i>et al.</i> [19, 23]; Colyer <i>et al.</i> [24]; Gauf <i>et al.</i> [25]; Baek <i>et al.</i> [22]; Dampc <i>et al.</i> [26]). . . . .	133
5.3	Proposed elastic momentum transfer cross section for electron scattering in THF, compared with existing data from which the set was constructed (Gauf [25]; Colyer [24]; Baek <i>et al.</i> [22]; Dampc <i>et al.</i> [26]). . . . .	134
5.4	Proposed vibrational ICS for electron scattering in THF. See legend for further details. . . . .	135
5.5	Comparison of a subset of the recommended ICS for electron induced vibrational processes in THF [27], with the summed modes of Khakoo <i>et al.</i> [28]. . . . .	136
5.6	Comparison of the proposed ionisation cross sections for electron scattering in THF with the available theoretical calculations of Mozejko and Sanche [29] and Dampc <i>et al.</i> [30], and the measured data from Fuss <i>et al.</i> [23]. . . . .	137
5.7	Proposed electronic excitation ICS for electron scattering from THF, as determined using the data of Do <i>et al.</i> [31]. . . . .	138
5.8	Proposed neutral dissociation ICS for THF, as compared with the earlier estimation of Fuss <i>et al.</i> [19]. . . . .	139
5.9	Proposed rotational ICS for electron scattering from THF, as compared with the estimation of Fuss <i>et al.</i> [19] and the calculated result of Chiari <i>et al.</i> [21]. . . . .	140
5.10	Mean energy and ionisation rate for electrons in THF as a function of the reduced electric field. . . . .	144
5.11	Bulk (dashed) and flux (solid) drift velocities for electrons in THF as a function of the reduced electric field. The inset uses a linear scale to emphasize the differences. . . . .	144
5.12	Reduced transverse and longitudinal flux diffusion coefficients for electrons in THF as a function of the reduced electric field. . . . .	145
5.13	Two-term and multi-term approximations for the reduced flux transverse and longitudinal diffusion coefficients for electrons in THF as a function of the reduced electric field. . . . .	145

5.14	Static structure factor of liquid THF at atmospheric conditions measured by Bowron <i>et al.</i> [32] compared to an analytic structure factor computed via (3.18) assuming an ideal atomic liquid. The ideal gas value of $S(\Delta k) = 1$ is plotted as a reference. . . . .	147
5.15	Input transport data of electrons in THF for local-field dependent electron fluid models. (Top-left) Drift velocity versus reduced field. (Top-right) Electron mean energy versus reduced field. (Bottom-left) Longitudinal reduced diffusion coefficient versus reduced field. (Bottom-right) Reduced ionisation and attachment collision rates versus reduced field. . . . .	149
5.16	Input collision rates of electrons in THF for mean energy dependent higher order fluid model. Dashed lines denote gas transport, dotted lines denote liquid transport. . . . .	150
5.17	Input closure terms for mean energy dependent higher order fluid model for electrons in THF. Momentum balance closure term $\theta_m = \langle v_z v_z \rangle$ . Energy flux balance closure term $\theta_\xi = \langle v^2 v_z v_z \rangle$ . Dashed lines denote gas transport, dotted lines denote liquid transport. . . . .	151
5.18	Electron density propagation within liquid THF. Pink dotted series denotes the initial condition. Evolution over time denotes major differences when using liquid data, compared to simply scaling gas phase data. . . . .	152
5.19	Ion density created within liquid THF. Solid lines denote $n_+$ produced via electron impact ionisation. Dashed lines denote $n_-$ produced via electron attachment. Pink dotted series denotes the initial $n_+$ condition. Evolution over time denotes major differences when using liquid data, compared to simply scaling gas phase data. . . . .	153
5.20	Evolution of the electron mean velocity experienced by a streamer front within liquid THF. Pink dotted series denotes the initial condition. Evolution over time denotes major differences when using liquid data, compared to simply scaling gas phase data. . . . .	153
5.21	Evolution of the reduced electric field experienced by a streamer front within liquid THF. Pink dotted series denotes the initial condition. Evolution over time denotes major differences when using liquid data, compared to simply scaling gas phase data. . . . .	154
A.1	Spatial discretisation scheme employed for FCT . . . . .	177
A.2	Examples of flux limiting outcomes as per the Boris-Book limiter. Evaluating cases A and C with (A.5) allows a limited flux to be applied, as non-zero values are produced by the min-max operator. Cases B and D produce a cancelled zero flux as the signs of adjacent gradients do not agree. . . . .	179
A.3	Variable spatial grid implemented for a typical liquid to gas electron transport simulation . . . . .	181
A.4	Simplified schematic of a time of flight experiment . . . . .	183
A.5	Example unit test results for: (top) a 1st order upwind spatial discretisation, (bottom) a FCT solution where 4th order central differences are limited by a 1st order upwind scheme. . . . .	184
A.6	Numerical error and conservation count of (top) a 1st order upwind spatial discretisation, (bottom) a FCT solution where 4th order central differences are limited by a 1st order upwind scheme. . . . .	185
A.7	Sod's shock tube solutions for: (top) a 1st order upwind spatial discretisation, (bottom) a FCT solution where 4th order central differences are limited by a 1st order upwind scheme. . . . .	187

# 1

## Introduction

### 1.1 Scope, motivation, and applications

---

Low temperature, non-equilibrium plasmas are generally defined where typical electron temperatures,  $T_e$ , are much higher than equilibrium ion,  $T_i$ , and background neutral species temperatures,  $T_0$  [33]. Typical plasma neutral densities,  $n_0$ , are on the order of  $10^{24} \text{ m}^{-3}$ , and ionisation rates are typically  $\sim 1\%$  [33,34]. Some well known examples of natural and man-made plasmas are shown in Figure 1.1, where the scope of low-temperature plasma electron temperatures and densities,  $n_e$ , are denoted.

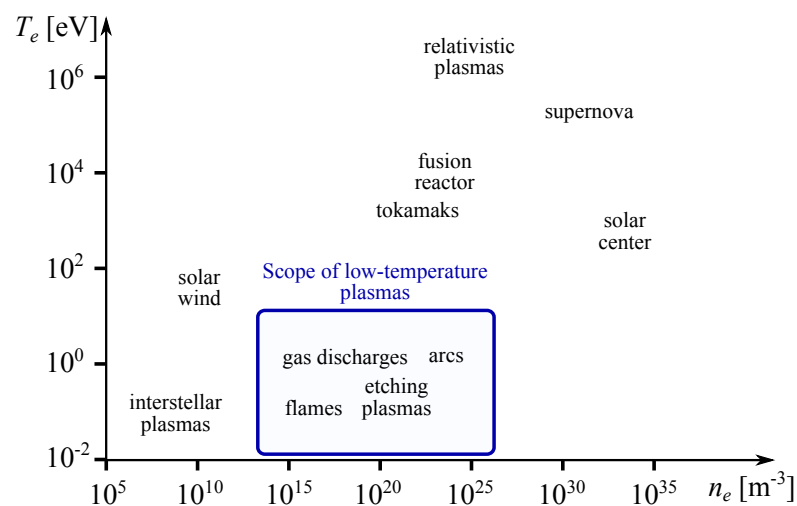


Figure 1.1: Electron temperature versus density landscape of typical natural and man-made plasmas

For decades the use of low-temperature plasma processes has allowed modern society

to prosper, primarily through the application of microelectronic device manufacturing. Alongside other manufacturing methods, such as wet chemical etching or lithographic methods, plasma etching of silicon, oxides, and metal substrates forms a vital step in the manufacturing process of complicated microelectronic devices that have formed the foundation of the technological revolution. In addition to highly profitable applications, such as microelectronic circuit manufacture, low-temperature plasma discharges are commonly found in nature when lightning forms and propagates through the atmosphere as outlined in Figure 1.2.



Figure 1.2: Lightning propagation demonstrating streamer filaments branching from the leader front

In these discharges, following an initial seed ionisation event, such as a spark, the high energy streamer tip (leader) propagates through space creating further electron/ion pairs at the front of the discharge. In doing so, the newly created charged particles render the space behind the propagating streamer front electrically neutral. As the front progresses, and further ionisation events occur, rapidly moving electrons can branch into essentially vacant regions of space and continue propagation of the discharge via transient filament branches.

Despite massively different length scales, both lightning and laboratory or industrial low-temperature plasma discharges are governed by the same underlying physics. Some present industrial applications of these discharges are in air purification or ozone generation, where high energy electrons are used to initiate the desired chemical reactions without having to expend a great deal of energy that would normally be required to heat up the entire body of gas [35–37]. A further use of streamer discharges is in the generation of so called “plasma bullets”, which are presently finding application in medical treatments.

While the previously discussed applications have focused on gas phase applications, there are some applications that employ gas-liquid interfacial transport to exploit the differences in liquid phase transport compared to gas phase. Liquid phase particle detectors are one such application, and they are used to detect ionisation events in

dense cryogenic liquids, such as argon or xenon, caused by (anti)neutrinos or weakly interacting massive particles (WIMPs) in the search for dark matter [38–41]. Large volumes of noble liquids are used for this purpose to take advantage of high liquid densities so to increase the probability of a desired particle interaction. In practice, dual phase configurations are often used to assist in extraction and detection of the desired ionisation events.

Dual phase detectors function by applying an external electric field across the device to extract electrons from liquid to gas, after which they are accelerated through gaseous electron multipliers (GEMs) that subject electrons to strong electric fields [39], outlined in the schematic in Figure 1.3. From the initial weak ionisation signal, an electron avalanche is produced through the GEM stage and a significant current is measured through the external observation equipment to indicate the detection of a collision event. In this thesis, the application of dual phase particle detectors is used as one motivator to study electron transport across the gas-liquid interface.

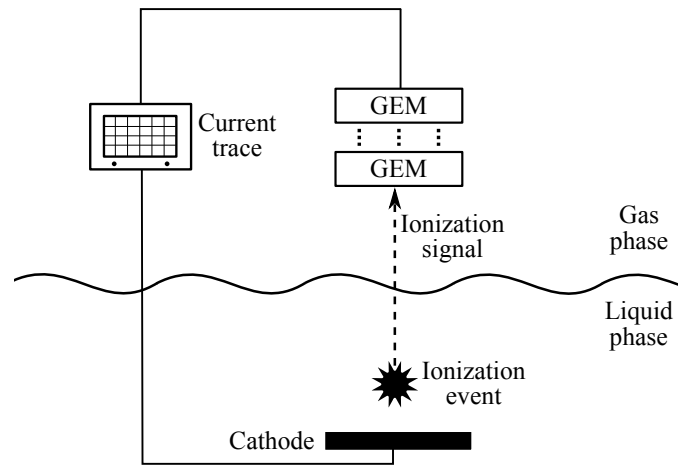


Figure 1.3: Dual phase particle detector schematic diagram.

At the nexus of gas and liquid discharge applications is the emerging application of plasma medicine [42–46]. One avenue of plasma medicine focuses on the treatment of solid surfaces, materials and devices in order to sterilise them or enhance their properties for medical purposes; for example, sterilisation of stainless steel surgical tools. Another focus of plasma medicine is the direct application of plasmas, or their products, to tissue with the aim of initiating biological responses for therapeutic treatment of infected wounds, skin conditions, and surgical incisions and haemorrhages. Generally, biological effects are divided into lethal or non-lethal. Lethal outcomes are the inactivation of microorganisms or cells, such as bacteria. Non-lethal outcomes can include metabolism stimulation, cell proliferation, or cell detachment from matrix complexes [6].

With a focus on treatment of tissue, by striking a balance between lethal and non-lethal effects, the overall aim of plasma medicine treatment is to use near room temperature, ambient pressure plasmas, shown in Figure 1.4, to first cauterise the area and then stimulate tissue regeneration and healing via beneficial metabolic reactions induced by reactive oxygen or nitrogen species (RONS) delivered via the atmospheric air

based plasma [42, 46]. Multiple laboratory and clinical studies have been performed in order to gauge the efficacy, and importantly the safety, of plasma medicine treatments, with prototype devices such as the kINPen developed by INP Greifswald, shown in Figure 1.4, leading this clinical field of study.

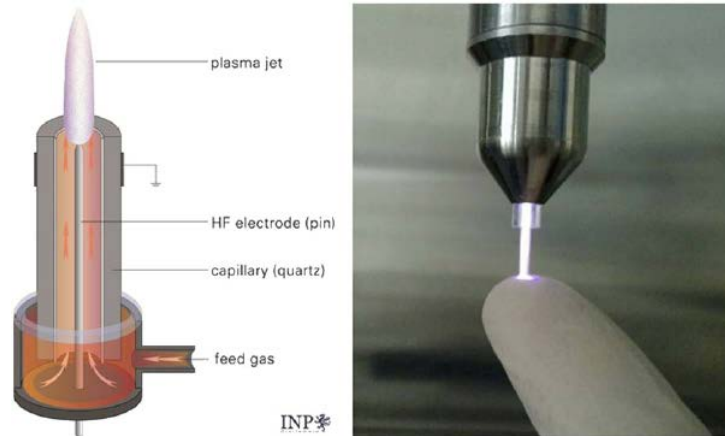


Figure 1.4: As an example of experimental plasma medicine apparatus (Left) APPJ plasma jet source, and (Right) kINPen prototype presented by Höntschi *et al.* [6]

Through the interaction of gas phase plasmas and dense soft tissue a wide array of physical processes occur during application of a plasma medicine treatment. Transfer of charge, mass, and energy via bombardment of reactive and excited species, charged particles, metastables, grounded neutrals, and photons generated from the low temperature plasma couple with absorption and emission from the surface of tissue to form a complex interfacial environment outlined in Figure 1.5. The penetration of the electric field into tissue has also been identified as a possible key variable in terms of moderating patient thermal tolerances, and also the types of reactions that may occur within a short depth into the tissue layer [47].

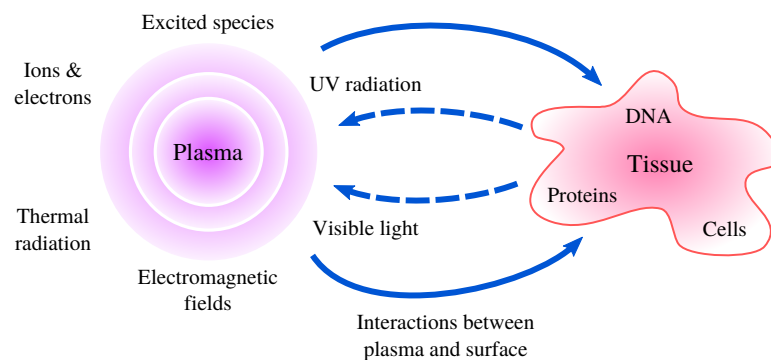


Figure 1.5: Plasma medicine schematic diagram demonstrating the array of physical processes that can occur throughout a typical plasma medicine treatment

A framework to analyze, understand, and improve how low temperature plasma interacts with soft condensed matter is essential to improve efficacy and understanding of emerging interfacial plasma technologies [47] and is a driving factor behind this current study.

## 1.2 Liquid transport modeling studies

---

In comparison to gas phase modeling, in liquid systems and discharges there considerably more complex processes involved, such as structure effects, electron solvation and evaporation, that make a comprehensive modeling approach difficult [48–53]. There have been various approaches to modeling free electron transport in atomic liquids, generally varying in the way structure effects such as electron coherent scattering and long-range interaction potentials are defined [54–56]. Foundations laid by Lekner [57], and later extended by the groups of Atrazhev [58–61], Schmidt [54,62], Sakai [55,56], and Borghesani [63,64], describe approaches to providing the effective scattering potential that the electron sees within the liquid. Recent Monte Carlo studies [65] have presented advances in modeling electron transport in atomic liquids through accommodation of coherent electron scattering effects.

In addition to fundamental electron transport in atomic liquids, modeling studies of liquid discharge and plasma-liquid interface applications have been undertaken. To simulate transport in liquids, some recent studies have used electric conductivity and permittivity changes between model material phases [50], density scaled gas phase electron diffusion coefficients [49,53], or constant empirical transport coefficients and rates [52,53] to provide new understanding of plasma species transport at gas-liquid interfaces. While previous pragmatic studies have provided some insight to important plasma applications, the incorporation of accurate, fundamental liquid transport physics into existing “gas phase models”, in order to describe liquid discharge and plasma-liquid interface applications, presents an open question for research.

## 1.3 Kinetic theory and the Boltzmann equation

---

In the previous sections it was highlighted that low-temperature plasmas are central to many natural and man-made processes and applications, and contain many complex physical phenomena. As science and industry seeks to improve performance of processes, such as plasma medicine or dual-phase particle detectors, the ability to provide accurate predictions of discharge properties becomes crucial. To acquire deep understanding of charged particle transport within such systems, mathematical descriptions of the complex transport and collision physics have been developed. The most detailed descriptor of charged particle transport within a plasma is the phase-space distribution function,  $f(\mathbf{r}, \mathbf{v}, t)$ , which describes the evolution in time,  $t$ , of charged particles through phase space,  $(\mathbf{r}, \mathbf{v})$ . The science of formulating and solving the charged particle distribution function is kinetic theory.

### 1.3.1 The Boltzmann equation

The Boltzmann equation [66] is a continuity equation in phase space and takes the form

$$\frac{\partial f}{\partial t} + \mathbf{v} \cdot \nabla f + \mathbf{a} \cdot \nabla_{\mathbf{v}} f = -J(f), \quad (1.1)$$

where  $\frac{\partial f}{\partial t}$  describes the local time rate-of-change of the distribution function,  $\mathbf{v} \cdot \nabla f$  describes variation of the distribution function due to particles streaming in and out of volume elements in position space due to pressure gradients in phase space. The  $\mathbf{a} \cdot \nabla_{\mathbf{v}} f$  term describes the variation of the distribution function due to external forces acting on the particles, often due to electromagnetic fields. The collision operator,  $J(f)$ , seeks to describe the change in the charged particle distribution function due to all types of particle collisions with all targets within the system.

The current state-of-the-art methods for solving (1.1) are accurate multi-term solutions [5, 10, 48, 67] found by decomposing  $f(\mathbf{r}, \mathbf{v}, t)$  to separate the speed and velocity angular component,  $\hat{\mathbf{v}}$ , via a spherical harmonic expansion

$$f(\mathbf{r}, \mathbf{v}, t) = \sum_{l=0}^{\infty} \sum_{m=-l}^l f_m^{(l)}(\mathbf{r}, v, t) Y_m^{[l]}(\hat{\mathbf{v}}), \quad (1.2)$$

where  $Y_m^{[l]}(\hat{\mathbf{v}})$  are spherical harmonics as a function of angles  $\hat{\mathbf{v}}$ . If a symmetry exists in the problem geometry, for example through an electric field being applied in plane-parallel configuration, then simpler expansion functions, such as Legendre polynomials,  $P_l$ , can be used instead of spherical harmonics [10].

Depending on the system under investigation, further expansions are often required. If the system is in a hydrodynamic regime, where only small space-time gradients persist, then it is common to represent, or project, the spatial dependence via gradients of the electron density,  $\nabla^k n$ . For systems in a non-hydrodynamic regime, a density gradient expansion may not be sufficient to resolve complex transport phenomena. In this regime the space dependence must be treated at the same level as the speed or time and full representations of the space dependence are required. Independent of the spatial dependencies, representation of the speed dependence is required and various options exist [10, 48, 68, 69]. The solution process always aims to yield a coupled hierarchy of equations that can be numerically solved to yield the expansion coefficients  $f_m^{(l)}$  of (1.2). When a distribution function is known, measurables and transport coefficients, such as drift velocity,  $W$ , and longitudinal and transverse diffusion coefficients,  $D_L$ ,  $D_T$ , previously mentioned, can be computed via appropriate velocity integrals over the distribution function. For example, the simplest transport variable is the electron number density  $n(\mathbf{r}, t) = \int f(\mathbf{r}, \mathbf{v}, t) d\mathbf{v}$ .

While very accurate, the numerical solution of the Boltzmann equation in multidimensional phase space is computationally demanding and there are a number of other factors that limit the application of this method for low-temperature plasma modeling, including (i) the combined complexity of evaluating the collision integral at each time step while transporting the solution in position and velocity space, and (ii) for non-trivial geometries the numerical implementation, including boundary conditions, is very difficult [10, 68, 70]. As a result, the use of kinetic methods for low-temperature plasma simulations has not been employed in this study, however existing codes developed from the kinetic solution framework of Boyle *et al.* [10] were utilised to generate input

data for fluid models used in this study.

### 1.3.2 Collision term and scattering cross sections

All collision processes can be described mathematically by a differential cross section,  $\sigma(g, \theta)$  where  $g$  is the relative velocity between two colliding particles in the centre-of-mass reference frame and  $\theta$  is the angle at which the incoming particle is scattered from the target in the centre-of-mass frame. Scattering cross sections can be obtained experimentally, through scattering or unfolding swarm experiments [4, 71–73], or from quantum mechanical calculations [74, 75]. A differential cross section is a measure of the probability that an incoming particle of a certain energy (such as an electron) interacting with a target particle for a given collisional process is scattered through an angle  $\theta$ , into a solid angle  $d\Omega$  [76]. If one integrates the differential cross section over all solid scattered angle elements then the total cross section of a process can be found to be

$$\sigma(g) = 2\pi \int_0^\pi \sigma(g, \theta) \sin \theta d\theta.$$

Electron scattering cross sections are functions of the relative speed,  $g$ . It is also common to write dependence as a function of the centre-of-mass energy,  $\epsilon = \frac{1}{2}\mu g^2$ , where  $\mu = \frac{m_e m_0}{m_e + m_0}$  is the reduced mass of the electron-target system for electron mass,  $m_e$ , and neutral target mass,  $m_0$ .

To evaluate the collision operator,  $J(f)$ , on right-hand-side of (1.1), the semi-classical collision integral of Wang-Chang-Uhlenbeck-deBoer [77] is often used for the rate of change of  $f$  due to conservative collisions, allowing for transitions in internal energy states of the neutral molecular targets due to inelastic collisions,  $j \rightarrow j'$ ,

$$\frac{\partial f}{\partial t} + \mathbf{v} \cdot \nabla f + \mathbf{a} \cdot \nabla_{\mathbf{v}} f = \sum_{j, j'} \int d^3 v_0 \int d^2 \Omega_{\mathbf{g}'} g \sigma(j, j'; \mathbf{g}, \mathbf{g}') [f(\mathbf{r}, \mathbf{v}', t) f_0(\mathbf{r}_0, \mathbf{v}'_0, t) - f(\mathbf{r}, \mathbf{v}, t) f_0(\mathbf{r}_0, \mathbf{v}_0, t)], \quad (1.3)$$

where subscript 0 denotes quantities of the neutral background, superscript ' denotes post-collision quantities,  $d^2 \Omega_{\mathbf{g}'}$  denotes the solid scattering angle,  $\mathbf{g}$  the relative velocity in the centre of mass frame, and  $\sigma(j, j'; \mathbf{g}, \mathbf{g}')$  is the electron-neutral differential scattering cross section which serves as the microscopic input to this solution method. Additional collision operators have been proposed to compute rates of change due to non-conservative collisions such as attachment and ionisation [76, 78, 79].

Within plasmas, various types of collisions occur between the various species (electrons, ions, neutrals). A knowledge of charged particle collisions is essential to accurately model the collision dynamics of a low-temperature plasma. For the types of plasmas investigated in this study, the collisions of primary concern are those of charged particles with the target neutral species. Collisions between ions and electrons themselves may occur, through recombination or Coulomb scattering, but it has been

noted in literature that for the densities pertinent to low-temperature plasmas these scattering processes are negligible compared to neutral target scattering [76,80].

### 1.3.3 Electron scattering in liquids

Up to this point, the treatment of charged particle collisions with dilute gas species has been under the assumption that each incoming particle interacts solely with one neutral target. When gas densities,  $n_0$ , are sufficiently high, or if any liquid discharge is considered, the effects of bringing adjacent neutral targets close together must be considered. The major scattering effects that are introduced at these densities are coherent elastic scattering and interaction potential screening [12, 48, 57, 81]. These density-dependent scattering effects must be considered when the incoming charged particle de Broglie wavelength,  $\lambda_{dB} = h/p$  where  $h$  is the Planck constant and  $p$  is the electron momentum, is on the order of the average intermolecular spacing  $n_0^{-1/3}$  [48]. For heavy charged particles such as ions the single scattering limit for dilute gases may be used. On the other hand, when considering transport of light charged particles, like electrons, in very dense fluids the  $\lambda_{dB} \sim n_0^{-1/3}$  criterion is approached and consequently liquid phase scattering phenomena must be considered.

As the neutral density of a medium increases beyond that of a dilute gas, such as that of a dense gas or liquid, the binary scattering approximation of an incoming electron interacting solely with one target breaks down. In this high density regime, adjacent neutral species experience temporal and spatial correlations between one another and collectively modify elastic electron scattering, resulting in coherent scattering [12, 15, 81]. To assist in quantitatively describing coherent scattering, the single scattering classical description must be reconsidered as a particle wave incident on multiple scattering centres as shown in Figure 1.6, where the classical properties are translated to equivalent wave properties of wave number,  $\mathbf{k}$ , and angular frequency,  $\omega$ ,

$$\hbar\mathbf{k} = m_e\mathbf{v}, \quad (1.4)$$

$$\hbar\omega = \frac{1}{2}m_e v^2. \quad (1.5)$$

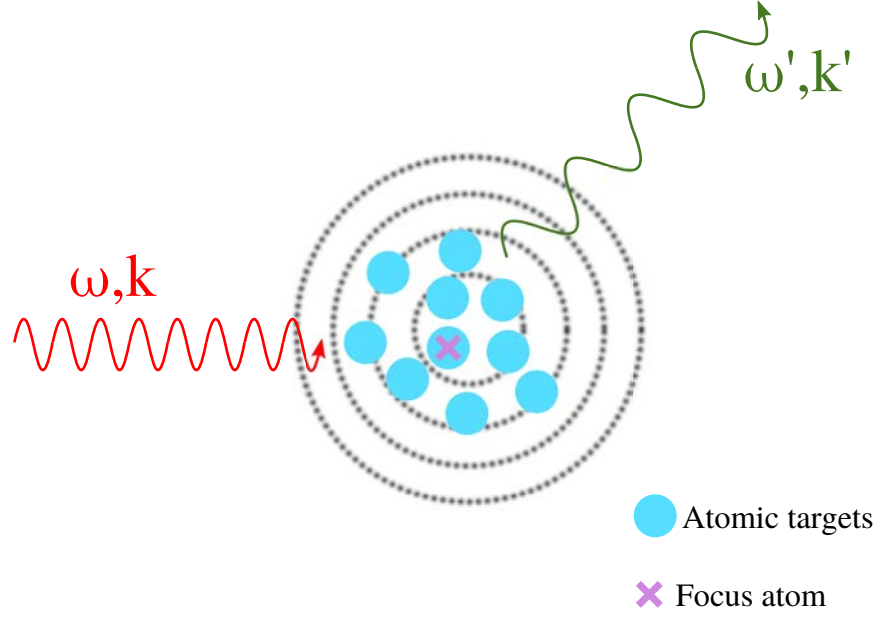


Figure 1.6: Schematic interaction of an incoming electron wave packet coherently scattering from multiple scattering centres, instead of a fixed centre, to an outgoing wave packet.

By now considering the electron as a wave a double differential cross section can be formulated to describe electron scattering in a structured medium as the product of: (i) a single particle differential cross section in the lab frame  $\sigma_{\text{lab}}(|\Delta\mathbf{k}|, \hat{\mathbf{k}}')$ , and (ii) the dynamic structure factor,  $S(\mathbf{k}, \Delta\omega)$  [82]

$$\frac{d\sigma}{d\hat{\mathbf{k}}'d\omega'} = \sigma_{\text{lab}}(|\Delta\mathbf{k}|, \hat{\mathbf{k}}') S(\mathbf{k}, \Delta\omega), \quad (1.6)$$

where  $\hat{\mathbf{k}}$  is the unit vector denoting wave number direction,  $\Delta\mathbf{k} = \mathbf{k} - \mathbf{k}'$  is the change in wave vector, and  $\Delta\omega = \omega - \omega'$  is the change in energy due to the coherent interaction with the structured medium.

The single particle differential cross section,  $\sigma_{\text{lab}}$ , is related to the interaction potential experienced by a single incoming electron, which may experience modifications from the gas phase cross section due to collective potential screening effects to be outlined in the next section. The dynamic structure factor is defined as the Fourier transform of the space-time pair-distribution function. In practice, however, one can evaluate the effects through a knowledge of the static structure factor,  $S(\mathbf{K})$ , through expanding  $S(\mathbf{k}, \Delta\omega)$  about a small relative energy exchange,  $\Delta\omega/\frac{1}{2}m_e v^2$  [48]. The static structure factor,  $S(\mathbf{K})$ , is computed via the Fourier transform of the pair correlation function, which can be obtained analytically for simple interaction potentials [83], from molecular dynamics simulations [84], or measured experimentally through neutron scattering [85]. The static structure factor provides information on how spatially correlated scattering centres are in the dense medium; ideal limits of static structure factors for the three states of matter are demonstrated in Figure 1.7.

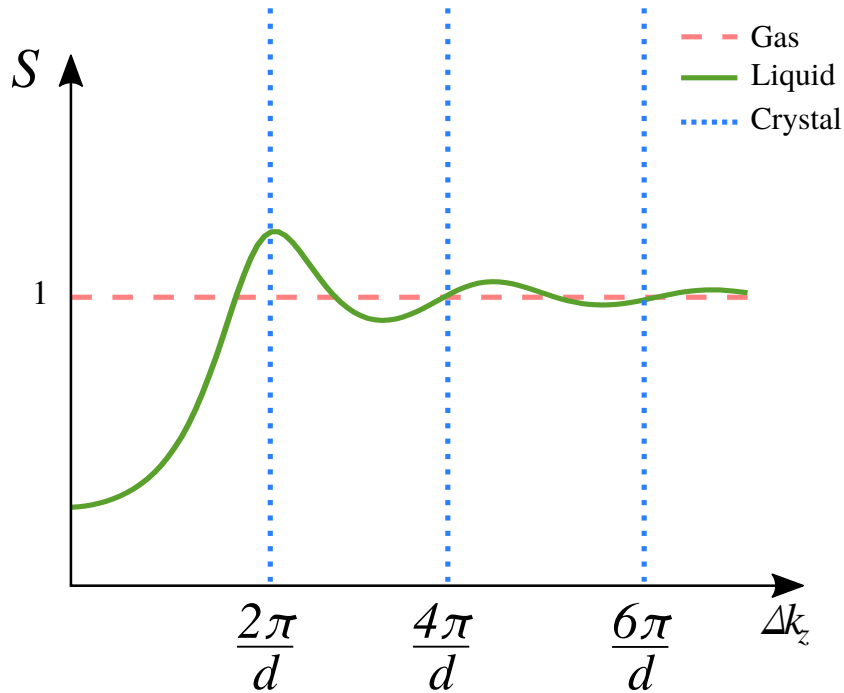


Figure 1.7: Typical static structure factors for gas, liquid, and solid (crystal) states of matter, where  $d$  is the crystal interatomic distance.

Only elastic collisions are coherent in nature, and hence influenced by the structure of the medium. In inelastic collisions, such as excitation or ionisation, energy is transferred on a localised site during scattering, which makes a particular target atom/molecule distinguishable from its neighbours. As a result these scattering events are incoherent and interference effects are not considered [15, 48]. There is an analogous effect for inelastic collisions, which is due to collective excitations. This occurs when the excited state in the liquid can be delocalised across several molecules; this effect can be seen in electron energy loss spectra [41, 63, 81].

In addition to the effects of coherent scattering on electron transport in liquids, the screening of the electron-neutral interaction potential must be considered. This screening effect occurs because more than one neutral particle is significantly polarised by the charged particle at any time. Overlapping polarisation fields act to screen the polarisation field of neighbouring polarisable neutral particles overlaps and acts to screen the long-range polarisation potential felt by an incoming electron. These effects and modifications have been recently studied for simple atomic liquids [12, 15] by extending the formalism of Lekner [57] to compute an ensemble average potential, that accounts for the collective effects of static and polarisation fields of nearby atoms on a fixed scattering centre. This ensemble average interaction potential is then used to compute an appropriately modified single-scattering differential cross section,  $\sigma_{\text{lab}}$ , introduced in the previous section. Recent studies of simple atomic liquids have applied an *ab initio* method to accurately account for these liquid scattering effects in the calculation of electron interaction cross sections [12, 15, 81].

### 1.3.4 Alternative stochastic modeling methods

While solution of the Boltzmann equation provides a deterministic approach to computing the phase space particle distribution function, stochastic methods are often employed to simulate collision dynamics and track the evolution of the charged particle distribution function in a low-temperature plasma. Stochastic simulation methods for low-temperature plasmas generally include Monte Carlo (MC) methods [56, 65, 86, 87] or hybrid Particle-in-cell (PIC) models that use MC methods to stochastically predict collision events [88–90]. Through the statistical power of having a large sample of test particles, and running many repeated simulations for a given configuration, an approximation to the distribution function, and hence ensemble averaged quantities describing discharge behaviour, can be found.

The general prescription for these methods is to begin with a known number of particles and then monitor the number, positions, and velocities of these particles as the discharge evolves over time. These methods stochastically predict collisions to simulate the effects of collision events on the distribution function, and deterministic expressions for the equations of motion are used to step-forward in time to predict particle velocities and positions

$$\mathbf{v}(t_0 + \Delta t) = \mathbf{v}(t_0) + \int_{t_0}^{t_0 + \Delta t} \mathbf{a}(t) dt, \quad (1.7)$$

$$\mathbf{r}(t_0 + \Delta t) = \mathbf{r}(t_0) + \int_{t_0}^{t_0 + \Delta t} \mathbf{v}(t) dt, \quad (1.8)$$

where  $\Delta t$  is a sufficiently small time increment from the current time,  $t_0$ , generally limited by the process with the highest collision frequency or a Courant-Friedrich-Lewy (CFL) condition [88].

In addition to using the equations of motion (1.7)-(1.8) for predicting a particle's phase-space position, the scheme will add or remove particles entering or leaving the system boundaries. Furthermore, once transport and collision processes have been computed, the self-consistent electric field is computed using Poisson's equation for the next time-step of the simulation. The program flow for a typical hybrid PIC-MC plasma discharge simulation is given in Figure 1.8, showing the computational sequences previously described for a hybrid scheme.

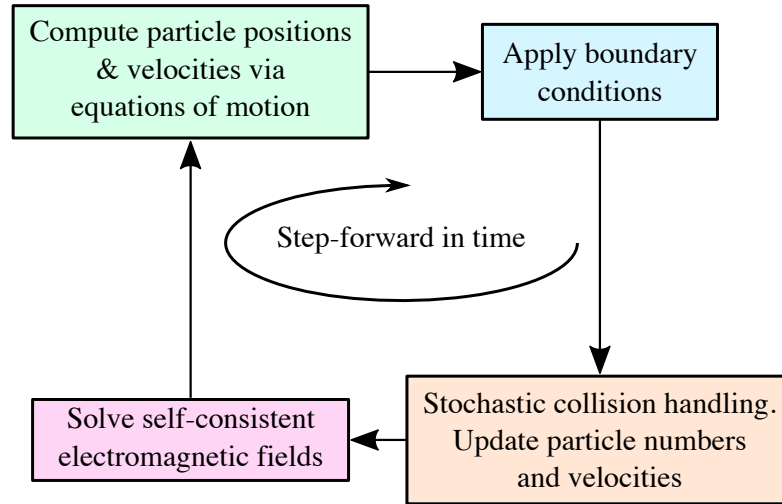


Figure 1.8: Computational flow diagram for a PIC-MC scheme.

Although hybrid kinetic models are rich in information of the system they have limitations. It has been observed that species with slow collision frequencies for production and loss are not easily implemented into PIC-MC simulations [33]. This is an important limitation to recognise as simulations of plasma-liquid systems considering both gas and liquid transport may often include large disparities in time scales. Computationally, particle based models are limited by the number of species they can simulate, as well as the sheer number of particles they can simulate in phase-space. As was the case for numerical solution of the Boltzmann equation, the necessary interfacial geometry and input data requirements in this study can add significant computational time overhead, and as such hybrid PIC-MC models were not used in this study.

## 1.4 Fluid modeling of low-temperature discharges

The origins of low-temperature plasma modeling can be traced back to the work of Ward in 1958 [91], but more recently the theoretical kinetic formulation of Robson [70] and Boeuf [92] can be viewed as solid foundations for modern low-temperature plasma models. The mathematical models for simulation of a plasma take many forms, each with varying orders of accuracy and complexity. Generally as the accuracy of a model increases so does the complexity. The balance between accuracy and complexity is important when it comes to choosing a modeling method.

Kinetic methods yield knowledge of a charged particle phase-space distribution function  $f(\mathbf{r}, \mathbf{v}, t)$ . While this provides a very accurate description of transport dynamics within a plasma, or swarm, the computational and mathematical overhead of these methods can be quite demanding, and as a result the low-temperature plasma community has adopted some simpler, macroscopic modeling methods as an alternative. Fluid models describe the space-time evolution of velocity averaged quantities such as number density, particle flux, and mean energy [92–95]. By integrating the Boltzmann equation

(1.3) over all velocities, a generic moment equation can be generated

$$\frac{\partial}{\partial t} (n \langle \Phi \rangle) + \nabla \cdot (n \langle \mathbf{v} \Phi \rangle) - n \langle (\mathbf{a} \cdot \nabla_{\mathbf{v}}) \Phi \rangle = \left. \frac{\partial}{\partial t} (n \langle \Phi \rangle) \right|_{\text{col}}, \quad (1.9)$$

where  $\Phi = \Phi(\mathbf{v})$  is some velocity dependent trial function chosen to generate the desired balance equation.

The first term of (1.9) describes the time rate-of-change of the extensive quantity  $n \langle \Phi \rangle$ . The second term is the divergence of a flux describing the spatial rate-of-change of  $n \langle \Phi \rangle$ . The third term is an effective source/sink term of the quantity  $n \langle \Phi \rangle$  due to an acceleration,  $\mathbf{a}$ , experienced due to applied forces that have no velocity dependence (e.g. electric or gravitational fields), or velocity dependence that acts perpendicular to the force (e.g. magnetic fields) [80]. The right hand side is a source/sink term describing the time rate-of-change of  $n \langle \Phi \rangle$  due to electron-neutral collisions.

In low-temperature plasma modeling applications, the following trial functions are often employed to generate an infinite hierarchy of coupled hyperbolic transport equations:

1.  $\Phi(\mathbf{v}) = 1 \rightarrow$  number density balance,
2.  $\Phi(\mathbf{v}) = m\mathbf{v} \rightarrow$  momentum balance,
3.  $\Phi(\mathbf{v}) = \frac{1}{2}mv^2 \rightarrow$  energy balance, and
4.  $\Phi(\mathbf{v}) = \frac{1}{2}mv^2\mathbf{v} \rightarrow$  energy flux balance.

An advantage of fluid models as defined is that the system of equations one solves has clear physical meaning (i.e. a momentum balance equation, an energy balance equation, and so on) and its solution immediately yields observables of a system, such as energy and density. Additionally, solving this system of equations is comparatively less computationally expensive than a full kinetic solution of the Boltzmann equation, or a PIC/MC solution over a large time period [95–97].

The downside of averaging over velocities is that it removes the ability to track evolution of the velocity distribution. Instead, it is common to assume a form of the velocity distribution function that is self-consistent with the observables of the fluid equations, such as a Maxwellian, or make other assumptions in the evaluation of collision terms [70]. Furthermore, because of the second term in the moment equation (1.9), the flux of each quantity is found from a higher velocity moment equation. To enable a solution, the system of equations must be closed through an assumption on a higher order moment. Depending on the level of approximation, closure is often formed by assuming an analytic form for the electron or ion heat flux and pressure tensor [96, 98] and therefore introduces an element of uncertainty into the model.

Various methods of closure and collision approximation commonly used in low-temperature plasma modeling. These closure assumptions are often a point of conjecture among the community [94–96], and present a knowledge gap in the field that this study seeks to address.

### 1.4.1 Field dependent drift-diffusion models

While a low-temperature plasma discharge can be a very complex, coupled, non-linear system there are some simple transport concepts valid when gradients of the charged particle density,  $\nabla n$ , are small. This small gradient regime is often called the hydrodynamic regime.

Considering electron transport, parallel to an applied electric field, the simplest fluid model is the electron continuity equation, found by evaluating (1.9) for  $\Phi = 1$

$$\frac{\partial n}{\partial t} + \nabla \cdot \mathbf{\Gamma} = n(\nu_I - \nu_a), \quad (1.10)$$

where  $n$  is the electron density,  $\mathbf{\Gamma} = n\mathbf{v}$  is the electron particle flux,  $\nu_I$  and  $\nu_a$  are collision frequencies for ionisation and attachment respectively. Recombination processes are generally included in the right-hand-side of (1.10). For the purposes of this work the process of recombination was neglected because comparatively low electron/ion densities, compared to neutral atoms, results in considerably more electron-neutral collisions than electron-ion collisions [76, 96].

To close the system via the particle flux, the electron momentum balance equation is generated by evaluating (1.9) for  $\Phi = m\mathbf{v}$ . A stationary, hydrodynamic regime is then assumed so that temporal gradients are assumed negligible and one projects spatial dependence onto the density gradient,  $\nabla n$ , to yield Fick's law

$$\mathbf{\Gamma} = n\mathbf{W}_F - \mathbf{D}_F \nabla n, \quad (1.11)$$

where  $\mathbf{W}_F$  is the electron (flux) drift velocity, and  $\mathbf{D}_F$  is the (flux) diffusion tensor, which typically is simplified via longitudinal,  $D_L^F$ , and transverse,  $D_T^F$ , diffusion coefficients. Other higher order transport coefficients proportional to higher order gradients of  $n$ , such as skewness or kurtosis, can be invoked if one wishes to add additional terms to (1.11) in order to describe more complicated transport behaviours using a hydrodynamic description [99].

For a one-dimensional system where transport is parallel to the applied electric field, the drift-diffusion equation obtained via Fick's law closure is

$$\frac{\partial n}{\partial t} + \frac{\partial}{\partial z} \left( nW_F - D_L^F \frac{\partial n}{\partial z} \right) = n(\nu_I - \nu_a). \quad (1.12)$$

The transport coefficients,  $W_F$  and  $D_L^F$ , as well as collision frequencies,  $\nu_I$  and  $\nu_a$ , are now input parameters to the model. Collision frequencies are defined from the collision cross sections and describe the number of collisions that occur per second for a certain collisional process [76]. A collision frequency,  $\nu$ , is related to the relevant cross section,  $\sigma$ , via

$$\nu = n_0 v \sigma, \quad (1.13)$$

where  $n_0$  is the neutral target atom density,  $v$  is the incoming scattering particle velocity.

To obtain input data values for (1.12), steady-state EEDFs are computed for a range of electric field strengths applied to the discharge medium being considered. These solutions are obtained from kinetic solutions to the Boltzmann equation [10, 94, 96] or simulated through Monte Carlo calculations [87, 89, 95]. Once the EEDFs are calculated, velocity averaged hydrodynamic transport coefficients and collision frequencies are computed using the steady-state distributions and a look-up table, shown in Table 1.1, is formed for interpolating input data.

Table 1.1: Look-up table for interpolation of fluid model input data

$E/n_0$ [Td]	$W_F$ [m/s]	$n_0 D_L^E$ [1/m.s]	$\langle \epsilon \rangle$ [eV]	...	$\nu_I/n_0$ [m <sup>3</sup> /s]	$\nu_a/n_0$ [m <sup>3</sup> /s]
⋮	⋮	⋮	⋮	⋮	⋮	⋮

The most common functional dependence of collision frequencies, as well as the transport coefficients, is to assume that electron dynamics depend upon the local reduced instantaneous electric field strength,  $E/n_0$ , [37, 96, 100] where  $E$  is the electric field strength and  $n_0$  is the neutral background density. This approximation is often termed the local field approximation. To evaluate the input quantities for (1.12) the look-up table is interpolated using the instantaneous value of  $E/n_0$  at each point in space. While pragmatic and very popular in the low-temperature fluid modeling community [92, 96, 100], studies have shown that non-equilibrium transport, featuring temporal and spatial non-locality, is poorly described by this model [93], and so extensions of this model have been used.

#### 1.4.2 Energy dependent drift-diffusion models

While the transport processes of the hydrodynamic regime provide an excellent entry point for describing charged particle transport in discharges, applications of low-temperature plasmas generally result in non-equilibrium conditions due to large spatial gradients, perhaps due to steep field gradients or surface interactions, or rapidly time varying applied fields, such as in radiofrequency (RF) plasmas [68, 100]. The effects of these spatio-temporal gradients result in non-local transport phenomena, which are so named because charged particle transport at a given point in space-time is heavily dependent on the properties of displaced charged species and fields at previous times, or at positions distinct from the point of interest. When non-local transport occurs in a plasma discharge, charged particle transport no longer follows the local instantaneous electric field strength,  $E(z, t)$ , like it generally would in a hydrodynamic regime [101, 102]. In these regimes, it has been demonstrated that electron transport can be better described by the local mean energy,  $\langle \epsilon \rangle(z, t)$ , rather than the field strength,  $E(z, t)$  [93, 101].

Utilising the same functional form of (1.12), a popular extension of the local field, drift-diffusion model is one that utilises a drift-diffusion equation for mean energy

density,  $n \langle \epsilon \rangle$ , in addition to electron number density [93, 103]. This allows the electron mean energy,  $\langle \epsilon \rangle$ , to be obtained directly, and thus used as the dependent variable for collision frequencies and transport coefficients in lieu of the reduced electric field,  $E/n_0$ . This approach has been demonstrated to be generally more accurate in resolving non-equilibrium electron transport, compared to local field approximations [101]. In order to obtain the two drift-diffusion equations for both number density and mean energy density, a closure on the energy balance equation must be used. Common examples of this closure are discussed in the following section.

### 1.4.3 Higher order models

Instead of assuming negligible temporal gradients of electron particle and energy flux required to form the previous drift-diffusion equations, recent studies [89, 95, 104] propose to solve a more detailed set of balance equations. This often involves a system of three or four equations for the extensive quantities of density,  $n$ , particle flux,  $n \langle v \rangle$ , mean energy density,  $n \langle \epsilon \rangle$ , and (less commonly) energy density flux  $n \langle \xi \rangle$ . To close the system of equations, most approaches prescribe forms on the electron pressure and electron heat flux. Electron pressure,  $\mathbf{P}$ , is accessible by expanding the unknown tensor,  $\langle \mathbf{v}\mathbf{v} \rangle$ , in terms of the average velocity,  $\langle \mathbf{v} \rangle$ , and peculiar velocity,  $\mathbf{V} = \mathbf{v} - \langle \mathbf{v} \rangle$ ,

$$\begin{aligned} nm_e \langle \mathbf{v}\mathbf{v} \rangle &= nm_e \langle \mathbf{v} \rangle \langle \mathbf{v} \rangle + nm_e \langle \mathbf{V}\mathbf{V} \rangle, \\ nm_e \langle \mathbf{v}\mathbf{v} \rangle &= nm_e \langle \mathbf{v} \rangle \langle \mathbf{v} \rangle + \mathbf{P}. \end{aligned}$$

Generally, models assume an isotropic electron velocity distribution function [96, 105], which yields a diagonal pressure tensor where the elements are proportional to electron mean energy

$$\mathbf{P} \approx \frac{2}{3} n \langle \epsilon \rangle \mathbf{I}. \quad (1.14)$$

In reality the electron velocity distribution function is generally anisotropic and the pressure tensor has perpendicular and parallel (to the applied electric field) components, which yield two perpendicular and parallel balance equations from the electron energy balance equation [106]. This method of resolving the pressure tensor can be considered more accurate, although adds complexity to the computational system.

Along with the pressure tensor, the electron heat flux,  $\mathbf{J}_q$ , is often used to truncate the hierarchy of equations at the energy balance stage. The heat flux can be obtained by expanded the energy flux in terms of average and relative velocities

$$\begin{aligned} n \left\langle \frac{1}{2} m v^2 \mathbf{v} \right\rangle &= n \langle \epsilon \rangle \langle \mathbf{v} \rangle + nm_e \langle \mathbf{v} \rangle \cdot \langle \mathbf{V}\mathbf{V} \rangle + n \left\langle \frac{1}{2} m_e V^2 \mathbf{V} \right\rangle, \\ n \left\langle \frac{1}{2} m v^2 \mathbf{v} \right\rangle &= n \langle \epsilon \rangle \langle \mathbf{v} \rangle + \langle \mathbf{v} \rangle \cdot \mathbf{P} + \mathbf{J}_q. \end{aligned}$$

To truncate this system of equations many works [107–110] utilise (1.14) to close the pressure tensor and favour simple, albeit physically questionable, closures for the heat

flux. Often, a Fourier Law treatment of the electron heat flux [96, 110] is used

$$\mathbf{J}_q \approx \kappa \nabla \langle \epsilon \rangle,$$

where  $\kappa$  is a thermal conductivity. Additionally, some works simply neglect the heat flux,  $\mathbf{J}_q = 0$ , in order to make the system of equations tenable [93, 96].

Recently, a physically accurate closure ansatz of the electron heat flux has been proposed and benchmarked for elastic and inelastic collisions [96–98] in relatively simple collision models. While this closure ansatz was demonstrated to be accurate for analytic collision models, application to non-trivial discharges is limited because the ansatz requires tuning of parameters for each discharge configuration. Finally, recent studies of Becker *et al.* [89, 94, 103] have indicated that in lieu of potentially non-physical, arbitrary closures, the steady-state EEDF may be used to evaluate quantities that require closure. Given that there is demonstrated variation amongst closure methods in plasma modeling literature, a physically based, parameter free form of equation closure was a focus of this study.

#### 1.4.4 Coupling electromagnetic fields

An important part of any low-temperature plasma model is the self-consistent calculation of electric,  $\mathbf{E}$ , and magnetic,  $\mathbf{B}$ , fields. Due to the creation or loss of charged particles in a plasma discharge, the electromagnetic field variation throughout the plasma must be self-consistently solved by coupling Maxwell’s equations where required. For the low-temperature plasmas considered in this work the presence of magnetic fields is generally ignored, requiring the instantaneous electric field,  $\mathbf{E}$ , to be computed via

$$\nabla \cdot \mathbf{E} = \frac{\rho_q}{\epsilon}, \quad (1.15)$$

$$\mathbf{E} = -\nabla V, \quad (1.16)$$

where  $\rho_q$  is charge density,  $\epsilon$  is the dielectric permittivity of the discharge medium, and  $V$  is the electric potential. When simulating gaseous, liquid, or interfacial discharge configurations, an appropriate dielectric constant for a given medium is required. This is particularly important when coupling electromagnetic fields to a transport model, especially in plasma medicine applications where air and tissue dielectric properties are vastly different [50, 111].

## 1.5 Modeling packages

There are a range of preexisting plasma modeling packages that the low-temperature plasma community have developed or adopted. A popular commercial software is the COMSOL Multiphysics software package, which has a range of plasma modules that provide some basic plasma modeling functionality [112]. In addition to general multiphysics packages, specific plasma modeling packages have been written by experts

in the field to enable the wider plasma research community to use their models and codes, some examples of this are the plasmaFOAM [113] module adapted from the openFOAM computational fluid dynamics (CFD) software [114], and the PLASIMO software [115] developed at the Eindhoven University of Technology.

While there are a range of excellent existing packages that provide modeling options for low-temperature plasmas, for the purposes of this research the preference was to develop original implementations of numerical algorithms and code necessary to solve the system of electron transport equations used in this work. This decision was primarily influenced by the time and length scale variations that are present in the multiphase problem addressed in this thesis.

## 1.6 Benchmark methods

---

In order to validate the accuracy and application of proposed low-temperature plasma models there are essentially three broad sources of validation for model output: experiment, analytic expressions, and other models. For this work, focusing on application of multiphase and interfacial electron transport, there are very few available experimental measurements that can be used to validate model output. As such, alternative model output and analytic expressions in certain limits must be used.

### 1.6.1 Experimental validation

Experimental investigations may be performed, in which a discharge is established and various environmental or control parameters are adjusted to assess how the discharge responds to well defined changes. Experimental studies of specific plasma applications serve as good feedback mechanisms for improving predictive models of that application by informing theoreticians of the accuracy, or inaccuracy, of their proposed model. The feedback loop between experiment and theory has been well supported in the low-temperature plasma community, from the first Gaseous Electronics Conference (GEC) reference cell proposed in the 1990s [88, 100], to the recent more sophisticated reference systems that have been proposed by the community for applications such as plasma medicine via the COST-Jet [116].

### 1.6.2 Validation against kinetic solutions

Previous low-temperature fluid model studies have demonstrated the utility of benchmarking proposed fluid models against solutions obtained through accurate (i) kinetic solution of the electron distribution function via the Boltzmann equation, or (ii) Monte Carlo simulation of the distribution function [89, 90]. Benchmarks of this nature are typically performed by specifying a well defined, simple system configuration to simulate. Simple benchmarks are preferred because this allows complex physical transport processes to be isolated, in order to (i) avoid ambiguity when analysing solutions for a given system, and (ii) allow targeted analysis of solution methods for certain transport

mechanisms, e.g. studying collisionally conservative systems to ensure numerical conservation is obtained. In this work both kinetic and Monte Carlo methods, developed previously by the JCU transport modeling group [10, 48, 65], were utilised to provide validation against fluid model solutions for simple benchmark problems.

Classic benchmark problems include:

- the hard-sphere model - where a constant momentum transfer cross section is assumed, often with one inelastic excitation process added [48, 70],
- the Maxwell model - where a constant collision frequency is assumed, yielding a cross section that varies as the inverse-square-root of incoming electron energy [70],
- the Lucas-Salee model - where a weighted combination of an inelastic excitation and electron ionisation process is defined to study non-conservative transport effects [117], and
- the Percus-Yevick simple liquid model - defined as a modification to a gas-phase collision model to add elastic coherent scattering described by an analytic static structure factor [65, 83].

### 1.6.3 Analytic time of flight solution

For a limited range of problem definitions, analytic solutions can be found to the governing transport equations. Most analytic solutions focus on developing an expression for the number density of charged species in a simple weak-gradient, hydrodynamic regime [96]. Temporal variation is sometimes ignored in favour of a simpler, steady-state solution [33], although time-dependent solutions have also been considered [118]. Although limited in practicality, an analytic solution offers a known basis for which vital benchmarks of numerical solvers can be made. Details of the analytic solutions used to benchmark numerical methods in this project are found in the Appendix Chapter A

## 1.7 Use of swarm experiments towards low-temperature plasma modeling

---

In addition to experimental studies of specific configurations of plasma discharges, swarm experiments are a vital part of the low-temperature plasma field [72, 119, 120]. Swarm experiments [72, 121, 122] are multiple scattering experiments as opposed to the single scattering beam experiments, requiring particle, momentum and energy balance for the entire ensemble of electrons in the swarms. Furthermore, the velocity distribution of the electrons is unknown and must be determined from transport theory in order to link the cross sections to the transport coefficients and properties

The two main configurations of swarm experiment used extensively are time of flight (ToF) [123], described in Figure A.4, and Townsend apparatuses [124]. ToF experiments typically measure the time it takes for a swarm of electrons to drift the

length of the apparatus in order to extract electron mobility, diffusion coefficients, and the net non-conservative collision frequency, while Pulsed Townsend (PT) experiments measure the arrival time spectra of the swarm to access slightly different measurables such as Townsend attachment and ionisation rates. Similar to the PT experiments is the Steady-State Townsend (SST) apparatus, where a constant source of electrons is emitted and measurement is conducted once an equilibrium has been reached.

While swarm experiments were initially designed to extract cross sections, in recent times this has changed. Swarm experiments are now used to either determine transport coefficients directly as input data for fluid models, or to act as experimental verification/testing of scattering cross section accuracy and completeness by comparing the measured transport coefficients with those calculated from a proposed cross section set [72, 125, 126]. An additional use of swarm experiment measurements is to provide an experimental benchmark for low-temperature plasma modeling methods in the limit of no space-charge fields.

To determine transport coefficients in the hydrodynamic limit, the ToF experiment yields currents and these can be interpreted using the drift-diffusion equation (1.12) referenced to the centre-of-mass of the swarm [76]. This data is referred to as bulk transport data. The coefficients measure centre-of-mass drift velocity of the swarm, as well as the spread about the centre-of-mass (i.e. diffusion) [68]. In addition to bulk transport properties, there are flux transport properties. These flux properties arise from Fick's law [76], and the relationship between the two, when considering drift velocity and diffusion, can be expressed as

$$\begin{aligned}\mathbf{W} &= \mathbf{W}_F + \Delta\mathbf{W}_r \\ D &= D_F + \Delta D_r,\end{aligned}$$

where the subscript  $F$  represent flux transport measurements and subscript  $r$  denote explicit correction terms, due to non-conservative contributions of reaction collisions, to the motion about the centre of mass.

Swarm experiments in liquid are not as common as those for dilute gases due to the increased experimental difficulties of storing and measuring transport through liquids compared to gases [54, 62]. This study makes use of the results generated during a relatively rich period in the late 20th century where use of cryogenic atomic liquids in particle detector applications led many experimentalists to measure transport properties of electrons in dense non-polar liquids such as xenon, argon, and krypton [55, 60, 63, 127]. It is anticipated that future liquid phase swarm and scattering experiments will be performed in order to facilitate improved understanding of the nuances of charged particle transport within liquid phase.

## 1.8 Electron transport data in biomolecules

While the modeling methods previously discussed in this introduction are the primary focus of this study, input data describing electron transport in biologically relevant materials is an essential component of a framework to describe plasma-tissue interactions. Ideally, information about electron transport in human tissue would be used for transport studies, but this is not available owing to the complex make-up of tissue. As a way to simulate human tissue, surrogate biomolecules have been identified for study so that they may be combined with water in a mixture of compounds, summarised in Figure 1.9, that collectively offer a better description to tissue than simply using density-scaled water vapour, which is the current standard [128, 129].

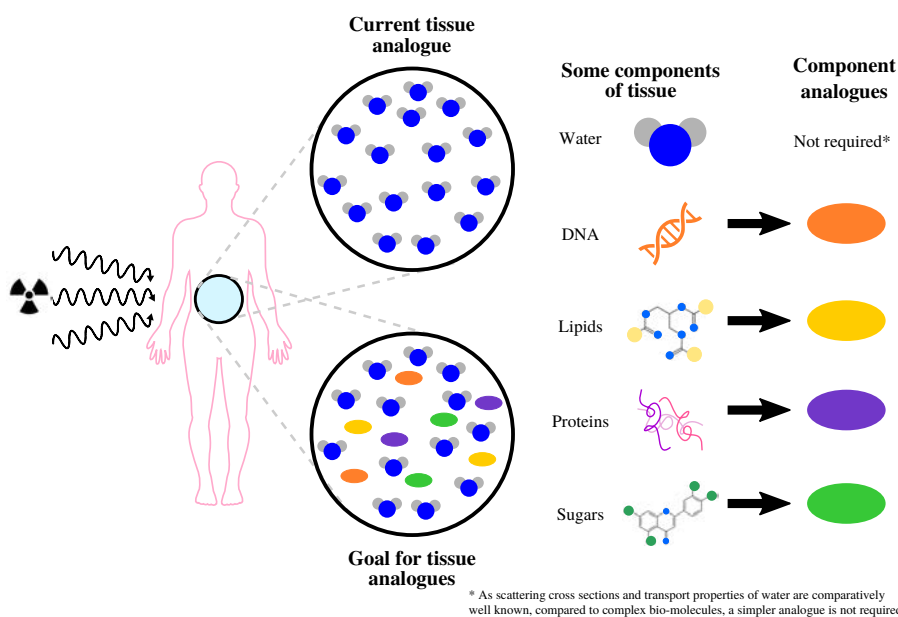


Figure 1.9: Summary of the ultimate goal of a tissue analogue input data for simulations

Electron transport in biological matter, stimulated by ionizing radiation or plasma medicine technologies, is of significant interest as it has been observed that low-energy electrons thermalize in human tissue through a variety of energy transfer collisions with water, sugars and the DNA bases. Although low in energy, sub-ionisation electrons have been shown to be a source of DNA damage [130]. For example, the process of dissociative electron attachment (DEA) can lead to single and double strand breaks directly, or indirectly through the formation of free radicals which interact with the DNA. The pioneering study of Sanche and co-workers [130, 131] has subsequently motivated much research into electron collision processes with sub-units and constituents of the moieties that constitute DNA and RNA.

A quantitative understanding of the transport of low-energy secondary electrons in human tissue is key to understanding the impact of both plasma and nuclear medicine applications, and will inform dosimetry models. Consequently, databases are required for electron induced processes in biomolecules for track simulations and transport studies. Water is generally assumed as the surrogate for human tissue, and recently

full/complete sets of cross sections have been developed and tested for electron-water interactions in the gas-phase [128,129]. Recent work has suggested that such gas-phase studies can be adapted to the soft-condensed phase through appropriate modifications using pair correlations functions [67,132]. While there has been much progress in the study of electron induced processes in the sugars and DNA bases, they have not developed to the same level of completeness as is the case for water. While DNA is currently not convenient to study, tetrahydrofuran (THF -  $C_4H_8O$ ) has been investigated as a model for low-energy electron interactions with 2-deoxyribose, a sugar that links phosphate groups in the DNA backbone. Considerable progress has been made in recent times establishing individual cross sections for electron impact processes in THF, at both the integral and differential levels. Experimentally, there have been measurements of the total [18,20], (quasi-) elastic [22,24,27,133], vibrational [27,28,134], electronic excitation [31,135] and ionisation [23,30] cross sections over a range of energies. Likewise, theoretical treatments using R-matrix methods [136], the Schwinger variational method [25,137], the complex Kohn variational method [138] and binary encounter-Bethe approach [29], the independent atom model (IAM) [29] and the recent IAM-screening corrected additivity rule (SCAR) treatment [19,21] have provided complementary information to the experimental data. Until the current work there has been no study on the accuracy and completeness of the entire cross section set.

## 1.9 Research goals of this study

---

A number of present technologies hinge on knowledge and understanding of the transport of low-temperature plasma species in both gas and liquid phase media. In addition to transport in homogeneous fluid phases, applications such as plasma medicine or noble liquid particle detectors rely on transporting species across the interface between adjacent gas and liquid phases. The goal of this thesis is to construct a novel modeling framework for electron transport in, and between, gas and liquid extrema, and apply this simulation framework to electron transport in biologically relevant media.

A model of electron transport across a gas-liquid interface was chosen as the subject of this research due to identified knowledge gaps in low-temperature plasma literature. Possible benefits of furthering understanding of electron transport at the plasma-liquid interface are:

- to enable tunable fluxes or energies of electrons to control reactions in the liquid [139], and
- to provide accurate electron number density and energy loss emission/absorption coefficients for use in macroscopic transport models [111].

The primary application that is motivating research and development of an interface continuum model of electron transport is plasma medicine, as the rich array of surface chemistry that occurs in the vicinity of a plasma-tissue interaction is largely dependent on the electron dynamics in this region [52,139,140]. In the long term, application

of such a modeling framework would yield better understanding of electron transport in this context and facilitate furthering the overall understanding of the fundamental mechanisms, efficacy, and most importantly safety of plasma-tissue treatments.

With the primary motivation of plasma medicine in mind, it is noted that a plasma-tissue interaction is a relatively complicated physical system. In order to provide an intermediate step to facilitate benchmarking and application of the proposed modeling framework in this work, a secondary application of noble liquid particle detectors also motivates this work. This application is relevant as a target for this study because the atomic liquids used in detectors (argon and xenon) are relatively well studied materials, compared to polar molecular liquids, and have readily available input data, making application of the modeling framework proposed in this study achievable. To achieve the overall goal of this research project a number of minor goals were formulated and they are listed and discussed below.

**Milestone 1:** Propose and validate a model of electron transport in gas and liquid media.

**Milestone 2:** Study neutral density effects on electron transport input data across the gas-liquid interface.

**Milestone 3:** Perform a physically grounded interfacial simulation including swarm and streamer propagation.

**Milestone 4:** Assemble electron scattering cross section set for biologically relevant molecules, and understand streamer propagation across the gas-liquid interface.

## 1.10 Structure of this document

---

The structure of this thesis dissertation is composed of six chapters, including this Introduction, presenting the foundations and methods applied to reach the goals set out in Section 1.9. The majority of the content presented in this document has been previously published in, or submitted to, peer-reviewed scientific journals. These works are collected in this document, with minor modifications to the introductory and concluding passages of each publication, to demonstrate the coherent and collective achievement of this doctoral research project.

In Chapter 2, a parameter-free higher order fluid model is proposed, where application to electron transport in both gas and liquid media is made explicit. Benchmarking of this fluid model against accurate Monte Carlo calculations is performed in order to validate the proposed model and highlight differences between higher order and local field models. Some limitations of fluid equation methods are highlighted through studying electron energy distribution functions of varying collision regimes.

In Chapter 3, the derivation and application of an approximation method to computing  $n_0$  dependent interfacial electron transport input data for fluid models is presented. The foundation and correspondence of this derivation in dilute gas mixture

theory is detailed. Validation of results from the proposed method against experimental data for simple atomic liquids, argon and xenon, highlight the applicability of the approximation.

In Chapter 4, the previous two chapter's components are drawn together to consider complete interfacial simulations of streamer propagation from gas to liquid, and swarm extraction from liquid to gas. The importance of various input data assumptions are discussed, and the best practices for handling electron transport across an interface are recommended.

In Chapter 5, the proposed modeling framework is applied to the biologically relevant molecule tetrahydrofuran (THF) by first assembling a self-consistent electron scattering cross section set from available theoretical and experimental data. Input transport data from the most recent cross section set, in addition to a known experimental structure factor, is utilised to perform streamer formation simulations of both gas and liquid mediums. A comparison of the resulting transport is made.

In Chapter 6, a summary of results of this research project is presented. A reflection and summary of the key findings of the preceding chapters are highlighted, along with recommendations for future directions of research that should follow from this work.

# 2

## Fluid modeling of electrons in gas and liquid

This chapter contains material that has been published in the following journal article:

[2] NA Garland, DG Cocks, GJ Boyle, S Dujko and RD White. Unified fluid model analysis and benchmark study for electron transport in gas and liquid analogs. *Plasma Sources Science and Technology*, 26 075003 (2017). Available online at doi:10.1088/1361-6595/aa73c6

This chapter includes Monte Carlo simulations by DG Cocks which were used to (i) provide input data for the original work, and (ii) provide benchmark comparisons for output results. All other work described in this chapter is that of the author.

### 2.1 Chapter Introduction

---

Motivated by the fundamental theory and recent research efforts outlined in Chapter 1, in this Chapter it is sought to extend a recent kinetic formulation [10, 48, 65] which introduced a structure factor modification to account for coherent scattering effects in dense media. Ultimately this Chapter aims to formulate and benchmark a generalized electron fluid model, that will later be applied to modeling electron transport between a plasma-liquid interface, where liquid processes, such as solvation, may be included at a fundamental level via electron collision cross sections [48]. The formulation of the fluid model for both gases and simple liquids with coherent scattering effects is presented in Section 2.2. A parameter-free, unified steady state closure assumption is introduced, along with a brief summary of existing closure approaches commonly used in fluid modeling. Steady state and transient benchmarking of the electron fluid model

against accurate Monte Carlo simulations and multi-term solutions of the Boltzmann equation are presented in Section 2.3 to demonstrate the utility of the fluid model. From this benchmarking, comparisons of results from the alternative fluid models presented in Section 2.2 are shown in order to highlight significant differences that can occur in various benchmark scenarios. Finally, a brief discussion of the impact of kinetic effects through the electron energy distribution functions is included to rationalize the limitations of the local mean energy approximation. Concluding remarks are detailed in Section 2.4.

## 2.2 Theory

---

### 2.2.1 Fluid Modeling

The microscopic dynamics of charged particle transport in gases or liquids alike can be described by particle-based simulations or directly solving the Boltzmann equation of kinetic theory [81, 141]

$$\frac{\partial f}{\partial t} + \mathbf{v} \cdot \frac{\partial f}{\partial \mathbf{r}} + \mathbf{a} \cdot \frac{\partial f}{\partial \mathbf{v}} = -J(f), \quad (2.1)$$

which describes the evolution of the charged particle ensemble distribution function  $f(\mathbf{r}, \mathbf{v}, t)$  in position-velocity phase space  $(\mathbf{r}, \mathbf{v})$  [70, 102, 132, 142], where  $\mathbf{a}$  is an acceleration vector due to applied field (e.g. electric, magnetic, gravitational). The right-hand side of (2.1) denotes the rate of change of  $f(\mathbf{r}, \mathbf{v}, t)$  due to collisions of charged particles with neutral background particles in a gas or soft condensed medium through the collision operator

$$J(f) = J_{\text{coherent}} + J_{\text{incoherent}} = J_{\text{elas}} + J_{\text{inel}} + \dots, \quad (2.2)$$

which describes all possible scattering processes, such as elastic collisions, inelastic collisions, attachment, and ionisation, through appropriate cross sections. An important distinction between coherent (i.e. elastic) and incoherent scattering processes needs to be made for the consideration of charged particle transport in liquid and soft-condensed structured systems [48].

Particle-in-Cell (PIC) or Monte Carlo (MC) are the leading particle-based methods used to simulate charged particle distributions in phase space [87, 104], while two-term [69] or modern multi-term solutions [10, 48] of the Boltzmann equation are the leading methods that solve directly for the particle distribution.

Microscopic kinetic approaches provide very accurate descriptions of charged particle transport but become mathematically complicated and computationally time consuming for applications containing complex geometries or boundaries, multiple spatial dimensions, or many charged species. Applications involving plasma-liquid interfaces typical contain these complications, and so a simpler, computationally efficient modeling

approach is sought. As such, the modeling approach chosen in this study is a fluid or moment model [89, 90, 93, 95, 96, 100, 105].

Fluid models provide a description of a swarm or plasma through velocity-averaged variables. This gives a macroscopic model of the discharge, which retains only the direct quantities important for evolution of the system. This approach gives a significant boost to calculation speed, while maintaining reasonable accuracy of quantities of interest. The simplest of these variables is the number density of a species, defined as

$$n(\mathbf{r}, t) = \int f(\mathbf{r}, \mathbf{v}, t) d\mathbf{v}, \quad (2.3)$$

while general velocity-averaged quantities are defined from the distribution function

$$\langle \Phi_k \rangle(\mathbf{r}, t) = \frac{1}{n(\mathbf{r}, t)} \int f(\mathbf{r}, \mathbf{v}, t) \Phi_k(\mathbf{v}) d\mathbf{v}, \quad (2.4)$$

where  $\Phi_k(\mathbf{v})$  is any velocity dependent function, and  $\langle \dots \rangle$  denotes the expectation value, a velocity average over  $f(\mathbf{r}, \mathbf{v}, t)$ .

Generally the moments of trial functions  $\Phi_1 = 1$ ,  $\Phi_2 = \mathbf{v}$ ,  $\Phi_3 = \frac{1}{2}mv^2$ ,  $\Phi_4 = \frac{1}{2}mv^2\mathbf{v}$  are performed to get balances on electron number, particle flux, energy density, and energy density flux respectively.

The generic moment equation may be derived by multiplying the Boltzmann equation (2.1) by an arbitrary, velocity dependent, trial function  $\Phi(\mathbf{v})$  and integrating over velocity space [95, 96]

$$\frac{\partial}{\partial t} (n \langle \Phi \rangle) + \nabla \cdot (n \langle \mathbf{v} \Phi \rangle) - n \mathbf{a} \cdot \langle \nabla_{\mathbf{v}} \Phi \rangle = C_{\Phi}, \quad (2.5)$$

where  $C_{\Phi}$  is the rate of change of the quantity  $\Phi$  due to collisions

$$C_{\Phi} = \left( \frac{\partial [n \langle \Phi(\mathbf{v}) \rangle]}{\partial t} \right)_{\text{coll}} = - \int \Phi(\mathbf{v}) J(f) d\mathbf{v}. \quad (2.6)$$

Where this approach departs from classical gas phase fluid models, is that the collision term can be written as the sum of coherent and incoherent components

$$C_{\Phi} = C_{\Phi \text{coherent}} + C_{\Phi \text{incoherent}}. \quad (2.7)$$

High densities in liquid like states require many modifications to the simple gas phase picture, and including coherent scattering is an attempt to do so. Coherent scattering is projected entirely onto the momentum transfer elastic scattering cross section while inelastic collisions off different molecules are incoherent as they modify the state of the background medium. Assuming, for simplicity, that excitations in a dense medium are localized to individual molecules, incoherent processes are computed by evaluating equation (2.6) with the semi-classical Boltzmann collision operator [77]. Hence, for all inelastic processes in gas or liquid media, and elastic scattering in dilute

gases, the incoherent collision term is found via the traditional collision term

$$C_{\Phi\text{incoherent}} = \sum_{j,j'} \int d\mathbf{v} f(\mathbf{v}) \int d^2\Omega_{\mathbf{g}'} n_0 v \sigma(j, j'; g, \chi) [\Phi' - \Phi]_{j,j'}, \quad (2.8)$$

where indices  $j, j'$  denote the before and after collision states due to each collisional processes causing internal energy transitions ( $\epsilon_j \rightarrow \epsilon_{j'}$ ) in the neutral particle. Furthermore,  $g$  denotes the relative speed between charged particle and neutral scattering center,  $d^2\Omega_{\mathbf{g}'}$  denotes the differential scattering angle  $d\psi d\chi \sin \chi$  (where  $\psi$  is the polar angle and  $\chi$  the azimuthal angle), and  $\sigma(j, j'; g, \chi)$  represents the partial cross section for scattering through the azimuthal angle  $\chi$  given an incoming speed  $g$ .

However, when dense mediums or low electron energies are considered, coherent scattering effects are vital. The most general view of charged-particle interactions with a dense medium is the scattering of a wave, representing the charged particle, by the medium as a whole and not a single fixed scattering center. A first approximation to the scattering is the *single-scatterer approximation* [82] in which the scattered wave is the coherent sum of contributions from many scattering centers in the molecule, which interfere to effectively produce a diffraction pattern of the medium [48]. These effects are significant when the electron de Broglie wavelength is comparable to the average background particle spacing,  $\lambda \sim \frac{1}{n_0^3}$ .

From the definition of the double differential cross section, the expression for the rate of change of  $\Phi(\mathbf{v})$  due to coherent elastic scattering is

$$\left. \frac{\partial}{\partial t} (n \langle \Phi \rangle) \right|_{\text{coherent}} = \int d\mathbf{v} f(\mathbf{v}) \int_0^\infty d\omega' \int_{\hat{\mathbf{k}'}} d\hat{\mathbf{k}}' n_0 v \frac{d^2\sigma}{d\hat{\mathbf{k}}' d\omega'} [\Phi(\mathbf{v}) - \Phi(\mathbf{v}')], \quad (2.9)$$

where  $\omega'$  and  $\mathbf{k}'$  denote the angular frequency and wavenumber of the charged particle wave after the interaction with the material. The double differential cross section is written as a product of the single atomic differential cross section and the dynamic structure factor [82]

$$\frac{d^2\sigma}{d\hat{\mathbf{k}}' d\omega'} = \sigma_{\text{lab}} \left( |\Delta\mathbf{k}| - \frac{\omega}{2}, \hat{\mathbf{k}}' \right) S(\Delta\mathbf{k}, \Delta\omega)$$

where  $\Delta\mathbf{k} = \mathbf{k} - \mathbf{k}'$  is the change in the wave vector, such that  $\mathbf{p} = m\mathbf{v} = \hbar\mathbf{k}$ , and  $\Delta\omega = \omega - \omega'$  is the change in energy, such that  $\epsilon = \hbar\omega = \frac{\hbar^2 k^2}{2m}$ . Dashed quantities refer to post-collision values. All expressions are evaluated in the laboratory frame in contrast to the single molecule scattering case where collisions are carried out in the center of mass frame, for interactions with many particles simultaneously this is not possible.

Equations (2.5) - (2.9) now provide a complete framework for generating charged particle fluid equations in both gas and liquid media alike. In the limit of high incoming particle energies or dilute gases, equation (2.9) reduces to equation (2.8) where  $S(\Delta\mathbf{k}, \Delta\omega)$  has zero contribution from correlations between atoms [10, 48].

### 2.2.2 Four Moment Electron Fluid Model

For electrons of charge  $q_e$  and mass  $m_e$ , in a gas or liquid subject to a homogeneous background electric field,  $\mathbf{E}$ , such that the acceleration vector is

$$\mathbf{a} = \frac{q_e}{m_e} \mathbf{E}, \quad (2.10)$$

the first four moment equations can be derived from equations (2.5) - (2.9) by substituting  $\Phi = 1$ ,  $\mathbf{v}$ ,  $\frac{1}{2}mv^2$ ,  $\frac{1}{2}mv^2\mathbf{v}$

$$\frac{\partial n}{\partial t} + \nabla \cdot \mathbf{\Gamma} = n(\nu_I^{\text{ss}}(\langle \epsilon \rangle) - \nu_a^{\text{ss}}(\langle \epsilon \rangle)), \quad (2.11)$$

$$\frac{\partial \mathbf{\Gamma}}{\partial t} + \nabla \cdot (n\theta_m) - n\frac{q_e}{m_e}\mathbf{E} = -\mathbf{\Gamma}\nu_m^{\text{ss}}(\langle \epsilon \rangle), \quad (2.12)$$

$$\frac{\partial n_\epsilon}{\partial t} + \nabla \cdot \mathbf{\Gamma}_\epsilon - q_e\mathbf{E} \cdot \mathbf{\Gamma} = -nS_\epsilon^{\text{ss}}(\langle \epsilon \rangle), \quad (2.13)$$

$$\frac{\partial \mathbf{\Gamma}_\epsilon}{\partial t} + \nabla \cdot (n\theta_\xi) - n\theta_m \cdot q_e\mathbf{E} - n_\epsilon\frac{q_e}{m_e}\mathbf{E} = -\mathbf{\Gamma}_\epsilon\nu_\xi^{\text{ss}}(\langle \epsilon \rangle), \quad (2.14)$$

where shorthand variables for particle flux, energy density, and energy density flux are

$$\mathbf{\Gamma} = n\langle \mathbf{v} \rangle = \int f(\mathbf{r}, \mathbf{v}, t) \mathbf{v} d\mathbf{v}, \quad (2.15)$$

$$n_\epsilon = n\langle \epsilon \rangle = \int f(\mathbf{r}, \mathbf{v}, t) \frac{1}{2}mv^2 d\mathbf{v}, \quad (2.16)$$

$$\mathbf{\Gamma}_\epsilon = n\langle \xi \rangle = \int f(\mathbf{r}, \mathbf{v}, t) \frac{1}{2}mv^2\mathbf{v} d\mathbf{v}, \quad (2.17)$$

with  $\langle \mathbf{v} \rangle$ ,  $\langle \epsilon \rangle$ , and  $\langle \xi \rangle$  being the electron average velocity, average energy, and average energy flux. Higher order tensor products  $\theta_m = \langle \mathbf{v}\mathbf{v} \rangle$  and  $\theta_\xi = \langle \frac{1}{2}mv^2\mathbf{v}\mathbf{v} \rangle$  are introduced, and require closure approximations in order to numerically solve the system.

Consistent with existing modeling literature [69, 89, 93, 100, 103, 104, 115, 143] the collision terms are approximated via pre-computing *steady state* expectation values of reduced collision rates,  $\langle \frac{\nu}{n_0} \rangle$ , through Monte Carlo simulations [65, 87] or multi-term solutions of the Boltzmann equation [10, 48] of a steady state distribution function, and interpolating as a function of the local mean energy.

It should be noted that in this work, input rates and closure input to follow have been written as parameter-free expectation values over the steady state distribution function, independent of the computational method such as MC simulation or a multi-term solution of the Boltzmann equation. For a given method there will be simplified expressions written in terms of isotropic and anisotropic distribution function components. For further details, the reader is referred to previous publications on the MC methods [65, 87] and multi-term kinetic methods [10, 48, 94, 132] used in evaluation of the input data for this study.

Given ionisation and attachment cross sections,  $\sigma_I$  and  $\sigma_a$ , expressions for the ionisation and attachment rates are

$$\nu_I^{\text{ss}} = \left\langle n_0 \sqrt{\frac{2\epsilon}{m_e}} \sigma_I(\epsilon) \right\rangle_{f_{\text{ss}}}, \quad (2.18)$$

$$\nu_a^{\text{ss}} = \left\langle n_0 \sqrt{\frac{2\epsilon}{m_e}} \sigma_a(\epsilon) \right\rangle_{f_{\text{ss}}}, \quad (2.19)$$

where subscript  $f_{\text{ss}}$  denotes the expectation value is performed by integration over the steady state distribution function.

The vector quantity collision rates for momentum and energy flux transfer are computed from the steady state distribution function by normalizing the loss-rate of each given quantity to its steady state value,

$$\nu_m^{\text{ss}} = \frac{\langle \Delta \mathbf{v} \nu_T(\epsilon) \rangle_{f_{\text{ss}}}}{\langle \mathbf{v} \rangle_{f_{\text{ss}}}}, \quad (2.20)$$

$$\nu_\xi^{\text{ss}} = \frac{\langle \Delta \xi \nu_T(\epsilon) \rangle_{f_{\text{ss}}}}{\langle \xi \rangle_{f_{\text{ss}}}}. \quad (2.21)$$

where  $\Delta \mathbf{v}$  and  $\Delta \xi$  denote the average change in velocity and energy flux per collision, averaged over all possible processes, and  $\nu_T$  is the total collision rate in the steady state.

The energy transfer rate  $S_\epsilon$  is the lump sum of average energy losses due to all collisional processes

$$S_\epsilon^{\text{ss}} = \langle \Delta \epsilon \nu_T(\epsilon) \rangle_{f_{\text{ss}}}, \quad (2.22)$$

where  $\Delta \epsilon$  is the average change of energy per collision averaged all possible processes, including any threshold and collision energy transfer.

### Steady State Closure

In lieu of assuming analytic forms of velocity distribution functions for closure approximations or parameterizing closure expressions as functions of known moment variables, as often done in the past [96,105], it is preferred to apply steady state electron distribution functions as recently proposed by Becker and Loffhagen [89,94,103,105,144] to evaluate closure terms, akin to the collision input terms. Motivated by the work in Ref [144] through equations 15a - 15d, one can utilize Monte Carlo simulations [65,87] or multi-term solutions of the steady state electron energy distribution function [10,48] to generate a look-up table of closure terms

$$\theta_m \approx \theta_m^{\text{ss}}(\langle \epsilon \rangle) = \langle \mathbf{v} \mathbf{v} \rangle_{f_{\text{ss}}}, \quad (2.23)$$

$$\theta_\xi \approx \theta_\xi^{\text{ss}}(\langle\epsilon\rangle) = \left\langle \frac{1}{2} m v^2 \mathbf{v}\mathbf{v} \right\rangle_{f_{ss}}, \quad (2.24)$$

as well as the usual collision rates, as a function of the local electron mean energy. This model will be referred to as *4MM-SS* in the remainder of this work.

Using steady state distribution closure ensures that electron transport evolves in a manner guided by a physically motivated distribution function. In regimes that are known to not produce oscillatory structures, due to reduced electric field and collision cross section effects, it is believed this fluid model has a higher potential to accurately resolve spatially averaged electron transport quantities, as demonstrated in Section 2.3.

In non-hydrodynamic regimes far from the steady state distribution detailed electron structures, such as periodic spatial phenomena [97, 98], will be difficult to generally replicate with this steady state closure approach, as shown by a benchmarked analytic steady-state heat flux ansatz [96, 98, 105]. Despite this limitation in the steady-state closure, it is apparent that using a parameter free, general closure assumption offers a flexible option to the fluid modeling community as it is applicable in time-dependent and steady state problems, and requires no tuning of input parameters or benchmarking.

Using the proposed closure approximation is sufficient to reproduce the general evolution of space-time electron transport, in a “line of best fit” sense sufficient for basic studies of discharges in either gaseous or liquid media. To be discussed in Section 2.3.6, the challenge of fluid models to resolve oscillatory structures lies in their inability to resolve distribution function variations due to the local mean energy approximation, and not in the choice of closure approximations.

### Drift-Diffusion Approximations

Often low-temperature plasma modeling studies will be concerned with long-time scale or steady state simulations [93, 103–105, 145], and drift-diffusion approximations (DDA) are commonly employed. As such, this section presents a simplified version of the previous four moment model into a two moment model consisting of the two continuity equations for number density (2.11) and energy density (2.13) but with steady state particle (2.25) and energy flux (2.26) expressions

$$\mathbf{\Gamma}^{\text{ss}} = \frac{1}{\nu_m^{\text{ss}}(\langle\epsilon\rangle)} \left[ \frac{q_e}{m_e} n \mathbf{E} - \nabla \cdot (n \theta_m^{\text{ss}}(\langle\epsilon\rangle)) \right], \quad (2.25)$$

$$\mathbf{\Gamma}_\epsilon^{\text{ss}} = \frac{1}{\nu_\xi^{\text{ss}}(\langle\epsilon\rangle)} \left[ q_e n \theta_m^{\text{ss}}(\langle\epsilon\rangle) \cdot \mathbf{E} + \frac{q_e}{m_e} n_\epsilon \mathbf{E} - \nabla \cdot (n \theta_\xi^{\text{ss}}(\langle\epsilon\rangle)) \right], \quad (2.26)$$

where collision and closure inputs are the same as prescribed for the four moment model, *4MM-SS*.

This approximate model is justified by assuming the relaxation collision frequencies of the vector quantities is much faster than the time scales for energy relaxation and

electron transport, through electric field driven advection or diffusive transport [96, 118]. This model will be referred to as DDA-SS in the remainder of this work.

### 2.2.3 Other Fluid Models

In order to facilitate comparison of the presented fluid model using steady state closure, three fluid models previously used in literature are briefly presented: parameterized four moment closure, zero heat flux, and a Fourier law heat flux closure.

It is noted a method of closure through an analytic heat flux ansatz benchmarked against an asymptotic perturbation solution of the balance equations has been proposed [96, 98]. There are benefits of this method, but concerns regarding the choices of tunable free parameters in benchmarking new collision models, as well as the fact this ansatz is grounded in the steady state, leads to this work preferring more generalized approaches to closure of the balance equations. The ansatz of Nicoletopoulos and Robson [96, 98] should however motivate future work on introducing the effects of energy transfer due to inelastic collisions into the closure of fluid models in order to model complex structures.

#### Parameterized Four Moment Model

In previous work by Dujko *et al.* [95, 104, 146] a four moment fluid model was presented with focus on application to streamer propagation; this model will be referred to as 4MM-D in the remainder of this work. Functionally, this model is identical to the four moment model presented in this study (2.11) - (2.14), but with different closure assumptions. Closure of the momentum balance higher order term,  $\theta_m$ , is achieved by assuming a Maxwellian distribution [95, 96] and isotropic temperature tensor in order to yield the following standard closure expression

$$\theta_m \approx \frac{2}{3m_e} \langle \epsilon \rangle \mathbf{l}, \quad (2.27)$$

where  $\mathbf{l}$  is the identity tensor.

Extending this assumption to closing the energy flux balance equation, and assuming the higher order energy flux closure term can be approximated by

$$\theta_\xi \approx \beta \left\langle \frac{1}{2} m v^2 \right\rangle \langle \mathbf{v} \mathbf{v} \rangle, \quad (2.28)$$

an ansatz is constructed for second closure term

$$\theta_\xi \approx \beta \frac{2}{3m_e} \langle \epsilon \rangle^2 \mathbf{l}, \quad (2.29)$$

where  $\beta$  is a parameterization factor nominally close to unity [95, 146]. In this study, it was assumed  $\beta = 1$  as per the author's original work.

### Drift Diffusion Models

One of the simplest, and most popular, approaches to fluid modeling is a drift diffusion model with hydrodynamic transport coefficients applied to a density gradient expansion [93, 96, 103, 104]. This approach utilizes two continuity equations for number density (2.11) and energy density (2.13), with particle and energy density flux expressions closing the system. Traditionally the particle flux is written

$$\mathbf{\Gamma} = -n\mu(\langle\epsilon\rangle)\mathbf{E} - D(\langle\epsilon\rangle)\nabla n, \quad (2.30)$$

where electron mobility and longitudinal diffusion coefficients,  $\mu$  and  $D_L$  in a 1D model, are tabulated as a function of the local reduced electric field or electron mean energy as per the collision input from previous models. In keeping with recent studies demonstrating non-local effects in gas discharges [93, 96, 97, 147–149], the local mean energy approximation is used in application of these drift diffusion models in lieu of the local field approximation.

In contrast to particle flux closure, a number of methods have been previously used to approximate the energy density flux expression [89, 93, 95, 96, 98, 100, 103, 104, 145]. The simplest approach is to neglect the heat flux by fixing it to zero [96, 104]; this model will be referred to as *DDA-Z* in the remainder of this work. The zero heat flux closure of equation (2.33) can be derived by expanding the energy density flux  $\mathbf{\Gamma}_\epsilon = \frac{1}{2}mn\langle v^2\mathbf{v}\rangle$  using the identity

$$\mathbf{\Gamma}_\epsilon = n_\epsilon\langle\mathbf{v}\rangle + \mathbf{P} \cdot \langle\mathbf{v}\rangle + \mathbf{J}_q, \quad (2.31)$$

where  $\mathbf{P}$  is the pressure tensor, simplified by assuming a Maxwellian energy distribution to yield the common isotropic pressure tensor expression

$$\mathbf{P} \approx \frac{2}{3}n_\epsilon\mathbf{I}. \quad (2.32)$$

If the heat flux is then assumed very small such that it can be neglected,  $\mathbf{J}_q^z = 0$ , one can rewrite equation (2.31) by substituting for the particle flux,  $\mathbf{\Gamma} = n\langle\mathbf{v}\rangle$ ,

$$\mathbf{\Gamma}_\epsilon = \frac{5}{3}n_\epsilon\langle\mathbf{v}\rangle = \frac{5}{3}\langle\epsilon\rangle\mathbf{\Gamma}, \quad (2.33)$$

where  $\mathbf{\Gamma}$  is the particle flux defined in equation (2.30).

Another common approach to constructing a heat flux ansatz is by assuming a Fourier's law of heat conduction style closure [80, 93]; this model will be referred to as *DDA-F* in the remainder of this work. A Fourier heat flux ansatz may be derived by assuming a Fourier law type relation for the heat flux

$$\mathbf{J}_q^F = -\frac{5}{3}nD\nabla\langle\epsilon\rangle, \quad (2.34)$$

such that the flux of heat transfer is proportional to some conductivity multiplied by the mean energy gradient [80, 93].

Combining equations (2.31) and (2.34) and rewriting as a gradient of  $n_\epsilon$

$$\mathbf{\Gamma}_\epsilon = -\frac{5}{3}n_\epsilon\mu(\langle\epsilon\rangle)\mathbf{E} - \frac{5}{3}\mathbf{D}(\langle\epsilon\rangle)\nabla n_\epsilon, \quad (2.35)$$

where  $\mu$  and  $\mathbf{D}$  are the electron mean energy dependent electron mobility and diffusion coefficients.

Despite being based on an analytic distribution, the closure expression (2.35) does allow for energy density spatial gradients to induce energy transfer - an improvement over the zero heat flux assumption. The formulation and further implications of the Fourier law assumption are detailed in [93, 96].

## 2.3 Benchmark Results and Discussion

Benchmarking is a valuable process in evaluating a model and the integrity of numerical solutions. A simple benchmark case was chosen, with a simple collision model for a gas and liquid analogue. This was done to allow comparison of the fundamental transport effects of the fluid equations and their approximations, without introducing nuances of real gases that may introduce phenomena specific to that molecule. A one dimensional steady state field perturbation benchmark problem and a non-hydrodynamic transient evolution benchmark are presented in this work. Benchmarks were performed in both gas phase and an approximated liquid phase through modifications to the gas phase model. The flux corrected transport (FCT) numerical method employed to solve the systems of hyperbolic equations in this study is based on popular methods used for many years [150–152], and is further outlined in Appendix A, along with the dimensional scaling of variables used in this work.

### 2.3.1 Gas Phase Collision Model

A simple constant cross section inelastic step collision model has been studied in this work, as per Table 2.1. The model was chosen because despite its simplicity, it can produce physically complex results such as periodic electron structures and relaxation behavior [98, 103, 105, 153] observed in real gases used in benchmark computations, such as argon or neon. With the simplicity of implementation, yet complex non-hydrodynamic transport behavior, this collision model provides a good analogue gas for benchmarking the performance of fluid models.

Table 2.1: Constant cross section Inelastic Step Collision Model

Variable	Value
$\sigma_m$	$6 \text{ \AA}^2$
$\sigma_{\text{inel}}$	$0.1 \text{ \AA}^2, \epsilon \geq \Delta\epsilon_{\text{inel}}$
$\Delta\epsilon_{\text{inel}}$	$2 \text{ eV}$
$m_0$	$4 \text{ amu}$
$m_e$	$5.486 \times 10^{-4} \text{ amu}$
$T_0$	$0 \text{ K}$

### 2.3.2 Liquid Phase Modification

To approximate transport in a simple, non-polar liquid-like medium a structure modification to the gas phase collision model in Table 2.1 was performed within the computation of steady state transport and collision input via kinetic solution or Monte Carlo simulation of the Boltzmann equation [10, 87, 96, 102]. This was done via including a static structure modification into the momentum transfer cross section, through the Percus-Yevick liquid model with the correction of Verlet and Weiss [65, 154]. The structure of neutral molecules is assumed to consist of an array of hard sphere potentials interacting coherently, with a density governed by a packing factor

$$\phi = \frac{4}{3}\pi r^3 n_0 \quad (2.36)$$

where  $r$  is the hard sphere radius, and  $n_0$  is the neutral number density.

A packing factor of  $\phi = 0$  corresponds to a classic dilute gas, while the maximum value of  $\phi \approx 0.64$  corresponds to a maximally packed solid of hard spheres. For the simple liquid approximation in this study a packing factor of  $\phi = 0.4$  was used [10]. Further details of this liquid phase modification in the Monte Carlo simulations or multi-term solution of Boltzmann's equation can be found in the recent work by the JCU group [10, 48, 65].

### 2.3.3 Input Data

Given the collision model specified in the previous section, a collection of steady state input data was generated via Monte Carlo simulations. By generating two sets of the necessary steady state input data for fluid models described in this study, one each for gas and liquid analogues, the same fluid model formulations can be used to simulate electron transport, given the basis of the gas phase collision model in Table 2.1 and simple liquid modifications previously outlined.

The inclusion of coherent scattering effects in the liquid phase results in variations of the fluid model input data from the classic dilute gas picture. A comparison of the gas and liquid phase transport input data is presented in the following figures.

### Hydrodynamic Transport Coefficients

The variation of the electron reduced mobility,  $n_0\mu$ , and reduced longitudinal diffusion coefficient,  $n_0D_L$ , between gas and liquid phase transport is shown in Figures 2.1 (a) and (b) respectively. The increased mobility and diffusion at low energy due to coherent scattering are clearly noted, as well as the asymptotic convergence of liquid transport to gas phase transport at higher energies.

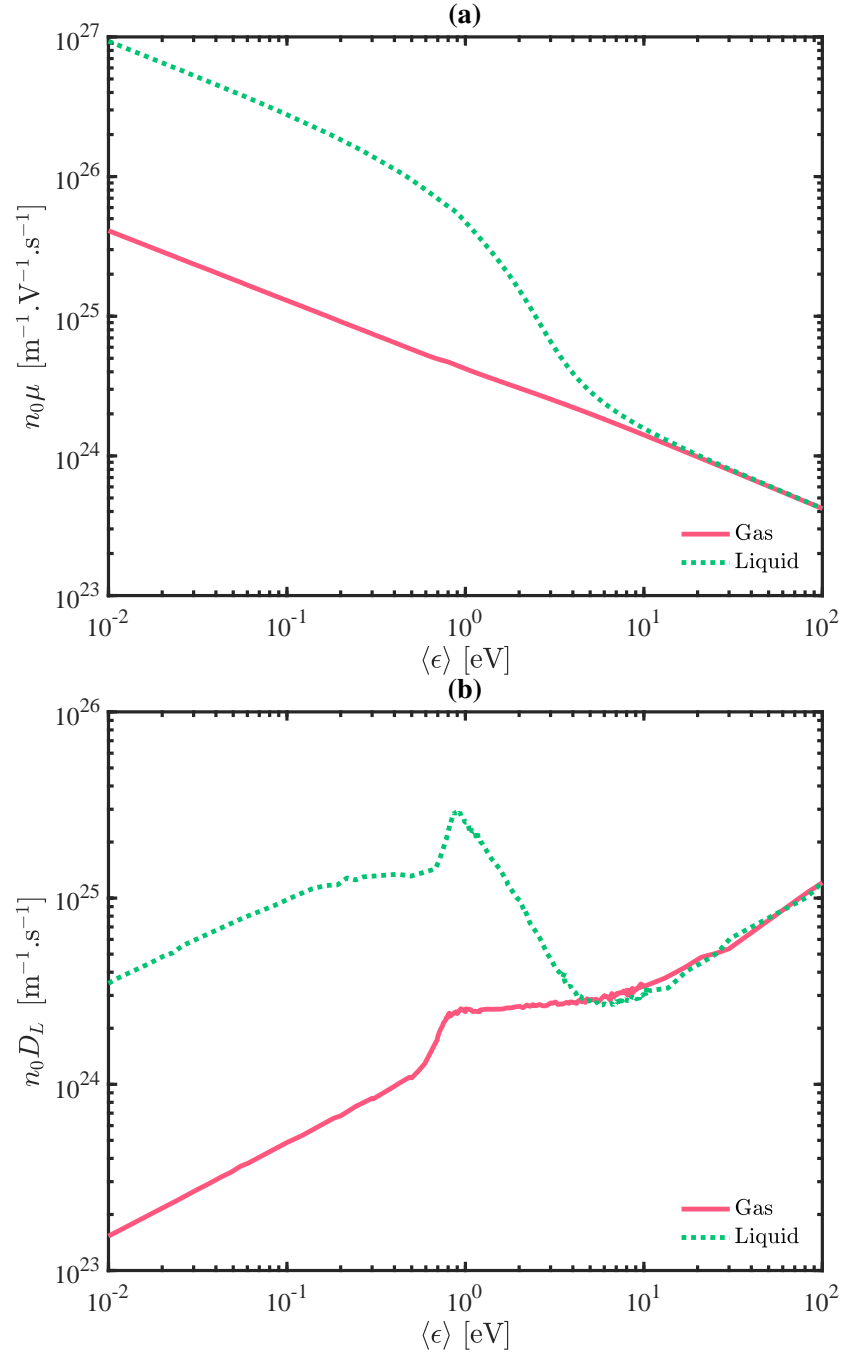


Figure 2.1: Hydrodynamic transport input data for gas and liquid phase transport for collision model in Table 2.1. (a) Reduced electron mobility coefficient; (b) Reduced electron longitudinal diffusion coefficient

### Collision Rates

The reduced collision frequencies of momentum, energy, and energy flux transfer computed from steady state distribution functions are presented in Figure 2.2.

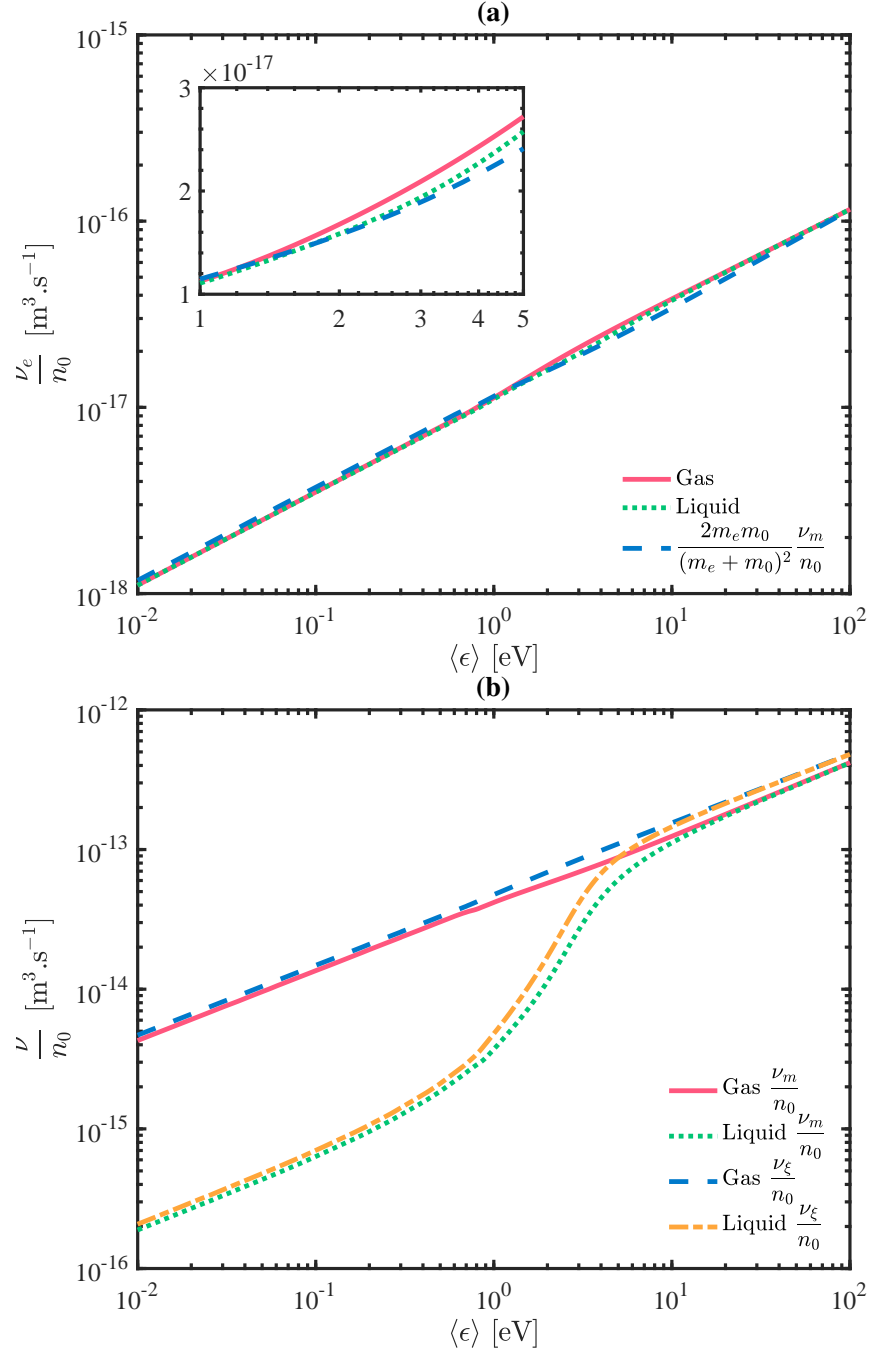


Figure 2.2: Electron collision rate input data for gas and liquid phase transport for collision model in Table 2.1. **(a)** Effective reduced energy transfer collision rate,  $\frac{\nu_e}{n_0}$ ; **(b)** Effective reduced momentum transfer,  $\frac{\nu_m}{n_0}$ , and energy flux transfer,  $\frac{\nu_\xi}{n_0}$ , collision rates.

An inset plot in Figure 2.2 (a) is included to demonstrate deviation of the curves within an energy range close to the inelastic threshold energy of 2 eV. For comparison, figures also include a plot of an alternative approach to computing the reduced energy transfer rate [48] often implemented in Momentum Transfer Theory (MTT)

$$\left. \frac{\nu_e}{n_0} \right|_{\text{gas \& liq}} \approx 2 \frac{m_e m_0}{(m_e + m_0)^2} \left. \frac{\nu_m}{n_0} \right|_{\text{gas}},$$

to demonstrate the importance of including a specifically computed energy loss rate,  $S_e^{\text{ss}}$ , and not simply multiplying the gas phase momentum transfer rate by the mass ratio prefactor, often used in MTT collision approximations [96, 118].

The effects of coherent scattering in the liquid phase approximation are clearly evident in Figure 2.2 (b), where  $\frac{\nu_m}{n_0}$  is multiple orders of magnitude smaller at low energies. As the mean energy of an incoming electron increases, the effects of coherent scattering are reduced and the liquid phase result converges to the gas phase value.

Previously the momentum transfer collision frequency has been used as the collision rate for the energy flux balance equation, owing to the physical similar collisional time scales for the two vector quantities [95, 104, 146]. However, it can be seen in Figure 2.2 that there is a difference between the momentum transfer frequency and a specifically computed energy flux transfer frequency, even in this simple benchmark problem, across both gas and liquid phase media. This supports the claim of using a dedicated energy flux transfer rate as also recommended by Becker and Loffhagen [103, 144].

### Closure Terms

The higher-order moment closure terms  $\theta_m^{\text{ss}}$  and  $\theta_\xi^{\text{ss}}$ , defined by equations (2.23) and (2.24) used in the  $4MM\text{-}SS/DDA\text{-}SS$  models, are plotted against the parameterized moment closure terms, defined by equations (2.27) and (2.29) used in the  $4MM\text{-}D$  model, in Figure 2.3.

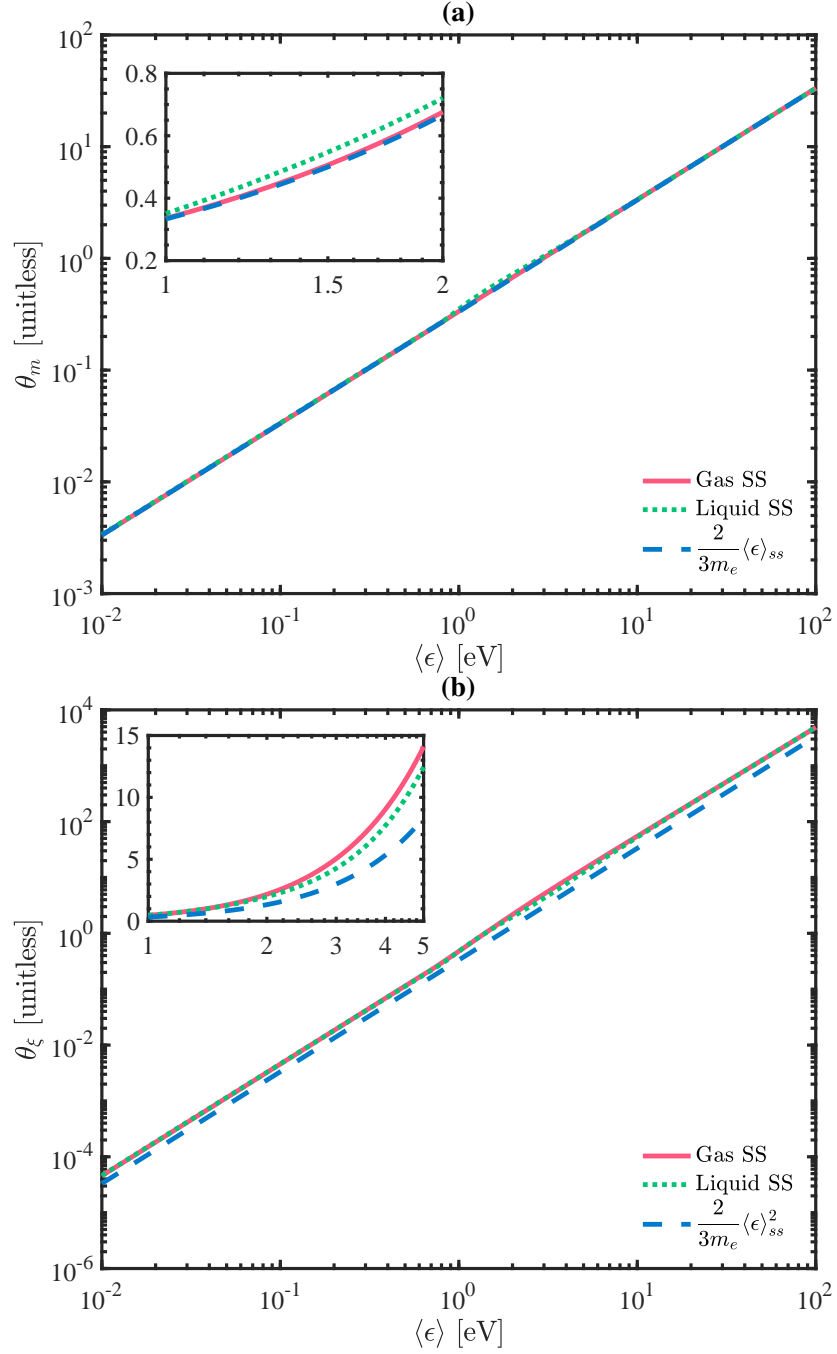


Figure 2.3: Higher order closure input for gas and liquid media according to collision model in Table 2.1: (a) Momentum balance term,  $\theta_m^{ss}$ ; (b) energy flux balance term,  $\theta_\xi^{ss}$ .

The inset plots demonstrate there is departure between the approximations once the inelastic channel begins to contribute significantly, specifically on intermediate energy ranges (0.1 eV - 10 eV) commonly experienced in non-equilibrium low-temperature plasma modeling. One should note a difference between gas and liquid phase values as well, which the parameterized closure does not allow for. This is the primary motivation to preference a direct substitution of steady state data as a function of the electron mean energy, as opposed to parameterizing or assuming a simpler form of the higher

order terms.

### 2.3.4 Hat Field Benchmarks

In order to verify against similar benchmarks used in previous works, a simple hat perturbation of a homogeneous background reduced electric field has been adopted [103,149]. The hat perturbation is placed downstream of an electron source emitting with a constant flux. Fluid models are solved in the steady state over the domain in order to resolve the response of macroscopic variables to the field change. The hat perturbation used previously increases the magnitude of the background reduced electric field with a step function over a defined distance. The geometry of this benchmark is outlined in Figure 2.4.

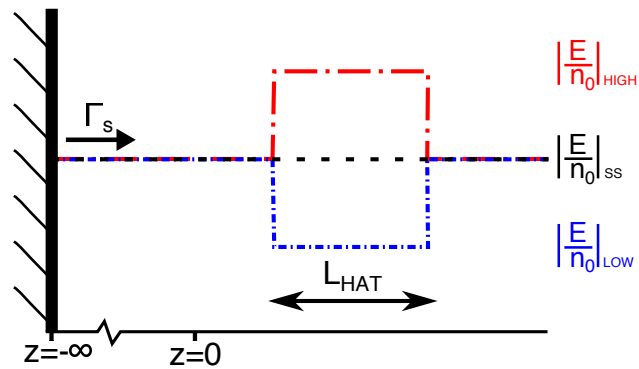


Figure 2.4: Hat and inverse hat field benchmark problem geometry

Studying the hat field benchmark allows the effect of inelastic collisions to be studied, and for the performance of fluid models to be evaluated in this field-enhanced collision regime. By increasing the reduced electric field the electron distribution function within the hat samples a larger portion of the inelastic cross section. If the increased reduced electric field is within a certain range a balance between field driven heating and inelastic cooling is reached. This *window phenomenon* in effect produces oscillating spatial structures in all macroscopic observables [98,153]. By studying the response of fluid models to this field, one may assess the ability, or inability, of these models to account for such spatial structures.

In addition to the hat field benchmark that increases the magnitude of the reduced electric field, one may also simulate an inverse hat field benchmark that reduces the magnitude of the reduced electric field. This inverse hat field model has been chosen in order to examine the relaxation of momentum and energy in low advection problems. Given that closure assumptions of the fluid equations directly impact the divergence of the higher order tensors, and hence the diffusive transport of electron number and energy, it is vital to study a low-field benchmark that emphasizes the impacts of diffusive transport.

Benchmarking against the discussed hat and inverse hat problems provides a suitable breadth of physical conditions to evaluate fluid models presented in this work. For example, the increasing hat field can be compared to potentially sharp gradients found

in field-enhanced tip regions of streamer propagation [95, 104, 146] or in sheath regions near boundaries [96, 100]. While conversely, the reduced magnitude of the inverse hat field can be compared to regimes where electric field screening occurs in the channel behind a propagating streamer [95, 104, 146] or where an electric field sheath transitions back into the bulk region of a plasma [96, 100].

### Initial and Boundary Conditions

A source emitting electrons at a constant rate at the background reduced field's steady state mean energy and drift velocity was placed far from the reduced electric field perturbation, such that the electrons had relaxed to a steady-state for the background field before reaching the field step.

Initially the domain was empty,  $n(z, 0) = 0$ , prior to the source being turned on. Each system of fluid equations was evolved in time, using the numerical method outlined in A, until a steady state solution was reached.

Simple boundary conditions for electron density, and thus fluxes and energy density, are used through fixed Dirichlet conditions

$$n\left(-\frac{L}{2}, t\right) = n\left(\frac{L}{2}, t\right) = 0 \quad (2.37)$$

where  $L$  is the length of the simulation domain. To further reduce the effect of boundaries the computational domain was extended to avoid significant density transport within a fixed distance of the boundaries.

### Goodness of Fit

In order to quantify how well each fluid model can produce physically accurate results this work uses a goodness of fit table for each benchmark. Normalized mean square error (NMSE) computations are performed for each fluid model solution when compared to the physically detailed Monte Carlo solution. The NMSE of an approximation,  $f_{\text{approx}}$ , compared to an exact value of the function,  $f_{\text{exact}}$ , is defined as

$$\text{NMSE} = \left\| \frac{f_{\text{exact}} - f_{\text{approx}}}{f_{\text{exact}} - \text{mean}(f_{\text{exact}})} \right\|^2, \quad (2.38)$$

where  $\|\dots\|$  indicates the 2-norm. In the interpretation of NMSE results, noting the bounds  $0 \leq \text{NMSE} \leq \infty$ , where  $\text{NMSE} = 0$  indicates a perfect fit,  $\text{NMSE} = \infty$  indicates a bad fit, and  $\text{NMSE} = 1$  implies the approximation is no better a fit than a straight line.

### Standard Hat Field

Figures 2.5 and 2.6 present steady state solutions of each fluid model for the standard hat field benchmark in both gas and liquid phase. Tables 2.2 and 2.3 include the NMSE goodness of fit values. For comparison a Monte Carlo (MC) solution of the benchmark

problem is included, computed from methods previously used by the JCU group [65, 87]. For the steady state closure method advocated in this work the presented results are the same for both  $\mathcal{4MM-SS}$  and  $DDA-SS$  models, since the solution is in the steady state.

The fluid model results presented in Figures 2.5 and 2.6 and NMSE values in Tables 2.2 and 2.3 demonstrate strong agreement among fluid models for this benchmark in both gas and liquid phases. None of the fluid models can reproduce the periodic structures found in the MC solution, consistent with previous studies [103]. The Fourier and zero heat flux closures offer similar solutions which tend to overshoot on rising and falling edges of the field perturbation. On the other hand, the  $\mathcal{4MM-D}$  and  $DDA-SS$  solutions are generally monotonic, with the exception of an irregular peak on the falling edge of the hat.

MC simulations demonstrating mean energy heating and cooling either side of the rising and falling edges of the hat are not reproduced to the same magnitude by fluid models. This demonstrates the non-local effects of the electric field change impacting transport properties some distance away. The fluid models appear to be capable of resolving some of this non-local transport but not to the extent found in the MC simulations, particularly in the liquid phase benchmark.

Overall there are minor observable differences among the fluid model results and all NMSE results are very consistent across all variables, approaching zero, indicating a reasonable approximation in the “line of best fit” sense for all variables with all fluid models used. It can be concluded that using any of the fluid models provides a reasonable approximation to the steady-state electron transport, excluding the periodic electron structures, in cases such as this benchmark

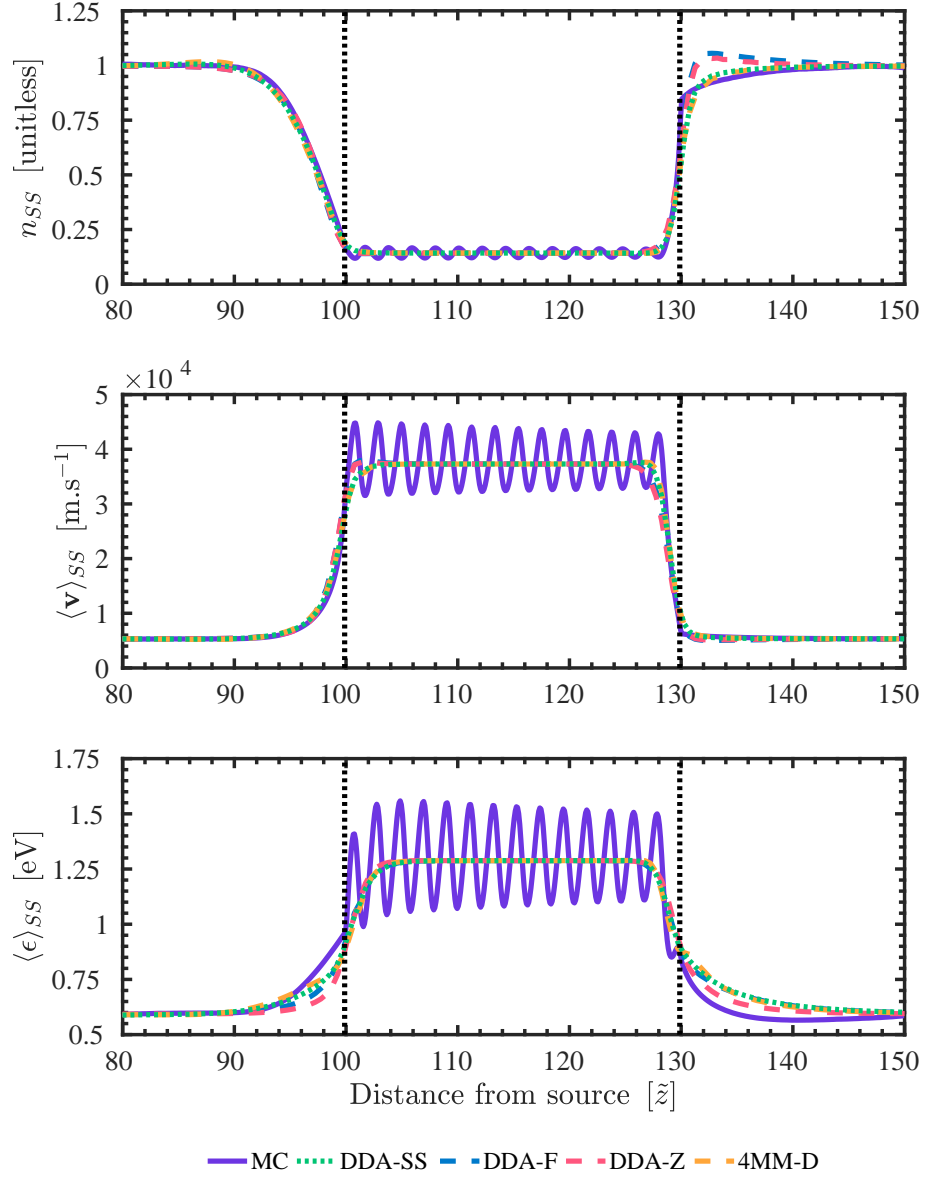


Figure 2.5: Gas phase hat field perturbation benchmark as per Figure 2.4 where  $\tilde{L}_{\text{HAT}} = 30$ ,  $\frac{\mathbf{E}}{n_0} = -1 \text{ Td} : -10 \text{ Td} : -1 \text{ Td}$

Table 2.2: NMSE for Figure 2.5 solutions for each fluid model compared against Monte Carlo result

Model	$n_{SS}$	$\mathbf{W}_{SS}$	$\langle \epsilon \rangle_{SS}$
DDA-SS	0.004	0.033	0.112
DDA-F	0.010	0.035	0.111
DDA-Z	0.007	0.037	0.111
4MM-D	0.005	0.032	0.112

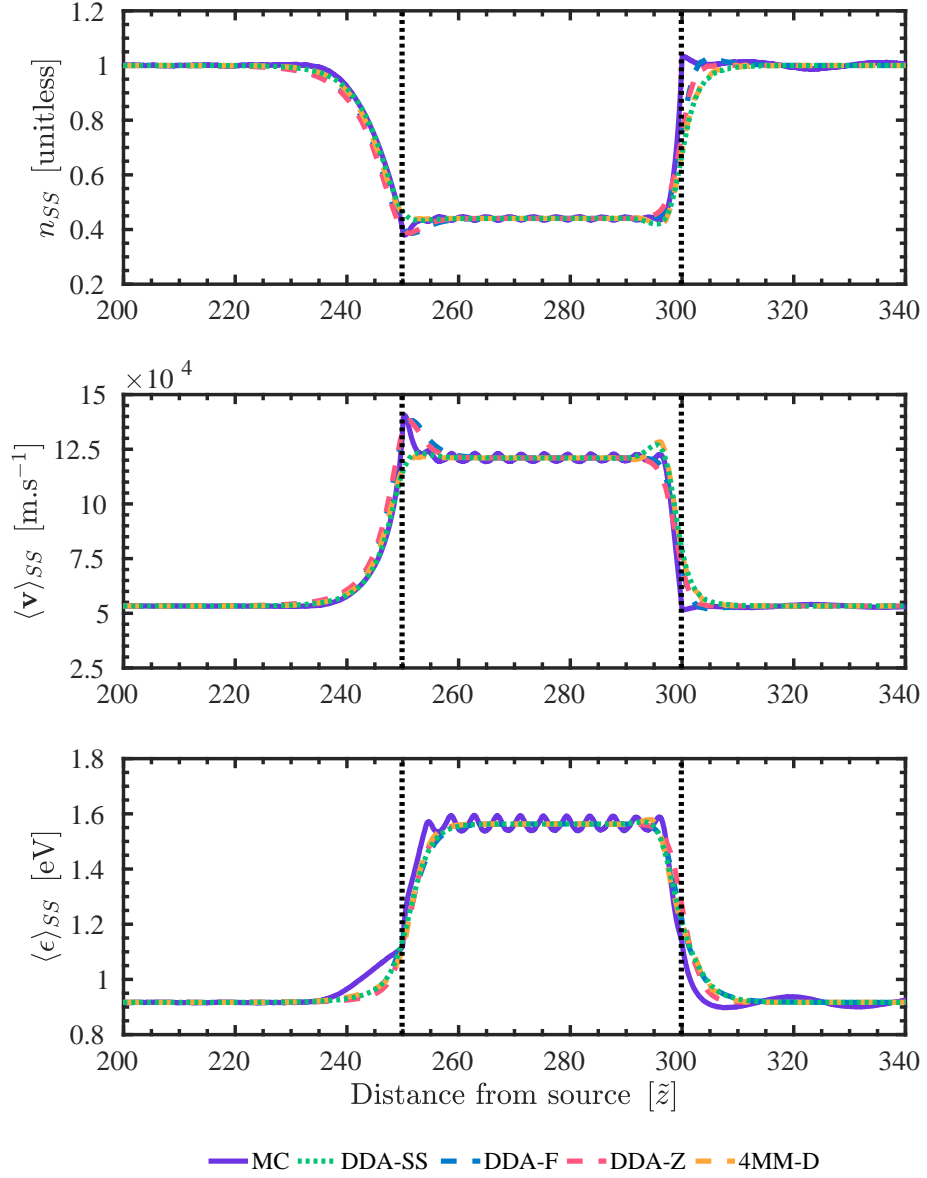


Figure 2.6: Liquid phase hat field perturbation benchmark as per Figure 2.4 where  $\tilde{L}_{\text{HAT}} = 50$ ,  $\frac{\mathbf{E}}{n_0} = -1 \text{ Td} : -5 \text{ Td} : -1 \text{ Td}$

Table 2.3: NMSE for Figure 2.6 solutions for each fluid model compared against Monte Carlo result

Model	$n_{SS}$	$\mathbf{W}_{SS}$	$\langle \epsilon \rangle_{SS}$
DDA-SS	0.024	0.016	0.015
DDA-F	0.013	0.011	0.015
DDA-Z	0.015	0.012	0.018
4MM-D	0.022	0.016	0.014

### Inverse Hat Field

Comparison of the fluid model results in Figures 2.7 and 2.8 and the NMSE goodness of fit metrics in Table 2.4 indicate a significant difference between fluid models in this study. It can be seen the Fourier and zero heat flux models significantly differ to

the MC solution, whereas the  $4MM-D$  and  $DDA-SS$  models provide a qualitatively closer approximation to the actual solution for number density and mean velocity. The number density profiles for the  $DDA-F$  and  $DDA-Z$  models offer a completely different qualitative result compared to the MC result because of the overshoot of the mean velocity profiles; in order for the particle flux to remain constant in the steady state, the number density must compensate for the overshoot in the mean velocity, leading to the erroneous results in Figures 2.7 and 2.8.

The discrepancy between MC results and fluid models isn't as pronounced for the liquid phase transport, compared to the gas phase. An effect of the inclusion of coherent scattering for the liquid phase results in a longer momentum relaxation distance in liquid phase transport, which appears to assist the fluid models in reproducing some of the results.

In contrast, the  $4MM-D$  and  $DDA-SS$  models provide a better approximation of the mean velocity leading to a closer approximation of the number density, and implying these models handle the low advection transport regime much better than the other two models.

The agreement in the mean energy profiles is much tighter than the lower two moments, with all fluid models doing reasonably well in approximating the MC solution. One should note that while  $4MM-D$  and  $DDA-SS$  models have very similar NMSE values, Figure 2.7 shows the  $4MM-D$  model produces incorrect relaxation behavior on the falling edge of the inverse hat. The Fourier model solution offers a very good fit within the hat region, but the inaccuracy of the number density and mean velocity results detracts from this positive result for the  $DDA-F$  model.

Noticeably, in Figure 2.8, none of the fluid models provide a good approximation to the liquid phase mean energy relaxation inside the inverse hat perturbation. It appears the longer liquid phase relaxation length is better approximated by the  $DDA-SS$  and  $4MM-D$  models when compared to the MC mean energy, but the attenuation of the energy is not well described. The opposite appears to be the case for  $DDA-F$  and  $DDA-Z$  results, which attenuate the mean energy to a lower value but the relaxation length is considerably different than the MC result.

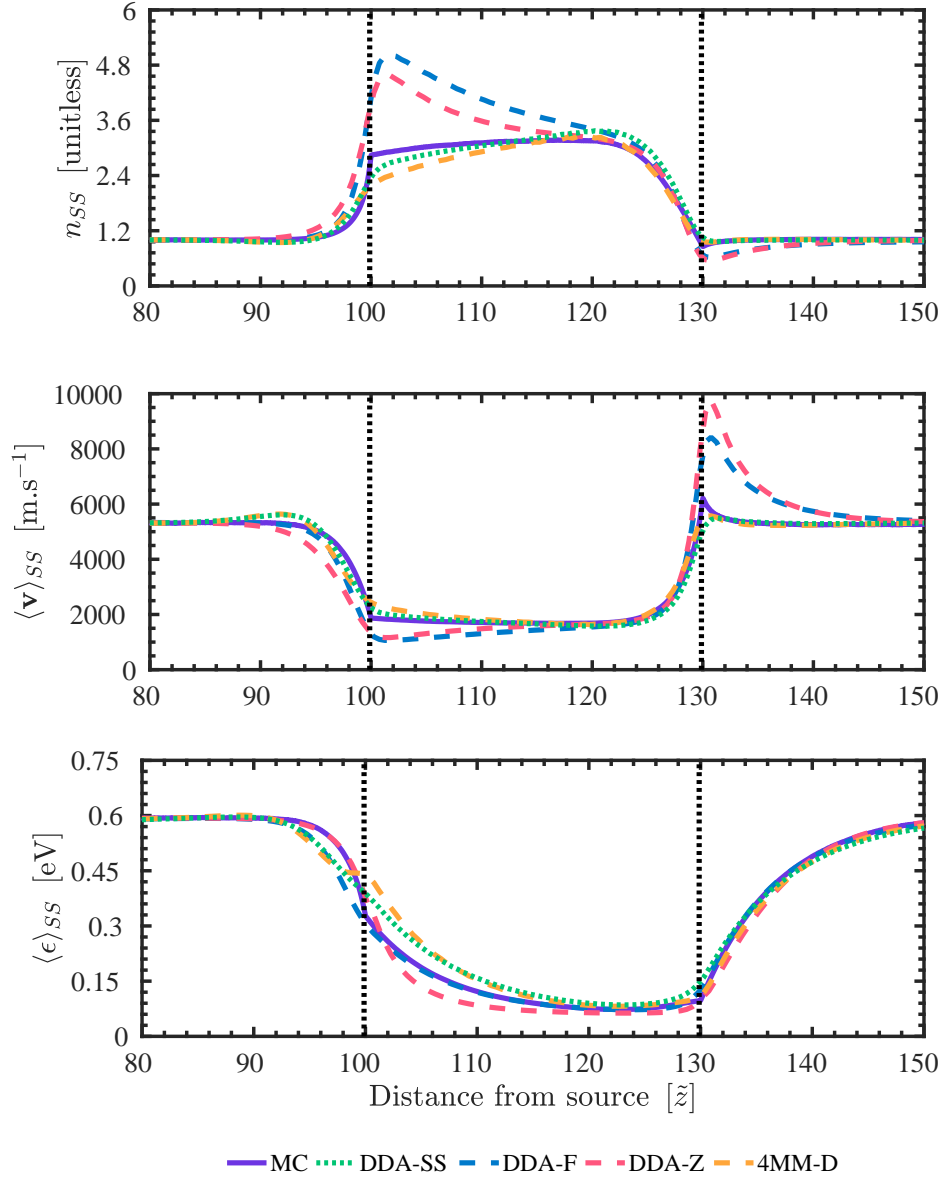


Figure 2.7: Gas phase inverse hat field perturbation benchmark as per Figure 2.4 where  $\tilde{L}_{\text{HAT}} = 30$ ,  $\frac{\mathbf{E}}{n_0} = -1 \text{ Td} : -0.1 \text{ Td} : -1 \text{ Td}$

Table 2.4: NMSE for Figure 2.7 solutions for each fluid model compared against Monte Carlo result

Model	$n_{SS}$	$\mathbf{W}_{SS}$	$\langle \epsilon \rangle_{SS}$
DDA-SS	0.018	0.011	0.017
DDA-F	0.491	0.170	0.008
DDA-Z	0.267	0.293	0.011
4MM-D	0.030	0.014	0.027

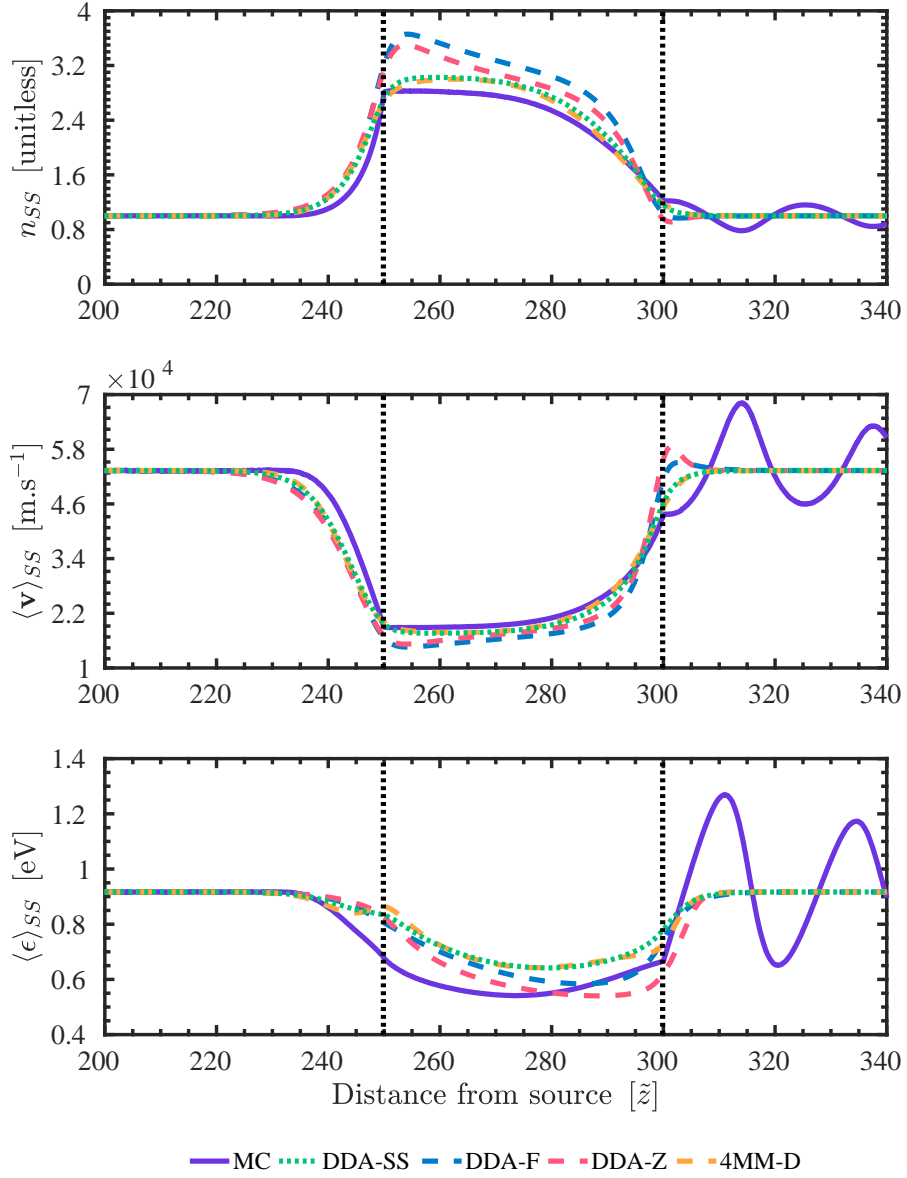


Figure 2.8: Liquid phase inverse hat field perturbation benchmark as per Figure 2.4 where  $\tilde{L}_{\text{HAT}} = 50$ ,  $\frac{\mathbf{E}}{n_0} = -1 \text{ Td} : -0.2 \text{ Td} : -1 \text{ Td}$

Table 2.5: NMSE for Figure 2.8 solutions for each fluid model compared against Monte Carlo result

Model	$n_{SS}$	$\mathbf{W}_{SS}$	$\langle \epsilon \rangle_{SS}$
DDA-SS	0.037	0.076	0.417
DDA-F	0.228	0.113	0.365
DDA-Z	0.136	0.121	0.361
4MM-D	0.032	0.076	0.421

### 2.3.5 Spatiotemporal Pulse Evolution

As a supplement to the steady state hat field benchmark, which provides some non-equilibrium effects near the field perturbations, the transient evolution of a Pulsed Townsend experiment initial pulse was studied to study the ability of the presented

fluid models to resolve time-dependent transport effects. Study of this benchmark allows the performance of the fluid models in a sharp gradient, non-hydrodynamic, and non-equilibrium regime to be assessed. For brevity this benchmark is presented for gas phase transport only, as liquid phase results were very similar.

This simulation takes place by releasing the narrow pulse in a homogeneous background reduced field, and simulating the space-time evolution. Sample times were taken at approximately 10 and 100 momentum transfer relaxation times, and 5 energy transfer relaxation times. These sample times were chosen to demonstrate the solution variations over different physical regimes in order to assess which fluid models provide the best overall response.

For this benchmark comparison a multi-term solution of the Boltzmann equation detailed by Boyle *et al.* [10] has been included as a reference solution. For this benchmark the reduced electric field was fixed at  $\frac{\mathbf{E}}{n_0} = -3$  Td such that  $W_z = 1.385 \times 10^4$  m s<sup>-1</sup>,  $\langle \epsilon \rangle = 0.8337$  eV are the steady state drift velocity and mean energy respectively.

### Initial and Boundary Conditions

The transient pulse benchmark was set by an initial condition of a narrow Gaussian number density

$$f_n(\tilde{z}) = \frac{1}{\Delta\tilde{z}_0\sqrt{2\pi}} \exp\left[-\frac{1}{2}\left(\frac{\tilde{z}}{\Delta\tilde{z}_0}\right)^2\right], \quad (2.39)$$

where  $\Delta\tilde{z}_0 = 0.1$ , and fixed in velocity space by a drifted Maxwellian distribution

$$f_v(\mathbf{v}) = f_n(z) \left(\frac{m}{2\pi k_B T}\right)^{\frac{3}{2}} \exp\left[-\frac{m}{2k_B T}(\mathbf{v} - \mathbf{W})^2\right], \quad (2.40)$$

where  $T = 10^4$  K and  $\mathbf{W} = 10^5$  ms<sup>-1</sup> $\hat{\mathbf{E}}$ .

Initial conditions for fluid model computational variables are determined by integrating (2.15) - (2.17) over the distribution function

$$f(U, \mathbf{r}, 0) = A f_n(\tilde{z}) f_v(\mathbf{v}), \quad (2.41)$$

where  $A$  is a normalization constant such that  $\int U^{\frac{1}{2}} f(U, \mathbf{r}, 0) dU = 1$ . Evaluation of these gives

$$\begin{aligned} n(\mathbf{r}, 0) &= f_n(\tilde{z}) \\ \mathbf{\Gamma}(\mathbf{r}, 0) &= f_n(\tilde{z}) \mathbf{W}, \\ n_\epsilon(\mathbf{r}, 0) &= f_n(\tilde{z}) \left(\frac{3}{2}k_B T + \frac{1}{2}m_e W^2\right), \\ \mathbf{\Gamma}_\epsilon(\mathbf{r}, 0) &= f_n(\tilde{z}) \left(\frac{5}{2}k_B T + \frac{1}{2}m_e W^2\right) \mathbf{W}. \end{aligned} \quad (2.42)$$

Dirichlet boundary conditions described for the steady state hat benchmark were employed for the transient pulse evolution.

### Number Density Evolution

The number density evolution displayed in Figure 2.9 demonstrates that at short times dominated by momentum relaxation no fluid model provides an exact replication of the kinetic result, consistent with expected accuracy bounds of fluid models [95, 96, 103]. Despite all fluid model results being more diffusive than the kinetic solution, none demonstrate concerning variation from the general qualitative behavior of the accurate kinetic solution.

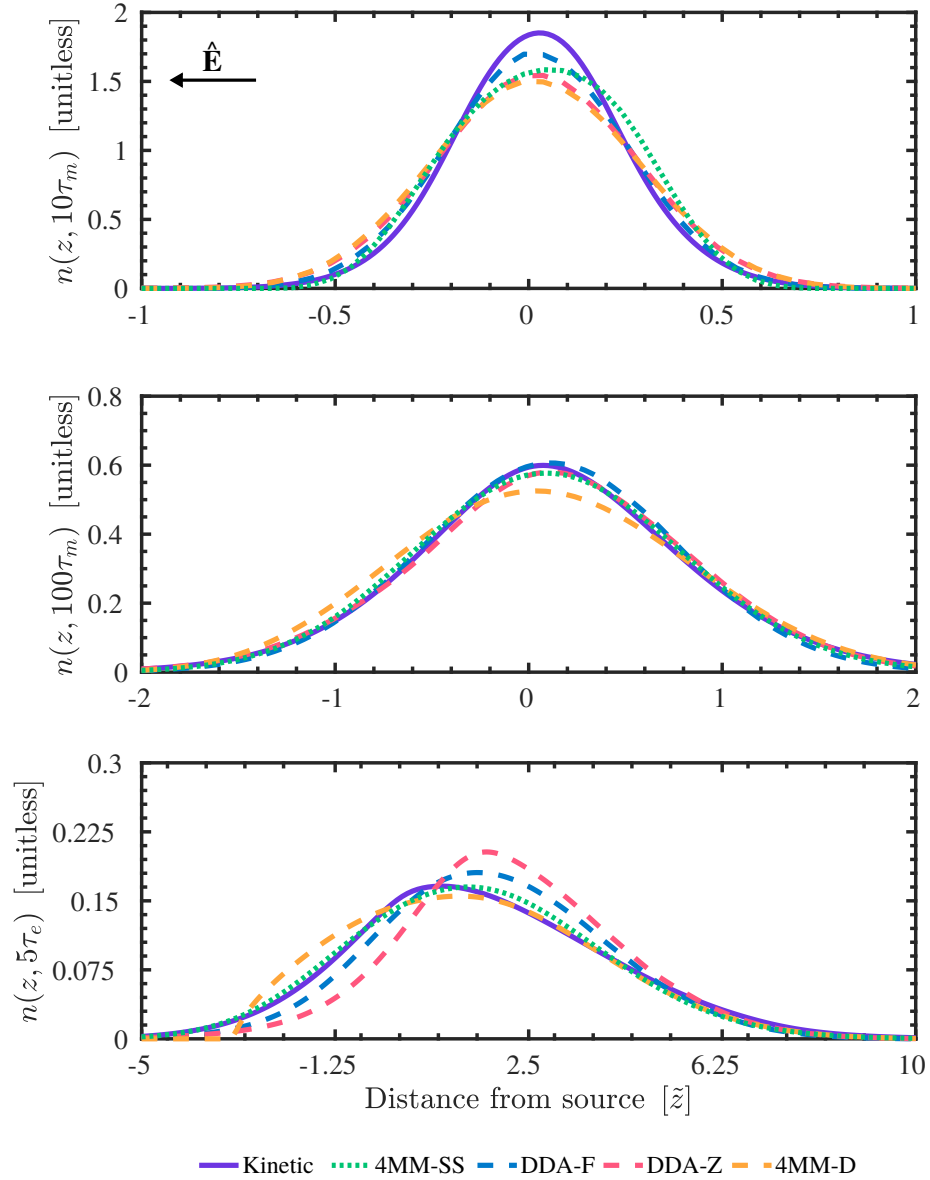


Figure 2.9: Transient evolution of electron density from narrow Gaussian pulse. Gas phase media as per Table 2.1 with background  $\frac{\mathbf{E}}{n_0} = -3$  Td.

Considering the intermediate regime between momentum and energy relaxation processes in Figure 2.9 shows better agreement to the kinetic solution for all fluid

models apart from the  $4MM-D$  model. This demonstrates the effects of higher density diffusivity due to closure assumptions in the  $4MM-D$  model.

As time continues, and energy relaxation becomes the dominant process, the variation between fluid solutions is shown in Figure 2.9. It can be plainly seen the zero heat flux and Fourier closure assumptions produce profiles that poorly fit the kinetic result. They are both forward peaked, and inaccurately predict the back-diffusion seen behind the bulk of the pulse. The  $4MM-D$  closure performs slightly better, except in the region behind the bulk of the pulse, where it appears back-diffusion has not been modeled accurately. Finally, the  $4MM-SS$  result remains a suitable “line of best fit” approximation to the kinetic solution.

### Mean Velocity Evolution

From the evolution of mean velocity shown in Figure 2.10 it can be seen that the  $4MM-SS$  continues to provide a closer approximation to the kinetic solution across all three time scales. At early times, the non-hydrodynamic transport of the kinetic solution is not replicated by any fluid model yet the steady state closure provides the closest comparison compared to the other discussed fluid models.

During the transition between momentum and energy relaxation times there’s better comparison for most of the fluid models, with the exception of the zero heat flux model. However at the longest time scale the discrepancies between each fluid model can be seen. In the regions close to, and behind, the origin the mean velocity is best predicted by the  $4MM-SS$  model. While the remaining fluid models provide an over estimation of the mean velocity, particularly in back diffusion regions behind the origin. As the pulse relaxes into a smooth-gradient hydrodynamic regime, the agreement becomes asymptotically better across all fluid models, as one might expect.

### Mean Energy Evolution

Mean energy variation is much simpler to identify in this benchmark compared to the previous macroscopic observables. At short times Figure 2.11 shows a qualitative agreement to the quadratic-like shape of the kinetic solution - apart from the  $4MM-D$  model. The zero heat flux model underestimates the mean energy consistently, while the Fourier closure appears to perform quite well. The  $4MM-SS$  model overestimates the mean energy in the bulk of the pulse, and underestimates on the fringes. Overall, the approximations of most fluid models perform qualitatively well in this time sample.

As time advances into the two final sample times in Figure 2.11, it can be seen most fluid models fail to approximate the kinetic solution well apart from the  $4MM-SS$  model. The  $DDA-Z$  and  $DDA-F$  models show that on the fringes of the pulse the mean energy is severely overestimated, while generally underestimating in the bulk of the pulse. The  $4MM-D$  model continues to suffer inaccuracies in regions experiencing back diffusion effects, but does regain some accuracy in the long time regime when predicting the energy relaxation into the hydrodynamic regime.

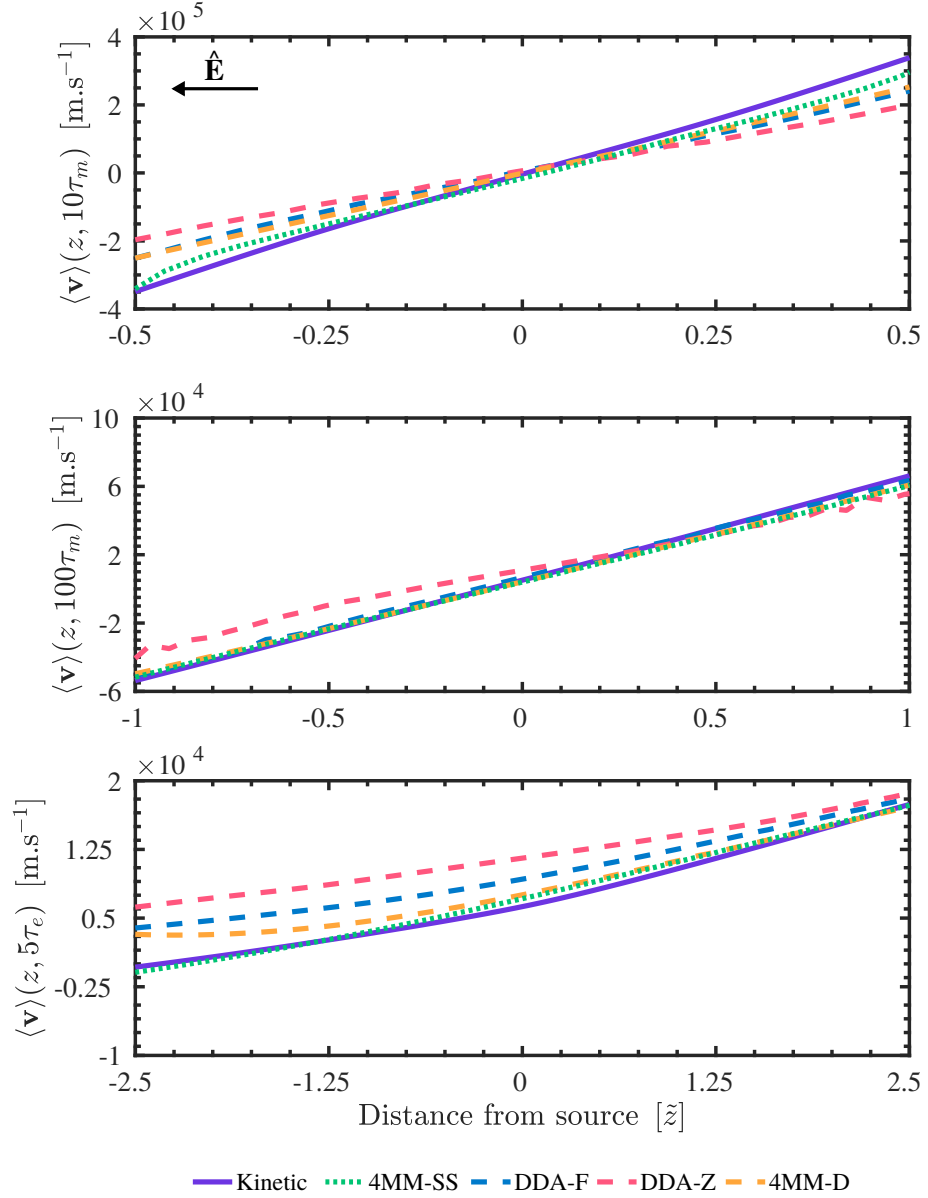


Figure 2.10: Transient evolution of electron mean velocity from narrow Gaussian pulse. Gas phase media as per Table 2.1 with background  $\frac{\mathbf{E}}{n_0} = -3$  Td.

The 4MM-SS demonstrates the ability to generally resolve a “line of best fit” approximation to the kinetic solution across multiple time scales. As a supplementary benchmark to the steady state hat field benchmark results, the presented transient evolution results are a good indicator of the general accuracy that the 4MM-SS steady state distribution closure provides. The strength of this model lies in reverting to a steady state limit to provide a physical distribution when predicting transport, this is especially clear in regions where back diffusion of energy and density are found.

### 2.3.6 Distribution effects and implications for fluid modeling

In order to understand the results and limitations of the presented fluid models the energy distribution function was studied. Given that the majority of modern fluid

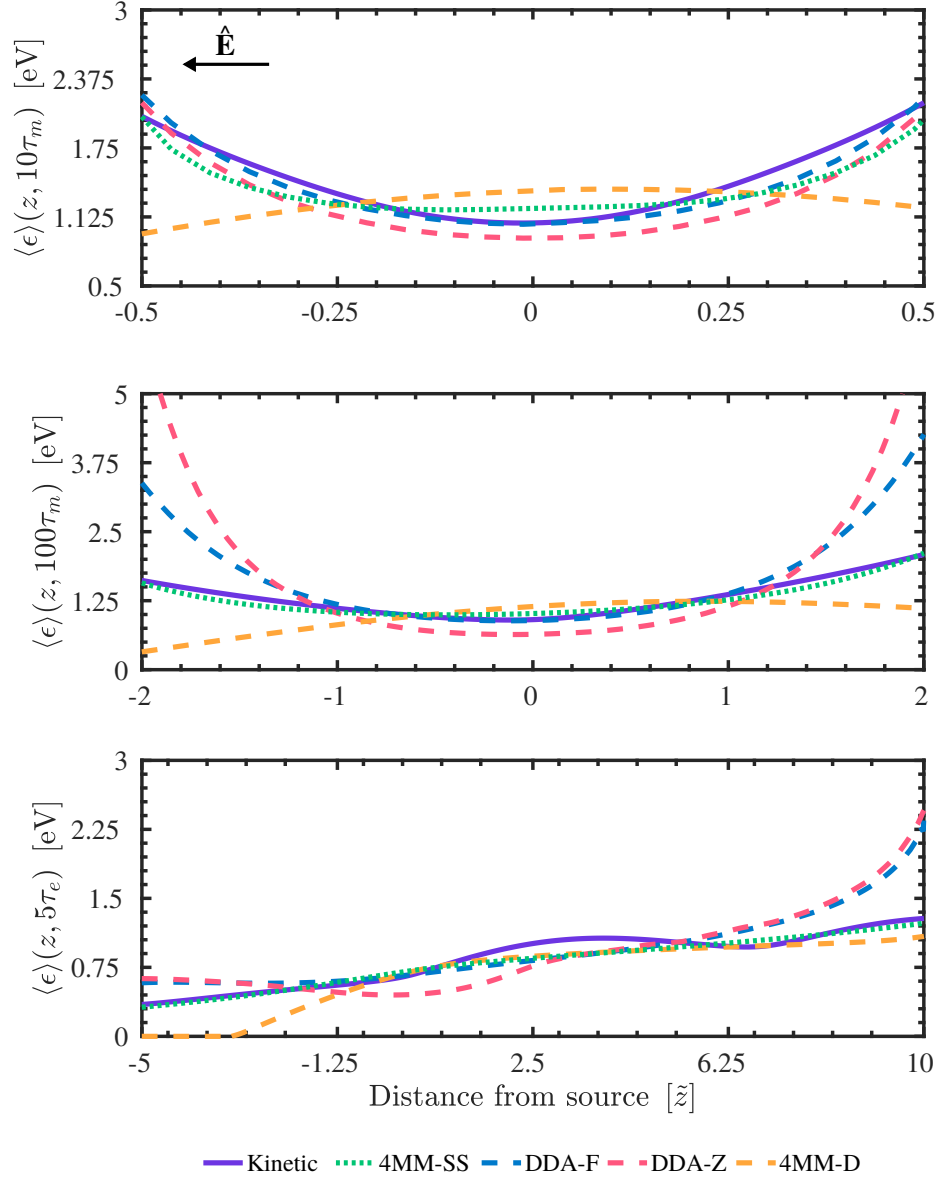


Figure 2.11: Transient evolution of electron mean energy from narrow Gaussian pulse. Gas phase media as per Table 2.1 with background  $\frac{\mathbf{E}}{n_0} = -3 \text{ Td}$ .

models utilize the local mean energy approximation in evaluation of collisions, and possibly closure, it is important to understand the role of the distribution function in producing results such as spatially periodic structures that fluid models currently cannot reliably produce.

In order to study the energy distribution function effects a transient kinetic solution of the Boltzmann equation, discussed in the previous section, was sampled after approximately five energy relaxation time periods,  $5\tau_e$ . At this time the initial energy distribution will have sufficiently relaxed to reduce sharp non-hydrodynamic effects. At the sample time the mean electron energy can be plotted, as shown in Figure 2.12, and samples in position-space can be taken where the mean-energy coincides with the steady-state mean energy value of 0.8337 eV.

The typical form of the distribution function component  $U^{\frac{1}{2}} f_0(U)$  at the spatial

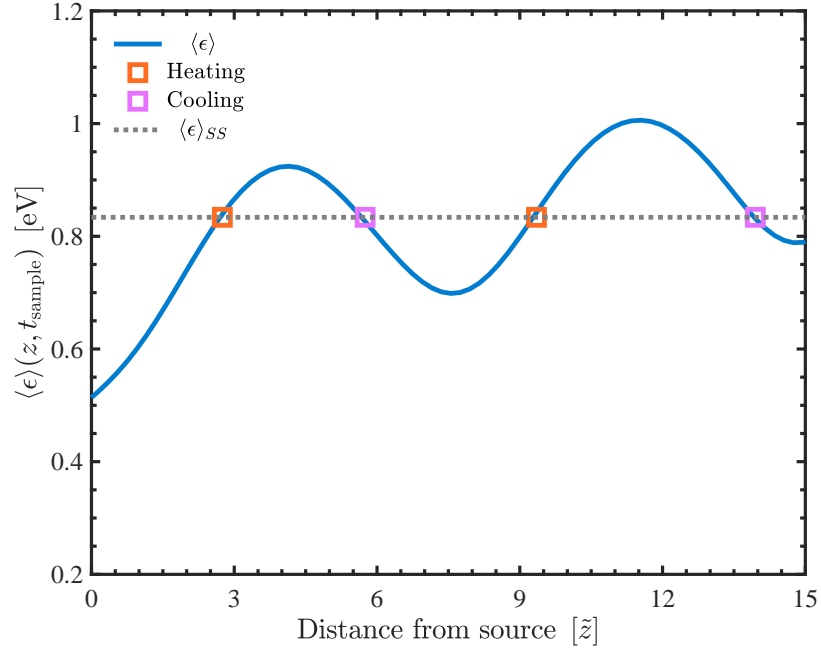


Figure 2.12: Transient mean energy evolution at  $t_{\text{sample}} \approx 5\tau_e$  indicating sample points coinciding with  $\langle \epsilon \rangle_{ss} = 0.8337$  eV

points corresponding to the same steady-state mean energy value are shown in Figure 2.13. For comparison the steady-state energy distribution function component, found by simulating the kinetic solution for a very long time, and that of a drifted Maxwellian energy distribution function, coinciding with the steady-state drift and energy, are also plotted.

From the representative distribution functions it can be seen the qualitative form of the energy distribution function varies significantly between heating and cooling regimes in the transient evolution. It was found that distribution functions on the leading edge of a so called Franck-Hertz oscillation correspond to a forward peaked distribution function, but do not significantly impinge past the inelastic threshold until they reach the peak of the oscillation. Conversely, samples on the falling edge of the oscillation contain a bi-modal distribution due to inelastic collisions shifting high energy electrons that were gradually heated on the leading edge regime down to a lower energy in the distribution.

Compared to the steady-state and drifted Maxwellian distribution function both heating and cooling distributions are quite different. As a result, this distribution variation is a key cause of the deficiencies in the local mean energy approximation used in plasma fluid modeling. Until the local mean energy approximation is improved, in order to capture distribution variation, the complex spatial structures such as Franck-Hertz oscillations, will not be resolvable with a fluid method.

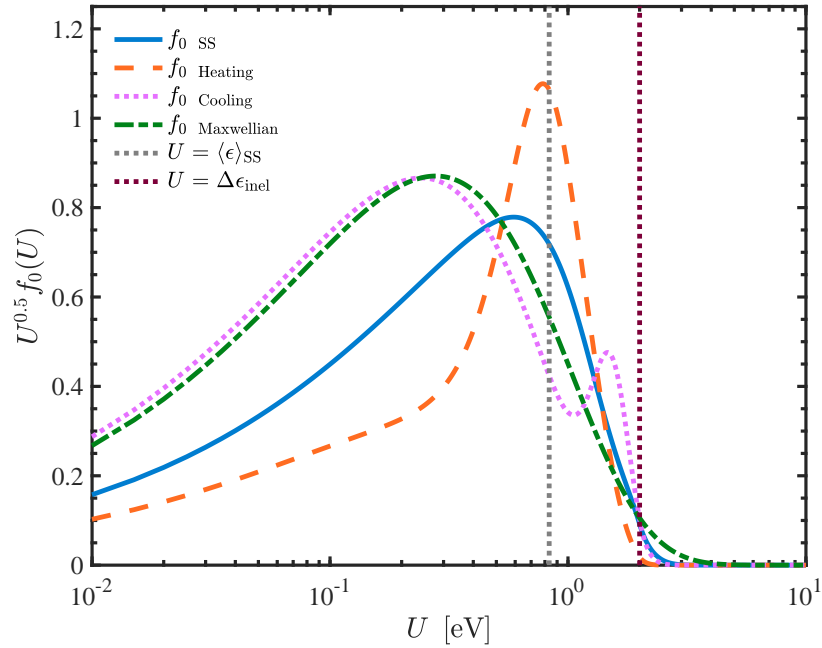


Figure 2.13: Comparison of typical energy distribution functions,  $U^{\frac{1}{2}} f_0(U)$ , for transient heating and cooling regimes. Steady state distribution and drifted Maxwellian shown for comparison.

## 2.4 Chapter Summary

This Chapter has presented the framework for a unified approach to electron fluid modeling in gas or liquid media. Through coherent scattering modifications, the fluid model accommodates some liquid structure effects which have a considerable effect on electron transport. Furthermore, the model has the flexibility of incorporating future additional liquid processes, such as solvation, via including additional electron collision cross sections into the computation of steady state collision rates.

Within the presented fluid model framework, this Chapter has implemented a fluid equation closure method that is believed to consistently produce physically sound approximations across a wide range of regimes in both gas and simple liquid media. Comparison to fluid models commonly used in the low-temperature plasma modeling community was performed, and demonstrated improvements were observed in low field regimes. This was demonstrated by a series of high electric field and low electric field hat benchmarks, solved for analogous gas and liquid phase electron transport with a simplified step-inelastic collision model. Despite the simplicity of the collision model, and the benchmarks, the results presented emphasize the importance of closure in fluid modeling, and the ability of the steady state closure method to obtain good approximations across different physical regimes.

To supplement the steady state hat field benchmarks, the impacts of closure on the transport of a transient non-hydrodynamic, non-equilibrium pulse in a homogeneous reduced electric field were also presented. It was shown that over multiple time scales, the approximation of an accurate multi-term Boltzmann equation solution was best

estimated by the steady state closure assumption.

Finally, this Chapter addressed an energy distribution effect that contributes significantly to the inability of fluid models to reproduce spatial periodic structures, such as Franck-Hertz oscillations. It was shown that although generally sound, in a spatially averaged sense, the local mean energy approximation of collision, and closure, terms will not be able to reproduce strongly varying distribution function effects in its current form. Field driven heating and inelastic collision driven cooling regimes were shown to produce widely different distribution functions in a periodic structure regime, which the local mean energy approximation simply cannot produce in its current form.

This Chapter has laid the foundation for applying the presented electron fluid model to the study of electron transport in simulated plasma-liquid interfaces in future work. It is hoped to motivate future additions of other liquid effects into fluid modeling, such as polar liquid effects and electron solvation processes. Additionally, this work hopes to stimulate further studies on improving collision approximation methods in order to capture distribution effects, and novel methods of closing higher order moments in charged particle fluid modeling.

In order to apply the proposed higher order fluid model in this Chapter to simulating gas-liquid systems, it is necessary to closely inspect the dependence of electron transport on neutral density. With a fluid model defined for gaseous or liquid systems, the following Chapter will now seek to extend the capability of the proposed model to accommodate spatially varying values of  $n_0$  via density-dependent input data.

# 3

## Density dependence of electron transport data

This chapter contains material that has been published in the following journal article:

[3] NA Garland, GJ Boyle, DG Cocks and RD White. Approximating the nonlinear density dependence of electron transport coefficients and scattering rates across the gas–liquid interface. *Plasma Sources Science and Technology*, 27 024002 (2018). Available online at doi:10.1088/1361-6595/aaaa0c

This chapter includes results of multi-term solutions of the Boltzmann equation provided by GJ Boyle which were used to provide input data for the original work. All other work described in this chapter is that of the author.

### 3.1 Chapter Introduction

---

This Chapter seeks to abstract the transport properties of intermediate fluid densities across a gas-liquid interface as a function of  $n_0$ , in order to facilitate modeling between the two distinct phases. This work will yield a method for approximating electron transport properties across the gas and liquid interface to include the effects of nonlinear density dependent scattering processes from dilute gas to a dense liquid. A successful method will be capable of providing moment model input data, described in Chapter 2, for electron transport at intermediate densities between two neutral particle density extremes, allowing a more accurate model of electron transport across a gas-liquid interface as a continuum over a neutral density transition.

This Chapter briefly revisits the formulation of moment models for electron transport in gases and liquids in Section 3.2, elaborating on the modifications needed for electron

transport in liquids. Section 3.2 also discusses the properties of a non-polar simple atomic liquid interface, and explicitly highlights the input data requirements for modeling electron transport across an interface with a spatially varying neutral density. Section 3.3 presents the derivation and benchmarking of approximate methods for a solution to the input data requirements, where benchmarking is performed for a simple model liquid. Application of the final proposed method is performed in Section 3.4 using only electron drift velocities in the dilute gas and liquid phases. Assessment of the accuracy of the method is made for argon and xenon cases through comparison with experimental and theoretical data.

## 3.2 Theory

### 3.2.1 Moment modeling for electron transport in gases and liquids

Moment modeling is a common technique used to simulate a swarm or plasma, in gas or liquid media, via balance equations of velocity-averaged variables, such as density, momentum, and energy [2, 76, 89, 95, 104]. This gives a relatively straightforward macroscopic model of a discharge, when compared to the complex mathematical and computational requirements of particle based methods such as Particle-in-Cell (PIC), Monte Carlo (MC), or kinetic solutions of the Boltzmann kinetic equation [90, 93, 95, 96, 100, 105]. The simplest variable in moment modeling is the number density of a species, defined as

$$n(\mathbf{r}, t) = \int f(\mathbf{r}, \mathbf{v}, t) d\mathbf{v}, \quad (3.1)$$

where  $f(\mathbf{r}, \mathbf{v}, t)$  is the electron velocity distribution function (EVDF).

Generic velocity moments can be then defined as

$$\langle \Phi \rangle(\mathbf{r}, t) = \frac{1}{n(\mathbf{r}, t)} \int f(\mathbf{r}, \mathbf{v}, t) \Phi(\mathbf{v}) d\mathbf{v}, \quad (3.2)$$

where  $\Phi(\mathbf{v})$  is any velocity dependent function, and  $\langle \dots \rangle$  denotes the expectation value, a velocity average over  $f(\mathbf{r}, \mathbf{v}, t)$ .

Multiplying the Boltzmann equation by an arbitrary velocity dependent trial function  $\Phi(\mathbf{v})$  and integrating over velocity space [95, 96] gives the generic moment equation

$$\frac{\partial}{\partial t}(n\langle \Phi \rangle) + \nabla \cdot (n\langle \mathbf{v}\Phi \rangle) - n\mathbf{a} \cdot \langle \nabla_{\mathbf{v}}\Phi \rangle = C_{\Phi}, \quad (3.3)$$

where  $\mathbf{a}$  is the acceleration experienced by electrons due to applied electromagnetic fields, and  $C_{\Phi}$  is the rate-of-change of  $n\langle \Phi \rangle$  due to collisions.

Up to this point, the moment modeling methods described have been independent of the background media of the swarm or discharge. However, the collisional rate-of-change

introduced in (3.3) is dependent on the medium and requires careful consideration of the coherent and incoherent scattering mechanisms within it [10, 48]

$$C_{\Phi} = C_{\Phi\text{coherent}} + C_{\Phi\text{incoherent}}. \quad (3.4)$$

In previous studies, the derivation [10, 48] and implementation [2] of structure dependent scattering into moment models has been presented through inclusions of elastic coherent scattering and electron interaction potential screening [15]. These effects are significant when the electron de Broglie wavelength is comparable to the average background particle spacing,  $\lambda \sim n_0^{-\frac{1}{3}}$ , and modifications to the electron collision frequencies used in moment modeling are derived.

It was shown that energy transfer collision rates, used in moment modeling, are not explicitly modified when coherent elastic scattering effects are included [48]. This allows the same form of equation to be used in dilute gas and soft condensed dense fluid background media [10, 48]. Energy transfer due to inelastic collisions is considered localized to the immediate target atom and is therefore unaffected by increased background densities, hence only the elastic scattering events require consideration in the formulation of a structure dependent kinetic theory. It is noted that other modifications to inelastic collisions can occur, such as collective excitations, however these remain incoherent and are not considered in this formulation.

In contrast to energy transfer, density dependent elastic coherent scattering produces explicit modifications to momentum transfer frequencies when the background medium is sufficiently dense, such as in a liquid [2, 10, 48]. The scattering effects due to increased densities of the background medium can be written as modifications of the dilute gas phase momentum transfer cross section

$$\sigma_m(v) = 2\pi \int_0^{\pi} \sigma(v, \chi) [1 - \cos \chi] \sin \chi d\chi, \quad (3.5)$$

where  $v$  is the incoming electron speed,  $\chi$  is the scattering angle from the target background medium, and  $\sigma(v, \chi)$  is the gas phase differential cross section.

These structure modifications are implemented through a density dependent momentum transfer cross section

$$\Sigma_m(v, n_0) = 2\pi \int_0^{\pi} \Sigma(v, \chi, n_0) [1 - \cos \chi] \sin \chi d\chi, \quad (3.6)$$

with  $\Sigma(v, \chi, n_0)$  being an effective differential cross section including coherent scattering via

$$\Sigma(v, \chi, n_0) = \tilde{\sigma}(v, \chi) S(\Delta k, n_0), \quad (3.7)$$

where  $\tilde{\sigma}(v, \chi)$  is the liquid phase differential cross section containing any screening and polarisation effects,  $S(\Delta k, n_0)$  is the static structure factor and  $\Delta k = \frac{2m_e v}{\hbar} \sin \frac{\chi}{2}$  is the wavenumber proportional to the change in momentum.

The static structure factor is a non-linear function of  $n_0$  of the target material, and may be calculated from molecular simulations, measured via experiments [15, 48, 65], or derived analytically through solutions of pair-correlation functions as per the Verlet-Weiss structure factor [83]. For detailed discussion on the static structure factor, and its implementation in liquid scattering, readers are directed to previous studies [15, 48, 65].

Applying this framework for modifying the momentum transfer cross section, the momentum transfer frequencies for dilute gas and liquid scattering, used as input to moment models, are

$$\nu_m(v) = n_0 v \sigma_m(v), \quad (3.8)$$

$$\tilde{\nu}_m(v, n_0) = n_0 v \Sigma_m(v, n_0), \quad (3.9)$$

where  $\nu_m(v)$  is the dilute gas momentum transfer frequency, and  $\tilde{\nu}_m(v, n_0)$  is the structure modified momentum collision frequency. It should be noted that  $\tilde{\nu}_m \rightarrow \nu_m$  in the limit of the electron de Broglie wavelength being much smaller than average background particle spacing,  $\lambda \ll n_0^{-\frac{1}{3}}$ .

Previously, moment models have been used to simulate electron transport in homogeneous media [2, 89, 94, 104] in both gas and liquid phases. Recalling the higher order moment model used in this study, where space dependence of  $n_0$  is explicitly included in the collision terms. Implementing the structure dependent scattering modifications, and the general moment integral (3.3), one can write a four moment model for electron transport, at any neutral density, where an electric field  $\mathbf{E}$  is applied in the medium [2]

$$\frac{\partial n}{\partial t} + \nabla \cdot \mathbf{\Gamma} = n(\tilde{\nu}_I^{\text{ss}}(\bar{\epsilon}, n_0) - \tilde{\nu}_a^{\text{ss}}(\bar{\epsilon}, n_0)), \quad (3.10)$$

$$\frac{\partial \mathbf{\Gamma}}{\partial t} + \nabla \cdot (n\theta_m^{\text{ss}}(\bar{\epsilon})) - n \frac{q_e}{m_e} \mathbf{E} = -\mathbf{\Gamma} \tilde{\nu}_m^{\text{ss}}(\bar{\epsilon}, n_0), \quad (3.11)$$

$$\frac{\partial n_\epsilon}{\partial t} + \nabla \cdot \mathbf{\Gamma}_\epsilon - q_e \mathbf{E} \cdot \mathbf{\Gamma} = -n \tilde{S}_\epsilon^{\text{ss}}(\bar{\epsilon}, n_0), \quad (3.12)$$

$$\frac{\partial \mathbf{\Gamma}_\epsilon}{\partial t} + \nabla \cdot (n\theta_\xi^{\text{ss}}(\bar{\epsilon})) - n\theta_m^{\text{ss}}(\bar{\epsilon}) \cdot q_e \mathbf{E} - n_\epsilon \frac{q_e}{m_e} \mathbf{E} = -\mathbf{\Gamma}_\epsilon \tilde{\nu}_\xi^{\text{ss}}(\bar{\epsilon}, n_0), \quad (3.13)$$

where shorthand variables for particle flux  $\mathbf{\Gamma}$ , energy density  $n_\epsilon$ , and energy density flux  $\mathbf{\Gamma}_\epsilon$  are defined as

$$\mathbf{\Gamma} = n \langle \mathbf{v} \rangle = \int f(\mathbf{r}, \mathbf{v}, t) \mathbf{v} d\mathbf{v}, \quad (3.14)$$

$$n_\epsilon = n \bar{\epsilon} = \int f(\mathbf{r}, \mathbf{v}, t) \frac{1}{2} m v^2 d\mathbf{v}, \quad (3.15)$$

$$\mathbf{\Gamma}_\epsilon = n \langle \boldsymbol{\xi} \rangle = \int f(\mathbf{r}, \mathbf{v}, t) \frac{1}{2} m v^2 \mathbf{v} d\mathbf{v}, \quad (3.16)$$

with  $\langle \mathbf{v} \rangle$ ,  $\bar{\epsilon} = \langle \epsilon \rangle$ , and  $\langle \boldsymbol{\xi} \rangle$  being the electron average velocity, average energy, and average energy flux. Input data is required via collision rates for ionisation,  $\tilde{\nu}_I^{\text{ss}}$ , attachment,

$\tilde{\nu}_a^{\text{SS}}$ , momentum transfer,  $\tilde{\nu}_m^{\text{SS}}$ , energy transfer,  $\tilde{S}_\epsilon^{\text{SS}}$ , energy flux transfer,  $\tilde{\nu}_\epsilon^{\text{SS}}$ , and higher order tensor product closure approximations,  $\theta_m^{\text{SS}} = \langle \mathbf{v}\mathbf{v} \rangle_{f_{ss}}$  and  $\theta_\epsilon^{\text{SS}} = \langle \frac{1}{2}mv^2\mathbf{v}\mathbf{v} \rangle_{f_{ss}}$ . The superscripts SS denote that all input data is computed via velocity averaging over the steady state EVDF found via MC [65, 87] or multi-term kinetic solution of the Boltzmann equation [10, 48, 94, 132], for a given density, and interpolated as a function of the local electron mean energy,  $\bar{\epsilon}$ . For further details on the moment model used in this study the reader is referred to the recent work of Garland *et al.* [2], in addition to other recent studies and reviews on the topic [89, 95, 104].

With a moment model for electron transport across a gas-liquid interface detailed above, it can be seen that collisional input rates to the model equations (3.10) - (3.13), such as  $\tilde{\nu}_m^{\text{SS}}(\bar{\epsilon}, n_0)$  and  $S_\epsilon^{\text{SS}}(\bar{\epsilon}, n_0)$ , are now functions of mean electron energy,  $\bar{\epsilon}$ , and the neutral atom density,  $n_0$ , which varies in space across the gas-liquid interface. In order to model electron transport across the interface, all steady state averaged collision rates must be known as a function of energy and each value of  $n_0$  across the interface. This data requirement is problematic because to measure this experimentally would be a consuming task, and to compute steady state distribution functions for all densities with coherent scattering and potential screening modifications would be computationally demanding [10, 15, 65, 87]. For a solution to this problem, an approximation to intermediate steady state electron transport properties and collision frequencies is needed, using computed dilute gas and liquid extreme transport properties only.

### 3.2.2 Interfacial density properties

In order to approximate the transport properties between vapor and liquid extremes, the composition of the interface must be known. For this study, it is assumed that an equilibrium interfacial density profile exists between dilute gas and liquid phases of some atomic fluid. For this study, non-polar systems (argon, xenon) have been chosen to begin formulating and benchmarking electron transport models between gas and liquid phases. This is in part due to the existence of good experimental data as well as the recent advances in liquid scattering and transport theory [8, 10, 15] which have allowed accurate computation of electron properties in non-polar atomic liquids.

Studies on the existence of an interface between a vapor and liquid surface in equilibrium were modeled in the late 1970s using molecular dynamics (MD) simulations once sufficient computing power became available [155]. Since then, many MD and Monte Carlo (MC) studies have been performed with noble liquids, often modeled using Lennard-Jones (LJ) potentials [7–9, 156]. Key measurables from these studies included equilibrium liquid and vapor densities, surface tension, and interface layer thickness. Kalos *et al.* [155] performed MD simulations of argon gas-liquid interface formation, resulting in a well defined interface thickness of approximately  $5\sigma_{\text{LJ}}$ , where  $\sigma_{\text{LJ}}$  is the atomic diameter used in the LJ potential. Later MD and MC studies of various noble liquids [7–9], such as krypton and xenon, confirmed the earlier simulation results of Kalos *et al.* [155].

The density profile between liquid and vapor was approximated as a hyperbolic tangent [7–9, 156] as shown in Figure 3.1, where key points on the interface are denoted I1 to I3. In the benchmarking and results to follow, the electron transport properties at these density points between gas and liquid will be approximated.

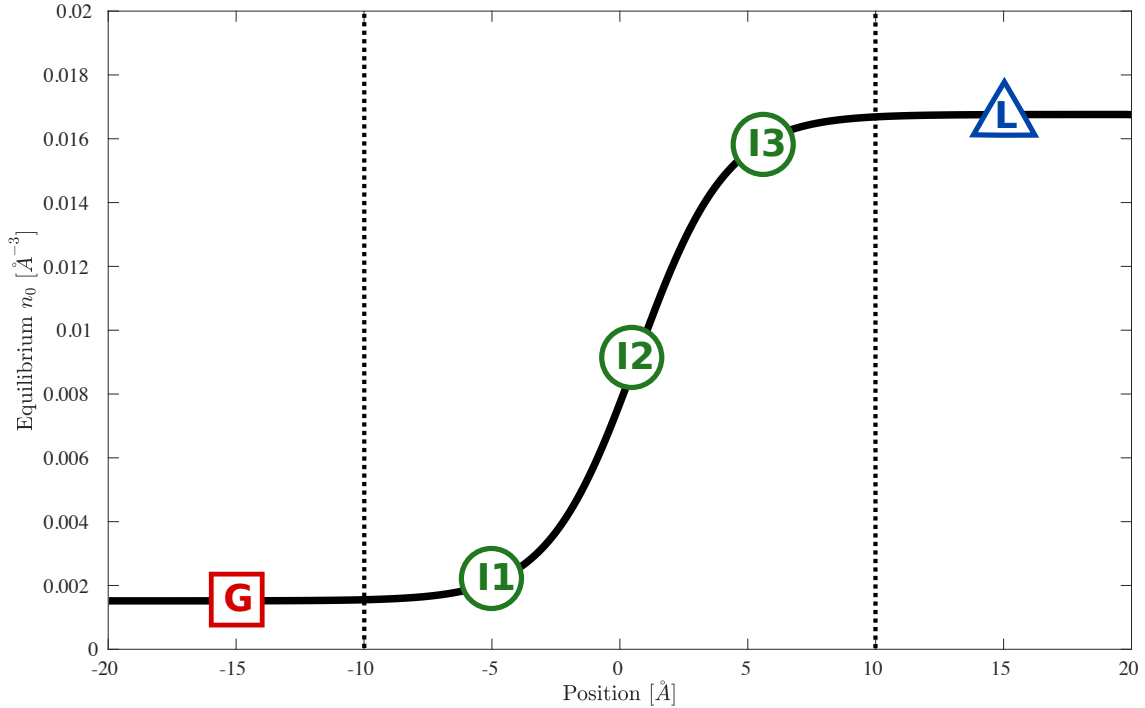


Figure 3.1: Argon vapor-liquid equilibrium interface as determined by molecular dynamics simulations [7–9]. Labels **G** and **L** denote dilute gas and liquid extremities respectively. Labels **I1**, **I2**, **I3** denote densities at one-quarter, half-way, and three-quarters along the density transition which will be used for benchmarking in Section 3.3.

The ratio between vapor and liquid densities in equilibrium ( $n_g/n_l$ ) was found to be variable depending on the atomic potentials chosen in the MD simulations [8, 9]. Trokhymchuk and Alejandre [8] studied different cut-off distances for LJ potentials to demonstrate liquid-vapor density ratios of 1/200 to 1/500, depending on the cut-off distance from  $2.5\sigma_{LJ}$  to  $5.5\sigma_{LJ}$ . In the future, to ensure a sensible liquid-vapor density ratio is employed in transport simulations across the liquid-vapor interface, the highlighted variation in neutral density ratios due to choice of the interaction potential will need to be considered. This cut-off distance is often employed in practice to make computational implementation of the exact LJ potential simpler by assuming a model potential that is fixed to be zero beyond the specified cut-off distance [8].

### 3.2.3 Simple model for benchmarking collisions in liquids

Before investigating electron transport in real atomic gases and liquids, it is beneficial to benchmark the performance of a proposed model against simple, well known collision models. For this study the Percus-Yevick liquid model with structure factor correction

of Verlet and Weiss [57, 65, 83] is employed to modify a simple gas phase collision model to induce structure and provide a well defined simple liquid model, used often in previous studies [10, 15, 48]. The collision (or interaction) model is defined as a hard-sphere elastic momentum transfer cross section  $\sigma_m = 6 \text{ \AA}^2$  with inelastic step function cross section  $\sigma_{\text{inel}}(\epsilon) = 0.1 \text{ \AA}^2$ , and a threshold energy  $\Delta\epsilon_{\text{inel}} = 2 \text{ eV}$ . Electron mass and neutral atom mass are defined as  $m_e = 5.486 \times 10^{-4} \text{ amu}$  and  $m_0 = 4 \text{ amu}$  respectively, with a neutral background temperature of  $T_0 = 300 \text{ K}$ .

A range of packing fractions  $\phi = 0, 0.1, 0.2, 0.3, 0.4$  were used to simulate increasingly dense fluids between a dilute gas,  $\phi = 0$ , and a final liquid phase,  $\phi = 0.4$ . For a given known neutral atom density the packing fraction is defined as

$$\phi = \frac{4}{3}r^3n_0, \quad (3.17)$$

where  $r$  is the hard sphere radius, which can be expressed as  $r = \sqrt{\frac{\sigma_m}{\pi}}$  for the hard sphere collision model or approximated by the van der Waal radius for a real atom.

The analytic static structure factor of Verlet and Weiss [83] was used in this study, and is defined as

$$S_{VW}(\Delta k, n_0) = \left(1 + \frac{24\eta(S_1 + S_2 + S_3)}{\Delta k^2}\right)^{-1}, \quad (3.18)$$

where the terms

$$\begin{aligned} S_1 &= \frac{2}{\Delta k^2} \left(12 \frac{\gamma}{\Delta k^2} - \beta\right), \\ S_2 &= \frac{\sin(\Delta k)}{\Delta k} \left(\alpha + 2\beta + 4\gamma - 24 \frac{\gamma}{\Delta k^2}\right), \\ S_3 &= \frac{2 \cos(\Delta k)}{\Delta k^2} \left(\beta + 6\gamma - 12 \frac{\gamma}{\Delta k^2}\right) - \cos(\Delta k)(\alpha + \beta + \gamma), \end{aligned}$$

are non-linear functions of the neutral number density via the packing fraction (3.17), and  $\eta = \phi - \frac{\phi^2}{16}$ ,  $\alpha = \frac{(1+2\eta)^2}{(1-\eta)^4}$ ,  $\beta = -6\eta \left(\frac{(1+0.5\eta)^2}{(1-\eta)^4}\right)$ , and  $\gamma = \frac{\eta\alpha}{2}$ .

With well defined properties of an equilibrium vapor-liquid interface and a simple liquid collision interaction model, the next Section aims to approximate drift velocities, and thus momentum transfer collision frequencies, for intermediate densities between gas and liquid extremes as depicted in the interface configuration in Figure 3.1.

### 3.3 Approximating electron transport at associated intermediate densities

The following section presents the derivation and associated benchmarking of approximations to input electron collision frequencies at intermediate densities between gas and liquid extremes. In order to derive necessary approximations this section takes inspiration from dilute gas swarm physics methods for approximating drift velocities

in gas mixtures as weighted combinations of each pure constituent gas's drift velocity. These mixture rules initially took the form of Blanc's law [157], which assumed that the EEDF in the gas mixture at a reduced field ( $E/N$ ) is the same as the EEDF in the pure constituent gases at the same  $E/N$ . This type of approximation was later described as a common  $E/N$  (CEON) procedure [158]. The CEON concept was extended and improved [158, 159] to the common mean energy (CME) method which assumes that the EEDF in the gas mixture at a given electron mean energy is the same as the EEDF in the pure constituent gases at the same mean energy.

The work to follow adapts the CME derivation presented by Jovanovic et al. [158] and considers steady state momentum and energy balance equations for gas, liquid, and intermediate densities to yield expressions for electron drift velocities at intermediate densities. Drift velocity was chosen as the benchmark variable in this study, as opposed to the collision frequencies needed as moment model input. This was decided because experimentally measuring drift velocity is straightforward compared to collision rates, allowing approximations produced in this study to be verified directly. Further discussion on these dilute gas mixture rules are presented in the Appendix.

### 3.3.1 Momentum balance method

One may first consider the steady state spatially averaged momentum balance form of equation (3.11) for electrons in a dense fluid, of neutral density  $n_{\text{int}}$ , within the interfacial region between the gas and liquid extremes, with neutral densities  $n_g$  and  $n_l$  respectively. It is assumed that the momentum transfer collision frequency is a slowly varying function of electron mean energy and first order momentum transfer theory (MTT) [70, 76, 96] can be used to write electron transport as a function of the electron mean energy. It is assumed there is a one to one relationship between the reduced field and electron mean energy [158]. This yields

$$\frac{e}{m_e} \check{E}_{\text{int}}(\langle \epsilon \rangle_{\text{int}}) = W_{\text{int}}(\langle \epsilon \rangle_{\text{int}}) \langle \check{\nu}_m^{\text{int}} \rangle(\langle \epsilon \rangle_{\text{int}}), \quad (3.19)$$

where  $\check{E}_{\text{int}} = E_{\text{int}}/n_{\text{int}}$  is the reduced electric field,  $W_{\text{int}}$  is the electron drift velocity, and  $\langle \check{\nu}_m^{\text{int}} \rangle = \langle \nu_m^{\text{int}} \rangle / n_{\text{int}}$  is the unknown electron reduced momentum transfer frequency in the fluid at this intermediate density. For emphasis, one should explicitly write that the steady state transport properties are functions of the mean electron energy,  $\langle \epsilon \rangle_{\text{int}}$ .

As per the CME method of dilute gas mixture rules [158], one can now assume the intermediate momentum transfer rate,  $\langle \check{\nu}_m^{\text{int}} \rangle$ , can be approximated by a weighted combination of collisions due to gas phase transport and collisions in the liquid extreme evaluated at a common electron mean energy

$$\langle \check{\nu}_m^{\text{int}} \rangle(\langle \epsilon \rangle_{\text{int}}) = x_g \langle \check{\nu}_m^g \rangle(\langle \epsilon \rangle_{\text{int}}) + x_l \langle \check{\nu}_m^l \rangle(\langle \epsilon \rangle_{\text{int}}), \quad (3.20)$$

where  $\langle \check{\nu}_m^{g,l} \rangle = \langle \nu_m^{g,l} \rangle / n_{\text{int}}$  denotes reduced collision frequencies of electrons in gas and liquid extremes, and the density fractions,  $x_{g,l}$ , follow the relation

$$x_l = 1 - x_g. \quad (3.21)$$

These density fractions are determined by defining the intermediate density as a sum of fractions of either density extreme

$$n_{\text{int}} = x_g n_g + x_l n_l, \quad (3.22)$$

such that one can find an expression for the density fraction

$$x_g = \frac{n_l - n_{\text{int}}}{n_l - n_g}. \quad (3.23)$$

Now consider the steady state momentum balance equation (3.19) of electrons in the two gas and liquid extremes taken at the same neutral density,  $n_{\text{int}}$ , as the interfacial density being approximated

$$\frac{e}{m_e} \check{E}_{g,l}(\langle \epsilon \rangle_{g,l}) = W_{g,l}(\langle \epsilon \rangle_{g,l}) \langle \check{\nu}_m^{g,l} \rangle(\langle \epsilon \rangle_{g,l}), \quad (3.24)$$

where  $\langle \epsilon \rangle_{g,l}$  is the electron mean energy,  $\check{E}_{g,l}$  is the reduced electric field, and  $W_{g,l}$  is the electron drift velocity in either gas or liquid extremes.

One can now invoke the CME assumption [158] so that electron transport is described as a function of a common electron mean energy,  $\bar{\epsilon}$ , in any intermediate fluid on the interfacial region, or in pure gas or liquid extremes. One may now substitute  $\langle \check{\nu}_m^{g,l} \rangle$  from equation (3.24) and combine equations (3.20) and (3.19) to find an expression, similar to the dilute gas mixture rule of Blanc's law [157], but which accounts for electric field variation as a function of mean energy

$$\frac{1}{W_{\text{int}}(\bar{\epsilon})} = x_g \frac{\check{E}_g(\bar{\epsilon})}{\check{E}_{\text{int}}(\bar{\epsilon})} \frac{1}{W_g(\bar{\epsilon})} + x_l \frac{\check{E}_l(\bar{\epsilon})}{\check{E}_{\text{int}}(\bar{\epsilon})} \frac{1}{W_l(\bar{\epsilon})}, \quad (3.25)$$

where all steady state drift velocities and reduced fields are interpolated as functions of the local electron mean energy  $\bar{\epsilon}$ .

To determine the accuracy of the proposed approximation from momentum balance (3.25) benchmark calculations were performed using the simple liquid collision model defined in Section 3.2.3. Using the momentum balance rule (3.25), steady state drift velocities were approximated for multiple packing fractions  $\phi = 0.1, 0.2, 0.3$  using only the properties of the extreme  $\phi = 0$  and  $\phi = 0.4$  fluids, as per the interface layout in Figure 3.1.

Approximations computed from (3.25) were compared against accurate results obtained from multi-term solutions of the Boltzmann equation [10, 15, 48]. All variables for the gas and liquid extremes were interpolated as functions of electron mean energy,  $\bar{\epsilon}$ , using the steady state mean energy of the intermediate density computed from a

multi-term kinetic solution [10]. It should be noted that the use of equation (3.25) necessitates a knowledge of the functional relationship between steady state reduced field and mean energy,  $\check{E}_{\text{mix}}(\bar{\varepsilon})$ , which in practice would not be known when approximating interfacial transport properties for input to a moment model. For these benchmarking calculations the steady state relationship  $\check{E}_{\text{mix}}(\bar{\varepsilon})$  computed from kinetic solutions was used at each intermediate  $\phi$  step; in this way the assumption of decomposing the intermediate collision frequency as a function of gas and liquid extremes can be solely tested.

Results of the benchmark calculations for the momentum balance rule (3.25) are shown in Figure 3.2 where approximate values of drift velocity are given by the dashed line series and, for comparison, solid lines denote accurate values obtained via multi-term solution of the Boltzmann equation. The accurate benchmark solutions of the Boltzmann equation used in this study are computed via the multi-term solution framework developed by the JCU group. For the formulation and implementation details of this framework the reader is referred to [10, 15, 48, 132, 160].

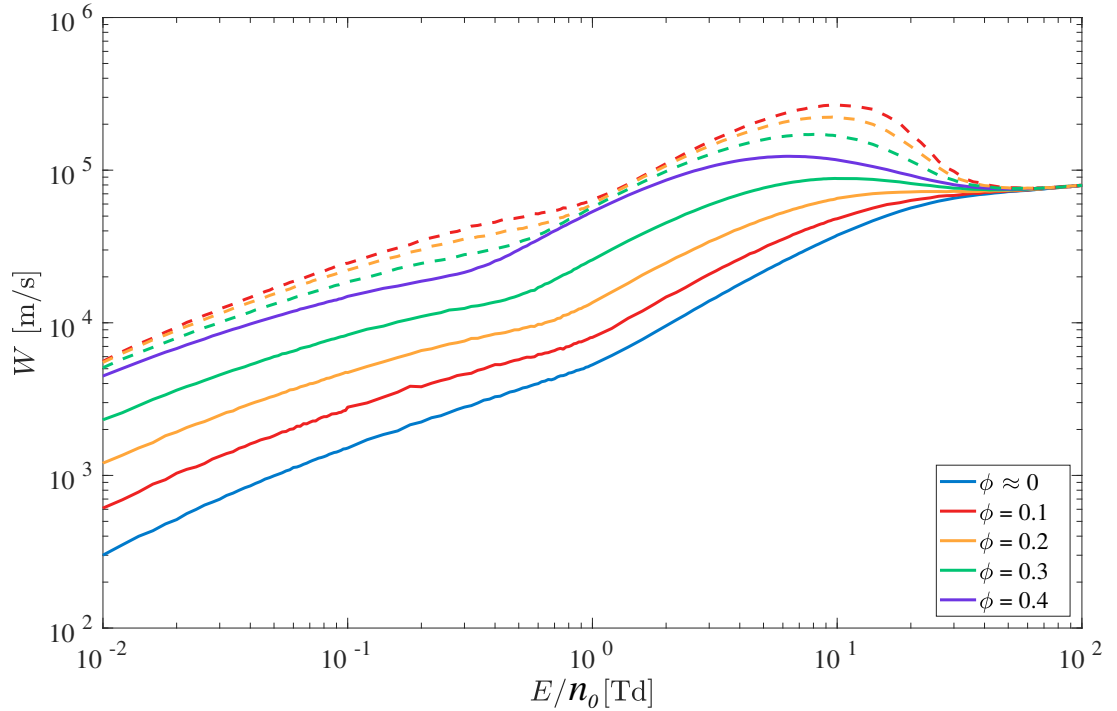


Figure 3.2: Comparison of electron drift velocities in model simple liquids for  $\phi = 0.1, 0.2, 0.3$ . Solid lines: multi-term solution of the Boltzmann equation [10]. Dashed lines: computed via approximation (3.25) derived from momentum balance.

Across all packing fractions it can be seen that the momentum balance rule severely overestimates the intermediate drift velocity, consistently predicting values above even the  $\phi = 0.4$  liquid extremity drift velocities. This is attributed to the failure of the additivity assumption for constructing  $\langle \nu_m^{\text{int}} \rangle$ , invoked in equation (3.20). This occurs because the background neutral number density  $n_0$  can no longer be factored out of the intermediate fluid's momentum transfer collision frequency,  $\tilde{\nu}_m$ , when coherent scattering effects are included.

The introduction of non-linearity in  $n_0$  can be seen by considering momentum transfer collision frequencies (3.8) and (3.9), where the structure modified momentum cross section is derived via an energy integral over the non-linear static structure factor, in this case the Verlet-Weiss analytic form,  $S_{VW}(\Delta k, n_0)$  as per (3.18). In the dilute gas case,  $\nu_m$  was directly proportional to  $n_0$  and so some proportionality to  $n_0$  can be reasonably expected when neutral densities are low. However, once coherent scattering effects are important, the non-linearity of the static structure factor clearly breaks down any simple proportionality relation between  $\tilde{\nu}_m$  and  $n_0$ . With the momentum balance approximation failing to sufficiently describe intermediate density drift velocities, the assumption invoked in equation (3.20) requires further improvement.

### 3.3.2 Energy balance method

This section now considers the steady state spatially averaged form of the energy balance equation (3.12) for an intermediate density between gas and liquid extremes. As per Section 3.3.1 one may apply first order momentum transfer theory (MTT) [70, 76, 96] and also assume there is a one to one relationship between the reduced field and electron mean energy [158] to write transport coefficients and collision rates as a function of the electron mean energy,  $\langle \epsilon \rangle_{\text{int}}$ , i.e.,

$$e\check{E}_{\text{int}}(\langle \epsilon \rangle_{\text{int}}) W_{\text{int}}(\langle \epsilon \rangle_{\text{int}}) = \left( \langle \epsilon \rangle_{\text{int}} - \frac{3}{2} k_B T_{\text{int}} \right) \langle \check{\nu}_e^{\text{int}} \rangle(\langle \epsilon \rangle_{\text{int}}) + \Delta \epsilon_{\text{inel}} \langle \check{\nu}_{\text{inel}}^{\text{int}} \rangle(\langle \epsilon \rangle_{\text{int}}), \quad (3.26)$$

where the elastic and inelastic collision rates are explicitly separated,  $\langle \check{\nu}_e^{\text{int}} \rangle = \langle \nu_e^{\text{int}} \rangle / n_{\text{int}}$  is the reduced elastic electron energy transfer collision frequency,  $T_{\text{int}}$  is the temperature of the fluid at an interfacial point,  $\Delta \epsilon_{\text{inel}}$  is the inelastic collision threshold energy, and  $\langle \check{\nu}_{\text{inel}}^{\text{int}} \rangle = \langle \nu_{\text{inel}}^{\text{int}} \rangle / n_{\text{int}}$  is the reduced electron inelastic energy transfer collision frequency due to internal energy state changes from inelastic threshold collisions <sup>1</sup>.

In contrast to Section 3.3.1, now assume additivity of *energy* transfer collision frequencies for both gas and liquid extremes, evaluated at the interfacial mean energy,  $\langle \epsilon \rangle_{\text{int}}$ , to approximate the collision frequencies at the intermediate density

$$e\check{E}_{\text{int}}(\langle \epsilon \rangle_{\text{int}}) W_{\text{int}}(\langle \epsilon \rangle_{\text{int}}) = \left( \langle \epsilon \rangle_{\text{int}} - \frac{3}{2} k_B T_{\text{int}} \right) \left[ x_g \langle \check{\nu}_e^g \rangle(\langle \epsilon \rangle_{\text{int}}) + x_l \langle \check{\nu}_e^l \rangle(\langle \epsilon \rangle_{\text{int}}) \right] + \Delta \epsilon_{\text{inel}} \left[ x_g \langle \check{\nu}_{\text{inel}}^g \rangle(\langle \epsilon \rangle_{\text{int}}) + x_l \langle \check{\nu}_{\text{inel}}^l \rangle(\langle \epsilon \rangle_{\text{int}}) \right], \quad (3.27)$$

where  $\langle \check{\nu}_e^{g,l} \rangle = \langle \nu_e^{g,l} \rangle / n_{\text{int}}$  denotes reduced electron energy transfer collision frequency with superscripts  $g, l$  denoting either the gas or liquid extremes,  $\langle \check{\nu}_{\text{inel}}^{g,l} \rangle$  is the reduced

<sup>1</sup>For clarity in the derivation, just one inelastic excitation scattering process is included. It is straightforward to demonstrate that the following results are unaffected by adding further inelastic scattering processes.

inelastic energy transfer collision frequency due to inelastic threshold collisions, and density fractions  $x_{g,l}$  are defined as per equations (3.21) - (3.23).

To obtain expressions for  $\langle \tilde{\nu}_e^{g,l} \rangle$  in either extreme, consider the steady state energy balance equations (3.26) of electrons in the gas and liquid extremes taken at the same neutral density,  $n_{\text{int}}$ , as the interfacial density being approximated

$$e\check{E}_{g,l}(\langle \epsilon \rangle_{g,l}) W_{g,l}(\langle \epsilon \rangle_{g,l}) = \left( \langle \epsilon \rangle_{g,l} - \frac{3}{2}k_B T_{g,l} \right) \langle \tilde{\nu}_e^{g,l} \rangle (\langle \epsilon \rangle_{g,l}) + \Delta\epsilon_{\text{inel}} \langle \tilde{\nu}_{\text{inel}}^{g,l} \rangle (\langle \epsilon \rangle_{g,l}). \quad (3.28)$$

If the temperature is assumed constant across all densities in the gas-liquid interface system, and once again the CME assumption is invoked to abstract steady state electron transport at all neutral densities as a function of some common mean energy,  $\bar{\epsilon}$ , one can rearrange (3.28) to obtain expressions for  $\langle \tilde{\nu}_e^{g,l} \rangle$  and substitute them into (3.27). It can be shown that the reduced inelastic scattering rates  $\langle \tilde{\nu}_{\text{inel}}^{g,l} \rangle$  cancel out yielding an expression for the drift velocity at the intermediate density

$$W_{\text{int}}(\bar{\epsilon}) = x_g \frac{\check{E}_g(\bar{\epsilon})}{\check{E}_{\text{int}}(\bar{\epsilon})} W_g(\bar{\epsilon}) + x_l \frac{\check{E}_l(\bar{\epsilon})}{\check{E}_{\text{int}}(\bar{\epsilon})} W_l(\bar{\epsilon}). \quad (3.29)$$

To establish the accuracy of the energy balance approximation (3.29), the same benchmark calculations for the simple Percus-Yevick atomic liquid were performed. Results of this approximation are shown in Figure 3.3, where solid lines denote accurate values obtained via multi-term solution of the Boltzmann equation and approximate values of drift velocity are given by the dashed line series.

In general, the approximation derived from energy balance (3.29) appears to be a better representation of the intermediate density than the momentum balance method (3.25). For higher packing fractions  $\phi = 0.2, 0.3$  the approximation of drift velocity by (3.29) demonstrates an excellent agreement with an accurate kinetic solution across all energy ranges. The agreement for the  $\phi = 0.1$  case is strong at low and high fields but loses accuracy at intermediate fields of approximately 1 Td - 5 Td, where a maximum error of approximately 30% is produced. In this field range the assumption that the energy transfer collision frequency can be approximated by a linear combination of the collision frequencies in gas and liquid extremes, as invoked in (3.27), appears to be insufficient. The effects of this inaccuracy are very apparent in the  $\phi = 0.1$  case in Figure 3.3, and present to a lesser degree in the  $\phi = 0.2$  case. This is a reflection of the approximations associated with the first-order momentum transfer theory used in developing the relation (3.29) [76, 161]. This inaccuracy could be improved through higher-order momentum transfer theory if desired.

To explain why an approximation derived from energy balance should perform better than one derived from momentum balance, recall the modifications of electron transport in gases required to simulate transport in liquid media, outlined in Section 3.2.1. Firstly, inelastic collisions result in largely localized energy transfer between electrons and the background medium, and it is assumed that these are incoherent

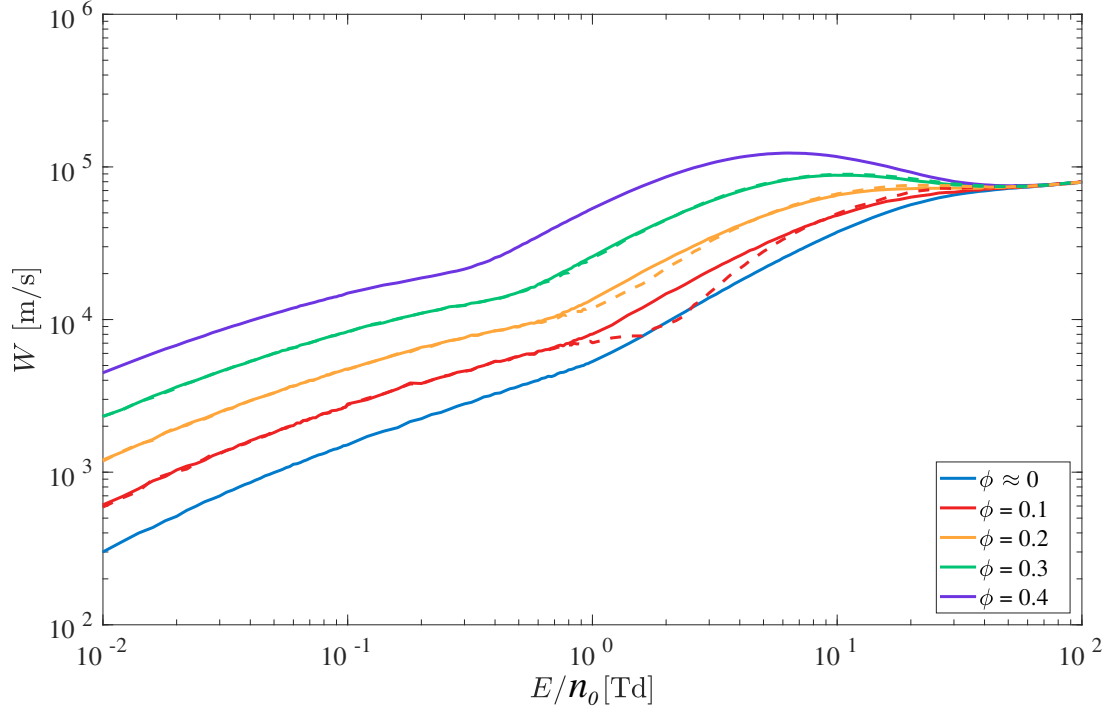


Figure 3.3: Comparison of electron drift velocities in model simple liquids for  $\phi = 0.1, 0.2, 0.3$ . Solid lines - multi-term solution of the Boltzmann equation [10]. Dashed lines - computed via approximation (3.29) derived from energy balance.

scattering events which can be treated by classical dilute gas kinetic theory [10, 15, 48]. On the other hand, in the structure modified kinetic theory [48] used to describe electron transport in condensed materials, coherent elastic scattering collisions are important. Since it is elastic scattering that carries the explicit density dependent coherent scattering effects, it is not surprising that momentum transfer is impacted more than energy transfer as the neutral density of the background fluids are increased.

In summary, from a rule based on largely structure independent energy transfer (3.29) a reasonable approximation to  $W_{\text{int}}$  is observed, as opposed to an approximation that ignores the non-linear density effects on momentum transfer (3.25). With this result, it appears suitable to approximate a lumped energy transfer collision frequency of an intermediate fluid by simply assuming additivity of the gas and liquid reduced collision frequencies as per (3.27). The next aim is to now correct the approximation derived from momentum balance in the previous section, in order to provide a better approximation to momentum transfer collision rates.

### 3.3.3 Modified momentum balance method

This section aims to propose a modified momentum balance approximation rule that aims to explicitly include some of the non-linear effects of density dependent coherent scattering in the approximation of  $\langle \nu_m^{\text{int}} \rangle$ . By only considering structure induced coherent scattering effects in this treatment, the approach henceforth neglect density dependent potential screening effects in the differential cross section (3.7). Future studies will endeavor to relax this assumption in order to more accurately describe

density dependent scattering via interaction potential screening and not just coherent scattering.

To isolate density dependence of the soft condensed phase scattering interaction, apply first order momentum transfer theory (MTT) [70,76,96] to evaluate the structure modified momentum transfer cross section as a function of electron mean energy,  $\bar{\varepsilon}$ ,

$$\Sigma_m(\bar{\varepsilon}, n_0) \approx \sigma_m(\bar{\varepsilon}) s(\bar{\varepsilon}, n_0), \quad (3.30)$$

where  $s(\bar{\varepsilon}, n_0)$  is an angle integrated structure factor with explicit  $n_0$  dependence

$$s(\bar{\varepsilon}, n_0) = \frac{1}{2} \int_0^\pi S\left(\frac{2}{\hbar} \sqrt{2m_e \bar{\varepsilon}} \sin \frac{\chi}{2}, n_0\right) [1 - \cos \chi] d\chi. \quad (3.31)$$

In the limit of isotropic scattering the approximations of equations (3.30) and (3.31) are exact [70,76,161]. Decomposing the structure modified momentum transfer cross section to isolate a density dependence, as per the approximation of equation (3.30), now allows dense phase collision rates to be approximated via scaling of dilute gas collision rates.

One may continue the use of MTT and evaluate the structure modified momentum transfer collision frequency (3.9) as the dilute gas phase momentum transfer collision frequency multiplied by the angle integrated structure factor each evaluated at the electron mean energy,  $\bar{\varepsilon}$ ,

$$\begin{aligned} \langle \tilde{\nu}_m \rangle(\bar{\varepsilon}, n_0) &\approx n_0 \sqrt{\frac{2\bar{\varepsilon}}{m_e}} \Sigma_m(\bar{\varepsilon}, n_0), \\ &\approx s(\bar{\varepsilon}, n_0) \langle \nu_m \rangle(\bar{\varepsilon}). \end{aligned}$$

Using this result, return to the steady state limit of the momentum balance equation (3.19), and now make the assertion that instead of simply combining certain fractions of gas and liquid reduced momentum transfer collision frequencies one must first normalize each input reduced collision frequency  $s_{g,l}$  and then rescale by the intermediate density's  $s_{\text{int}}$

$$\frac{e}{m_e} \tilde{E}_{\text{int}}(\bar{\varepsilon}) = W_{\text{int}}(\bar{\varepsilon}) \left[ x_g \frac{s_{\text{int}}(\bar{\varepsilon})}{s_g(\bar{\varepsilon})} \langle \tilde{\nu}_m^g \rangle(\bar{\varepsilon}) + x_l \frac{s_{\text{int}}(\bar{\varepsilon})}{s_l(\bar{\varepsilon})} \langle \tilde{\nu}_m^l \rangle(\bar{\varepsilon}) \right], \quad (3.32)$$

where  $s_{g,l,\text{int}}$  are the angle-integrated structure factors for gas and liquid extremes, and the intermediate density respectively, all evaluated at a common mean energy  $\bar{\varepsilon}$ , and density fractions  $x_{g,l}$  are defined as per equations (3.21) - (3.23).

In practice, when approximating transport properties between gas and liquid extremes over a range of  $n_0$  values,  $s_{\text{int}}$  must be specified at each point along the interface. Obtaining a function for  $s_{\text{int}}$  at each point would be very computationally demanding, and is generally not available experimentally. As a result this method proposes a further approximation for  $s_{\text{int}}$  as a combination of the limiting gas and

liquid angle-integrated structure factors

$$s_{\text{int}} \approx w s_g + (1 - w) s_l, \quad (3.33)$$

where to ensure the approximation is physically grounded in both the high and low energy limits, the weighting factor,  $w$ , is fixed in the low energy limit by

$$w = \frac{S_{\text{int}}(0, n_{\text{int}}) - S_l(0, n_l)}{S_g(0, n_g) - S_l(0, n_l)}, \quad (3.34)$$

where  $S(0)$  is the  $\Delta k = 0$  limit of the static structure factor, which is also proportional to the fluid's compressibility.

To benchmark the assumptions used to define equation (3.33) the approximate and exact angle-integrated structure factors, computed by integrating the analytic Verlet-Weiss structure factor, are compared in Figure 3.4, where solid lines denote exact values via integrating (3.31) and approximate values of  $s_{\text{int}}$  are given by the dashed line series. Note that for a dilute gas  $s_g = 1$  and so this variable is not referenced in the remainder of this treatment.

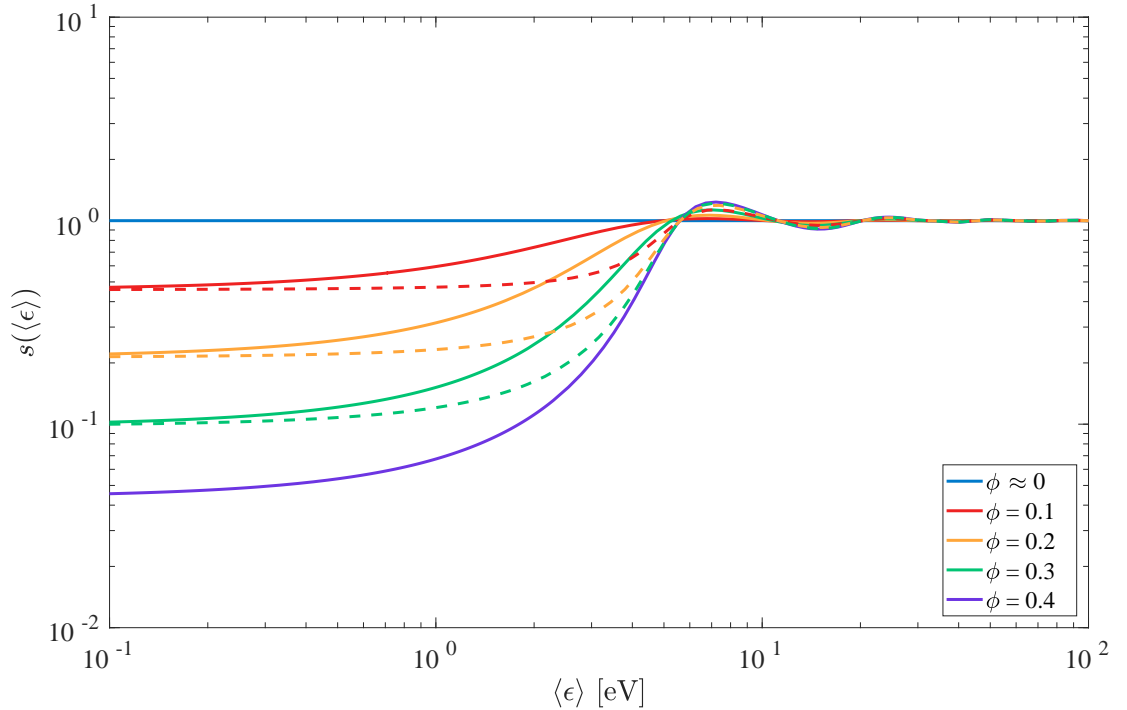


Figure 3.4: Comparison of approximated angle-integrated structure factors for Percus-Yevick model liquids. Solid lines - exact values via (3.31). Dashed lines - approximated  $s$  via equations (3.33) and (3.34).

As expected, the low and high energy limits are fixed exactly, while intermediate energies show some differences once the structure factor begins to peak. By substituting an expression for  $\langle \tilde{v}_m^{g,l} \rangle$  from the momentum balance for either gas or liquid extremes (3.24) into the intermediate fluid momentum balance (3.32), and assuming the common mean energy assumption, one can yield a modified approximation for drift velocity

accounting for some non-linear density effects

$$\frac{1}{W_{\text{int}}(\bar{\varepsilon})} = x_g s_{\text{int}}(\bar{\varepsilon}) \frac{\check{E}_g(\bar{\varepsilon})}{\check{E}_{\text{int}}(\bar{\varepsilon})} \frac{1}{W_g(\bar{\varepsilon})} + x_l \frac{s_{\text{int}}(\bar{\varepsilon})}{s_l(\bar{\varepsilon})} \frac{\check{E}_l(\bar{\varepsilon})}{\check{E}_{\text{int}}(\bar{\varepsilon})} \frac{1}{W_l(\bar{\varepsilon})}. \quad (3.35)$$

Once again this approximated was benchmarked with results shown in Figure 3.5, where solid lines denote accurate values obtained via multi-term solution of the Boltzmann equation and approximate values of drift velocity are given by the dashed line series.

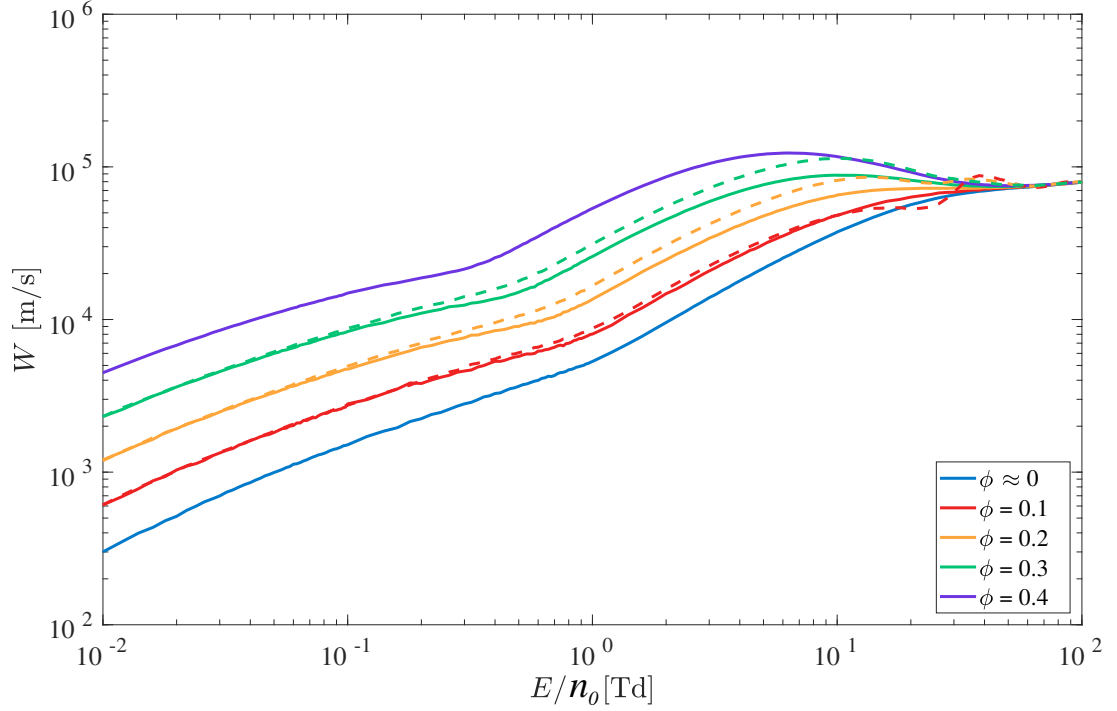


Figure 3.5: Comparison of electron drift velocities in model simple liquids for  $\phi = 0.1, 0.2, 0.3$ . Solid lines - multi-term solution of the Boltzmann equation [10]. Dashed lines - computed via approximation (3.35) derived from structure modified momentum balance.

It can be seen that this modified momentum balance rule produces a better outcome than the results of the unmodified momentum balance method, shown in Figure 3.2, for all benchmark intermediate densities. As observed for the energy balance approximations in Figure 3.3, the  $\phi = 0.2, 0.3$  cases in Figure 3.2 perform consistently well under the modified momentum balance approximation. In contrast to the approximation derived from energy balance, the  $\phi = 0.1$  case now demonstrates strong agreement between 1 Td - 10 Td, demonstrating insensitivity to inelastic scattering effects. Inaccuracies due to equation (3.35) are observed in the  $\phi = 0.1$  case between 10 Td - 50 Td due to the error in approximating  $s_{\text{int}}$  as a combination of the gas and liquid extrema structure factors, shown in Figure 3.4.

Despite the noted shortcomings at intermediate fields, the structure-modified drift velocity approximation (3.35) provides a much better general approximation to  $W_{\text{int}}$  than the original approximation derived from a simpler momentum balance (3.25), and

demonstrates potential to provide an improved approximation to electron transport at densities between gas and liquid extrema.

### 3.3.4 Practical implementation for plasma modeling

So far two approximation rules (3.29) and (3.35) have been derived and were demonstrated to have potential in approximating electron drift velocities at intermediate densities between gas and liquid extrema. Each equation is a function of a common mean energy  $\bar{\epsilon}$ , and steady state values of  $W_{g,l}$  and  $\check{E}_{g,l,\text{int}}$  are interpolated at these energies to provide input from either phase extreme. As previously discussed, when used independently, each equation requires knowledge of the steady state relationship between  $\check{E}_{\text{int}}$  and  $\bar{\epsilon}$  at the intermediate density between gas and liquid. This requirement is problematic because the gas-liquid interface steady state properties are generally unknown and hence the motivation for this study.

As a way to form an approximation that can be applied in practice, without any knowledge of the steady state transport properties at each intermediate density, combine the two benchmarked approximation rules from energy balance (3.29) and modified momentum balance (3.35) and solve for  $W_{\text{int}}$ , to eliminate  $\check{E}_{\text{int}}$ ,

$$W_{\text{int}}^2(\bar{\epsilon}) = \frac{x_g \check{E}_g(\bar{\epsilon}) W_g(\bar{\epsilon}) + x_l \check{E}_l(\bar{\epsilon}) W_l(\bar{\epsilon})}{x_g s_{\text{int}}(\bar{\epsilon}) \check{E}_g(\bar{\epsilon}) \frac{1}{W_g(\bar{\epsilon})} + x_l \frac{s_{\text{int}}(\bar{\epsilon})}{s_l(\bar{\epsilon})} \check{E}_l(\bar{\epsilon}) \frac{1}{W_l(\bar{\epsilon})}}. \quad (3.36)$$

To test the performance of the approximation (3.36), the benchmark model used throughout this study was again applied. The most straightforward measurable that can be used to verify the accuracy of the approximation is the electron steady state drift velocity. Despite not being a direct input in higher order moment models [2, 89, 104], it provides a solid measure on the validity of approximations of input collision frequencies. For the Percus-Yevick model of a simple atomic liquid, multiple packing fractions,  $\phi = 0.1, 0.2, 0.3$ , were used to approximate electron drift velocity and were compared with accurate calculations of the steady state drift velocity as shown in Figure 3.6.

By only specifying the  $\Delta k = 0$  analytic limit of the structure factor  $S_{VW}(0, n_{\text{int}})$  of the intermediate densities the combined approximation (3.36) provides a good representation of the exact results. As discussed earlier, the higher-density fluids perform very well, while the lower-density fluid demonstrates variations from the exact result due to the assumptions on the fluid structure. For packing fractions of  $\phi = 0.2, 0.3$  the maximum error observed was 12%, which occurred near the peak value of  $W$  before the region of negative differential conductivity (NDC) began. For the lower packing fraction,  $\phi = 0.1$ , a maximum error of 25% was observed. This approximation was not as accurate because the simple intermediate structure assumptions used in this study didn't accurately represent the transition to near-dilute gas phase. An additional encouraging feature of the proposed approximation was the ability to predict structure induced NDC in the model liquids, which has previously been reported to occur at packing fractions above  $\phi = 0.2$  [48], using only the analytic  $\Delta k = 0$  limit of the static structure factor, and dilute gas and liquid extreme transport data.

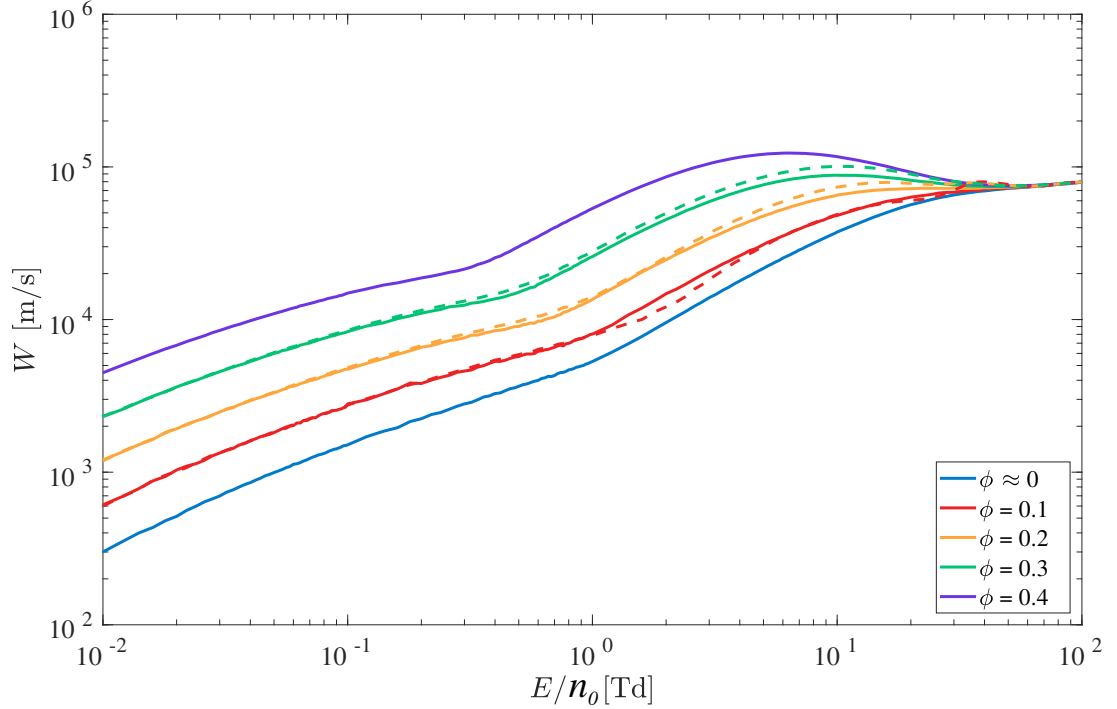


Figure 3.6: Comparison of electron drift velocities in model simple liquids for  $\phi = 0.1, 0.2, 0.3$ . Solid lines - multi-term solution of the Boltzmann equation [10]. Dashed lines - computed via the practical approximation (3.36).

### 3.3.5 Approximating collision frequencies across an interface

In practice, when simulating electron transport with higher order moment models [2, 89, 104] the required inputs are not drift velocities or diffusion coefficients (which could be computed via an Einstein relation once  $W_{\text{int}}$  is known), but rather reduced collision frequencies. Once an approximate drift velocity is found one may simply compute a reduced momentum transfer frequency via

$$\check{\nu}_m^{\text{int}}(\bar{\varepsilon}) = \frac{e\check{E}_{\text{int}}(\bar{\varepsilon})}{m_e W_{\text{int}}(\bar{\varepsilon})}, \quad (3.37)$$

in order to approximate the steady state momentum collision rate at the intermediate densities between gas and liquid extremes. The results of using the collision frequency approximation (3.37) are shown in Figure 3.7 for multiple packing fractions.

It can be seen that the approximation to  $\check{\nu}_m^{\text{int}}$  performs quite well without much knowledge of the intermediate fluid's structure and steady state transport properties. Higher density fluids,  $\phi = 0.2, 0.3$ , demonstrate the best agreement, while the inaccuracies in approximating structure for the  $\phi = 0.1$  case are highlighted by the deviation at intermediate energy ranges. This result demonstrates potential for the final approximation rule (3.36) to be used in conjunction with higher order moment models [2, 89, 95, 103] to provide a foundation for simulating electron transport between gas and liquid extremes as a continuum.

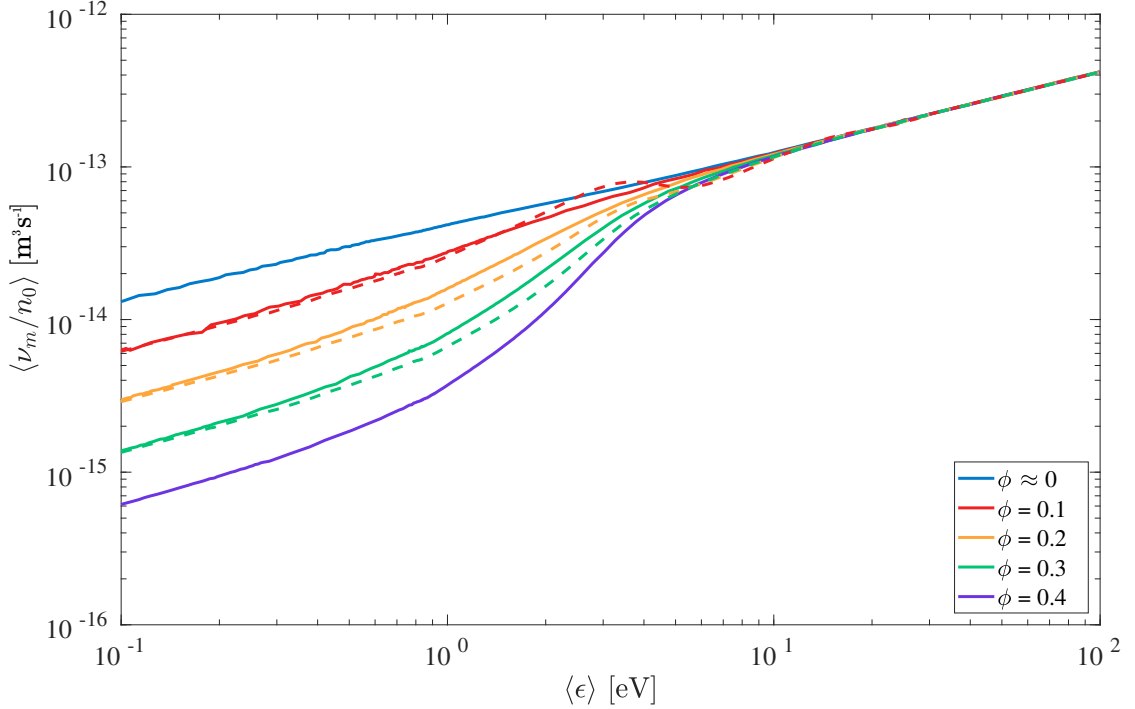


Figure 3.7: Approximated  $\bar{\nu}_m^{\text{mix}}$  for multiple packing fractions of Percus Yevick model liquid. Solid line: exact via multi-term kinetic solution [10], --: approximation via (3.37).

### 3.4 Application to noble gas-liquid systems

In order to further verify the suitability of the derived approximation (3.36), one should consider application to real gases and liquids. This Section seeks to use the derived approximation method, with known steady state transport properties of a dilute gas and dense liquid, to estimate steady state electron drift velocities measured in a fluid of intermediate density. In contrast to the previous model where only explicit coherent effects were considered, real atomic systems require additional modifications to the interaction potential associated with varying the neutral density [15]. A classic example of the variation between cross sections at gas and liquid densities is observed in some rare gases and their liquids, where the low-energy Ramsauer minimum found in gas phase cross sections is suppressed and eventually completely non-existent as the liquid density increases [15]. As a result of the complex scattering variations from gas to liquid states, in conjunction with accessible experimental data, liquid argon and liquid xenon were chosen for comparison in this study.

Experimental data of Gushchin *et al.* [11] for drift velocity, electric field, and mean energy of electrons in liquid argon and liquid xenon were digitized as a basis for experimental validation of the proposed approximation (3.36). This data set was chosen over other existing data sets [16, 162] because an approximation to the electron mean energy, scaled from measurements of the characteristic energy  $D/\mu$ , was included in the original study and so provided the necessary mean energy input needed to use the derived approximations. Table 3.1 outlines the approximate gas to liquid transition

assumed for each atomic fluid.

Table 3.1: Benchmark atomic gas-liquid systems used for validating proposed drift velocity approximation rule against experimental data

	Liquid - Calc. [10, 15]	Intermediate - Exp. [11]	Gas - Calc. [10, 15]
Argon	85 K	130 K	300 K
Xenon	165 K	230 K	300 K

As opposed to the Percus-Yevick model atomic liquid, temperature,  $T$ , as well as neutral atom density,  $n_0$ , varies between the densities used in experiment. In order to account for this, the neutral densities at each temperature were calculated by interpolating the argon and xenon saturated liquid curves as a function of  $T$  [163, 164]. Dilute gas neutral density was approximated as being 300 times smaller than the liquid extreme neutral density based on the equilibrium liquid-gas density ratios found in molecular dynamics simulations of Lennard-Jones liquids [7–9, 156].

In contrast to the simplified collision model used in the benchmark system in the previous Section, each real fluid in Table 3.1 was measured at different temperatures as well as densities. Note that a modification to the approximation method (3.36) is required to account for varying temperatures and densities. To account for temperature variation the derivation of the approximation (3.29) via energy balance (3.26) was slightly modified to allow thermal components,  $\frac{3}{2}k_B T$ , to vary between the gas, liquid, and intermediate densities.

Assuming the same CME assumption as previous derivations, and allowing  $T_g \neq T_{\text{int}} \neq T_l$  it is found that ratios of the common mean energy minus thermal components do not cancel in the approximation derived from energy balance, and one yields a temperature-modified approximation rule

$$W_{\text{int}}^2(\bar{\varepsilon}) = \frac{\left( x_g \frac{\bar{\varepsilon} - \frac{3}{2}k_B T_{\text{int}}}{\bar{\varepsilon} - \frac{3}{2}k_B T_g} \check{E}_g(\bar{\varepsilon}) W_g(\bar{\varepsilon}) + x_l \frac{\bar{\varepsilon} - \frac{3}{2}k_B T_{\text{int}}}{\bar{\varepsilon} - \frac{3}{2}k_B T_l} \check{E}_l(\bar{\varepsilon}) W_l(\bar{\varepsilon}) \right)}{x_g s_l(\bar{\varepsilon}) \check{E}_g(\bar{\varepsilon}) W_l(\bar{\varepsilon}) + x_l \check{E}_l(\bar{\varepsilon}) W_g(\bar{\varepsilon})} \times \frac{s_l(\bar{\varepsilon}) W_g(\bar{\varepsilon}) W_l(\bar{\varepsilon})}{s_{\text{int}}(\bar{\varepsilon})}. \quad (3.38)$$

To ensure accurate input data to the approximation method (3.38), multi-term solutions of Boltzmann's equation [10, 15] were computed to obtain transport properties for argon and xenon in both dilute gas and liquid extreme conditions. In low density dilute gas and high density liquid states, electron scattering cross sections were taken from the recent *ab initio* refinements that take into account density dependent scattering and screening effects [12, 15] to obtain increased accuracy. To demonstrate the validity of the calculated transport data in gas and liquid extremes, comparison against experimental results is included in Figures 3.8 and 3.9. Gas phase drift velocity measurements are taken from the work of Pack *et al.* [14], while liquid argon and liquid xenon measurements are taken from Miller *et al.* [13] and Huang and Freeman [16] respectively.

The angle-integrated structure factors for the liquid extrema and the intermediate fluid,  $s_l$  and  $s_{\text{mix}}$ , were approximated as per the benchmark model atomic liquid used in Section 3.3.3. For liquid argon and xenon this work evaluates the analytic static

structure factor expression of Verlet and Weiss (3.18) using relevant parameters for argon and xenon, because it has been shown that despite the complex interaction at high densities the expression of Verlet and Weiss is a good approximation to the structure factor for noble liquids [8,65]. With accurate data for gas and liquid extremes, and a temperature modification to the approximation rule (3.38), benchmarking was performed to compare the approximation of the steady state drift velocity at an intermediate temperature/density for both liquid argon and liquid xenon against experimental results of Gushchin *et al.* [11]. The results are shown in Figures 3.8 and 3.9.

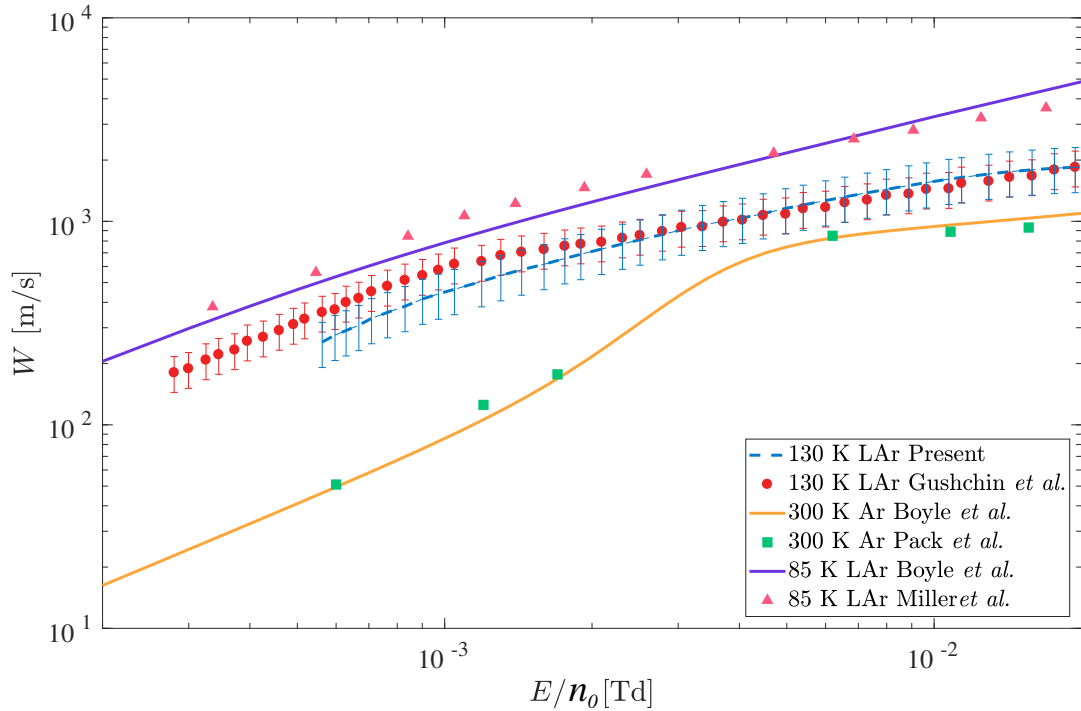


Figure 3.8: Electron drift velocity in liquid argon at 130 K. Present approximation computed via equation (3.38) compared with experimental results of Gushchin *et al.* [11]. Reference data: Boyle *et al.* [10,12], Miller *et al.* [13], Pack *et al.* [14].

From the experimental work of Gushchin *et al.* [11] errors of approximately 5% each were quoted for measurement of the drift velocity and applied electric field, and errors of approximately 10% was quoted for the computation of electron mean energy. Carrying these errors through the approximations used in this study, one can include estimated error bars on each line series for the intermediate drift velocities in Figures 3.8 and 3.9.

In Figures 3.8 and 3.9, there is a good agreement between the approximate values computed via (3.38) and experimental measurements within the uncertainties displayed. Despite no knowledge of the intermediate steady state transport properties, the complexities of the electron scattering cross section changing between gas and liquid densities, and an approximate treatment of the effects of structure, both approximations provide a good estimation of the drift velocity in the intermediate fluid densities.

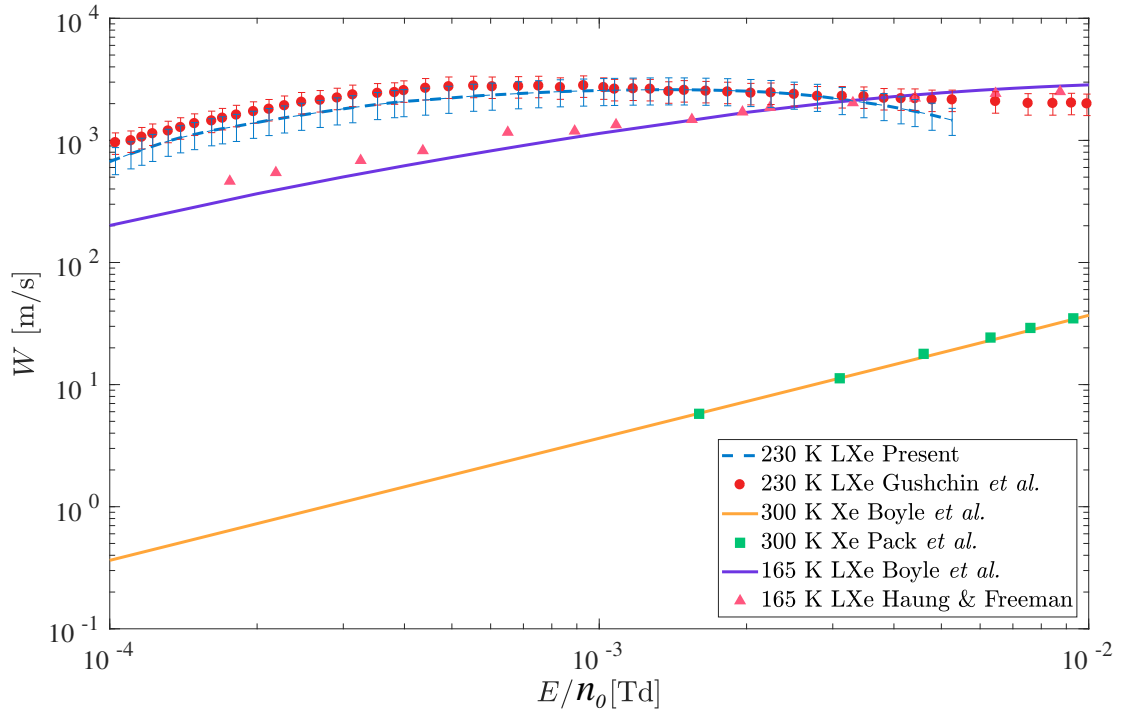


Figure 3.9: Electron drift velocity in liquid xenon at 230 K. Present approximation computed via equation (3.38) compared with experimental results of Gushchin *et al.* [11]. Reference data: Boyle *et al.* [10,15], Huang and Freeman [16], Pack *et al.* [14].

The liquid argon approximation provides the best fit of the two atomic systems considered, with a strong qualitative and functional agreement between experiment and calculated data. An encouraging feature of the liquid argon result is the ability of the approximation to demonstrate a gradient change that occurs at roughly  $10^{-3}$  Td. For liquid xenon, the prediction of NDC at low fields is also an encouraging result of the approximation. The magnitude and window of reduced fields at which the approximated NDC occurs is not exactly replicated, but the ability of the approximation rule to predict NDC by employing very simple structure assumptions shows the utility of the proposed approximation. Future improvements in approximating the intermediate density structure effects via experimental structure factors, and including interaction potential screening effects, may yield even greater accuracy in approximating complex transport behavior.

### 3.5 Chapter Summary

The work in this Chapter has proposed expressions (3.36) and (3.38) to approximate electron transport at intermediate densities in the gas-liquid interfacial region from data in the gas and liquid extreme phases only. To formulate the approximation method, this Chapter extended well known mean energy dependent gas phase mixture rules into high density fluids which exhibit non-linear density dependent transport properties. The final approximation applies a simple analytic structure modification to account for non-linear density effects on electron momentum transfer, and this was benchmarked

with simple atomic liquid models. Following analysis of structure induced momentum transfer effects, an approximation derived from energy balance between electrons and structured media was benchmarked and demonstrated suitable accuracy for a wide range of reduced fields. Improved accuracy could be achieved with higher-order momentum transfer theory [76, 161]. Finally, to form a practical approximation rule that can be used without any knowledge of the reduced field's dependence on mean energy, approximations derived from energy balance and modified momentum balance were combined and the subsequent expression was benchmarked.

Steady state transport properties of a simple atomic liquid model plus experimental data of argon and xenon liquids were assembled for comparison. By applying the final combined drift velocity approximation (3.36), and (3.38) for including temperature variation in the experimental benchmarks, this Chapter demonstrated the utility of the approximation in predicting drift velocities of intermediate fluids between gas and liquid extremes. It was subsequently demonstrated that reduced momentum collision frequencies can be approximated with sufficient accuracy, to serve as input data in higher order electron moment modeling. For the majority of model and experimental gases and liquids the qualitative agreement between approximations and known results was strong. Despite the encouraging performance of the proposed approximation rule, comparison against argon and xenon experimental results demonstrated the complex interaction potentials of real liquids pose a challenge and further study should be carried out on including low-energy screening effects into the approximation of intermediate structure factors,  $s_{\text{mix}}$ . In addition, further enhancements on the implementation of an angle-integrated structure factor should be studied to account for the structure of even more complex liquids, such as polar molecular liquids like water.

With the foundation of an interfacial modeling framework proposed in the previous two Chapters, the following Chapter aims to bring together the results presented thus far in this work. Application of the higher order fluid modeling method, along with density-dependent input data proposed in this Chapter, will be made to simulating swarm and streamer propagation between the two extremes of an argon gas-liquid system.

## Chapter Appendix: Dilute gas mixture rules

---

To provide the foundation for an approximation of electron collision rates at intermediate densities between a gas and liquid, methods of approximating drift velocities in dilute gas mixtures were reviewed. Various rules have been used in literature, but all are based on the premise of density fractions,  $x_\alpha = n_\alpha/n_{\text{total}}$ , computed for each constituent gas being used to scale steady state drift velocities of each constituent gas to provide an approximate of the mixture's steady state transport data.

Blanc's law

The origin of mixing rules in gas phase charged particle transport can be traced to Blanc's empirical law [157]

$$\frac{1}{W_{\text{mix}}\left(\frac{E}{n_0}\right)} = \sum_{\alpha} \frac{x_{\alpha}}{W_{\alpha}\left(\frac{E}{n_0}\right)}, \quad (3.39)$$

where  $W_{\text{mix}}$  is the mixture drift velocity,  $x_{\alpha}$  is the density fraction of gas  $\alpha$  such that  $\sum_{\alpha} x_{\alpha} = 1$ , and  $W_{\alpha}$  is the drift velocity in gas  $\alpha$ . All drift velocities are evaluated at a common value of reduced electric field,  $E/n_0$ ; which has since been termed a common  $E/n_0$  (CEON) approach [158].

By the mid 20th century experimental results necessitated modifications to Blanc's law,

$$\frac{1}{W_{\text{mix}}\left(\frac{E}{n_0}\right)} = \sum_{\alpha} \frac{x_{\alpha}}{W_{\alpha}\left(\frac{E}{n_0}\right)} + \delta_B\left(\frac{E}{n_0}\right), \quad (3.40)$$

where  $\delta_B$  is some deviation from the original law to include higher order effects and inelastic collisions [158, 165, 166]. Multiple approaches to computing deviations were presented, from rigorous kinetic theory arguments to empirical observations based on new experimental observations. It was shown that Blanc's law was suitable for approximating ion transport in gas mixtures, whereas it failed significantly for electron transport, without severe modifications to the original law [158, 159, 166–168].

The breakdown of Blanc's law for electrons can be understood as a failing of the following two assumptions:

1. that electron impact cross sections can be added in simple linear combinations at a given value of  $E/n_0$  [165], and
2. the steady state EEDF is the same for each gas, and the combination mixture, at a given value of  $E/n_0$  [158].

In general, these assumptions will fail owing to the rapidly varying electron mean energy with increasing  $E/n_0$ , and the strong dependence of energy transfer on inelastic collisions, which may occur at vastly different field ranges for different gases. These failings of the CEON method led to an alternative mixing rule based on a common mean energy (CME) as proposed by Chiffikian [159].

### Common mean energy procedure

The CME rule is in the spirit of modern plasma moment modeling in the sense that transport is defined as a function of charged particle mean energy  $\bar{\epsilon}$  [69, 89, 96, 97, 104, 145], instead of the reduced field  $E/n_0$ . Two variations of a CME rule may be derived from the steady state momentum and energy balance equations for charged particle transport

in a plasma to yield two slightly different equations, corresponding to either momentum ( $p = +1$ ) or energy balance ( $p = -1$ )

$$1 = \sum_{\alpha} \frac{\check{E}_{\alpha}(\bar{\varepsilon})}{\check{E}_{\text{mix}}(\bar{\varepsilon})} \left[ \frac{W_{\text{mix}}(\bar{\varepsilon})}{W_{\alpha}(\bar{\varepsilon})} \right]^p,$$

where  $\check{E}_{\text{mix}} = E_{\text{mix}}/n_0$  of the mixture,  $\check{E}_{\alpha} = E_{\alpha}/n_0$  in gas  $\alpha$ ,  $W_{\text{mix}}$  is the drift velocity in the mixture, and  $W_{\alpha}$  is the drift velocity in gas  $\alpha$ . All terms are evaluated at the same value of mean energy  $\bar{\varepsilon}$ .

Adopting either of the two CME approximations was shown to be suitable for both ions and electrons in various gas mixtures. In contrast to Blanc's Law, inelastic collisions are natively included in the general theory [158, 159]. Furthermore, the accuracy of the rule is also not restricted to a two-term EEDF theory, as arbitrary steady state EEDFs are assumed in the derivation [158].

# 4

## Electron swarm and streamer transport at the gas-liquid interface

This chapter contains material that was submitted as the following journal article:

NA Garland, I Simonović, GJ Boyle, DG Cocks, S Dujko and RD White. Electron swarm and streamer transport across the gas-liquid interface: a comparative fluid model study. Submitted to *Plasma Sources Science and Technology* on the 29 of April 2018.

This Chapter includes electron transport data computed by GJ Boyle via multi-term solution of the Boltzmann equation. This data serves as input to the fluid model discussed in this Chapter.

### 4.1 Chapter Introduction

---

The aims of this Chapter are to extend the proposed and benchmarked higher order four moment fluid model [2], as well as drift diffusion fluid models [76, 89, 93, 95, 104], to simulate electron transport across gas-liquid interfaces and formulate a recommendation for best practice future interfacial modeling. Interfacial considerations will be addressed by comparing the types of fluid model used but also through comparison of functional form assumptions for neutral density,  $n_0$ , variation of the interface. Inclusion of gas-liquid interface effects, such as variation of delocalized electron energy level,  $V_0$ , and dielectric permittivity,  $\varepsilon$ , into the proposed modeling framework is also addressed.

This Chapter begins by briefly reviewing fluid models used for electron transport in gases and liquids in Section 4.2 where distinctions between gas and liquid phase electron transport are highlighted. In Section 4.3 a continuous fluid model of electron transport between gas and liquid media is proposed, with modifications to include

certain interfacial effects discussed. The results of the proposed interfacial fluid models are detailed in Section 4.5, with key advantages and disadvantages of each model highlighted. Finally, in Section 4.6, key recommendations drawn from the results of this study are made, with a focus on how to best accommodate interfacial electron transport in future fluid models.

## 4.2 Fluid modeling in gases and liquids

### 4.2.1 Fluid models for electron transport

Fluid models have been used to describe plasma phenomena such as streamers [95, 104, 169], industrial plasmas used in fabricating microelectronics [100, 170], and more recently bio-medical [34, 50] applications of discharges. Fluid models are essentially continuity equations of velocity-averaged, spatially varying macroscopic variables, such as particle density, momentum, and energy [2, 76, 89, 95, 104] derived via velocity moments of the Boltzmann equation [2, 94]. This gives a relatively straightforward macroscopic model that provides a good description of the discharge dynamics, without the computational overhead of comprehensive microscopic methods such as particle based methods like Partice-in-Cell (PIC) or Monte Carlo (MC) [65, 171, 172], or kinetic solutions of the Boltzmann kinetic equation [90, 93, 95, 96, 100, 105] that directly yield an electron velocity distribution function (EVDF) as a function of space, velocity, and time  $f(\mathbf{r}, \mathbf{v}, t)$ .

This study selected three approaches to fluid modeling, and examined the results and subsequent appropriateness of each model towards describing interfacial electron transport between gas and liquid densities of liquid argon. Here a brief review of the selected fluid models is presented, with the finer details of the origins and formulations of the models deferred to previous comprehensive studies on fluid modeling specifically [2, 76, 89, 93, 95, 104].

#### Drift diffusion models

The most popular approach to fluid modeling of electron transport in gaseous plasmas has traditionally been a hydrodynamic drift diffusion continuity equation (4.1) of the electron density,  $n_e(z, t) = \int f(\mathbf{r}, \mathbf{v}, t) d\mathbf{v}$ . The electron flux is obtained by assuming a steady-state of the momentum balance equation, and that the field-driven component of electron energy is much greater than the thermal contribution [93, 96, 103, 104]. The resulting one dimensional continuity equation is

$$\frac{\partial n_e}{\partial t} - \frac{\partial}{\partial z} \left[ n_e W \left( \frac{E}{n_0} \right) + D \left( \frac{E}{n_0} \right) \frac{\partial n_e}{\partial z} \right] = n_e \left[ \nu_I \left( \frac{E}{n_0} \right) - \nu_a \left( \frac{E}{n_0} \right) \right], \quad (4.1)$$

where input data terms are the drift velocity,  $W$ , diffusion coefficient,  $D$ , and ionisation/attachment collision rates,  $\nu_I$  and  $\nu_a$ . All input data are assumed to be functions of the local instantaneous reduced electric field,  $\frac{E}{n_0}$ , during the simulation.

Interpolation of steady state transport coefficients and collision rates is used to provide values for these input parameters. The steady state values are obtained from the steady state electron velocity distribution function (EVDF) which can be found via Monte Carlo simulations [65, 87] or a multi-term kinetic solution of the Boltzmann equation [10, 48, 94, 132], given appropriate microscopic inputs of electron scattering cross sections for the target gas (see Section 4.2.2).

In addition to the electron continuity equation (4.1), continuity equations for positive,  $n_+$ , (via ionisation reactions) and negative,  $n_-$ , (via attachment reactions) ion densities are used

$$\frac{\partial n_+}{\partial t} = n_e \nu_I \left( \frac{E}{n_0} \right), \quad \text{and} \quad \frac{\partial n_-}{\partial t} = n_e \nu_a \left( \frac{E}{n_0} \right), \quad (4.2)$$

where ion transport has been neglected over the transient time scales considered in this study for ionisation front propagation [95, 104]. Recombination of electrons with positive ions, and negative ions with positive ions is neglected in this study.

Alongside the continuity equations for charged species densities (4.1) - (4.2), the space charge effects on the electric field,  $E$ , must be computed to determine any screening effects due to the creation of electrons and ions. This is done by solving the Poisson equation for electric potential,  $V$ , to obtain the electric field

$$\frac{\partial^2 V}{\partial z^2} = \frac{e}{\varepsilon_r \varepsilon_0} (n_e + n_- - n_+), \quad (4.3)$$

$$E = -\frac{\partial V}{\partial z}, \quad (4.4)$$

where  $e$  is the elementary charge,  $\varepsilon_r$  and  $\varepsilon_0$  are the fluid's relative and the vacuum dielectric permittivities respectively.

While the model described by (4.1) - (4.4) has been traditionally used to describe charged particle transport within gases, the functional form of the model has been demonstrated to be applicable to describe transport within liquid discharges assuming appropriate modifications to the input data are made [2]. As the neutral density increases the single-scattering assumption used for gas transport breaks down as the effects of elastic coherent scattering and electron interaction potential screening and polarization become important [10, 15, 48]. These effects are significant when the electron de Broglie wavelength is comparable to the average background particle spacing,  $\lambda \sim n_0^{-\frac{1}{3}}$ , which corresponds to low-energy electron scattering or scattering in very dense liquids.

Comprehensive formulations are available on how to modify gas phase electron interaction cross sections of non-polar atomic targets, such as noble liquids, to account for coherent scattering [48], and later the interaction potential screening and polarization [12, 15]. These structure modifications were implemented through a density dependent

momentum transfer cross section

$$\Sigma_m(v, n_0) = 2\pi \int_0^\pi \Sigma(v, \chi, n_0) [1 - \cos \chi] \sin \chi d\chi, \quad (4.5)$$

where  $v$  is the incoming electron speed,  $\chi$  is the electron scattering angle off the target atom, and  $\Sigma(v, \chi, n_0)$  is an effective differential cross section including coherent scattering and interaction potential modifications via

$$\Sigma(v, \chi, n_0) = \tilde{\sigma}(v, \chi) S(\Delta k, n_0), \quad (4.6)$$

where  $\tilde{\sigma}(v, \chi)$  is the liquid phase differential cross section containing any screening and polarization effects [12,15],  $S(\Delta k, n_0)$  is the static structure factor and  $\Delta k = \frac{2m_e v}{\hbar} \sin \frac{\chi}{2}$  is the wave number proportional to the change in momentum [48], where  $m_e$  is the electron mass and  $\hbar$  is reduced Planck's constant. The static structure factor is a non-linear function of  $n_0$  of the target material, and may be calculated from molecular simulations, measured via experiments [15, 48, 65], or derived analytically through solutions of pair-correlation functions as per the Verlet-Weiss corrected Percus-Yevick structure factor [83]. For detailed discussion on the static structure factor, and its implementation in liquid scattering, readers are directed to previous studies [15, 48, 65].

These fundamental liquid transport studies demonstrated substantially different cross sections for liquid transport at low incoming electron energies compared to transport in gas phase, particularly in reduced momentum transfer from preferential forward scattering [12,15]. It was shown that, while energy transfer was impacted by modifications of the cross section due to potential screening, energy transfer was not explicitly modified by including coherent elastic scattering effects [48,76] and energy transfer due to inelastic excitation collisions is considered localized to the immediate target atom. In summary, the functional form of the balance equations used to model electron transport is the same whether transport is in gas or liquid. However, explicit modifications to include liquid phase physics must be performed [10,48] to obtain the appropriate cross sections for computing electron transport data. If the correct cross sections are used to generate input data for either gas or liquid transport, then the drift diffusion model (4.1) - (4.2) can then be applied directly.

### Higher order models

In addition to drift diffusion fluid models, so called higher order fluid models have gained popularity for modeling charged particle transport in plasmas [2, 94, 95, 146]. In these models, the hierarchy of velocity moments of Boltzmann's equation is not truncated at the electron flux, but often extends to include four continuity equations for electron density,  $n_e$ , electron particle flux,  $\mathbf{\Gamma} = n_e \langle \mathbf{v} \rangle = \int f(\mathbf{r}, \mathbf{v}, t) \mathbf{v} d\mathbf{v}$ , electron mean energy density,  $n_e \langle \epsilon \rangle = \int f(\mathbf{r}, \mathbf{v}, t) \frac{1}{2} m v^2 d\mathbf{v}$ , and electron energy flux,  $\mathbf{\Gamma}_\epsilon = n_e \langle \boldsymbol{\xi} \rangle = \int f(\mathbf{r}, \mathbf{v}, t) \frac{1}{2} m v^2 \mathbf{v} d\mathbf{v}$ , where  $\langle \mathbf{v} \rangle$ ,  $\langle \epsilon \rangle$ , and  $\langle \boldsymbol{\xi} \rangle$  denote the electron average velocity, average energy, and average energy flux. Following the formulation of a four

moment higher order model benchmarked in gas and liquid transport [2], the system of equations are

$$\frac{\partial n_e}{\partial t} + \frac{\partial \Gamma}{\partial z} = n_e(\nu_I(\langle \epsilon \rangle) - \nu_a(\langle \epsilon \rangle)), \quad (4.7)$$

$$\frac{\partial \Gamma}{\partial t} + \frac{\partial}{\partial z} (n_e \theta_m(\langle \epsilon \rangle)) + n_e \frac{e}{m_e} E = -\Gamma \nu_m(\langle \epsilon \rangle), \quad (4.8)$$

$$\frac{\partial n_\epsilon}{\partial t} + \frac{\partial \Gamma_\epsilon}{\partial z} + eE\Gamma = -nS_\epsilon(\langle \epsilon \rangle), \quad (4.9)$$

$$\frac{\partial \Gamma_\epsilon}{\partial t} + \frac{\partial}{\partial z} (n\theta_\xi(\langle \epsilon \rangle)) + n\theta_m(\langle \epsilon \rangle) eE + n_\epsilon \frac{e}{m_e} E = -\Gamma_\epsilon \nu_\xi(\langle \epsilon \rangle), \quad (4.10)$$

$$\frac{\partial n_+}{\partial t} = n_e \nu_I(\langle \epsilon \rangle), \quad \frac{\partial n_-}{\partial t} = n_e \nu_a(\langle \epsilon \rangle), \quad (4.11)$$

where input data is required via collision rates for for ionisation,  $\nu_I$ , attachment,  $\nu_a$ , momentum transfer,  $\nu_m$ , energy transfer,  $S_\epsilon$ , energy flux transfer,  $\nu_\xi$ , and higher order tensor product closure approximations,  $\theta_m$ , and  $\theta_\xi$ .

In this model, the higher order moments,  $\theta_m = \langle \mathbf{v}\mathbf{v} \rangle$  and  $\theta_\xi = \langle \frac{1}{2}mv^2\mathbf{v}\mathbf{v} \rangle$ , are closed by evaluation over the equilibrium steady-state EEDF used to also evaluate collision input rates, similar to that of the input data described in Section 4.2.1. This choice of closure was demonstrated to provide a parameter free, physically sound alternative to other closure assumptions, such as heat flux assumptions or parameterizing the moments in terms of  $\langle \epsilon \rangle$ , previously used in literature [2, 95, 146].

The same process for generating a look-up table of steady state input data via an equilibrium EEDF, described in Section 4.2.1, is used for this higher order model also. Higher order models differ to drift-diffusion models because more information of electron dynamics is natively included, so that phenomena such as temporal and spatial non-locality can be resolved [104]. In lieu of using  $\frac{E}{n_0}$  to determine input data as per the drift-diffusion model, here the electron mean energy,  $\langle \epsilon \rangle$ , is used as the interpolating variable to determine input data at each point in space during the simulation [101].

As discussed in Section 4.2.1, for a local field dependent model, a higher order model can also be equally applicable in gas or liquid, assuming the correct modifications have been made to generate accurate input data to account for liquid effects. For further details on the higher order moment model used in this study the reader is referred to a recent formulation and benchmarking study [2].

#### 4.2.2 Transport data in gaseous and liquid argon

This Section presents the microscopic input of electron scattering cross sections for electrons with gaseous and liquid argon, in addition to the resulting transport and collision data that serves as input to the fluid models presented in Section 4.2.1.

### Electron scattering cross sections

As this study involves both gas and liquid extremes of argon, two sets of electron scattering cross sections are required in order to generate input data for fluid models via kinetic solutions of the Boltzmann equation or Monte Carlo simulations.

The gaseous argon electron scattering cross sections of Hayashi [17] were used as input to a multi-term solution of the Boltzmann equation to generate input data for this study. The set comprising of an elastic momentum transfer cross section (MTCS), twenty five inelastic excitation cross sections, and an ionisation cross section were retrieved from the online database [www.lxcat.net](http://www.lxcat.net) [69].

As recommended by recent studies of electron transport and negative planar streamer fronts in atomic liquids [173, 174], liquid argon cross sections were compiled from recent works on accurate low-energy liquid cross sections, combined with necessary modification of the gas phase Hayashi cross sections for inelastic processes. To form the basis of the MTCS scattering cross section, the low-energy ( $\leq 10$  eV) MTCS for liquid argon proposed by Boyle et al. [12] was taken in order to include the effects of coherent scattering and atomic potential screening which are critical for low-energy electron scattering in dense liquids. At higher incoming electron energies, where the liquid cross section converges to the gas cross section, the gaseous argon MTCS of Hayashi [17] was once again used. These two elastic scattering cross sections were joined and smoothed at  $\sim 10$  eV to form a single elastic scattering cross section.

As precise measurements, or calculations, of liquid phase ionisation cross sections do not exist for atomic argon, a liquid argon ionisation cross section was constructed by modifying the gaseous argon ionisation cross section as detailed in [62, 175–177]. The liquid argon ionisation threshold energy,  $I_{\text{liq}}$ , was computed by modifying the the gaseous argon threshold energy,  $I_{\text{gas}} = 15.68$  eV, to account for dense liquid effects. The known gaseous ionisation cross section of Hayashi [17] was then translated to the new threshold energy for liquid. The foundation and derivation of these modifications are detailed in [62], and the key result relevant to this present study can be summarized by the expression

$$I_{\text{liq}} = I_{\text{gas}} + P_+ + V_0 + E_{\text{val}}, \quad (4.12)$$

where  $P_+$  is the ion polarization energy of the positive ion ( $P_+ = -1.08$  eV for argon [62]),  $V_0$  is the energy of the delocalized electron level in the liquid i.e. the bottom of conduction band ( $V_0 = -0.3$  eV for the liquid argon density used in this study [175]), and  $E_{\text{val}}$  is the change in energy of valence bands due to condensing the gas ( $E_{\text{val}} = 0.1$  eV for argon [62]). This process yields the ionisation threshold energy of  $I_{\text{liq}} = 14.4$  eV.

The inelastic excitation cross sections of the Hayashi database set were then slightly modified to form a set of inelastic excitation cross sections for liquid argon. This was done by excluding any excitation process with a threshold energy above the new ionisation threshold energy [173, 174], which for liquid argon is  $I_{\text{liq}} = 14.4$  eV. As a

result, the excitation cross sections corresponding to threshold energies of 14.71 eV and 15.2 eV were excluded from the data set, and the remaining twenty three cross sections formed the final inelastic excitation cross section set for liquid argon. The final sets of electron scattering cross sections in both gas and liquid argon are shown in Figure 4.1.

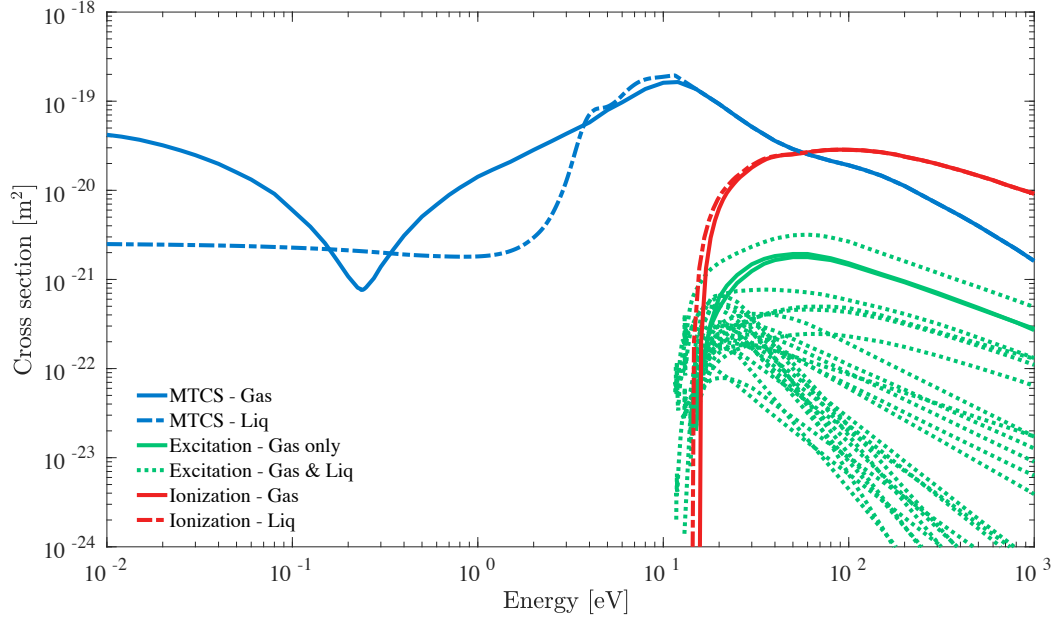


Figure 4.1: Gas and liquid argon electron scattering cross sections utilized in this study. Gas cross section data of Hayashi [17] via [www.lxcat.net](http://www.lxcat.net). Liquid cross section data of Boyle *et al.* [12] and necessary modifications of Hayashi set detailed in Section 4.2.2.

### Fluid model input electron transport data

Using the electron scattering cross sections for both gas and liquid argon extremes (see Figure 4.1) equilibrium electron transport data was calculated to serve as input data for the fluid models used in this study. A multi-term solution of the Boltzmann kinetic equation [10, 12, 76] was used to calculate EEDFs over a range of reduced electric field values at 85 K, a common cryogenic temperature, near the triple point, used in argon applications and experimental studies [11, 155, 178, 179]. These energy distribution functions were then used to calculate the steady state transport data necessary for input to the fluid models used in this study. Plots of electron drift velocity, longitudinal diffusion, and ionisation collision rate, used as input for (4.1) - (4.2), are shown in Figure 4.2; though not used as a model input, a plot of the electron mean energy as a function of reduced field is included to demonstrate key differences between gas and liquid transport.

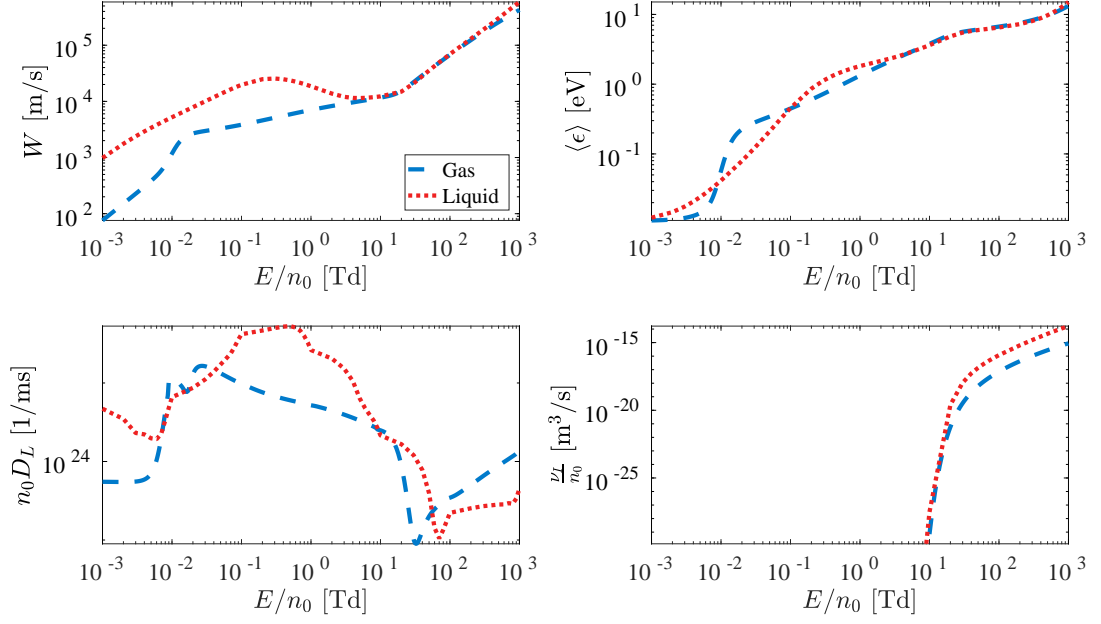


Figure 4.2: Input transport data of electrons in argon for local-field dependent electron fluid models. Dashed lines denote gas transport, dotted lines denote liquid transport. (Top-left) Drift velocity versus reduced field. (Top-right) Electron mean energy versus reduced field. (Bottom-left) Longitudinal reduced diffusion coefficient versus reduced field. (Bottom-right) Reduced ionisation collision rate versus reduced field.

Reduced collision rates for input to the higher order fluid model, computed from equilibrium steady-state EEDFs found via multi-term solution of the Boltzmann equation [10], are presented in Figure 4.3 demonstrating the variation of collision rates for momentum transfer  $\nu_m/n_0$ , energy flux transfer  $\nu_\xi/n_0$ , lumped energy loss  $S_\epsilon/n_0$ , and ionisation  $\nu_I/n_0$ . Input closure terms  $\theta_m = \langle v_z v_z \rangle$  and  $\theta_\xi = \langle v^2 v_z v_z \rangle$  for the higher order model are shown in Figure 4.4, where the expectation value is computed over the steady-state EEDF [2, 94].

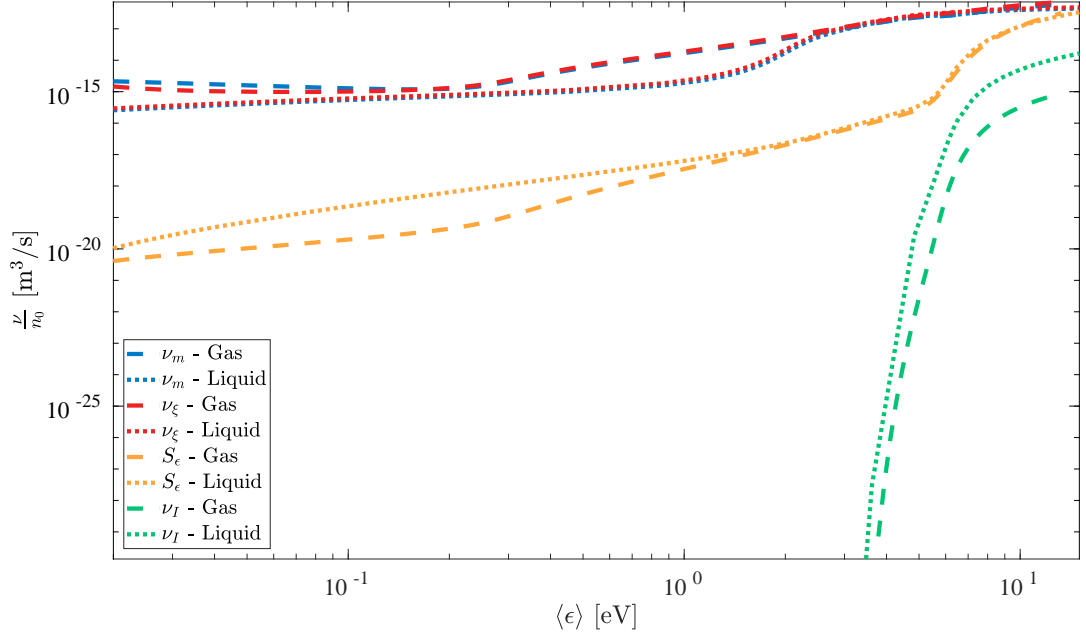


Figure 4.3: Input collision rates of electrons in argon for mean energy dependent higher order fluid model. Dashed lines denote gas transport, dotted lines denote liquid transport.

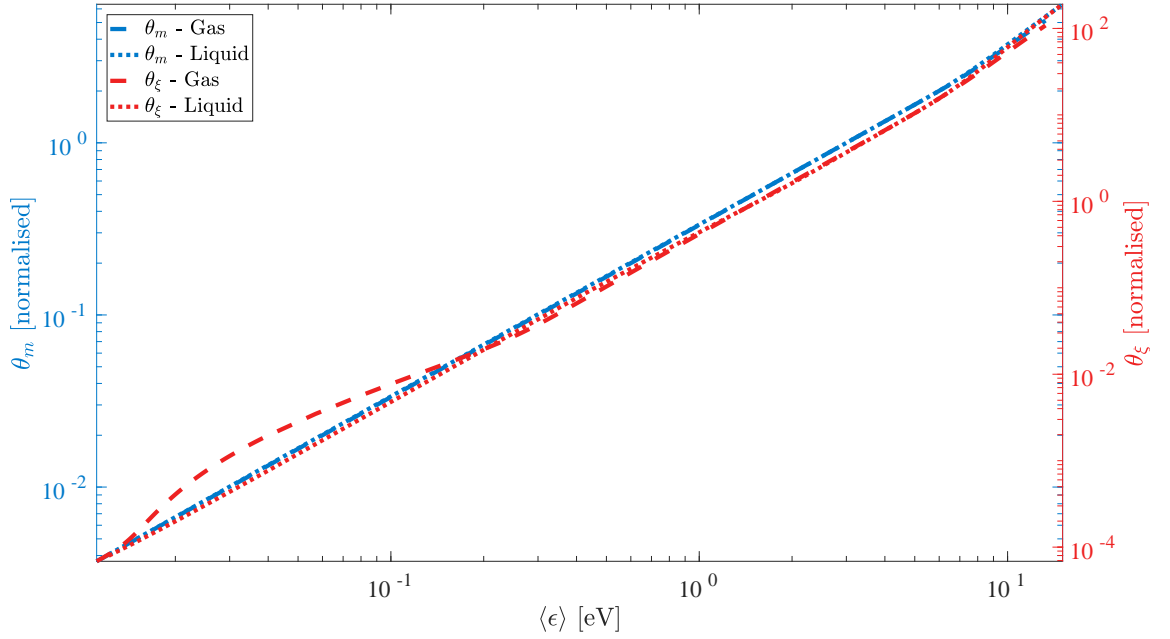


Figure 4.4: Input closure terms for mean energy dependent higher order fluid model for electrons in argon. (Left axis) Momentum balance closure term  $\theta_m = \langle v_z v_z \rangle$ . (Right axis) Energy flux balance closure term  $\theta_\xi = \langle v^2 v_z v_z \rangle$ . Dashed lines denote gas transport, dotted lines denote liquid transport.

### 4.3 Modeling at the gas-liquid interface

Following the brief review of fluid modeling methods and associated input data for electrons in either gas or liquid presented in Section 4.2, it is pertinent to now discuss

necessary interfacial effects that should be considered when trying to model electron transport between gas and liquid extrema as a continuous process. This study considers four important variations across the gas-liquid interface: (i) functional form of the variation in  $n_0$ , (ii) variation of input data for fluid models across the interface, (iii) variation of the delocalised electron energy level,  $V_0$ , across the interface, and (iv) variation of the relative dielectric permittivity,  $\epsilon_r$ , across the interface.

#### 4.3.1 Density profile variations

In order to accurately model electron transport between a gas phase plasma and a condensed liquid, the composition of the interfacial region must be known. This study assumes the existence of an equilibrium interfacial density profile formed between gas and liquid phases for atomic fluids, as outlined in Figure 4.5. The existence of this interfacial profile in non-polar atoms, such as argon and xenon, has been probed in various molecular dynamics (MD) and Monte Carlo (MC) studies [7–9, 156]. These simulations employ Lennard-Jones (LJ) potentials as an approximation to the atomic interaction potentials between each atom [7–9, 156]. Key measurables from these studies were equilibrium liquid and vapor densities, surface tension, and interface layer thickness,  $\delta_{\text{int}}$ . Kalos *et al.* [155] performed MD simulations of argon gas-liquid interface formation, resulting in a well defined interface thickness of approximately  $5\sigma_{\text{LJ}}$ , where  $\sigma_{\text{LJ}}$  is the atomic diameter used in the LJ potential. Later MD and MC studies of various noble liquids [7–9, 180] confirmed the earlier simulation results of Kalos *et al.* [155].

To implement the density change over the gas-liquid interface, this work assumes the equilibrium liquid density is 300 times greater than the equilibrium vapor density, which is consistent with the computational and experimental results found in literature [8, 9, 180]. The ratio between liquid and vapor densities in equilibrium ( $n_l/n_g$ ) reported was variable depending on the cut-off distance chosen for the LJ potential used in the MD simulations [8, 9, 180]. Trokhymchuk and Alejandre [8] studied the impact of cut-off distances for LJ potentials and found liquid-vapor density ratios from 200:1 up to 500:1, depending on the cut-off distance from  $2.5\sigma_{\text{LJ}}$  to  $5.5\sigma_{\text{LJ}}$ , while Ishiyama *et al.* [180] simply cut-off the LJ potential at  $15 \text{ \AA}$  in all their simulations.

A commonly proposed functional form describing the interfacial density variation is a hyperbolic tangent function [9, 180]

$$n_0(z) = \frac{1}{2}(n_g^{\text{eq}} + n_l^{\text{eq}}) - \frac{1}{2}(n_g^{\text{eq}} - n_l^{\text{eq}}) \tanh\left(\frac{2(z - z_{\text{int}})}{\delta_{\text{int}}}\right), \quad (4.13)$$

where  $n_g^{\text{eq}}$  and  $n_l^{\text{eq}}$  are the gas and liquid equilibrium densities,  $z_{\text{int}}$  is the center position of the interface, and  $\delta$  is a measure of the thickness of the interface, defined as the distance between 90% and 10% of the liquid density. This value,  $\delta_{\text{int}}$ , can be defined

as [9]

$$\delta_{\text{int}} = -(n_g^{\text{eq}} - n_l^{\text{eq}}) \left( \frac{dn_0(z)}{dz} \Big|_{z=z_{\text{int}}} \right)^{-1}, \quad (4.14)$$

or is fitted from a least squares method [180].

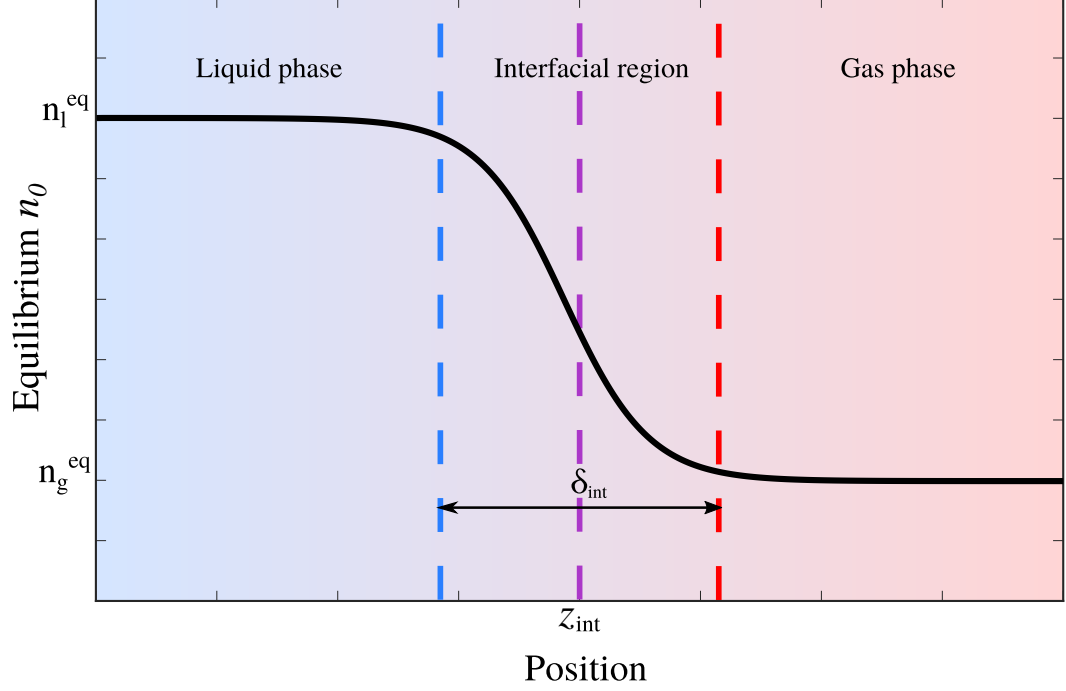


Figure 4.5: Equilibrium argon vapor-liquid interface as determined by molecular dynamics simulations [7–9]. The interface transition region is marked explicitly.

#### 4.3.2 Fluid model input data for continuum models between gas and liquid phases

With a well defined density configuration of the equilibrium interface between gas and liquid argon extremes, now consider the effects of this density variation on the required fluid model input data. One question to probe in this study, is whether or not one must use  $n_0$  dependent input data between gas and liquid density extremes, or if it is sufficient to simply use pure gas and liquid data either side of a defined interface point,  $z_0$ , akin to a step-function profile. One factor to consider in answering this question is the electron-neutral collisional mean free path

$$\lambda_{\text{mfp}} \approx \frac{1}{n_0 \sigma}, \quad (4.15)$$

where  $n_0$  is some neutral background density and  $\sigma$  is an electron scattering cross section. For gas, liquid, or intermediate densities, a range of mean free paths can be calculated to determine if the collisional scattering dynamics and any non-equilibrium behavior

will impact transport in the interfacial transition between gas and liquid. Typical liquid argon densities are  $n_l^{\text{eq}} \approx 10^{28} \text{ m}^{-3}$  while the gas density at the equilibrium interface used in this study is roughly 300 times smaller than the liquid, resulting in mean free paths for electron scattering in liquid argon in the range 1 – 100 nm, while the corresponding mean free path range in gaseous argon is 0.3 – 30  $\mu\text{m}$ . Since the equilibrium interfacial region in argon is on the order of nanometers one must consider  $n_0$  dependence in fluid model transport data in this interfacial region.

At this point, it is worthwhile to appropriately label fluid models introduced in Section 4.2.1, and define explicitly whether  $n_0$  dependent input data is used. Firstly, the simplest fluid model used in this study will not consider liquid effects at all, as an instructive example to the validity (or otherwise) of simply “scaling-up” gas phase transport data to liquid densities. This fluid model is a drift-diffusion model described by equations (4.1) - (4.2), and utilizes the gas phase input data presented in Figure 4.2 as a function of  $\frac{E}{n_0}$ . As argon is a non-attaching gas, the attachment rate,  $\nu_a$ , is neglected for the remainder of this work. This model is henceforth referred to as **LFA**, as it uses a local field approximation with gas phase data only.

Secondly, a local-field dependent drift-diffusion model (4.1) - (4.2) will be utilized with provision for  $n_0$  dependent input data. This dependence is introduced by asserting the  $W$ ,  $D_L$  and  $\nu_I$  input parameters of (4.1) - (4.2) are now functions of both the instantaneous reduced electric field and neutral density across the interface,  $f\left(\frac{E}{n_0}\right) \rightarrow f\left(\frac{E}{n_0}, n_0\right)$ . This model will henceforth be referred to as the **LFA** model.

Finally, taking the higher order model presented in (4.7) - (4.11) one may recast the functional form of the input parameters such that any input parameter dependent on electron mean energy is now also a function of the neutral density  $f(\langle\epsilon\rangle) \rightarrow f(\langle\epsilon\rangle, n_0)$ . As this is a higher order four moment model this model will henceforth be referred to as the **4MM** model. Input data requirements accounting for the density variation for both the LFA and 4MM models are discussed and presented in 4.6 using the results of a recently proposed and benchmarked study [3].

### 4.3.3 Space-charge field & spatially varying permittivity

With any plasma problem a self-consistent calculation of the instantaneous electric field,  $E = E(z, t)$ , must be included alongside equations describing particle transport. This is generally achieved via solutions of a Poisson equation for the spatially varying electric potential,  $\varphi = \varphi(z, t)$ , before differentiating to find the electric field,  $E$ . Here it is necessary to account for the variation in dielectric properties between gas and liquid densities. A spatially varying relative dielectric constant,  $\varepsilon_r = \varepsilon_r(z)$ , was computed using the same tanh function (4.13) used to modulate  $n_0$ , where liquid and gaseous argon constants were taken as  $\varepsilon_r^l = 1.504$  and  $\varepsilon_r^g = 1.0005$  respectively [181]. To accommodate the spatially varying dielectric constant in an inhomogeneous, isotropic material one may then self-consistently solve

$$\frac{\partial}{\partial z} (\varepsilon_r(z) \varepsilon_0 E) = e (n_{\text{ion}} - n_e), \quad (4.16)$$

given that  $E = -\frac{\partial}{\partial z}\varphi$ , where boundary conditions on the electric potential are  $\varphi(0, t) = 0$  and  $\varphi(L, t) = \varphi_{\text{applied}}$  where  $\varphi_{\text{applied}}$  is a fixed voltage to produce the desired applied electric field in the absence of space-charge contributions.

#### 4.3.4 Accommodating spatial variation of $V_0$ across the interface

As gas densities increase to liquid values, it is vital to also consider the variation in the energy of the delocalized electron level in the liquid,  $V_0$ . This can be positive (neon, helium) or negative (argon, xenon) and is largely a function of the electron scattering length,  $a_0$ , of the target atom [62, 175]. The dependence of  $V_0$  on the neutral atomic density of argon,  $n_0$ , demonstrates an approximate linear roll-off of from 0 eV in gas down to approximately -0.3 eV at the maximum liquid density used in this study [62, 175]. Given a known equilibrium  $n_0(z)$  profile, and thus an equilibrium  $V_0(z)$ , an effective electric field is found by differentiating  $V_0(z)$ , and combined with the electric field,  $E$ , computed via (4.16) to yield the total electric field

$$E_{\text{total}} = E + E_{V_0}. \quad (4.17)$$

## 4.4 Numerical solution of system of hyperbolic PDEs

Numerical solution of each fluid model was performed by a custom Flux-Corrected Transport (FCT) code, with explicit fourth order Runge-Kutta time-integration used to advance forward in time [150–152]. Spatial discretization was performed by augmenting a monotonic first order upwinding scheme [182], with a second order conservative finite difference scheme. The flux limiting algorithm of Boris and Book [150, 151] was used to enable resolution of sharp gradients found in ionisation fronts. To account for the varying length scales present in the problems, this research employed variably spaced grids to allow spatial steps appropriate to liquid, gas, and interfacial regions. Given spatial grid sizes, time step size was chosen as the smallest step computed via: (i) a Courant–Friedrichs–Lewy (CFL) condition of 0.05, or (ii)  $1/20$  of the the fastest collisional relaxation time. To ensure the accuracy of this scheme, systematic benchmarking was performed by comparing numerical solutions against known analytic solutions, and ensuring particle conservation was guaranteed at each time step. Typical systems used for benchmarking are square-wave advection, Gaussian pulse advection-diffusion, and the solution of Euler’s equations for Sod’s shock-tube [150–152].

Initial conditions for simulation of streamer formation and propagation were assumed as a narrow Gaussian pulse of electron/ion densities created by an arbitrary ionisation event prior to the simulation start. Electron average velocity, mean energy, and energy flux were assumed to be the steady-state values corresponding to the applied value of  $E/n_0$  in liquid argon. Continuous boundary conditions were implemented to allow passage of information outside of the solution domain to avoid impacting the solution. To further assist in this aim, streamer formation and propagation was performed well

inside the solution domain, away from the necessary boundaries, to minimize the impact of boundary conditions.

## 4.5 Results and discussion

Using the fluid models and input data presented in Sections 4.2 and 4.3, transient simulations of electron transport from liquid argon into gaseous argon (left to right in this study's frame of reference) and gaseous argon to liquid argon (right to left) were performed. It is believed to be most instructive to start investigations with essentially swarm transport in the liquid phase transitioning to gas phase, where fields and ionisation rates are low, before considering cases where space-charge field considerations are important due to ionisation events. To examine the impacts of electron transport experiencing a gas-liquid interface transition in cryogenic argon, results from (i) large macroscopic length scales to examine the overall qualitative nature of the results, and (ii) small length scales at the immediate vicinity of the interfacial region in order to examine the impact of the interface transition. Results are presented at early (2 ps), intermediate (15 ps), and late (50 ps) times to demonstrate the physics of electron transport over different time scales.

### 4.5.1 Simulation conditions

An applied reduced field magnitude of  $|E/n_0| = 300$  Td in gas phase, corresponding to 0.8 Td in the liquid, was applied to drive electrons into the gas-liquid interface; the appropriate sign was assigned in each simulation to drive electrons left to right or vice versa. In this study the neutral atom temperature was kept constant at  $T_0 = 85$  K, a commonly used cryogenic temperature for liquid argon experiments [41, 178, 183]. The neutral density,  $n_0$ , was varied using the the tanh function interfacial density ramp (4.13), where  $n_l^{\text{eq}} = 1.8 \times 10^{28} \text{ m}^{-3}$  was obtained from the liquid argon coexistence curve at 85 K [183]. The equilibrium gas density,  $n_g^{\text{eq}} = n_l^{\text{eq}}/300$ , and the 10-90 interface width,  $\delta_{\text{int}} = 10r_{\text{Ar}}$ , were taken from the equilibrium properties found in literature [8, 9, 180], where  $r_{\text{Ar}} = 188$  pm is the Van der Waals radius of argon. Using the specified reduced field strengths, and the density profile provided by a tanh function, the initial total effective reduced electric field (4.17) is shown in Figure 4.6.

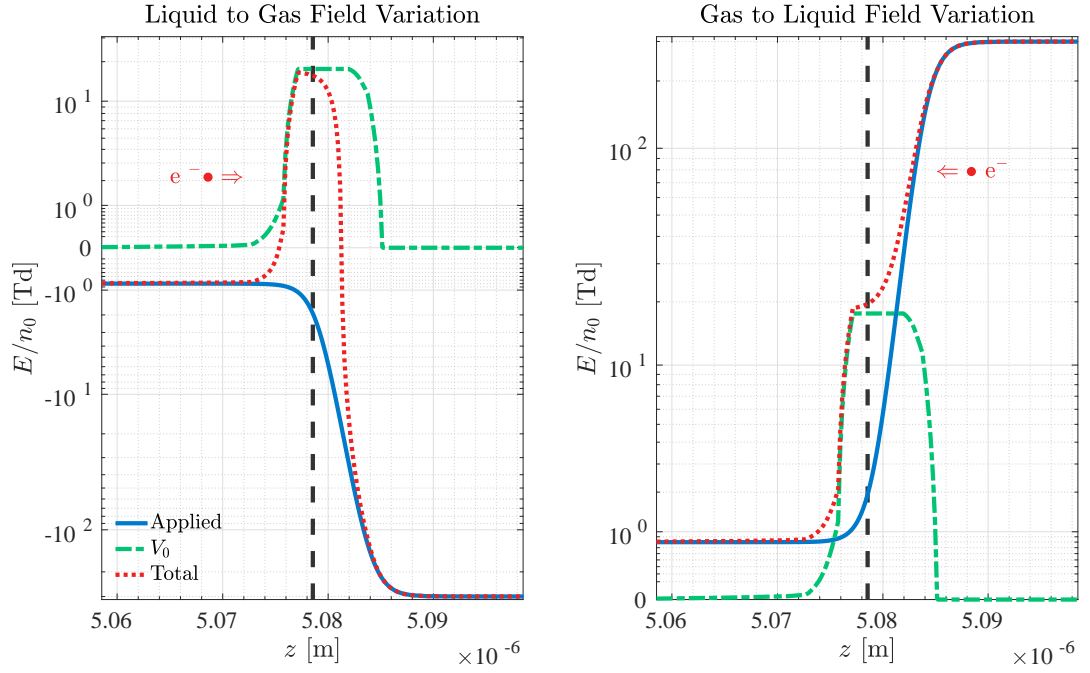


Figure 4.6: Reduced electric field profiles for applied and  $V_0$  contributions for both simulation configurations presented. Note that zero is included on the  $E/n_0$  logarithmic axis to reinforce the zero contribution via the  $V_0$  potential far from the interface.

Naturally, the space-charge field effects will evolve over the course of simulations but by simply considering the initial total fields assists in understanding of the results presented in Sections 4.5.2 and 4.5.3. From the liquid to gas plot of Figure 4.6 it is clear that the effective field due to  $V_0$  variation acts to impede electron transport from the liquid to the gas, while conversely it enhances electron transport into the liquid when the applied field is reversed on the right-hand plot.

#### 4.5.2 Electron transport from liquid argon into gaseous argon

Initial conditions of narrow Gaussian pulses were used in a simulation of electron transport across an interface, analogous to a single ionisation event within a liquid argon detection chamber. Evolution of the electron density in Figure 4.7 shows the initial pulse of electrons diffuses very quickly, leading to electron extraction from liquid into the gas phase as electrons impinge on the interface region. Qualitatively, both models predict similar results over all times however, it is clear the 4MM model demonstrates higher rates of electron extraction from the liquid. The LFA model predicts at least twice as much charge blocking on the liquid side of the interface compared to the 4MM model. Examining the expanded interfacial region of Figure 4.7, one sees the charge build-up at a narrow scale, with the 4MM result demonstrating two distinct roll-off gradients across the interface. To interpret this structure it is beneficial to consider the average electron velocity.

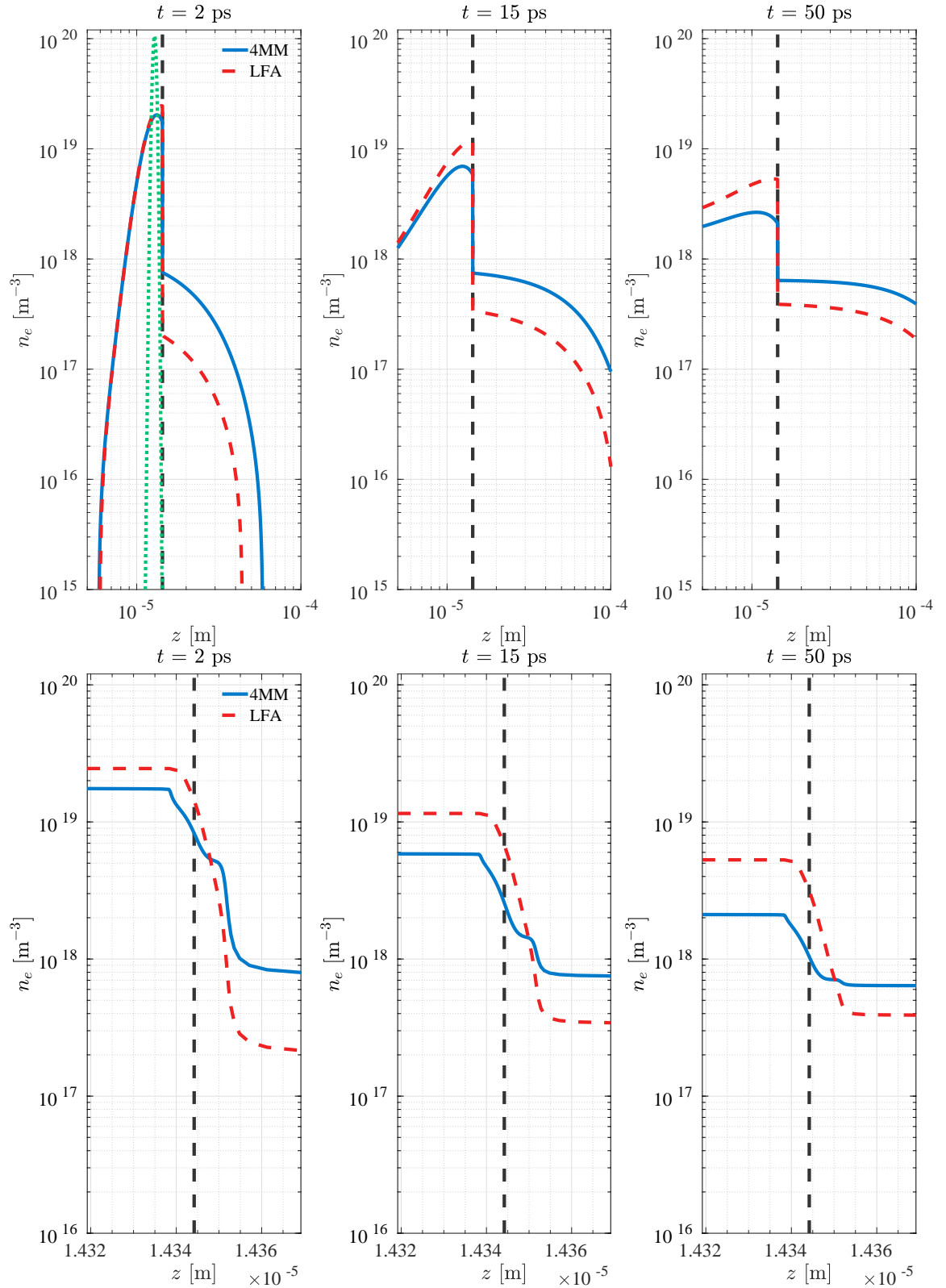


Figure 4.7: Electron density evolution for 4MM and LFA models at short, intermediate, and longer times as the electron swarm propagates from liquid to gaseous argon. Top view: Macroscopic results. Bottom view: Expanded view of interfacial results. Initial condition given by green dotted green line. Direction of field-driven propagation is from left to right.

Figure 4.8 demonstrates that far from the interfacial region, the average electron velocity has relaxed to an equilibrium value. However, near the interface it can be seen that initially the 4MM result predicts a large positive velocity, due to the large initial diffusive flux, and never becomes negative. In contrast, at the immediate vicinity of the interface the LFA model predicts a negative average velocity due to the blocking field contribution of the  $V_0$  potential in liquid argon. As time continues, the magnitude of these initially large velocities decreases but their sign differences remain. As the distance over which the blocking field is applied is very small, and the time for mean energy relaxation is quite long, the mean energy does not rapidly respond to the field variation. This is an example of non-local electron transport that the LFA model cannot predict, but the 4MM model can. These major differences in the average electron velocity at the interface are the drivers for deviations in electron density results observed in Figure 4.7.

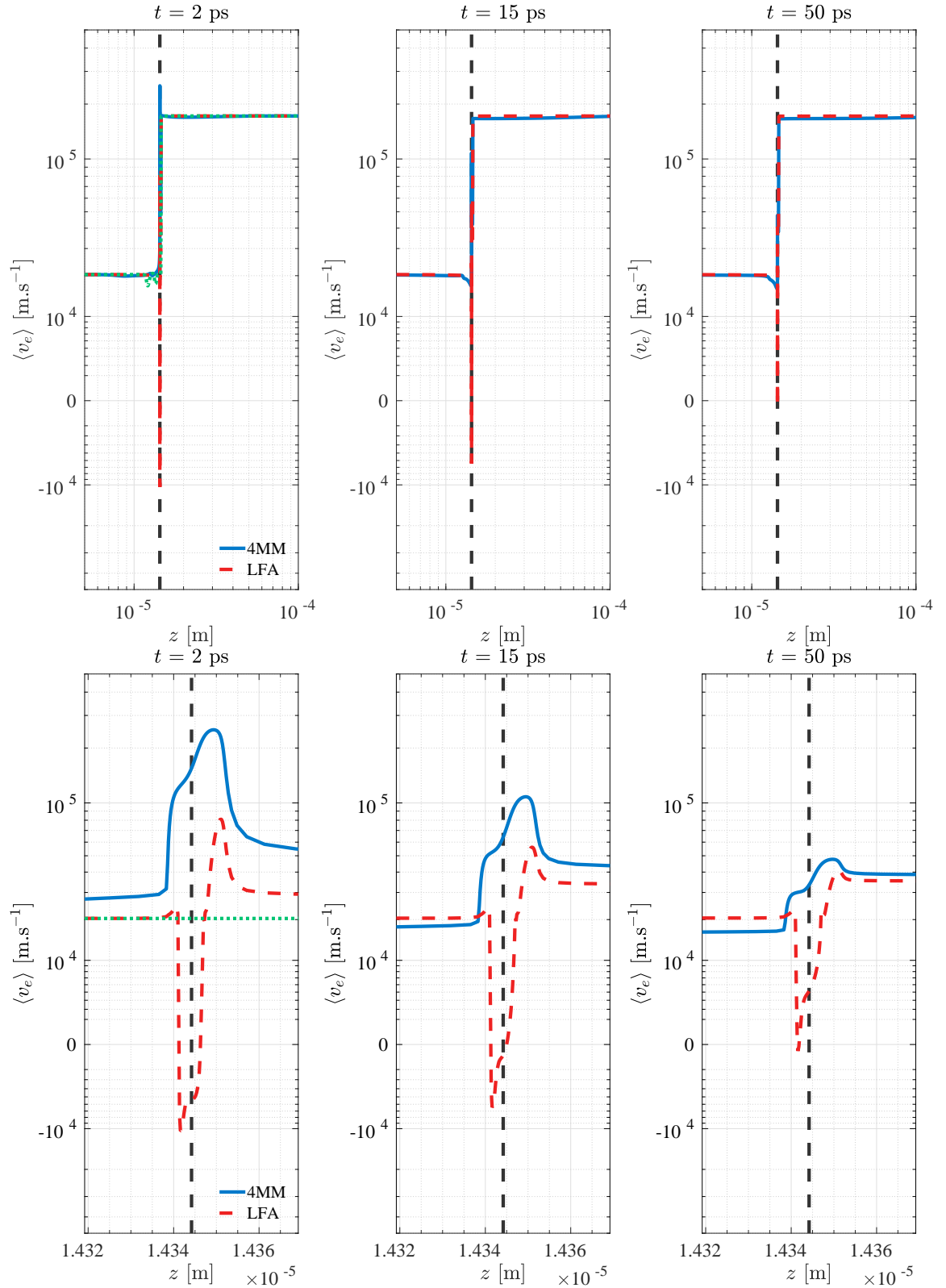


Figure 4.8: Average electron velocity for 4MM and LFA models at short, intermediate, and longer times as the electron swarm propagates from liquid to gaseous argon. Top view: Macroscopic results. Bottom view: Expanded view of interfacial results. Initial condition given by green dotted green line. Direction of field-driven propagation is from left to right.

The top half of Figure 4.8 also demonstrates a short, but persistent, relaxation length on the liquid side of the interface well before the interface is encountered. It is believed this gradual decrease in electron average velocity prior to the interface is a further demonstration of spatial non-locality being predicted by the mean energy dependent model, which the LFA model simply cannot predict owing to its reliance on the instantaneous electric field, shown in Figure 4.9. From Figure 4.9 it is difficult to see a significant variation in the total  $E/n_0$  over the lifetime of this transient simulation; this is a result of the space charge effects being small compared to the applied field, as indicated in the figure where the isolated contributions of space-charge effects are plotted.

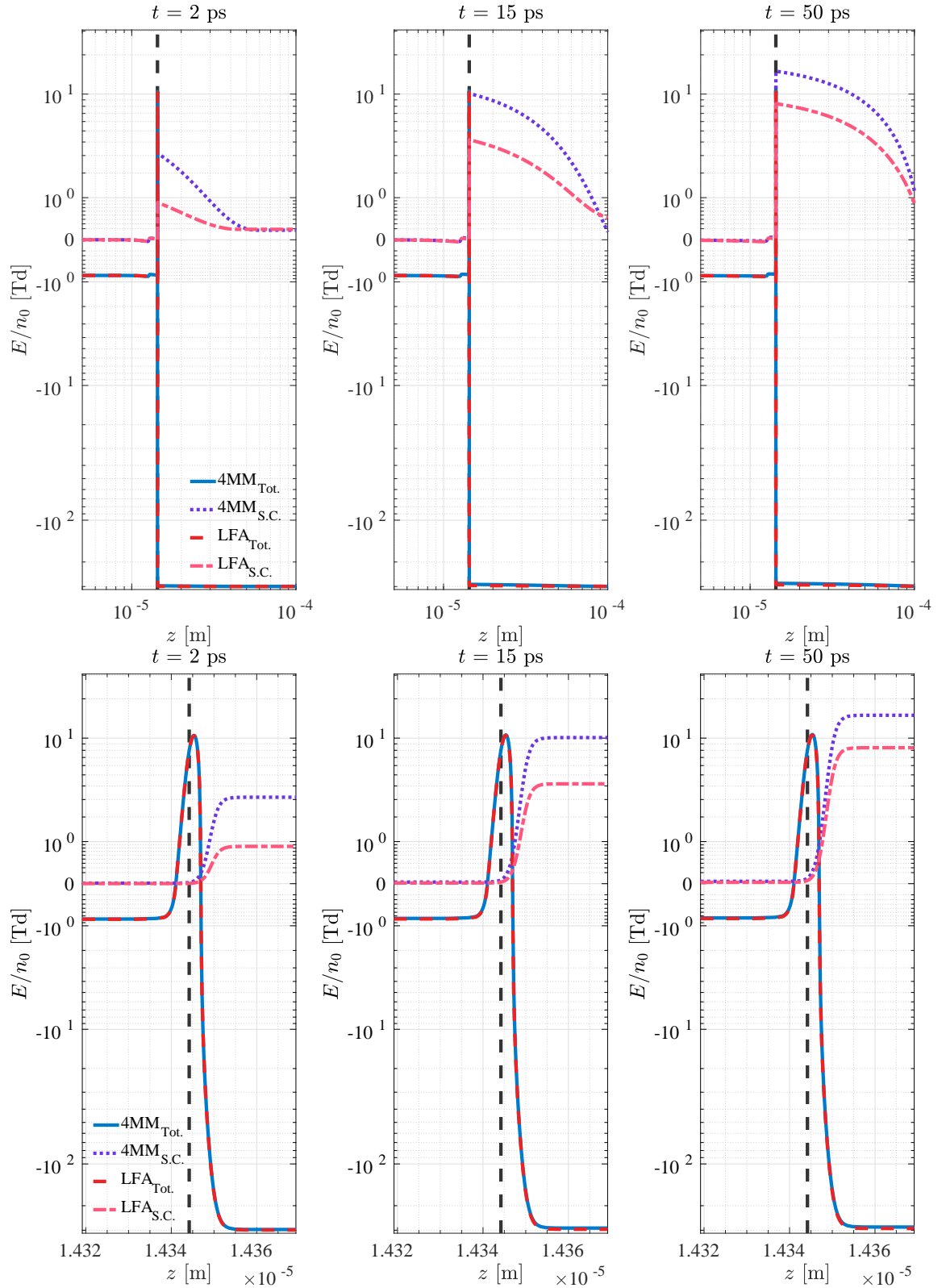


Figure 4.9: Total  $E/n_0$  and space-charge (S.C.) contribution to  $E/n_0$  for 4MM and LFA models at short, intermediate, and longer times as the electron swarm propagates from liquid to gaseous argon. Top view: Macroscopic results. Bottom view: Expanded view of interfacial results.

Figure 4.10 demonstrates the electron mean energy of the 4MM model to assist

in interpreting the results of the preceding figures. It is clear that there is a gradual relaxation of  $\langle \epsilon \rangle$  on the liquid side of the interface, consistent with the observed non-local effects on electron transport in Figure 4.8. Far from the interface the mean energy relaxes to the equilibrium value given by the value of  $E/n_0$  in the gas or liquid. One should note a clear minimum in mean energy is observed at short times in the expanded interface region of Figure 4.10 due to the relatively high transient electron flux combining with the blocking field provided by the  $V_0$  potential through the  $\Gamma \cdot E$  term in the energy balance equation (4.9). This energy reduction immediately at the interface is only present at short times because of the large initial diffusive electron flux. As this large initial diffusive flux subsides over time, the energy loss via the  $\Gamma \cdot E$  term becomes less significant, demonstrated at 15 and 50 ps.

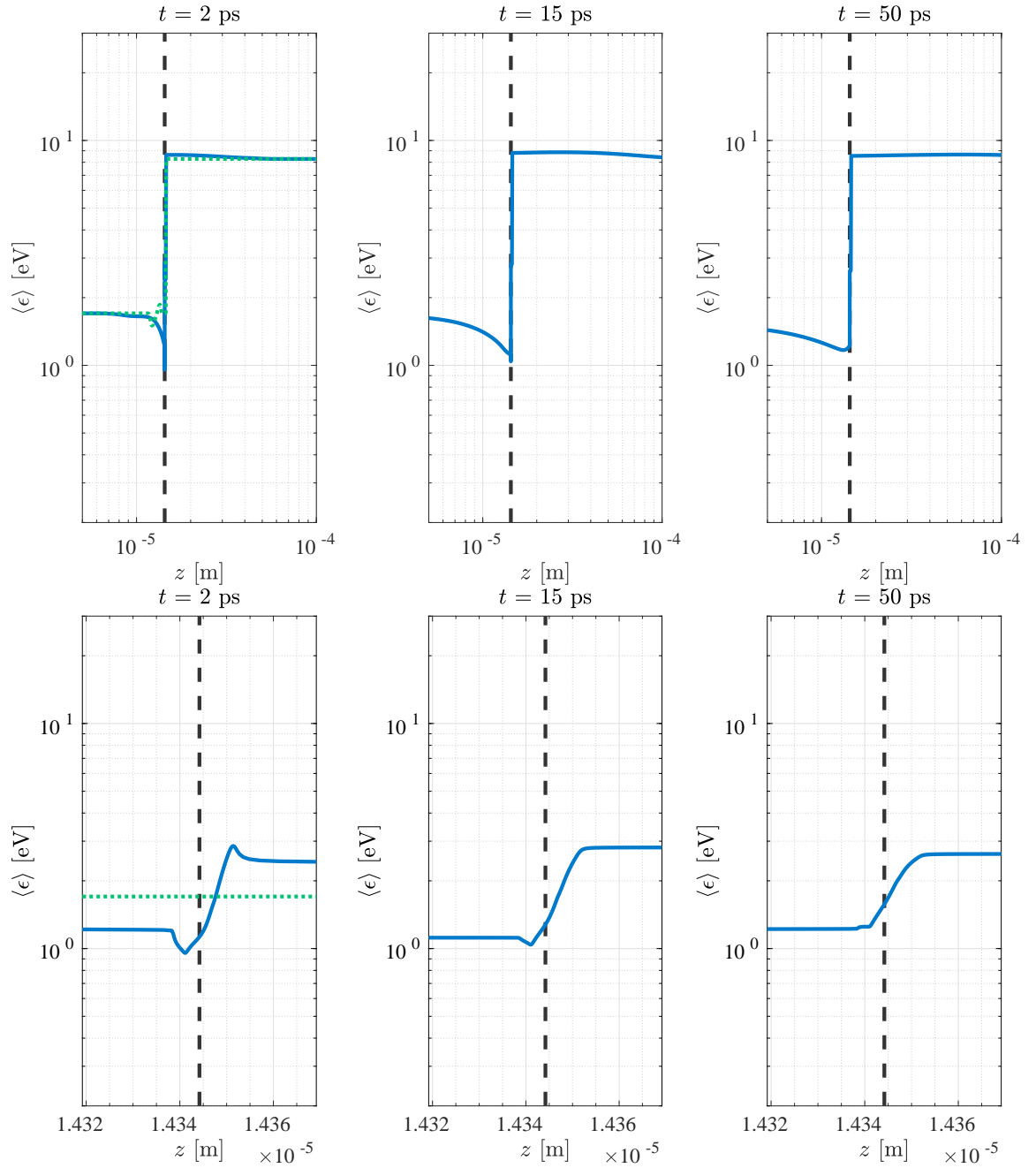


Figure 4.10: Electron mean energy for 4MM model at short, intermediate, and longer times as the electron swarm propagates from liquid to gaseous argon. Top view: Macroscopic results. Bottom view: Expanded view of interfacial results. Initial condition given by green dotted line. Direction of field-driven propagation is from left to right.

#### 4.5.3 Electron ionisation front transport from gaseous argon into liquid argon

This Section now presents and discusses results of directing an electron streamer front in gaseous argon into liquid argon. This simulation was performed under the same conditions as the previous section, apart from simply reversing the sign of the applied electric field to yield a total reduced electric field configuration as shown in Figure 4.6.

The initial condition to this simulation was provided by allowing a streamer front to form in gaseous argon.

Examining the evolution of the electron density in Figure 4.11, one sees that the initial electron density of the streamer tip is transported across the interface with a notable attenuation of the electron density further into the liquid. At all times the LFA model predicts a larger charge-build up at the gas side of the interface compared to the 4MM model, consistent with the noticeably lower speed at the interface arising from the combination of the increase in  $n_0$  at the interface as well as space-charge screening effects on  $E/n_0$  observable in both Figure 4.12 and 4.13 respectively.

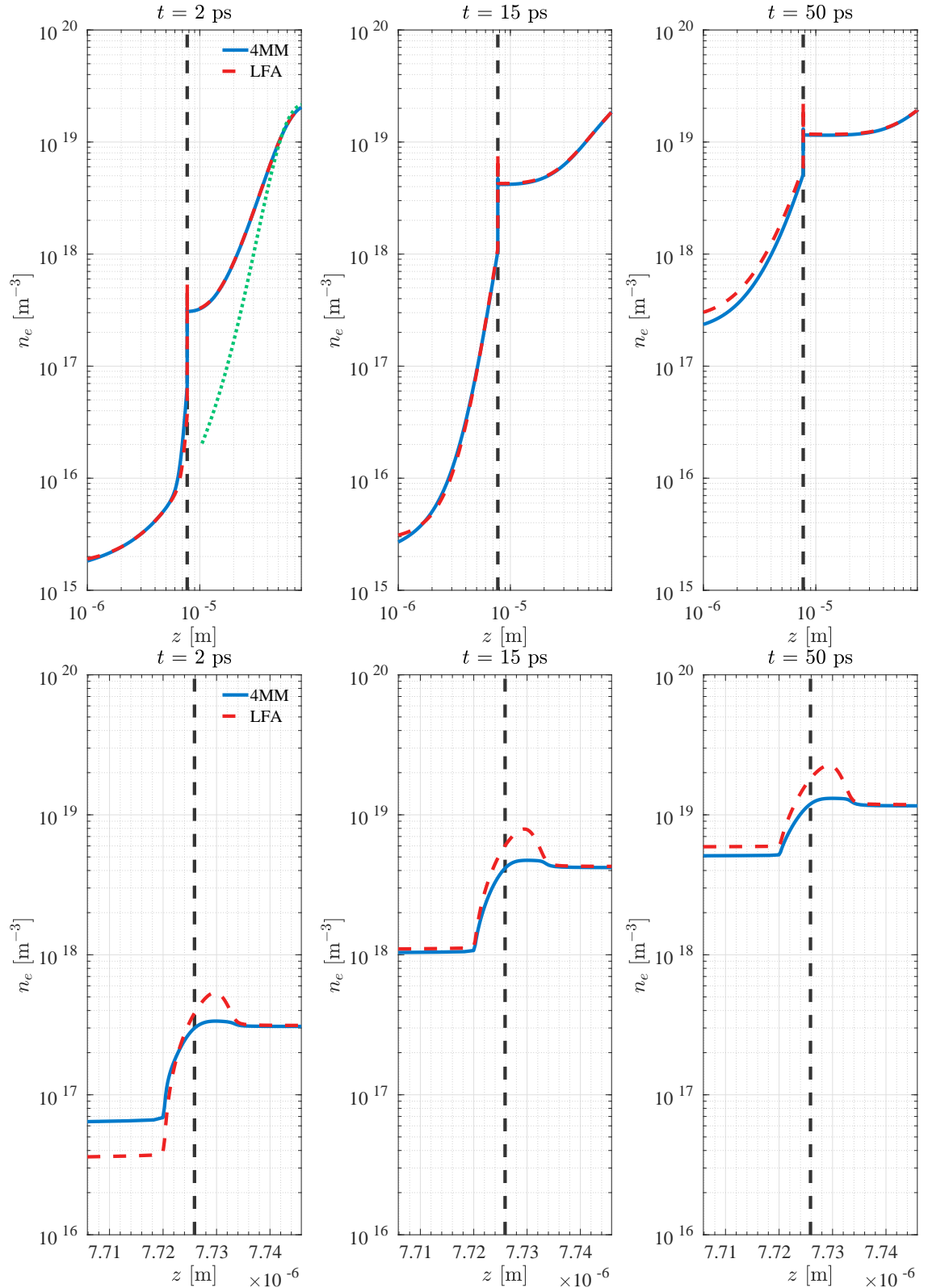


Figure 4.11: Electron density evolution for 4MM and LFA models at short, intermediate, and longer times as the electron streamer tip propagates from gaseous to liquid argon. Top view: Macroscopic results. Bottom view: Expanded view of interfacial results. Initial condition given by green dotted green line. Direction of field-driven propagation is from right to left.

At longer times, the trailing electrons behind the initial streamer tip can be seen to build-up on the gas side of the interface, while increased densities of electrons continue to be transported through the liquid. Interestingly, at earlier times the 4MM model predicts higher electron densities in the liquid but later at longer times the LFA model predicts higher electron densities. This observation can be reconciled by comparing the electron average velocity of Figure 4.12, where the 4MM average electron velocity on the liquid side of the transition reaches a lower value than the LFA result. Once again a clear spatial relaxation to the equilibrium drift velocity value is observed in liquid argon for the 4MM model, which demonstrates the presence of spatial non-locality. By experiencing lower speeds just after the interface transition, 4MM results predict smaller values of  $n_e$  in liquid at later times compared to the LFA model, which responds directly to the instantaneous value of  $E/n_0$ .

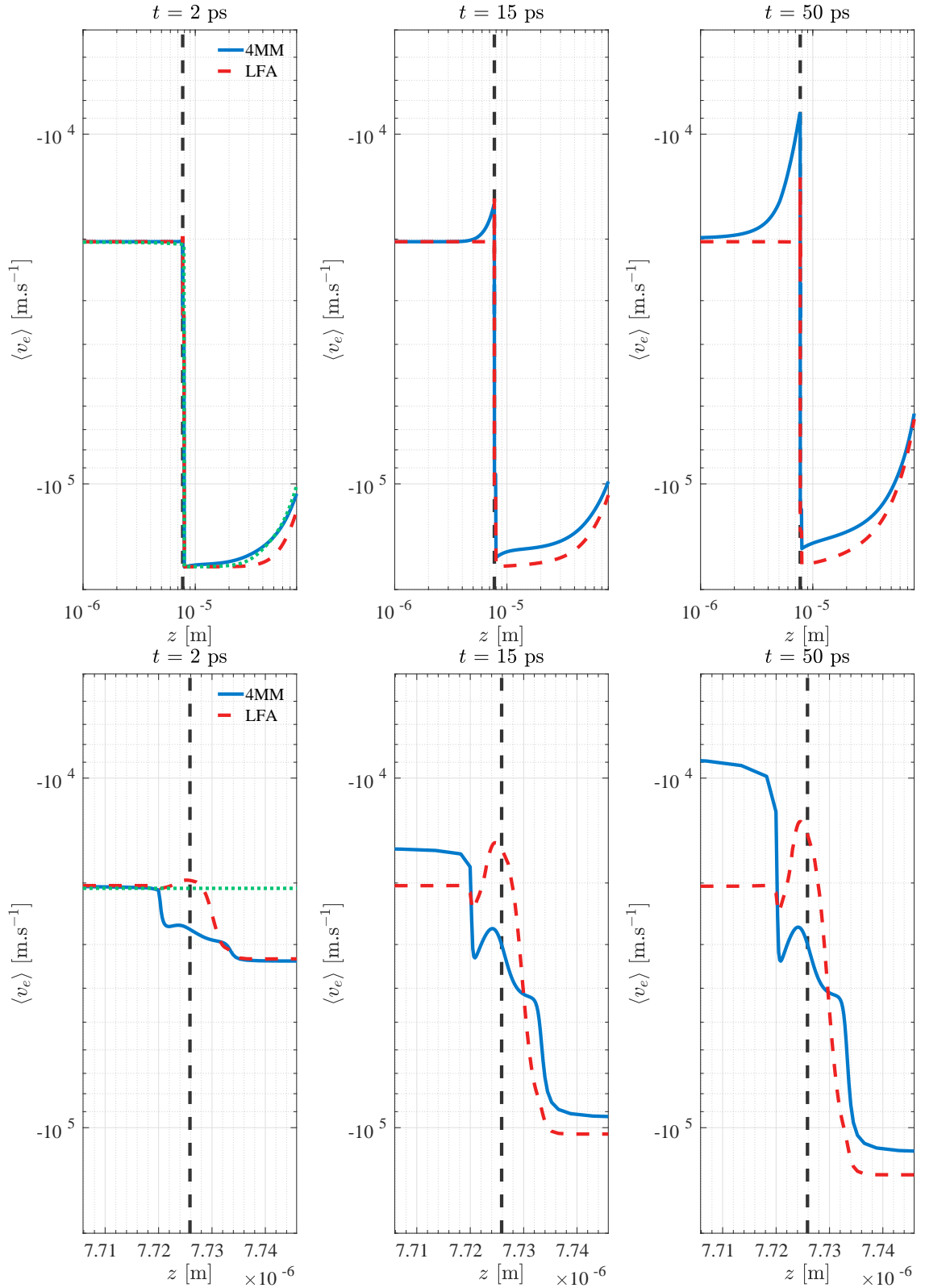


Figure 4.12: Average electron velocity for 4MM and LFA models at short, intermediate, and longer times as the electron streamer tip propagates from gaseous to liquid argon. Top view: Macroscopic results. Bottom view: Expanded view of interfacial results. Initial condition given by green dotted green line. Direction of field-driven propagation is from right to left.

In Figure 4.13 the explicit space-charge screening field is presented, alongside the total field. It is the only time-varying contribution to the field, but has a small magnitude compared to the fields presented in Figure 4.6, making its effect on the total field difficult to see at these time scales. At longer time scales however, further ion creation would occur and screening will begin to dominate the total reduced field experienced by electrons.

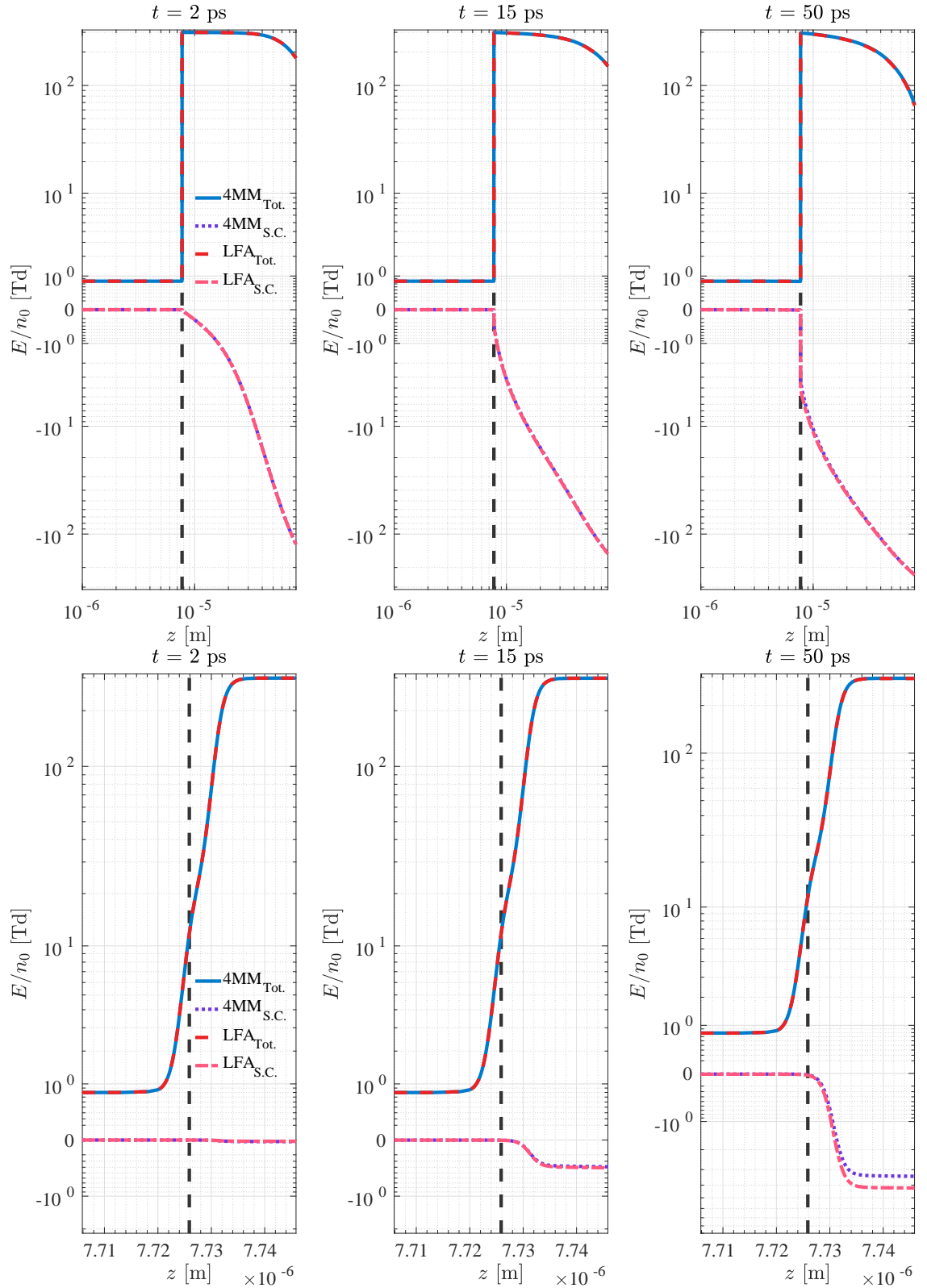


Figure 4.13: Total  $E/n_0$  and space-charge (S.C.) contribution to  $E/n_0$  for 4MM and LFA models at short, intermediate, and longer times as the electron streamer tip propagates from gaseous to liquid argon. Top view: Macroscopic results. Bottom view: Expanded view of interfacial results.

Finally, to assist further in interpreting the 4MM results, it is valuable to consider

the electron mean energy in Figure 4.14. On the gas side of the interface one sees the mean energy gradually decay; as the high energy streamer tip makes its way through the interface to the liquid argon, leaving the lower energy electrons at the rear of the propagating streamer. On the liquid side of the interface, the mean energy gradually rises before decaying to the equilibrium value, due to the high energy incoming electrons entering from the gas. Once again the clear relaxation length has formed in the liquid argon. It is instructive to note that in the expanded interfacial region of Figure 4.14 the reduction in mean energy on the gas side, due to increasing collisional energy losses from an increasing  $n_0$ , experiences a slight increase over the interface due to the restorative effects of the  $V_0$  field via the  $\Gamma \cdot E$  term in the energy balance equation (4.9).

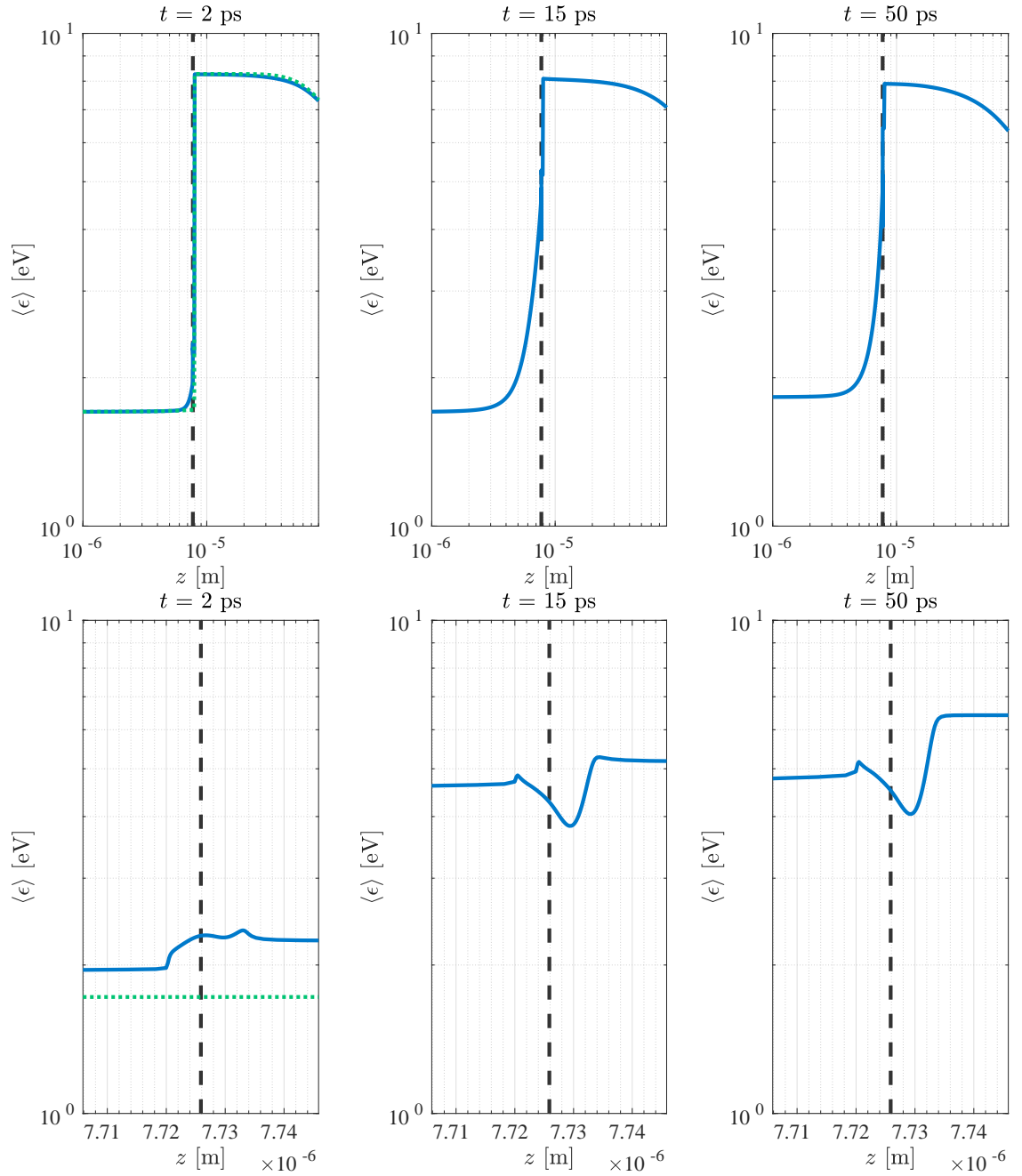


Figure 4.14: Electron mean energy for 4MM model at short, intermediate, and longer times as the electron streamer tip propagates from gaseous to liquid argon. Top view: Macroscopic results. Bottom view: Expanded view of interfacial results. Initial condition given by green dotted green line. Direction of field-driven propagation is from right to left.

#### 4.5.4 Impact of step function input data

To determine if using a tanh function to modulate  $n_0$  at the interface, which necessarily requires the density dependent fluid model input data, between gas and liquid extrema is actually required over just a standard step function variation in the density, simulations were repeated using a step-function between liquid on the left and gas on the right.

From Figure 4.15, one sees that by assuming a step-function for the LFA model the electron densities are much higher at all times over the macroscopic length scale. Approximately twice as many electrons are transported into the liquid as compared with any of the previous results. At the narrow length scale of the interface, the step-function LFA result actually decreases prior to the interface before experiencing a sharp build up of electrons on the liquid side; this is a starkly different qualitatively result compared to any of the previous results obtained using the smooth tanh function. On the other hand, while the step-function 4MM results are not equal to those achieved through the tanh assumption, they are very similar and produce no notable deviations compared to the LFA results.

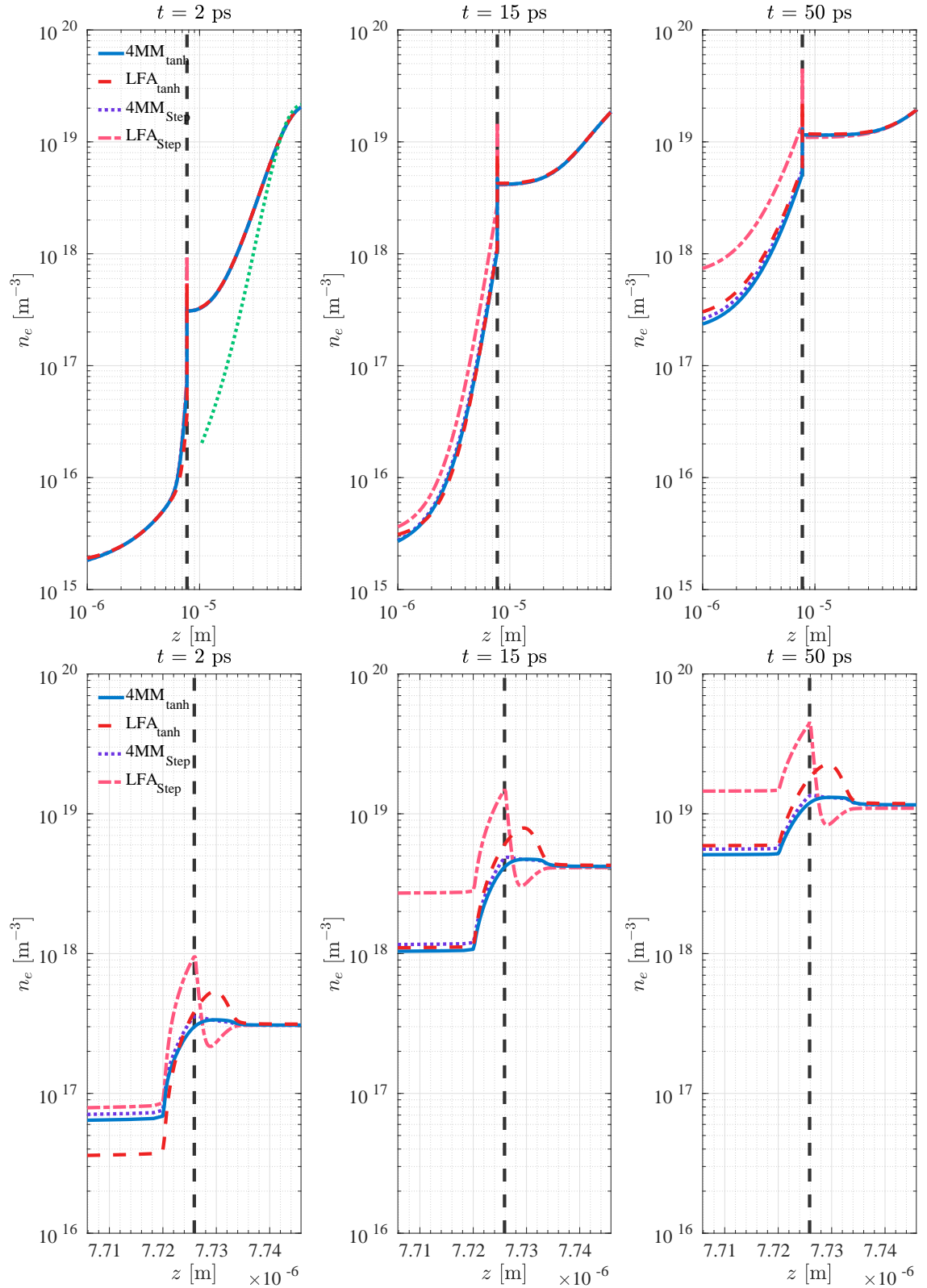


Figure 4.15: Effects of tanh or step-function interface on electron density evolution for 4MM and LFA models at short, intermediate, and longer times as the electron streamer tip propagates from gaseous to liquid argon. Top view: Macroscopic results. Bottom view: Expanded view of interfacial results. Initial condition given by green dotted green line. Direction of field-driven propagation is from right to left.

The step-function LFA electron density differences are consistent with a very high average velocity at the interface, demonstrated in Figure 4.16, compared to any of the previous simulation results. This order of magnitude difference in the average velocity transports electrons into the liquid at a considerably higher rate compared to the results using the tanh interface assumption. This high average velocity occurs due to a large  $E/n_0$ , produced due to the small, gaseous argon value of  $n_0$  assumed near the interface instead of a gradually increasing value. Once again, compared to the distinctly different observations of the LFA models there is no major deviation between 4MM results, with the only noticeable difference being the discontinuity immediately at the interface.

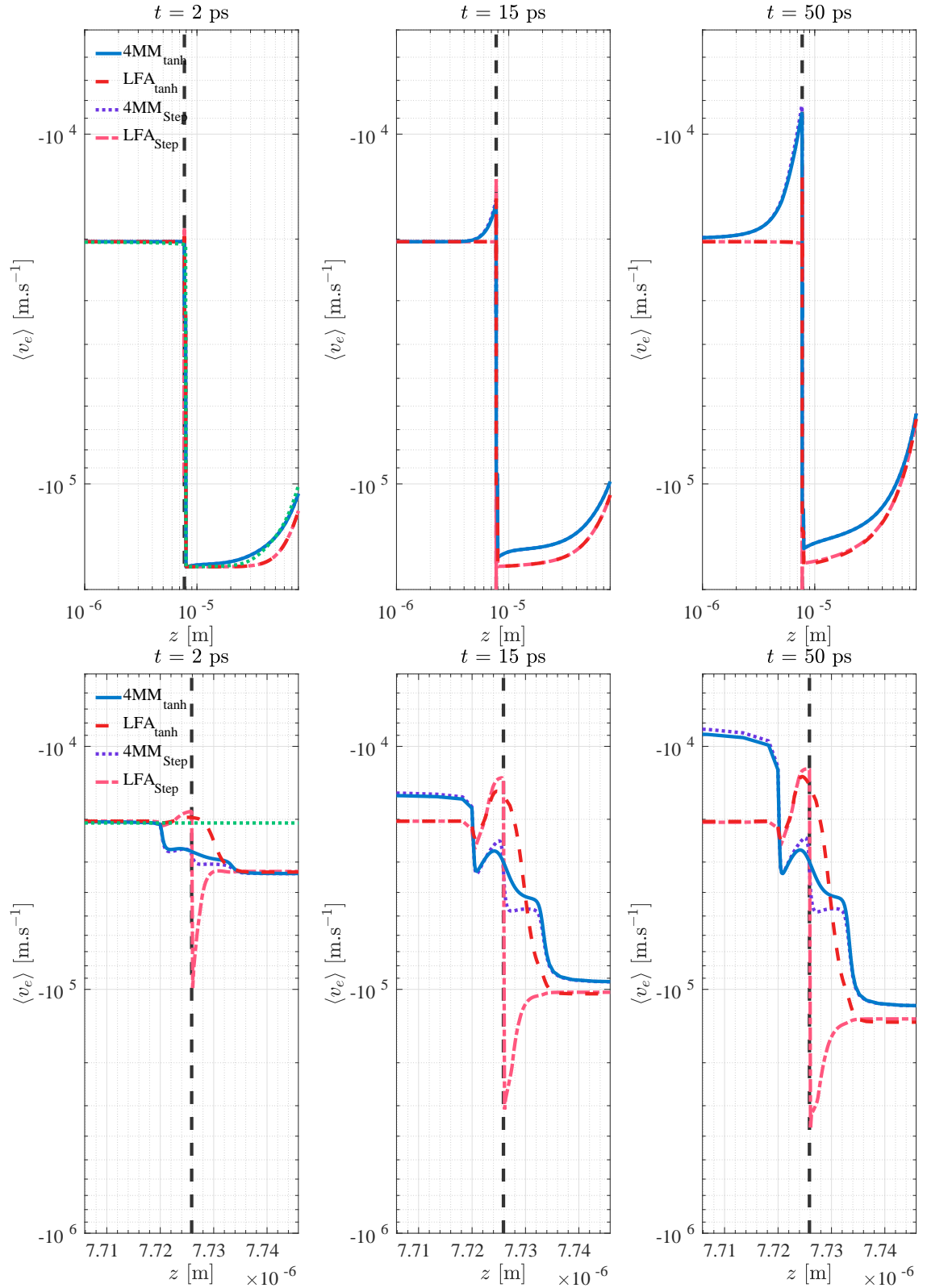


Figure 4.16: Effects of tanh or step-function interface on average electron velocity for 4MM and LFA models at short, intermediate, and longer times as the electron streamer tip propagates from gaseous to liquid argon. Top view: Macroscopic results. Bottom view: Expanded view of interfacial results. Initial condition given by green dotted green line. Direction of field-driven propagation is from right to left.

For completeness, Figure 4.17 shows the electron mean energy for the 4MM models using both tanh and step-function assumptions. No major differences in  $\langle \epsilon \rangle$  are observed for the two results, indicating why differences between 4MM results were quite negligible in Figures 4.15 and 4.16. Since  $\langle \epsilon \rangle$  is observably insensitive to the form of interface assumptions, and demonstrably a continuous variable, it is believed that it is a much more reliable variable to use when determining input data compared to  $E/n_0$  which suffers from being explicitly related to the assumptions imposed on  $n_0$ .

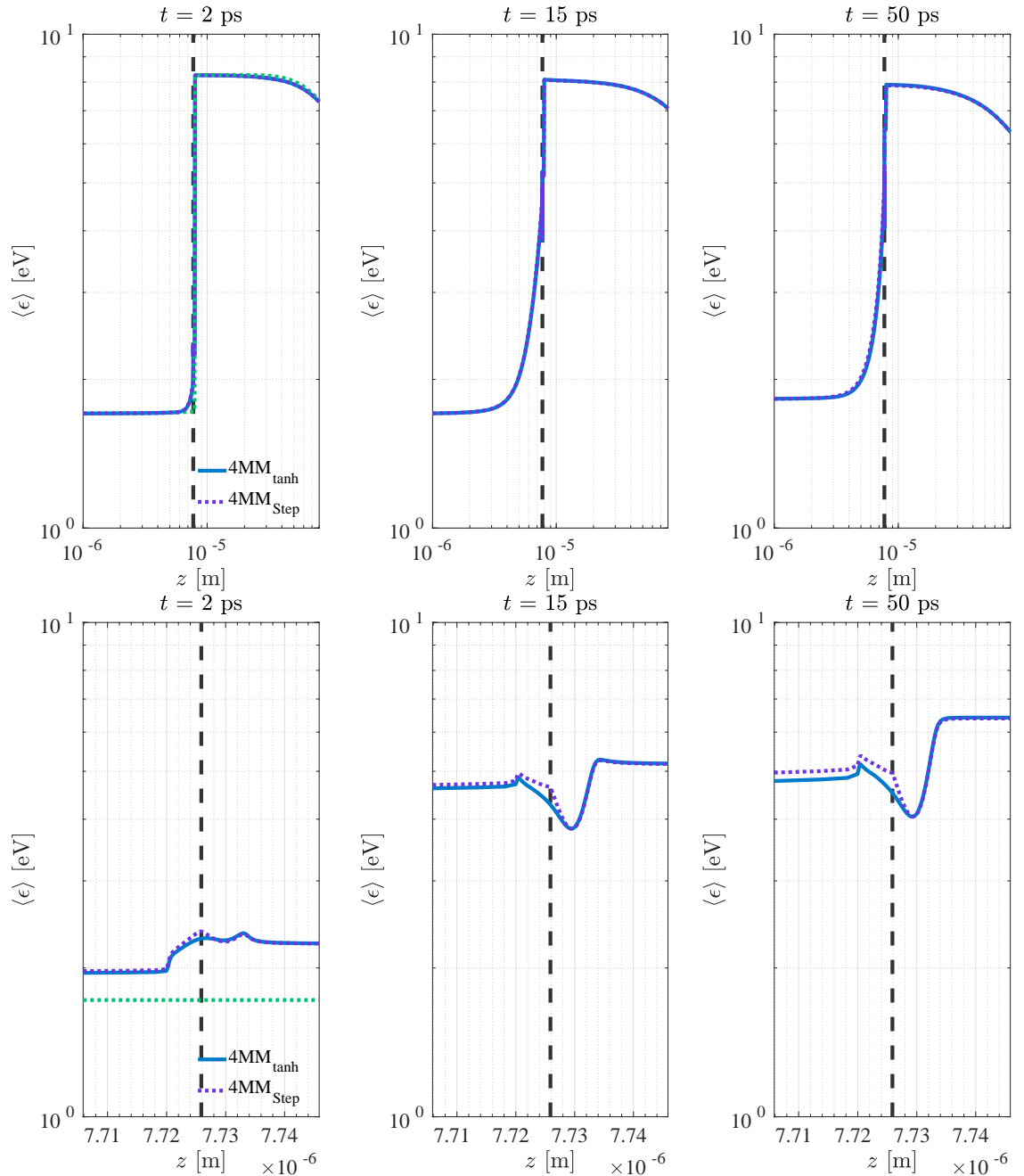


Figure 4.17: Effects of tanh or step-function interface on electron mean energy for 4MM model at short, intermediate, and longer times as the electron streamer tip propagates from gaseous to liquid argon. Top view: Macroscopic results. Bottom view: Expanded view of interfacial results. Initial condition given by green dotted green line. Direction of field-driven propagation is from right to left.

## 4.5.5 Use of gas phase data to simulate liquid transport

As discussed previously in this study, there are major differences between gas phase and liquid phase electron transport. To adequately model electron transport in liquids, one should use input data derived with liquid state modifications, instead of simply using density-scaled gas phase data. To demonstrate the disparity caused by using density-scaled gas phase data over liquid phase data, this Section presents (i) a propagating streamer simulation in homogeneous liquid argon, and (ii) a repeat of the interfacial simulation presented in Section 4.5.2.

In Figure 4.18 the three fluid models used in this study predict varying stages of streamer formation and then propagation in liquid argon. As streamer simulations in *homogeneous* media are not the explicit focus of this study, further results and discussion on liquid streamer modeling are deferred to an upcoming study, conducted in parallel to this work, which will extend on previous liquid streamer modeling foundations [173, 174]. In these simulations an initial narrow Gaussian pulse of electron/ion pairs is created by an initial ionisation event. The simulation then follows the transport of these electrons, and creation of ions, over time until the formation of a propagating streamer front is obtained. It is very clear that by the time streamer fronts predicted by 4MM and LFA models have formed, and subsequently propagated through the liquid, the LFAG model prediction is still in the infancy of formation.

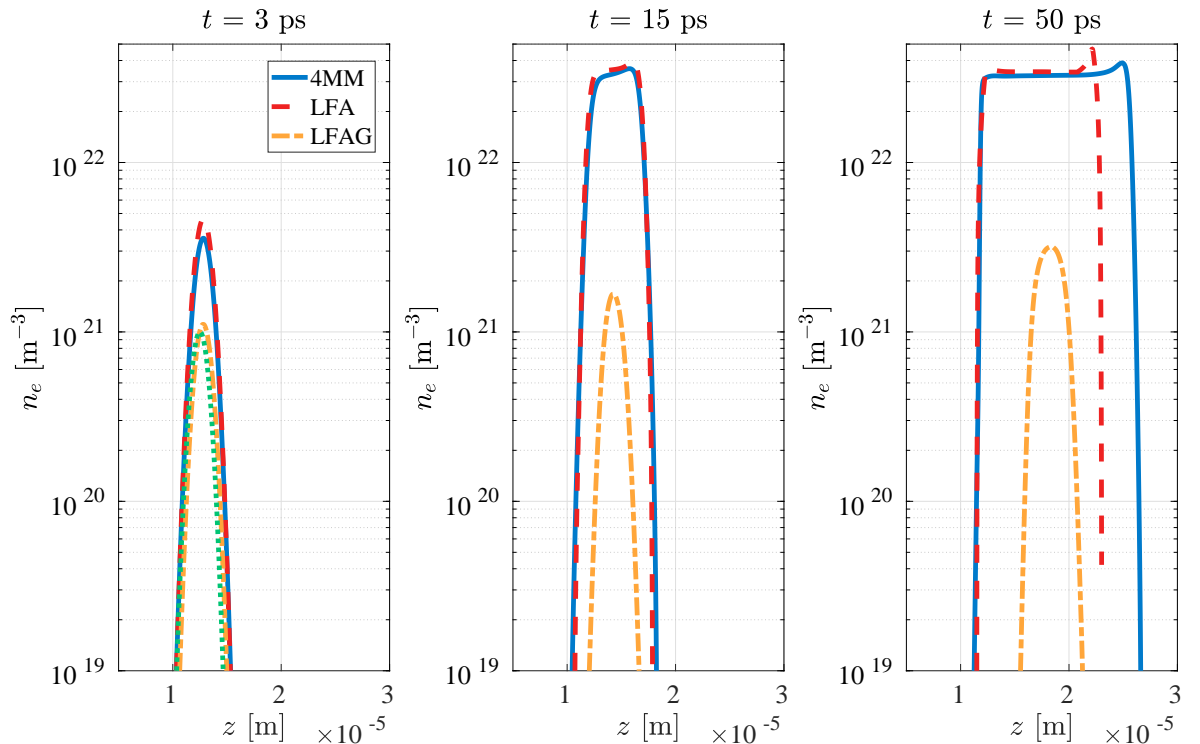


Figure 4.18: Electron propagation of electrons in a streamer front within liquid argon. Green dotted series denotes the initial condition. Evolution over time denotes major differences when using liquid data, compared to simply scaling gas phase data.

Electron number density and average velocity results of the LFAG model, applied to the electron swarm propagating from liquid argon to gaseous argon, are shown in

Figures 4.19 and 4.20 alongside the previously discussed results of Section 4.5.2. At all time samples, the LFAG model predicts fewer electrons extracted into the argon vapor compared to both 4MM and LFA models. This observation is consistent with the fact that at a given  $E/n_0$  the electron drift velocity is higher in liquid argon than gas, enhancing electron extraction when accurate liquid phase data is used.

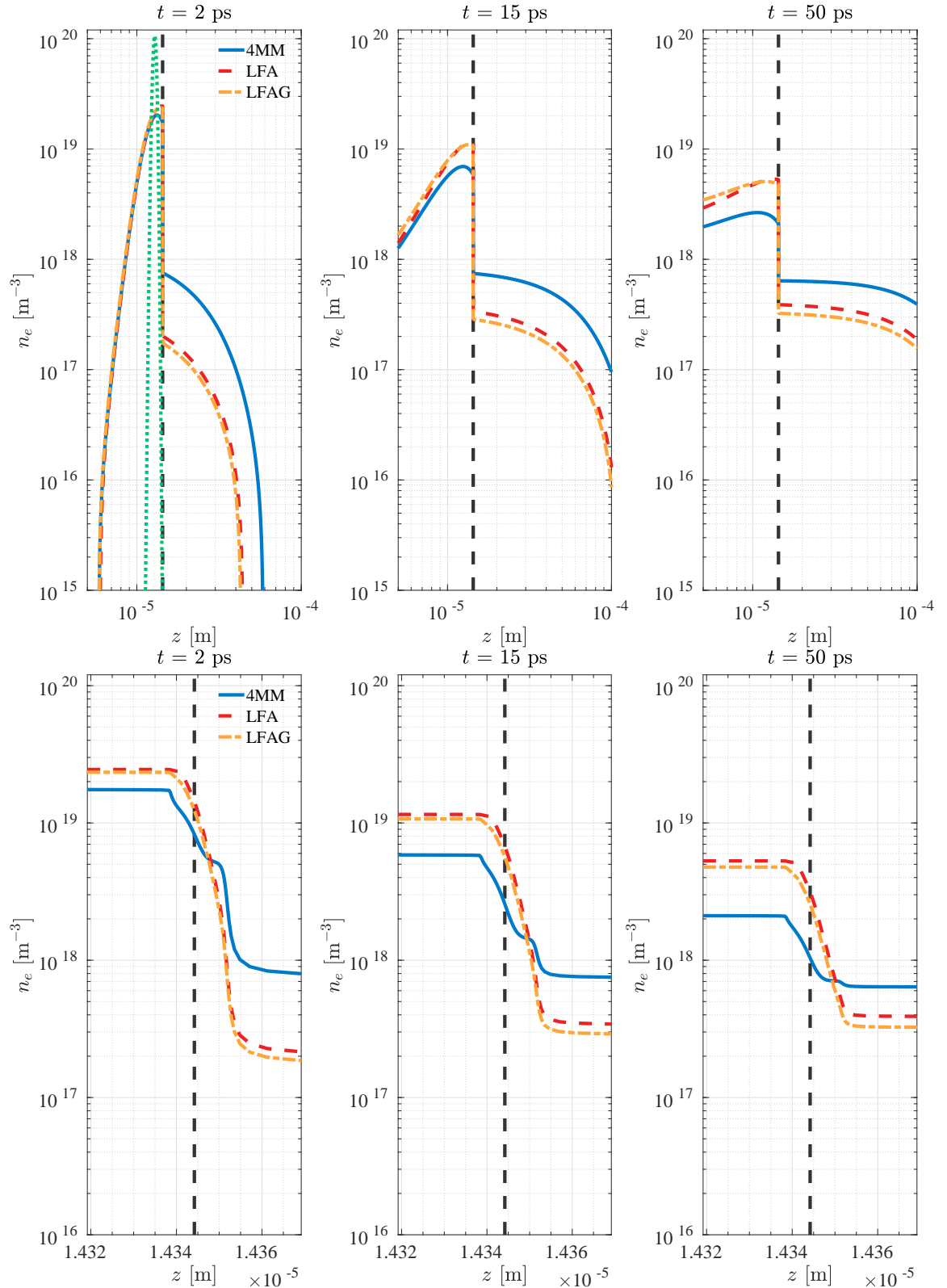


Figure 4.19: Electron density evolution for 4MM, LFA, and LFAG models at short, intermediate, and longer times as the electron swarm propagates from liquid to gaseous argon. Top view: Macroscopic results. Bottom view: Expanded view of interfacial results. Initial condition given by green dotted green line. Direction of field-driven propagation is from left to right.

In Figure 4.20 one can clearly see deviations from using gas phase data to predict average electron velocities in the LFAG model, compared to previous results. As time increases, the LFAG average velocity relaxes from the initial velocity, from liquid phase data, to the gas phase equilibrium drift velocity corresponding to  $E/n_0 = 0.8$  Td. Similarly, in the expanded interfacial plot the average velocity follows the general trend of the LFA result, by following the instantaneous electric field, however with consistently slower speeds predicted. These disparities in electron average velocity predictions, which are consistent with the electron density observations in Figure 4.19, demonstrate that care must be taken when choosing input data; gas phase data may be readily available to the community, and is a tempting choice, but for reliable, and physically grounded, predictions accurate liquid phase data must be incorporated into the model.

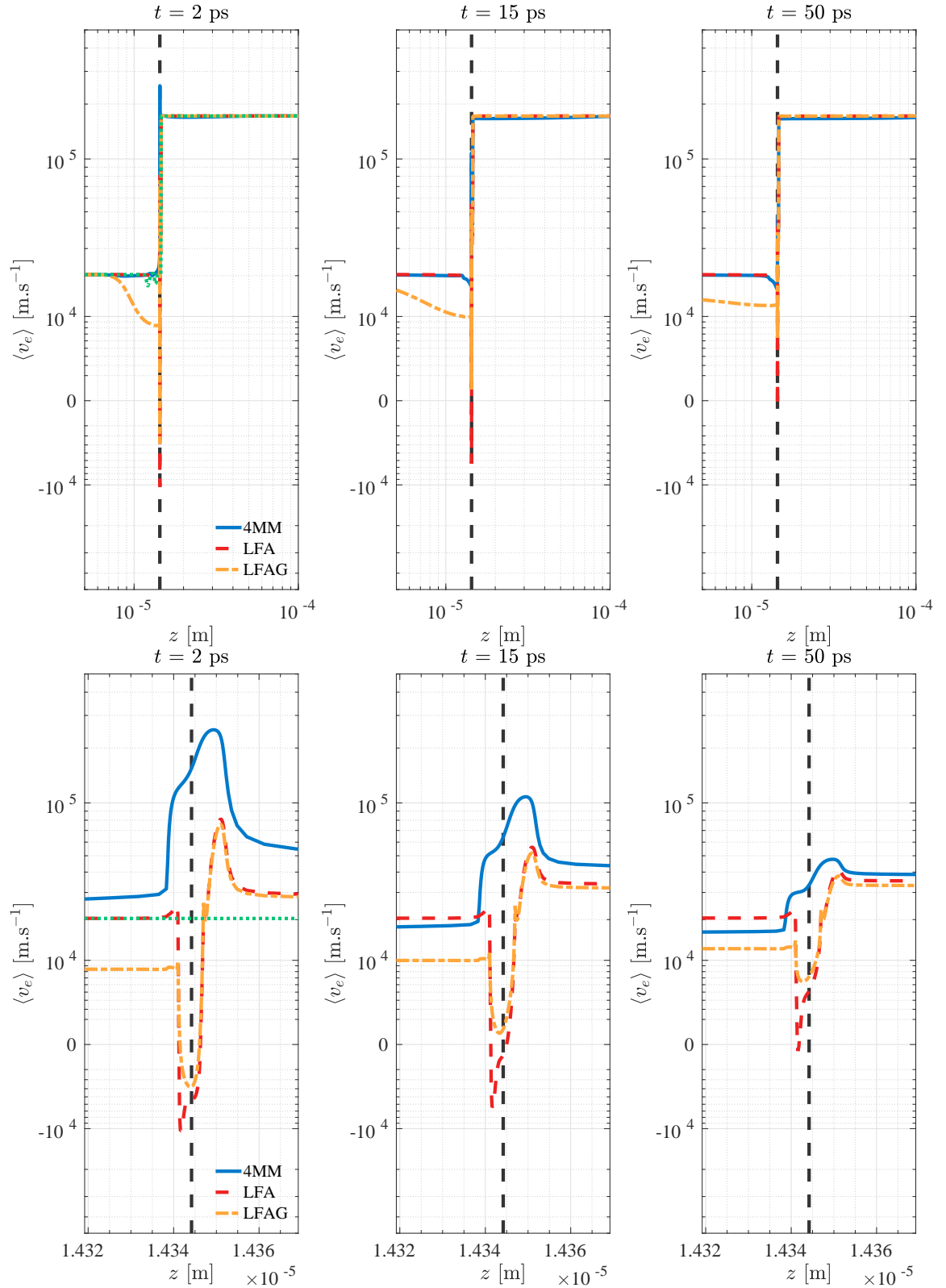


Figure 4.20: Average electron velocity for 4MM, LFA, and LFAG models at short, intermediate, and longer times as the electron swarm propagates from liquid to gaseous argon. Top view: Macroscopic results. Bottom view: Expanded view of interfacial results. Initial condition given by green dotted green line. Direction of field-driven propagation is from left to right.

---

## 4.6 Chapter Summary

---

This Chapter has presented results from multiple fluid models simulating (i) an electron swarm propagating from liquid argon into gaseous argon over an equilibrium interface density variation, and (ii) an electron streamer front being driven out of gaseous argon across the interface into liquid argon. The Chapter presented a method to account for large density variation from gas to liquid phase by assuming both a realistic density profile and step-function variation of  $n_0$  in order to implement approximation rules for density dependent input transport data between gas and liquid extremes. Furthermore, this work has accommodated interfacial effects of the spatial variation of both the dielectric constant,  $\epsilon_r$ , through solution of Poisson's equation, and binding energy of an electron in liquid,  $V_0$ , through an effective applied electric field.

Using the proposed methods to compare local (LFA) and non-local transport (4MM) models and their sensitivities, the key recommendation of this Chapter, to best describe electron transport between gas and liquid densities, is to adopt a mean energy dependent higher order fluid model, such as the 4MM method used in this study. This model demonstrated greater flexibility and reliability in resolving non-local physics and interfacial electron transport compared to the local field drift-diffusion model. It was demonstrated that a drift-diffusion continuity equation (LFA) model required careful treatment of input data between gas and liquid extremes by way of approximating field dependent input data for intermediate densities using a tanh function, whereas the non-local 4MM model was relatively insensitive to the functional form of  $n_0$  variation.

In summary, this work has presented the findings of a preliminary modeling study of electron transport across cryogenic argon gas-liquid interfaces. This Chapter demonstrated the importance of modifying gaseous electron transport models to account for interfacial and liquid effects when considering transport at the gas-liquid interface. A key result of this study is that vastly different electron transport is produced if gas phase input data is simply scaled to liquid densities, compared to using accurate liquid phase data. While this study has focused on a simple atomic liquid-gas system, it is hoped that this work will stimulate further modeling and experimental efforts to benchmark and refine the work presented. By expanding on the work of this study, extensions to complex interfacial systems, like those found in plasma medicine, can eventually be made to better understand important plasma applications. Further physical processes that should be considered in interfacial modeling may include electron solvation processes in polar liquids [140,184], and condensed phase evaporation [180].

With this Chapter having demonstrated that the proposed modeling framework can be applied to electron transport at a relatively simple argon gas-liquid interface, the final Chapter of this thesis will now seek to extend the modeling approach to a biologically relevant medium, tetrahydrofuran (THF). Assembly of a complete cross section set for electron-THF interactions will be discussed, and calculated electron transport data for gaseous THF will be presented. Application of vital liquid phase modifications, such as coherent scattering and modification of the ionisation potential,

will be demonstrated in the final Chapter to modify the assembled gas phase electron transport data for THF to simulate streamer formation and propagation in liquid THF.

## Chapter Appendix: Input data at densities intermediate to the gas and liquid phases

In order to accommodate  $n_0(z)$  variation of input data, this Chapter has implemented an approximation method recently proposed, and benchmarked for simple atomic liquids, by Garland *et al.* [3] that seeks to approximate input transport data and collision rates as weighted combinations of the gas and liquid extreme values. This process is analogous to Blanc's Law [157], or the energy-dependent approach proposed by Chiflikian [159], used for approximating transport data in gas mixtures, where instead one now seeks to describe transport at intermediate densities between two density extremes of one substance instead of mixing two distinct gases. Where necessary to account for the differences in momentum transfer for gas and liquid systems, non-linear weightings of gas and liquid extreme data are combined [3]. Using a zeroth order momentum transfer theory (MTT) approximation [3, 76, 161], the non-linear dependence is extracted via the angle-integrated structure factor evaluated at a given electron mean energy,  $\langle \varepsilon \rangle$ , and at a neutral atom density

$$s(\langle \varepsilon \rangle, n_0) = \frac{1}{2} \int_0^\pi S\left(\frac{2}{\hbar} \sqrt{2m_e \langle \varepsilon \rangle} \sin \frac{\chi}{2}, n_0\right) [1 - \cos \chi] d\chi, \quad (4.18)$$

where, for this work, the static structure factor,  $S\left(\frac{2}{\hbar} \sqrt{2m_e \langle \varepsilon \rangle} \sin \frac{\chi}{2}, n_0\right)$ , is assumed to be the analytic Verlet-Weis corrected Percus-Yevick structure factor [83] which has been demonstrated to be a good approximation of atomic liquid structure [12, 15, 57, 65]. The full analytic expression is included in a preceding study [3]. When considering largely localized energy transfer due to inelastic excitations, one may use simpler linear combinations of gas and liquid extrema data as this was demonstrated to provide a sufficient first-order approximation to the intermediate density's transport data because explicit modifications to the energy balance equation (4.9) aren't required [3, 48].

### Local field dependent input data

For the LFA model the drift velocity at intermediate densities,  $W_{\text{int}}$ , is approximated as function of reduced field,  $\frac{E}{n_0}$ . A weighted sum of reciprocals of gas,  $W_g$ , and liquid,  $W_l$ , extreme values was used

$$\frac{1}{W_{\text{int}}\left(\frac{E}{n_0}\right)} = x_g s_{\text{int}}\left(\frac{E}{n_0}\right) \frac{1}{W_g\left(\frac{E}{n_0}\right)} + x_l \frac{s_{\text{int}}\left(\frac{E}{n_0}\right)}{s_l\left(\frac{E}{n_0}\right)} \frac{1}{W_l\left(\frac{E}{n_0}\right)}, \quad (4.19)$$

where the density fractions,  $x_{g,l}$ , follow the relation

$$x_l = 1 - x_g. \quad (4.20)$$

These density fractions are determined by defining the intermediate density,  $n_{\text{int}}$ , as a sum of fractions of either density extrema

$$n_{\text{int}} = x_g n_g^{\text{eq}} + x_l n_l^{\text{eq}}, \quad (4.21)$$

and by combining (4.20) and (4.21) one finds

$$x_g = \frac{n_l^{\text{eq}} - n_{\text{int}}}{n_l^{\text{eq}} - n_g^{\text{eq}}}. \quad (4.22)$$

The approximated angle-integrated structure factor at any intermediate points is given by

$$s_{\text{int}} \approx w s_g + (1 - w) s_l, \quad (4.23)$$

where  $s_g$  is defined as unity for the gas,  $s_l$  for the liquid extreme is evaluated via (4.18), and to ensure the approximation is physically grounded in both the high and low energy limits, the weighting factor,  $w$ , is fixed in the low energy limit by

$$w = \frac{S_{\text{int}}(0, n_{\text{int}}) - S_l(0, n_l)}{S_g(0, n_g) - S_l(0, n_l)}, \quad (4.24)$$

where  $S(0, n)$  is the  $\Delta k \rightarrow 0$  limit of the analytic structure factor [83], or otherwise proportional to the fluid compressibility which is a measurable input.

Using (4.19) in conjunction with the accurate data of gas and liquid extremes described in Section 4.2.2, effectively generates a drift velocity surface, shown in Figure 4.21, which can be used to interpolate onto as a function of the instantaneous  $\frac{E}{n_0}$  and  $n_0$  given at each point in space during the simulation.

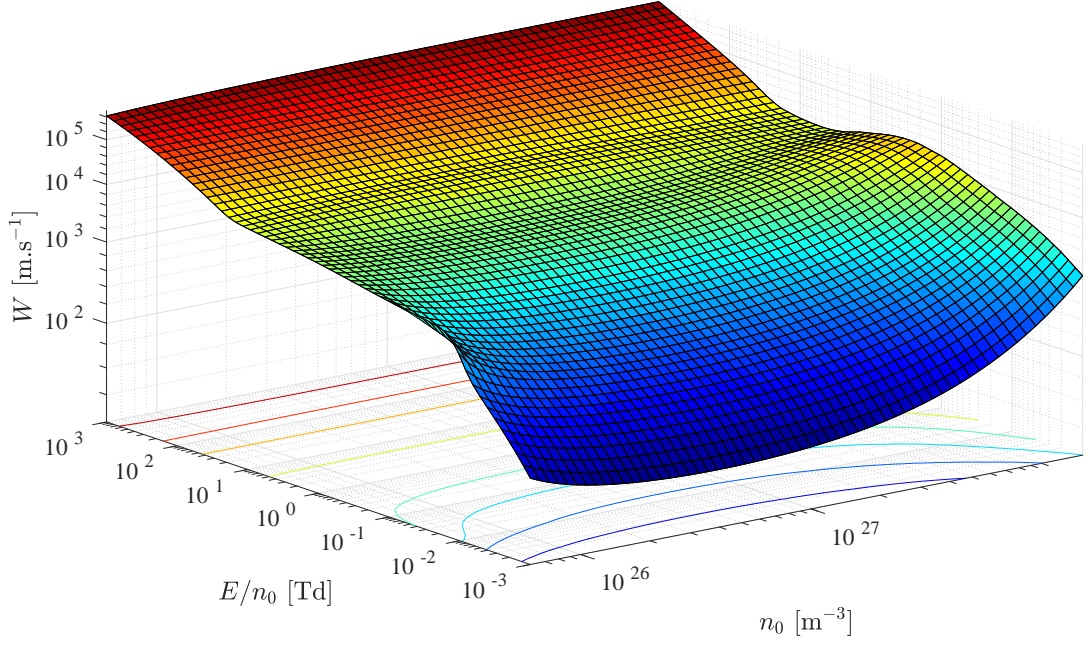


Figure 4.21: Drift velocity surface of electrons in argon as a function of  $\frac{E}{n_0}$  and  $n_0$  used to interpolate input data for LFA models.

The reduced longitudinal diffusion coefficient  $n_0 D_L$  was computed via a generalized Einstein relation (GER) [185] once the drift velocity was known via (4.19).

$$\frac{D_L^{\text{int}}}{\mu_{\text{int}}} = \frac{k_B T_0}{q} \left( 1 + (1 + \Delta_{\text{int}}) \frac{\partial \ln \mu_{\text{int}}}{\partial \ln E} \right), \quad (4.25)$$

where  $\mu_{\text{int}} = \frac{W_{\text{int}}}{E}$  is the electron mobility derived from the drift velocity (4.19),  $T_0$  is the neutral atom temperature, and the correction factor [185]

$$\Delta_{\text{int}} = \frac{\xi_{\text{int}}}{2k_B T_0 W_{\text{int}}}, \quad (4.26)$$

where  $\xi_{\text{int}}$  is the electron heat flux which can be approximated via a similar rule as used for  $W_{\text{int}}$  via non-linear combinations of gas,  $\xi_g$ , and liquid,  $\xi_l$ , extreme values

$$\frac{1}{\xi_{\text{int}}\left(\frac{E}{n_0}\right)} = x_g s_{\text{int}}\left(\frac{E}{n_0}\right) \frac{1}{\xi_g\left(\frac{E}{n_0}\right)} + x_l \frac{s_{\text{int}}\left(\frac{E}{n_0}\right)}{s_l\left(\frac{E}{n_0}\right)} \frac{1}{\xi_l\left(\frac{E}{n_0}\right)}. \quad (4.27)$$

The resulting surface of  $n_0 D_L$  generated via (4.25) is shown in Figure 4.22 for the range of densities and reduced field values used in this study.

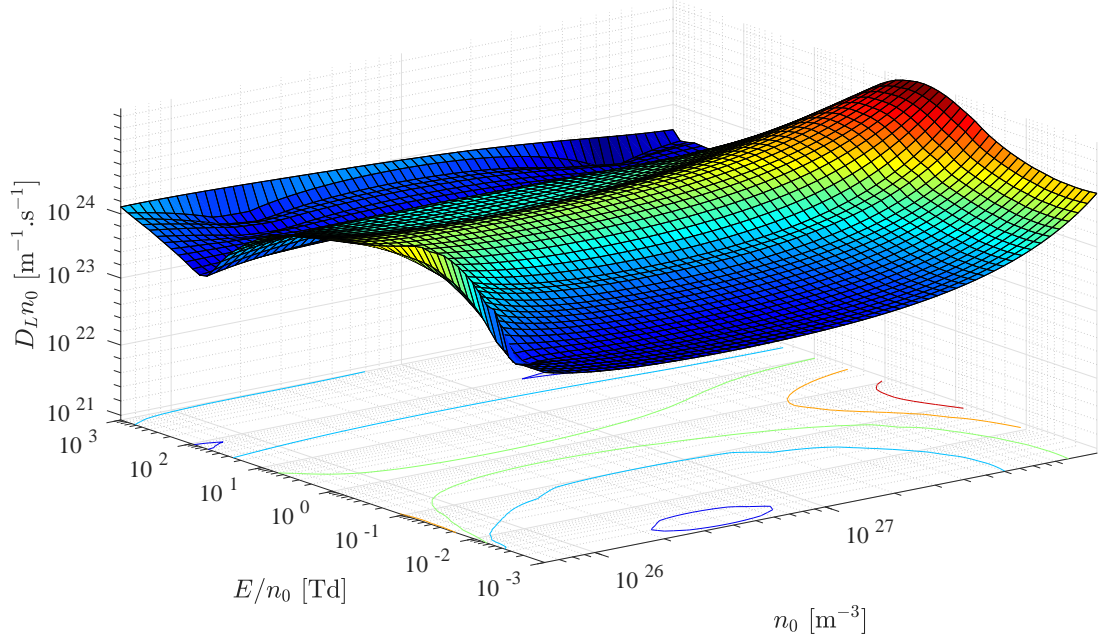


Figure 4.22: Reduced longitudinal diffusion coefficient,  $n_0 D_L$ , surface of electrons in argon computed via the GER (4.25) as a function of  $\frac{E}{n_0}$  and  $n_0$  used to interpolate input data for LFA models.

The final input parameter for the LFA model is the ionisation collision rate which, for densities between the gas and liquid extremes  $\nu_I^{\text{int}}$ , was approximated in this study by a simple linear weighted sum of gas,  $\nu_I^g$ , and liquid,  $\nu_I^l$ , extreme ionisation rates

$$\nu_I^{\text{int}}\left(\frac{E}{n_0}\right) = x_g \nu_I^g\left(\frac{E}{n_0}\right) + x_l \nu_I^l\left(\frac{E}{n_0}\right). \quad (4.28)$$

The reduced ionisation collision rate surface generated via (4.28) is shown in Figure 4.23 for the range of densities and reduced field values used in this study.

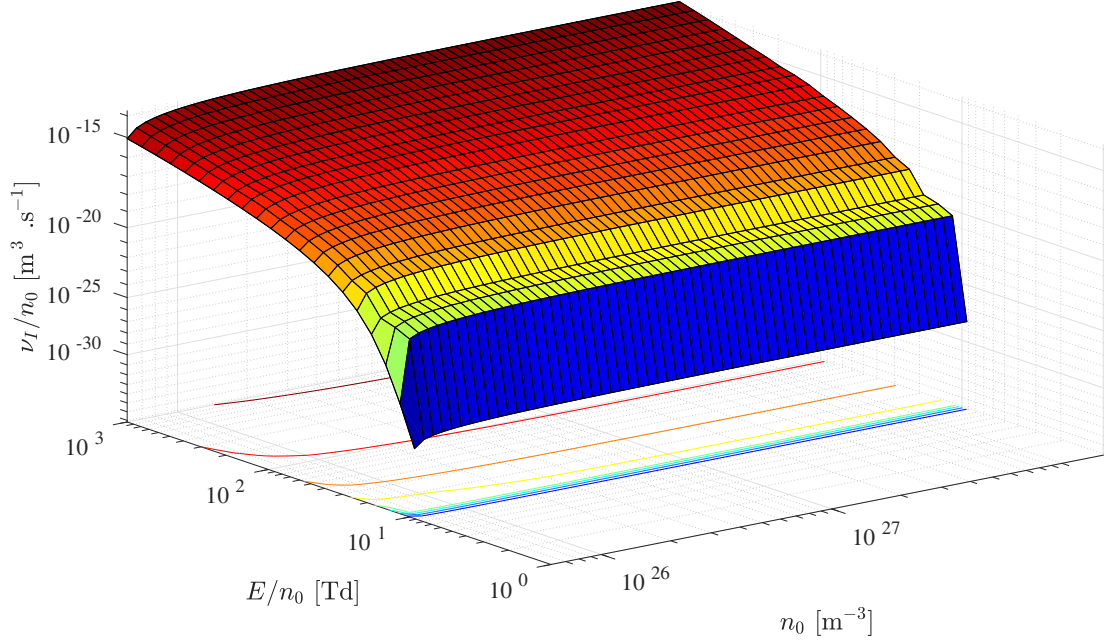


Figure 4.23: Reduced ionisation collision rate,  $\nu_I/n_0$ , surface of electrons in argon computed via (4.28) as a function of  $\frac{E}{n_0}$  and  $n_0$  used to interpolate input data for LFA models.

#### Higher order model input data

The 4MM model collision data can be approximated between gas and liquid densities with energy dependent approximation methods [3]. As was done for the drift velocity, non-linear weights taken from the angle-integrated structure factor are used to generate a sum rule using gas,  $\check{\nu}_m^g$ , and liquid,  $\check{\nu}_m^l$ , data to yield a reduced momentum transfer collision frequency at intermediate densities,  $\check{\nu}_m^{\text{int}}$ , evaluated at a common mean energy,  $\langle \varepsilon \rangle$ ,

$$\check{\nu}_m^{\text{int}}(\langle \varepsilon \rangle) = x_g s_{\text{int}}(\langle \varepsilon \rangle) \check{\nu}_m^g(\langle \varepsilon \rangle) + x_l \frac{s_{\text{int}}(\langle \varepsilon \rangle)}{s_l(\langle \varepsilon \rangle)} \check{\nu}_m^l(\langle \varepsilon \rangle), \quad (4.29)$$

where  $\check{\nu}$  notation is used to denote a reduced collision rate scaled by  $n_0$ . The same formulation can be applied to approximate the input collision rate for the energy flux balance equation - the energy flux transfer collision rate,  $\check{\nu}_\xi^{\text{int}}$ , using gas,  $\check{\nu}_\xi^g$ , and liquid,  $\check{\nu}_\xi^l$ , quantities

$$\check{\nu}_\xi^{\text{int}}(\langle \varepsilon \rangle) = x_g s_{\text{int}}(\langle \varepsilon \rangle) \check{\nu}_\xi^g(\langle \varepsilon \rangle) + x_l \frac{s_{\text{int}}(\langle \varepsilon \rangle)}{s_l(\langle \varepsilon \rangle)} \check{\nu}_\xi^l(\langle \varepsilon \rangle). \quad (4.30)$$

To demonstrate the application of the non-linear sum rules the reduced momentum transfer collision frequency surface generated via (4.29) is included in Figure 4.24, demonstrating the reduction in momentum transfer collisions as the argon density increases.

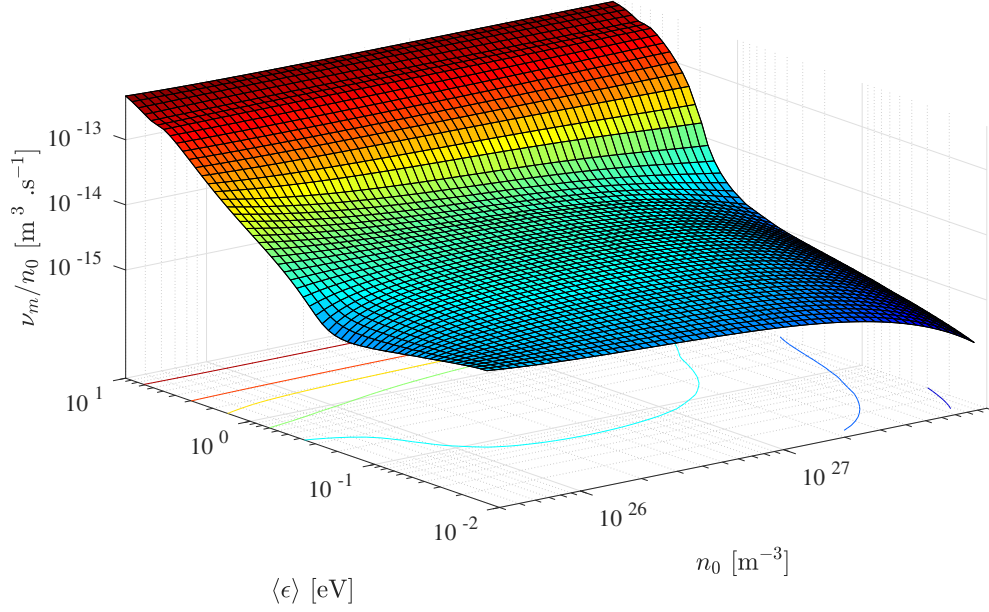


Figure 4.24: Reduced momentum transfer collision frequency,  $\frac{\nu_m}{n_0}$ , surface of electrons in argon computed via (4.29) as a function of  $\langle \epsilon \rangle$  and  $n_0$  used to interpolate input data for the 4MM model.

The input collision parameter for the energy balance equation (4.9) is a lumped energy loss rate,  $S_\epsilon$ , which describes the total loss of energy per second due to all collision processes. As modifications for non-linear liquid effects manifest through explicit modification of vector quantity balance equations, and not the mean energy balance equation [3, 48], this work has instead used a simpler linear combinations of gas,  $\check{S}_\epsilon^g$ , and liquid,  $\check{S}_\epsilon^l$ , lumped energy loss rates to yield the loss rate for an intermediate density,  $\check{S}_\epsilon^{\text{int}}$ ,

$$\check{S}_\epsilon^{\text{int}}(\langle \epsilon \rangle) = x_g \check{S}_\epsilon^g(\langle \epsilon \rangle) + x_l \check{S}_\epsilon^l(\langle \epsilon \rangle). \quad (4.31)$$

The application of this lumped energy loss rate sum rule is demonstrated in Figure 4.25 where the surface plot shows the variation with neutral density and electron mean energy.

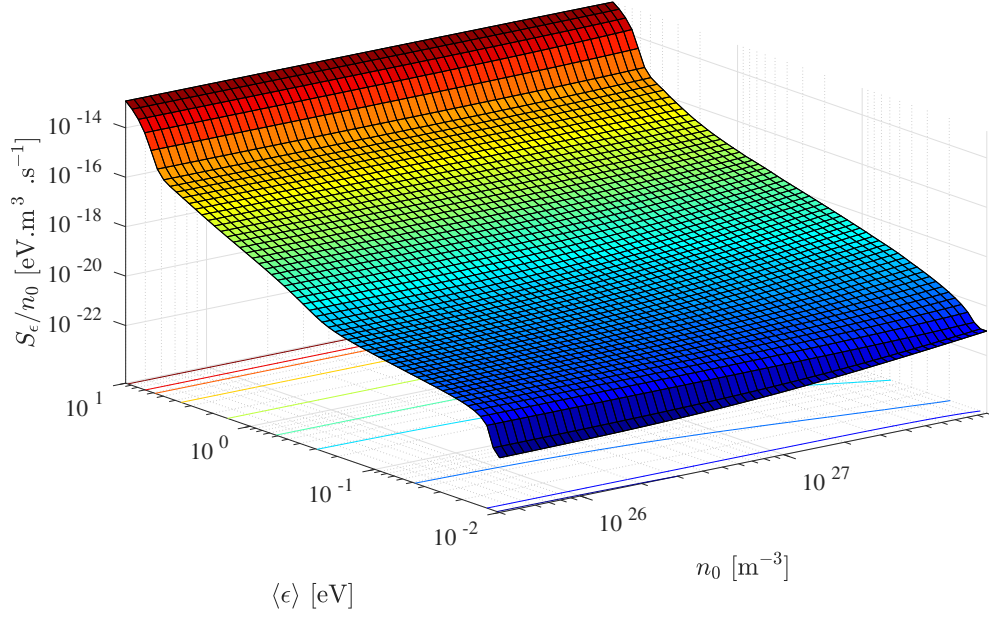


Figure 4.25: Reduced lumped energy transfer rate,  $\frac{S_\epsilon}{n_0}$ , surface of electrons in argon computed via (4.31) as a function of  $\langle \epsilon \rangle$  and  $n_0$  used to interpolate input data for the 4MM model.

As per the linear sum approximation of gas and liquid input data for  $\check{S}_\epsilon$  (4.31), the intermediate variation of the reduced ionisation collision rate,  $\check{\nu}_I^{\text{int}}$ , was approximated via

$$\check{\nu}_I^{\text{int}}(\langle \epsilon \rangle) = x_g \check{\nu}_I^g(\langle \epsilon \rangle) + x_l \check{\nu}_I^l(\langle \epsilon \rangle), \quad (4.32)$$

and the resulting surface plot is shown in Figure 4.26. As expected from (4.12), contours shown in Figure 4.26 demonstrate the decreasing ionisation threshold energy as  $n_0$  increases due to the variation in  $V_0$  with  $n_0$  [175].

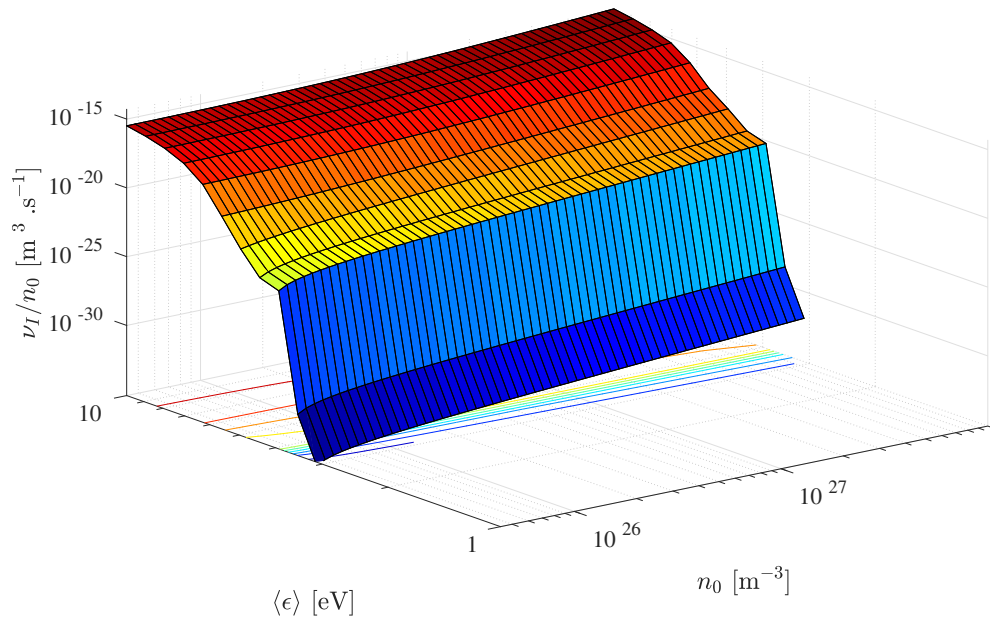


Figure 4.26: Reduced ionisation collision frequency,  $\frac{\nu_I}{n_0}$ , surface of electrons in argon computed via (4.32) as a function of  $\langle\epsilon\rangle$  and  $n_0$  used to interpolate input data for the 4MM model.

# 5

## Scattering, transport, and simulation of electron transport in THF

This chapter contains material that has been published in the following journal article:

[1] NA Garland, MJ Brunger, G Garcia, J de Urquijo, and RD White. Transport properties of electron swarms in tetrahydrofuran under the influence of an applied electric field. *Physical Review A*, 88 062712 (2013). Available online at doi:10.1103/PhysRevA.88.062712

This chapter includes results and figures from multi-term solutions of the Boltzmann equation performed by RD White using data assembled during this research. Listed co-authors provided advice and feedback on the featured data and analysis. Experimental measurements and considerations were contributed by J de Urquijo. Transport data used as input for ionisation front simulations in Chapter 5 was provided by MJE Casey.

### 5.1 Chapter Introduction

---

Quantitative modeling of electron transport in biological matter requires the compilation of the best available set of cross sections for all collisional processes (e.g. elastic, rotations, vibrations, ...). As outlined in Chapter 1, tetrahydrofuran (THF) has been identified as a suitable biomolecule to study. Deeper knowledge of electron transport in THF will facilitate modeling of complex charged particle transport in tissue surrogates to better understand emerging plasma medicine technologies. The agreement between available experimental and calculated cross sections for some scattering processes is adequate for elastic and ionisation collisions, while for other processes, such as neutral dissociated, dissociative electron attachment (DEA), and vibration, electronic, and

rotational excitations, definitive agreement is elusive. To facilitate electron transport simulations in gaseous, liquid, or interfacial THF the necessary transport coefficients and collision data will be calculated from a complete cross section set, formed by studying and assessing the available experimental and calculated cross section data. Using gas phase transport data, along with corrections to account for transport in soft-condensed structured matter, electron transport is simulated using the modeling framework developed in this study. From this modeling, demonstration of formation and propagation of ionisation fronts in both gaseous and structured THF is presented and discussed.

Section 5.2 presents a survey of existing total, integral and differential cross sections in THF, and propose an almost complete set of electron impact cross sections for THF including elastic, rotational, vibrational, electronic, ionisation and neutral dissociation processes in the energy range 0-300 eV. Section 5.3 then discusses issues that were found in attempts to measure swarm transport coefficients in THF, and presents calculated transport coefficients using a Boltzmann equation treatment aimed to motivate further experimental swarm studies in THF. Section 5.5 will employ the modeling framework developed in this research project, along with the most recently available gaseous and structured THF data, to model the formation and propagation of ionisation fronts. Finally, in Section 5.6 some conclusions from the present investigation are drawn.

## 5.2 cross sections in THF

---

This Section presents the development of a recommended set of cross sections for electrons in THF. This work is restricted to the energy region less than 300 eV. Above this energy, agreement between theory and experiment is sufficiently good that theory can in general be used [19,21]. This Chapter will focus on the development of a set of cross sections for implementation into a Boltzmann equation transport theory (or Monte-Carlo simulations), and hence is restricted to discussions of the integral cross sections (ICS), while the differential cross sections are sufficiently represented through implementation of the integrated forms including the momentum transfer cross sections (MTCS).

### 5.2.1 Grand total cross section set

The grand total cross section (GTCS) for THF mainly consists of contributions from the elastic  $\sigma_{elas}$ , rotational  $\sigma_{rot}$ , vibrational  $\sigma_{vib}$ , electronic  $\sigma_{elec}$ , ionisation  $\sigma_{ion}$  and neutral dissociation  $\sigma_{neutral}$  integral cross sections. The GTCS has been extensively studied both experimentally [18,20] and computationally [19,21]. This work proposes a GTCS based on the most recent set of Chiari *et al.* [21], although modified by the Chiari *et al.* data to account for the resonance at approximately 6 eV that has been observed in the previous experimental measurements [18,20]. To construct the resonance in the proposed set, the slopes either side of the measured resonances in the GTCS from references [18,20] were computed and found to be similar. This characteristic of the

resonance from both data sets was subsequently used to splice in the known resonance into the Chiari *et al.* data set. The resulting proposed GTCS for electrons in THF is presented in Figure 5.1, where they are compared with other experimental and theoretical data.

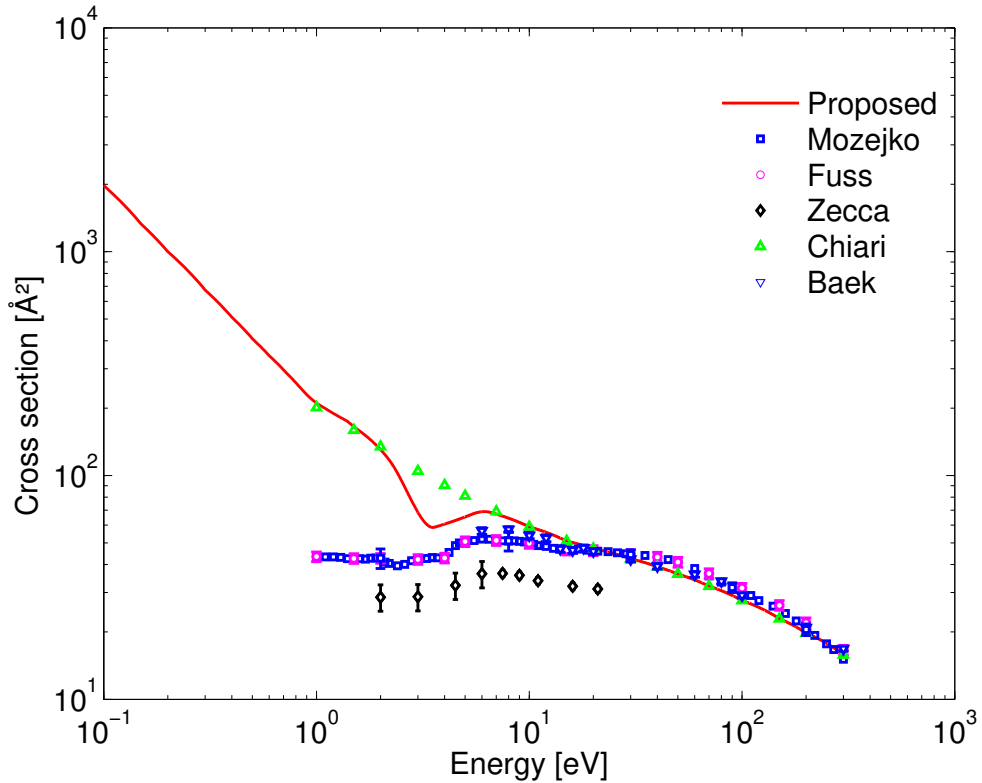


Figure 5.1: Proposed grand total cross section for electron scattering in THF, as compared with existing GTCS data (Mozejko *et al.* [18]; Fuss *et al.* [19]; Zecca *et al.* [20]; Chiari *et al.* [21]; Baek *et al.* [22]).

### 5.2.2 Elastic cross section set

There have been a number of measurements of the elastic differential and integral cross sections for a variety of energy and angular ranges [22, 24, 25, 27, 133]. These have been complemented by theoretical calculations using the R-matrix [136], Schwinger variational method [137] (more recently accounting for the long range scattering by the strong permanent electric dipole of THF [25]), and the independent atom model (IAM-SCAR) [19, 21, 23]. Multiple elastic ICS were sourced from Fuss *et al.* [19], Colyer *et al.* [24] and Gauf *et al.* [25], in order to construct the proposed elastic ICS by capturing the relative strengths of the various approaches. For energies higher than 50 eV, there is relatively good agreement between results from the various techniques and so the theoretical elastic ICS from Fuss *et al.* [19] was used. For energies less than 50 eV, however, the elastic ICS was spliced into a mixture of data from Colyer *et al.* [24] and Gauf *et al.* [25]. Specifically, the Colyer *et al.* data were used in the range 10-50 eV, while the ratio of the Colyer *et al.* and Gauf *et al.* data points at 10 eV were used to scale down the Gauf *et al.* data points for the sub-10 eV energies down to 1 eV.

Finally, for energies less than 1 eV (to 0.1 eV), the set has extrapolated the proposed elastic ICS as shown in Figure 5.2. In summary, the proposed elastic ICS is compared with the data used to construct it [19, 24, 25] in Figure 5.2. An equivalent process was also employed to establish the elastic momentum transfer cross section displayed in Figure 5.3.

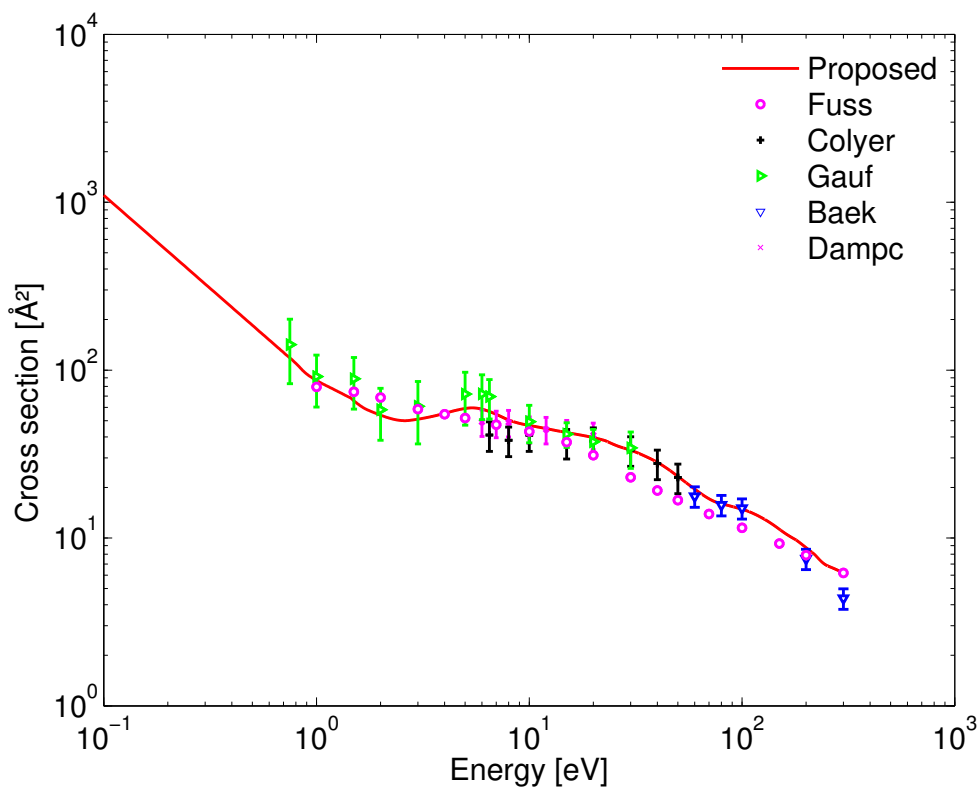


Figure 5.2: Proposed elastic ICS for electron scattering in THF, compared with existing data from which the set was constructed (Fuss *et al.* [19, 23]; Colyer *et al.* [24]; Gauf *et al.* [25]; Baek *et al.* [22]; Dampc *et al.* [26]).

### 5.2.3 Vibrational excitation and ionisation cross section sets

Electron impact vibrational excitation cross sections for scattering in THF have been measured by various groups [27, 28, 134]. This work proposes a set of six ICSs for the identified vibrational modes of THF in the work from Allan [27]. In general, if the angular distribution of a DCS is isotropic at some incident electron energy  $\varepsilon$ , then for any scattering angle  $\theta = \theta_0$  the integral cross section is simply given by  $\text{ICS}(\varepsilon) = 4\pi\text{DCS}(\varepsilon, \theta_0)$ . The DCS of Khakoo *et al.* [28] suggest that, with the exception of their lowest energy work at 2 eV, the assumption of isotropic angular distributions for the DCS is quite adequate. Nonetheless, in an attempt to lessen the effects of any anisotropic scattering, there has been an averaging of the measured vibrational excitation functions of Allan [27], for each respective mode, at  $\theta = 45^\circ, 90^\circ, 135^\circ$  and  $180^\circ$ , before multiplying by  $4\pi$  to generate an  $\text{ICS}(\varepsilon)$  in each case.

The results from the analysis are displayed in Figure 5.4. For comparison, Figure 5.5 plots the vibrational cross section of Khakoo *et al.* [28], whose measurements

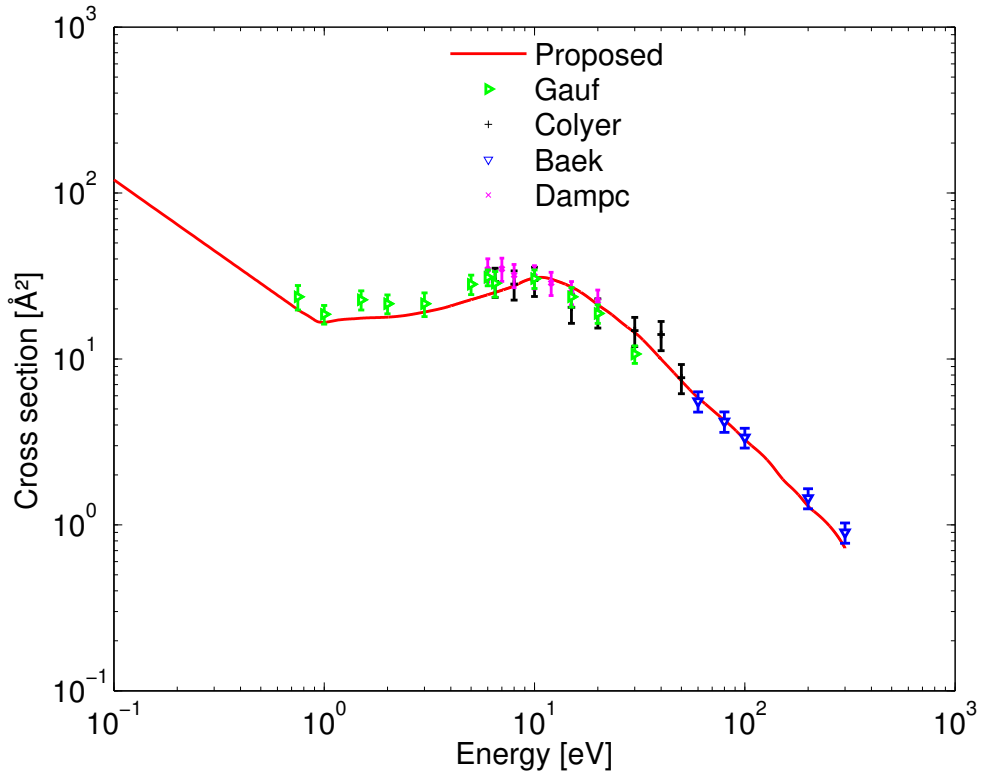


Figure 5.3: Proposed elastic momentum transfer cross section for electron scattering in THF, compared with existing data from which the set was constructed (Gauf [25]; Colyer [24]; Baek *et al.* [22]; Dampc *et al.* [26]).

were conducted at a lower energy resolution and therefore incorporate several of the individual modes measured by Allan [27], with the relevant summed modes proposed in Figure 5.4. One sees in Figure 5, to within the stated uncertainties from the analysis and the measurements of Khakoo *et al.*, that the level of agreement between them is generally quite good, with the proposed ICS being systematically smaller in magnitude. Nonetheless, the results embodied in Figure 5.5 gives some confidence in the validity of the current approach in determining the THF vibrational ICSs.

For implementation into transport theories, and or Monte-Carlo simulations, it is important to have differentiated (rather than lumped) processes, where possible, to ensure that the relevant threshold energies are included in the transport results [128]. This is the main reason this work prefers using the data of Allan [27] to that in Khakoo *et al.* [28].

There have been limited investigations of electron impact ionisation in THF. Here one should note the theoretical studies from Mozejko and Sanche [29] and Dampc *et al.* [30], and the experimental study of Fuss *et al.* [23]. This investigation implements the measured ionisation ICS of Fuss *et al.* [23]. As the data of Fuss *et al.* only extend down to 50 eV, the proposed set has used a linear extrapolation to extend their ICS to a value of  $0 \text{ \AA}^2$  at the 11.72 eV ionisation threshold for THF. The proposed ionisation ICS is compared with the available theoretical calculations and the results of Fuss *et al.* in Figure 5.6.

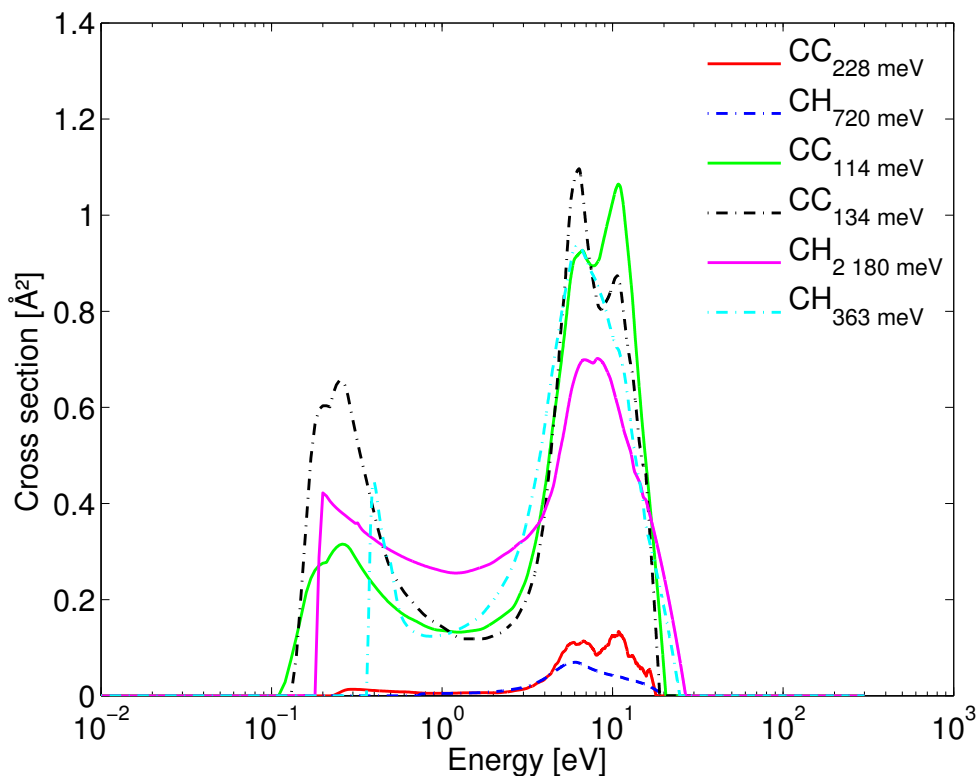


Figure 5.4: Proposed vibrational ICS for electron scattering in THF. See legend for further details.

#### 5.2.4 Electronic-state excitation cross section sets

Investigations of electronic-state excitation of THF are restricted to the experimental studies of Do *et al.* [31] and Zubek *et al.* [135]. The first three Rydberg bands of integral cross sections for electronic excitation ( $\sigma_{\text{elec}}^{(1)}$ ,  $\sigma_{\text{elec}}^{(2)}$ ,  $\sigma_{\text{elec}}^{(3)}$ ) have been reported by Do *et al.* [31]. cross sections for the three higher level bands of electronic excitations, which are apparent in the energy-loss spectra in Do *et al.* and converge to the ionisation threshold of THF, are not available, although the threshold energies for the processes are known [31]. The remaining three electronic mode ICS ( $\sigma_{\text{elec}}^{(4)}$ ,  $\sigma_{\text{elec}}^{(5)}$ ,  $\sigma_{\text{elec}}^{(6)}$ ) were assumed to have the same functional form as  $\sigma_{\text{elec}}^{(3)}$ . Their magnitudes were estimated by adding respectively 10%, 20%, and 30% of the maximum value of  $\sigma_{\text{elec}}^{(3)}$  to the cross section  $\sigma_{\text{elec}}^{(3)}$ . It should be noted that these scaling factors are not random; they were estimated on the basis of the energy-loss spectra in Do *et al.* [31] and the many other energy-loss data measured by the Flinders group. While they do represent, in this use, a form of average scaling factor, they are believed to be accurate to within the typical uncertainties of experimental electronic-state ICS determination (45%-50%).

These cross sections ( $\sigma_{\text{elec}}^{(4)}$ ,  $\sigma_{\text{elec}}^{(5)}$ ,  $\sigma_{\text{elec}}^{(6)}$ ) were also shifted to their relevant thresholds for each of the electronic excitation processes. The proposed set of electronic-state excitation ICSs are displayed in Figure 5.7.

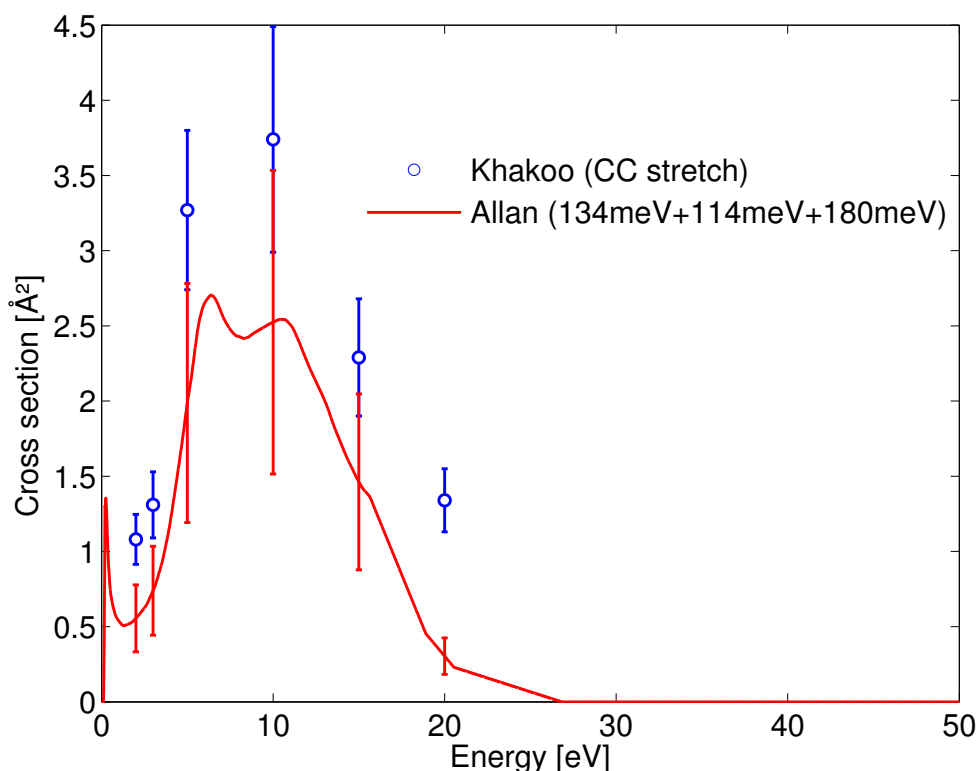


Figure 5.5: Comparison of a subset of the recommended ICS for electron induced vibrational processes in THF [27], with the summed modes of Khakoo *et al.* [28].

### 5.2.5 Unknown cross sections: rotations and neutral dissociation

To estimate the unknown remnant ICS for electron collisions with THF, the known/proposed cross sections (elastic, vibrational, electronic excitation and ionisation) were subtracted from the grand total cross section set proposed in Figure 5.1. The remaining cross section, after subtraction, was assumed to be composed of the sum of rotational excitation ICS and the neutral dissociation ICS. Electron attachment and dissociative electron attachment (DEA) are of course other possible channels to consider. At the time of this investigation, no absolute ICS for DEA or attachment of electrons in THF are currently available, and so they have not been considered in this immediate study.

In order to isolate the contribution of neutral dissociation from the rotational processes, it was assumed that the neutral dissociation cross section would display similar attributes to the equivalent cross section in other targets [186–189]: namely a relatively low-energy threshold and being quite sharply peaked over quite a small energy domain. This naturally emerged from the remnant cross section, and the proposed neutral dissociation cross section is displayed in Figure 5.8, with a threshold energy of 5.98 eV and being sharply peaked at around 10 eV. This is compared with the neutral cross section proposed by Fuss *et al.* [19]. Their cross section is broader but of approximately the same magnitude as that proposed. However, the ICS of Fuss *et al.* has a somewhat larger threshold energy and energy range.

The remainder of the remnant cross section was assumed to be the contribution due to (lumped) rotational excitations and is shown in Figure 5.9. This investigation

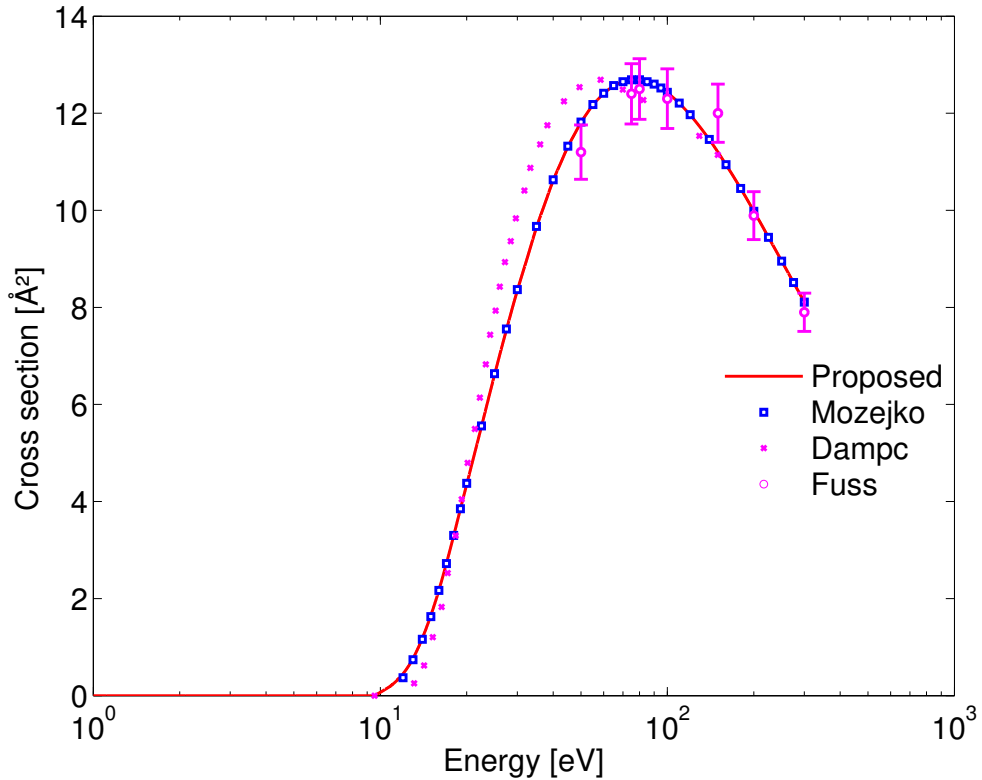


Figure 5.6: Comparison of the proposed ionisation cross sections for electron scattering in THF with the available theoretical calculations of Mozejko and Sanche [29] and Dampc *et al.* [30], and the measured data from Fuss *et al.* [23].

was unable to extract the individual rotational cross sections. Calculations indicate that the lowest threshold for rotational excitation is less than 1 meV, and with an average excitation threshold of 1.205 meV. In the proposed set, it was assumed rotational processes can be characterised by a single (lumped) rotational integral cross section with representative threshold energy of 1.205 meV. The present derived results are compared with the corresponding results given in Fuss *et al.* [19], using the IAM-SCAR approach, and with a revised set calculated using the Born-dipole rotational excitations [21]. The extracted rotational cross sections are in good agreement with the results presented in Chiari *et al.* [21], as seen in Figure 5.9.

### 5.3 Transport properties of electrons in gaseous THF

To model macroscopic systems, one needs complete and accurate cross section sets. One of the key discriminative tests on the accuracy and completeness of cross section sets is made through comparison of results from swarm experiments [121, 190]. Electrons are released into a drift tube containing the gas and experience a spatially uniform electric field ( $E$ ). Completeness and accuracy of the cross section set is investigated by correspondence of the measured transport coefficients with those calculated or simulated using that cross section set. These transport coefficients include the drift velocity  $W$ , transverse and longitudinal diffusion coefficients  $D_T$  and  $D_L$  respectively, and the rate

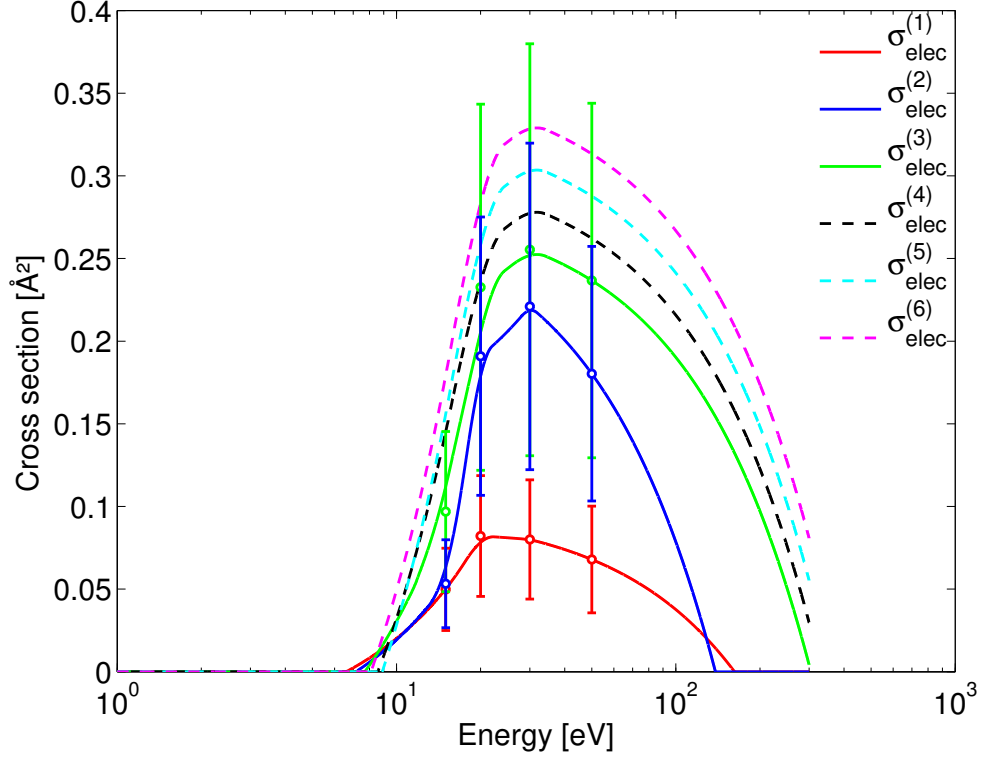


Figure 5.7: Proposed electronic excitation ICS for electron scattering from THF, as determined using the data of Do *et al.* [31].

coefficients for a range of applied reduced fields  $E/n_0$ . It should be noted that  $n_0$  is neutral gas density. This Section implements the above set of proposed cross sections, to study the macroscopic transport properties of electron swarms in THF under typical swarm conditions [121, 190]. Analysis starts with a brief description of what transport coefficients are measured, and how one relates them to the microscopic cross sections through an appropriate transport theory.

### 5.3.1 Swarm transport coefficients

Experimental swarm investigations of transport behaviour are generally made by sampling charged particle currents or densities  $n(\mathbf{r}, t)$ . The connection between experiment and theory is generally made through the equation of continuity

$$\frac{\partial n(\mathbf{r}, t)}{\partial t} + \nabla \cdot \mathbf{\Gamma}(\mathbf{r}, t) = S(\mathbf{r}, t), \quad (5.1)$$

where  $\mathbf{\Gamma}(\mathbf{r}, t) = n \langle \mathbf{v} \rangle$  is the electron flux and  $S(\mathbf{r}, t)$  represents the production rate per unit volume per unit time arising from non-conservative collisional processes, such as ionisation. In the *hydrodynamic regime*, the space-time dependence is projected onto functionals of the number density through a density gradient relation [132], and so the

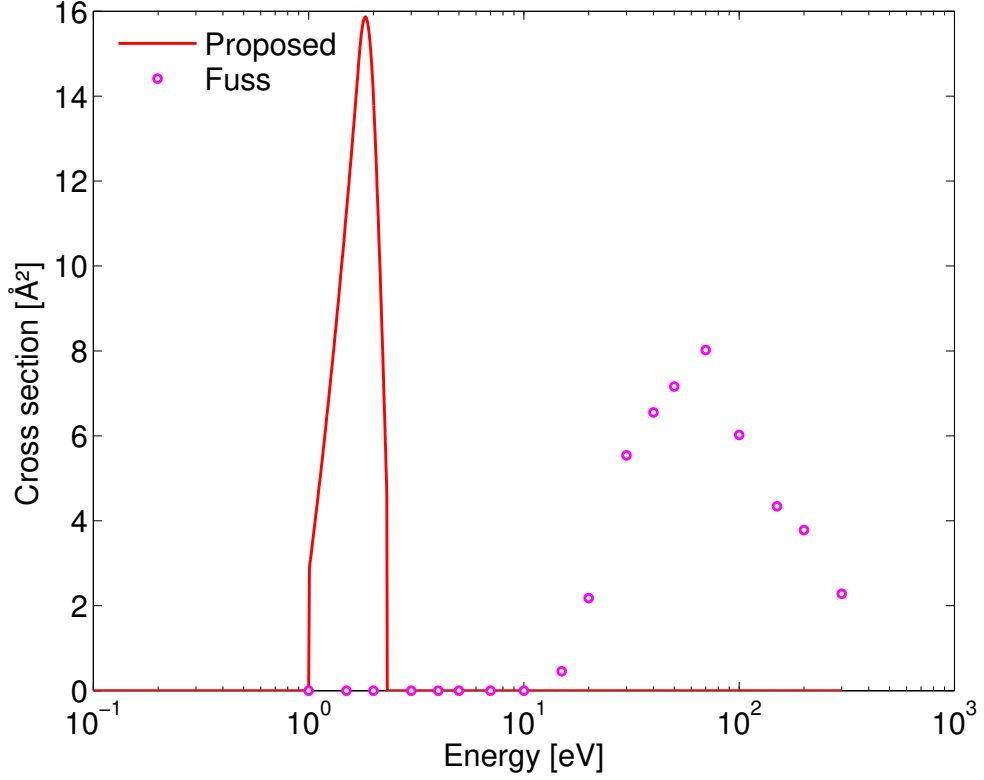


Figure 5.8: Proposed neutral dissociation ICS for THF, as compared with the earlier estimation of Fuss *et al.* [19].

flux  $\Gamma(\mathbf{r}, t)$  and source term  $S(\mathbf{r}, t)$  in equation (5.1) are expanded as follows:

$$\mathbf{\Gamma}(\mathbf{r}, t) = \mathbf{W}_F n(\mathbf{r}, t) - \mathbf{D}_F \cdot \nabla n(\mathbf{r}, t) + \dots \quad (5.2)$$

$$S(\mathbf{r}, t) = S^{(0)} - \mathbf{S}^{(1)} \odot \nabla n(\mathbf{r}, t) + \mathbf{S}^{(2)} \odot \nabla \nabla n(\mathbf{r}, t) + \dots, \quad (5.3)$$

where  $\mathbf{W}_F$  is the *flux* drift velocity and  $\mathbf{D}_F$  is the *flux* diffusion tensor. These are often reported in the pulsed Townsend experiment configuration [73]. Substitution of expansions (5.2) and (5.3) into the continuity equation (5.1) yields the diffusion equation

$$\frac{\partial n}{\partial t} + \mathbf{W} \cdot \nabla n - \mathbf{D} : \nabla \nabla n + \dots = -R_I n, \quad (5.4)$$

where  $R_i = S^{(0)}$  is the loss-rate and bulk transport coefficients are defined as

$$\mathbf{W} = \mathbf{W}_F + \mathbf{S}^{(1)} \quad (5.5)$$

$$\mathbf{D} = \mathbf{D}_F + \mathbf{S}^{(2)}. \quad (5.6)$$

Swarm experiments, such as the time of flight approach, are generally analysed on the basis of the diffusion equation and hence the bulk coefficients, not the flux, are determined in those swarm experiments [96].

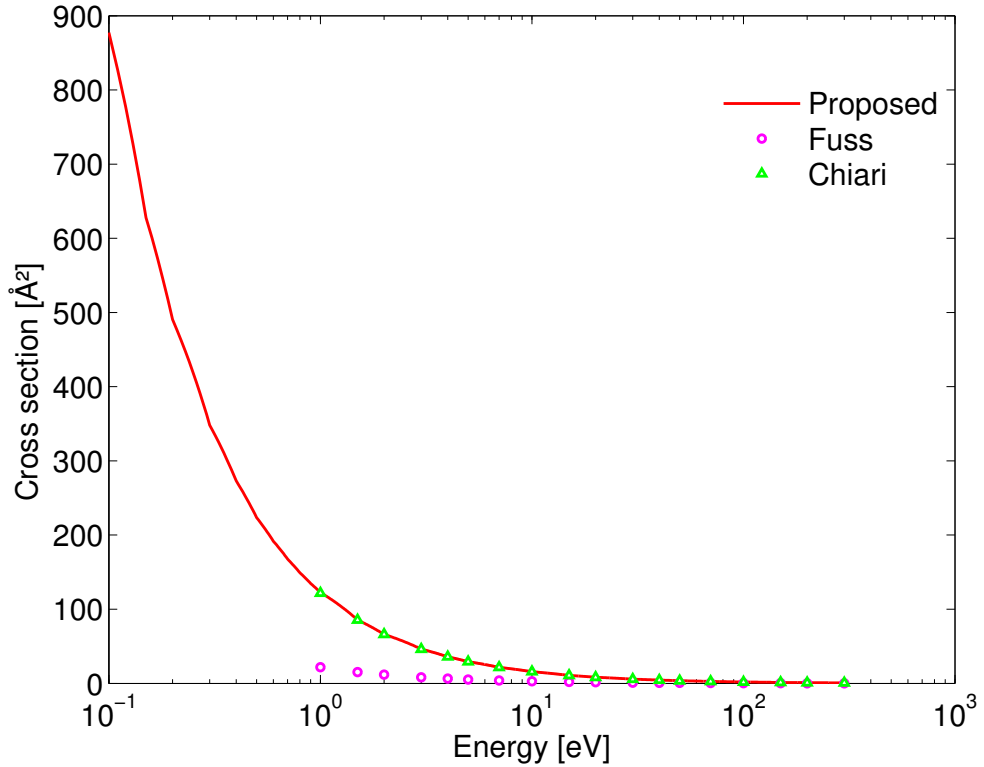


Figure 5.9: Proposed rotational ICS for electron scattering from THF, as compared with the estimation of Fuss *et al.* [19] and the calculated result of Chiari *et al.* [21].

### 5.3.2 Boltzmann equation and its solution

The connection between the macroscopic transport properties discussed above, and the microscopic processes governed by the cross section set proposed, is made through kinetic theory. Importantly, in swarm experiments, electric fields drive the electrons out of equilibrium with the background gas and hence the distribution of velocities of the electrons often becomes distinctly non-Maxwellian. In this case, the macro-micro connection must be made through a solution of Boltzmann's equation (or equivalently a Monte-Carlo simulation). The motion of a dilute swarm of electrons (mass  $m$ ) moving through a background of dense neutral THF molecules in the presence of an applied electric field  $E$  can be described by the linear Boltzmann equation

$$\frac{\partial f}{\partial t} + \mathbf{v} \cdot \nabla f + \frac{q\mathbf{E}}{m} \cdot \frac{\partial f}{\partial \mathbf{v}} = -J(f, f_0), \quad (5.7)$$

where  $f(\mathbf{r}, \mathbf{v}, t)$  is the single-particle phase space distribution function, which is a function of position  $\mathbf{r}$ , velocity  $\mathbf{v}$  and time  $t$ . The acceleration on an electron of mass  $m$  is due to the external homogeneous electric field  $\mathbf{E}$ . The collision operator  $J(f, f_0)$  takes into account binary interactions between the electrons and the THF molecules, where  $f_0$  denotes the THF molecule distribution function, which is assumed to be Maxwellian at the gas temperature  $T_0$ . The details of the collision operator used can be found in Ness *et al.* [142].

Equation (5.7) is an integro-differential equation for  $f(\mathbf{r}, \mathbf{v}, t)$ , a knowledge of

which permits determination of all quantities of interest describing the behaviour of the electron swarm. In the hydrodynamic regime in which swarm experiments are conducted, the space-time dependence of  $f$  is assumed to have the form

$$f(\mathbf{r}, \mathbf{v}, t) = \sum_{j=0} f^{(j)}(\mathbf{v}) \cdot (-\nabla)^j n(\mathbf{r}, t), \quad (5.8)$$

where the  $f^{(j)}$  are tensors of rank  $j$ , the dot denotes a  $j$ -fold scalar product and the local charged particle density at time  $t$  is given by:

$$n(\mathbf{r}, t) = \int f(\mathbf{r}, \mathbf{v}, t) d\mathbf{v}. \quad (5.9)$$

Substitution of the hydrodynamic expansion (5.8) into equation (5.7), and equating coefficients of the gradient expansion, results in a hierarchy of equations to solve for the velocity distribution functions  $f^{(j)}(\mathbf{v})$  [191]:

$$\frac{q\mathbf{E}}{m} \cdot \frac{\partial f^{(j)}}{\partial \mathbf{v}} + J(f^{(j)}, f_0) = \mathbf{v} f^{(j-1)} \quad j = 0, 1, \dots \quad (5.10)$$

This is the microscopic picture. Solution of the hierarchy for the distribution functions  $f^{(j)}(\mathbf{v})$  enables calculation of the macroscopic measurable quantities through appropriate averages e.g.

$$\mathbf{W}_F = \frac{1}{n} \int \mathbf{v} f^{(0)}(\mathbf{v}, t) d\mathbf{v}, \quad (5.11)$$

$$\mathbf{D}_F = -\frac{1}{n} \int \mathbf{v} \mathbf{v} f^{(1)}(\mathbf{v}, t) d\mathbf{v}, \quad (5.12)$$

$$\mathbf{S}^{(i)} = \frac{1}{n} \int J_R(f^{(i)}, F_0) d\mathbf{v} \quad (5.13)$$

Solution of the hierarchy of kinetic equations (5.10) requires decomposition of  $f^{(j)}(\mathbf{v})$  in velocity space. The first step in any analysis is typically the representation of the distribution function in terms of the directions of velocity space through an expansion in spherical harmonics [70]:

$$f^{(j)}(\mathbf{v}, t) = \sum_{l=0}^{\infty} \sum_{m=-l}^l f_m^{j(l)}(\mathbf{v}, t) Y_m^{[l]}(\hat{\mathbf{v}}), \quad (5.14)$$

where  $Y_m^{[l]}(\hat{\mathbf{v}})$  are the spherical harmonics and  $\hat{\mathbf{v}}$  denotes the angles of  $\mathbf{v}$ . While common practice is to set the upper bound of the  $l$ -summation to 1 (i.e., the two-term approximation) and consider only  $m = 0$  (i.e., a Legendre polynomial expansion), this formulation does not make any such restrictive assumptions in this theory. In best practice, the integer  $l_{\max}$  is successively incremented until a prescribed accuracy criterion is met, as considered below. This is a multi-term solution of Boltzmann's equation. Combining equations (5.7) and (5.14) leads to the following hierarchy of

coupled integro-differential equations for  $f_m^{j(l)}$ :

$$\sum_{l'm'} \langle lm | \left[ \frac{e\mathbf{E}}{m} \cdot \frac{\partial}{\partial \mathbf{v}} + J | l'm' \rangle \right] f_{m'}^{j(l')} = - \sum_{l'm'} \langle lm | v | l'm' \rangle f_{m'}^{j-1(l')}. \quad (5.15)$$

Expressions for the matrix elements of the streaming operators are given in Robson *et al.* and Ness *et al.* [70,142]. The collision matrices e.g.  $\langle lm | J | l'm' \rangle = [J_{elas}^l + J_{inel}^l + J_a^l + J_{ion}^l] \delta_{l',l} \delta_{m',m}$  are all diagonal in  $l$  and  $m$ , since the collision operators are all scalars. Further representation of the speed dependence is required to solve the hierarchy of coupled operator equations. This study implemented an expansion in terms of Sonine polynomials, and the reader is referred to White *et al.* [132] for further details on relating transport coefficients to the coefficients  $f_m^{j(l)}$ .

### 5.3.3 Electron transport in THF

Figures 5.10 - 5.12 present results for swarm transport properties of electrons in THF, including the mean energy, drift velocity, diffusion and rate coefficients. The results presented are in a quasi-steady state determined by a balance between power input from an applied electric field  $E$  and energy loss rate via collisions between electrons in the swarm and particles. All results are presented as a function of the reduced electric field  $E/n_0$ , in the range 0.01 - 10000 Td (1Td = 1 Townsend =  $10^{-21}$  Vm<sup>2</sup>). The temperature of the background gas of THF molecules is fixed at 293 K.

In the low field regime ( $E/n_0 < 1$  Td), the electron swarm is essentially in thermal equilibrium with background THF molecules. As shown in Figure 5.10 the mean energy is approximately equal to the background temperature and the field is a perturbation on the swarm's behaviour. In this regime, the drift velocity (see Figure 5.11) is essentially linear representing an essentially constant mobility. Likewise, as displayed in Figure 5.12 the diffusion is approximately equal to the thermal value and it is essentially isotropic ( $D_L \approx D_T$ ). All collision processes are essentially conservative as highlighted in the ionisation rate in Figure 5.10, and hence there are no differences between the bulk and flux coefficients in this regime.

When considering higher fields ( $1 \text{ Td} < E/n_0 < 100 \text{ Td}$ ), the thermal equilibrium state is finally broken. The rapidly falling cross section magnitudes for elastic collisions results in a rapidly increasing mean energy with field in this regime as demonstrated in Figure 5.10. This rapid rise in the mean energy is then quenched by the quite large neutral dissociation cross section and the ionisation cross sections shown in Figures 5.6 and 5.8, which sees a plateauing of the mean energy above  $\sim 100$ Td (see Figure 5.10). This behaviour is also reflected in the diffusion coefficients presented in Figure 5.12. While the diffusion coefficients have a thermal contribution to them, in this regime, one observes that diffusion becomes distinctly anisotropic (i.e. diffusion parallel and transverse to the electric field are distinctly different). As the thermal contribution to diffusion is relatively isotropic in this regime, this indicates that the primary source of anisotropic diffusion comes from the ‘‘differential velocity effect’’ [160] arising from

a rapidly varying collision frequency with energy and spatial variation of the average energy through the swarm.

In the high field regime ( $E/n_0 > 100$  Td), non-conservative effects associated with ionisation (see Figure 5.10) begin to impact on the transport properties. For the mean energy, the ionisation process generates another electron with lower energy, resulting in a dilution of the energy and a reduced rate of increase with reduced field in the mean energy of the swarm. Importantly, there are explicit effects on the transport coefficients. Figure 5.11 displays both the flux and bulk drift velocities. The flux represents the velocity averaged over all electrons in the swarm, while the bulk drift velocity represents the time rate of change of the center of mass of the electron swarm. Non-conservative processes have an implicit effect on the velocity distribution function and hence on the flux drift velocity. In particular the non-conservative processes explicitly modify the center of mass of the swarm through non-uniform creation of electrons, and consequently modify the bulk drift velocity. In Figure 5.11, one may observe that the bulk drift velocity is enhanced over the flux component, indicating that electrons are getting preferentially created at the front of the swarm and so shifting the center of mass in the direction of the field force.

Lastly this analysis makes comment on the validity of the two-term approximation for describing electron transport in THF. In Figure 5.13 a comparison of the two-term and multi-term approximations for the diffusion coefficients is shown. For low-fields, the two-term approximation is accurate to within 1% or better. As one moves to higher fields however, it is observed that the two-term approximation can be in error by as much as 25%. This is indicative of a highly anisotropic velocity distribution function. At high field, this anisotropy is evidenced by temperatures transverse and parallel to the electric field differing by 10% or more. Analysis of swarm experiments at high fields will necessarily require a multi-term analysis or Monte-Carlo simulation.

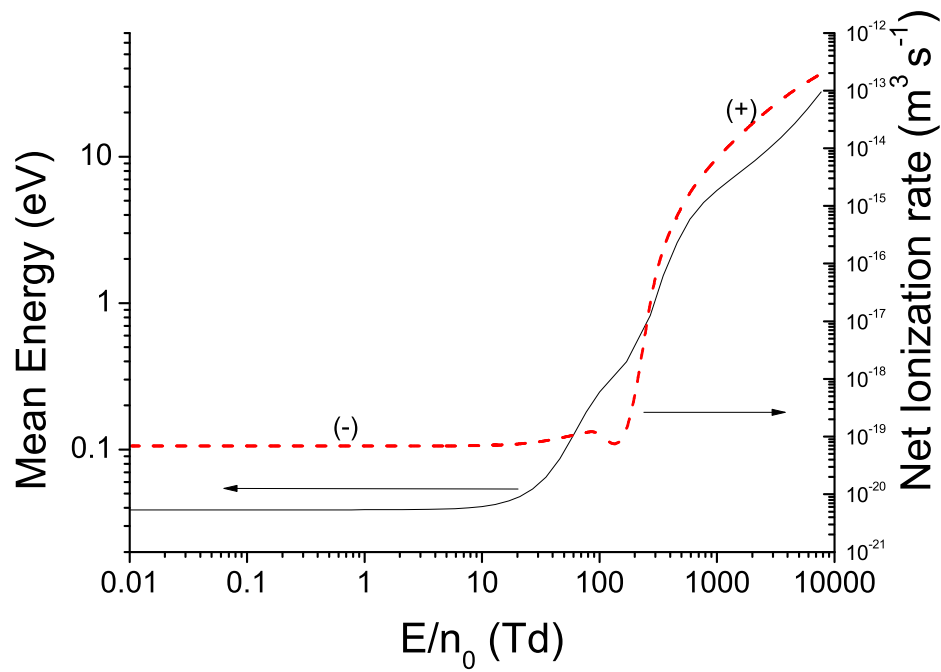


Figure 5.10: Mean energy and ionisation rate for electrons in THF as a function of the reduced electric field.

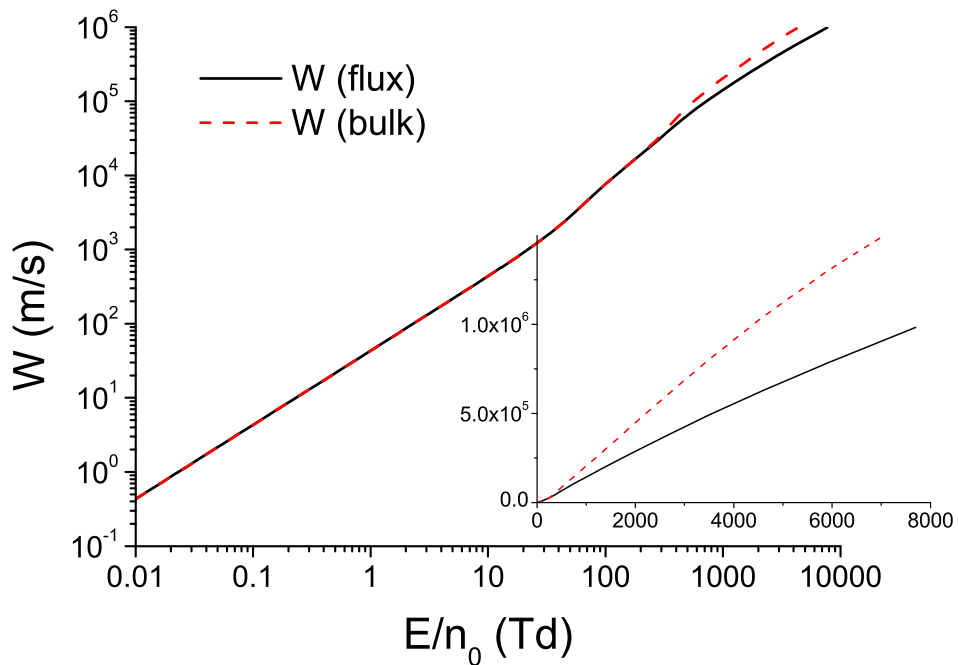


Figure 5.11: Bulk (dashed) and flux (solid) drift velocities for electrons in THF as a function of the reduced electric field. The inset uses a linear scale to emphasize the differences.

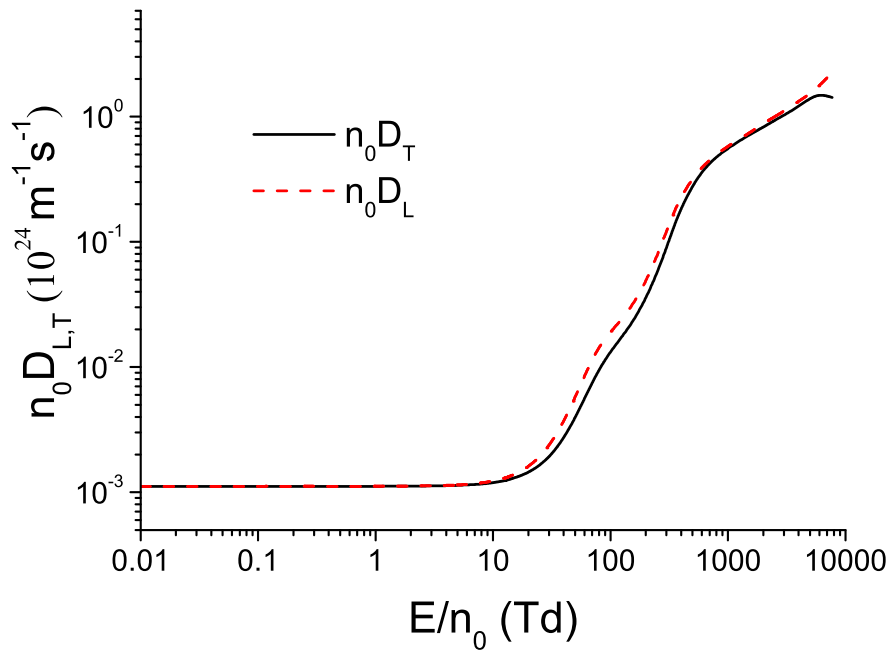


Figure 5.12: Reduced transverse and longitudinal flux diffusion coefficients for electrons in THF as a function of the reduced electric field.

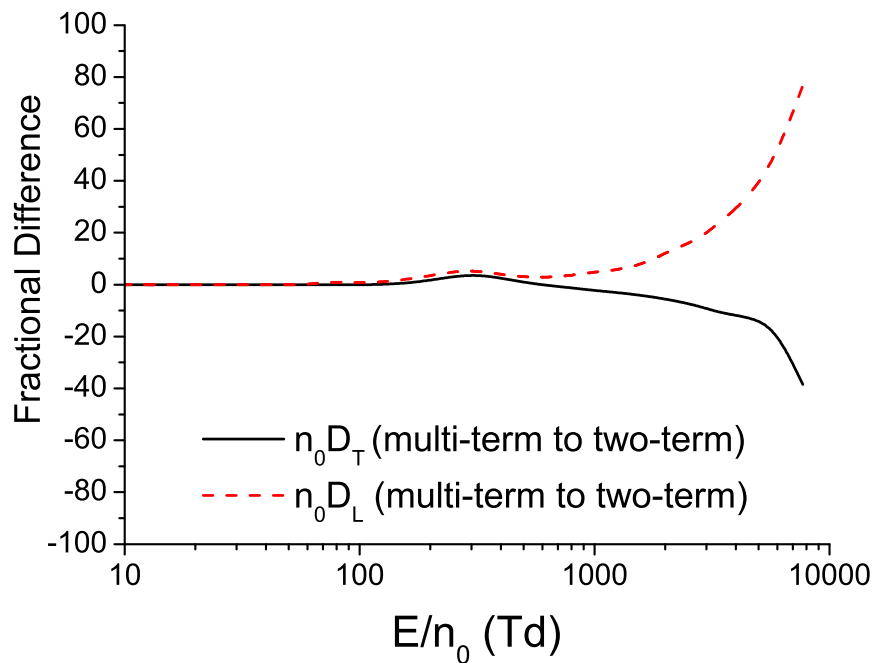


Figure 5.13: Two-term and multi-term approximations for the reduced flux transverse and longitudinal diffusion coefficients for electrons in THF as a function of the reduced electric field.

### 5.3.4 Swarm experiment considerations in THF using the pulsed-Townsend technique

Several attempts were made to measure electron swarm coefficients (electron drift velocity, longitudinal diffusion coefficient and effective ionisation coefficient) in THF using the pulsed Townsend technique [168, 192]. At the time of performing the experiments, attempts to measure electron avalanches in pure THF were unsuccessful because of a hitherto unobserved phenomenon. Since then, recent enhanced experimental methods have been developed to facilitate further refinement of the electron-THF cross section set [193].

THF vapour was injected into the evacuated discharge chamber to pressures close to  $2 \times 10^{-6}$  Torr. It was observed that the measured drift velocities did not reproduce for fixed  $E/n_0$  and pressure. Large variations of up to 30% were observed in the measurement of the electron drift velocity  $W$ , which are far beyond common uncertainties of  $\pm 1$ -2% in this coefficient. These measurements were followed with tests of drift velocities in pure  $N_2$ , for which the electron swarm coefficients are well known. These results were in error. The vacuum vessel, electrode system and all contacts and surfaces were all cleaned and washed to remove the layer of THF adhered to it. The system was retested with pure nitrogen, this time rendering values of  $W$  which were within  $\pm 1$ -2% of the accepted values. Thus it became clear that an effect due to the THF vapour in the discharge chamber was the cause of the noted failure. It is hypothesised that a thin dielectric layer of THF forms on the cathode and anode surfaces, these becoming charged, thereby producing an additional electric field which affects the external one, and so changes the  $E/n_0$  value across the discharge gap.

A second series of measurements in THF were performed after several months of successful measurements with other gases such as water vapour, He,  $N_2$  and Ar. Initial measurements of  $W$  in 1% THF in  $N_2$ , over a range of applied reduced fields 5-45 Td, were found to be quite close to the pure  $N_2$  values. Subsequent measurements carried out 12 hours later rendered  $W$  values much higher than those measured previously. Drift velocity measurements in pure THF in fact produced such high values that they were difficult to understand.

A new discharge chamber has been built to measure electron swarm coefficients at higher (25-120°C) and lower (down to -20°C) temperatures. A plan was established by experimental members of the study to try and measure these coefficients at higher temperatures, to avoid the formation of dielectric layers on the electrodes. Furthermore, it is anticipated that measurements in low concentrations of THF mixtures with  $N_2$  or Ar, for instance, will be most feasible and avoid constant cleaning of the apparatus.

## 5.4 Modifications for transport in liquid THF

So far, this Chapter has been devoted to assembling a complete set of electron scattering cross sections for electron transport in gaseous THF, to enable electron transport data to be computed as input to the modeling framework presented in Chapters 2, 3, and

4. Using what has been proposed for electron transport in gaseous THF, this Section proposes modifications to the gas phase cross section set as a way to capture some of the modifications that occur at high liquid densities. Similar to the prescription detailed for liquid argon in Chapter 4, this Section applies modifications using an experimental static structure factor for liquid THF [32], a lower ionisation threshold energy [194], and a reduced number of inelastic excitation cross sections as a result of the modified ionisation energy. Modification of the electron-neutral interaction potential is not considered in this study, as the methodology for non-polar, simple atomic liquids [12, 15] requires extension for polar liquids.

Using neutron diffraction techniques Bowron *et al.* [32] measured correlation functions of liquid THF structure at 298 K in ambient conditions. The static structure obtained from the measured correlation functions was digitised and is shown in Figure 5.14. To emphasise the fact that experimental data, such as that of Bowron *et al.* [32], is important for modeling complex molecular liquids, as opposed to relatively simple treatments used for atomic liquids, comparison to an analytic structure factor of Percus-Yevick [83] has been made. The analytic structure factor was computed using an estimated van der Waals radius for THF of 2.596 Å [195] with a known liquid density of  $n_0 = 7.4 \times 10^{27} \text{ m}^{-3}$ , corresponding to a packing fraction of  $\phi \approx 0.55$ , and is included in Figure 5.14.

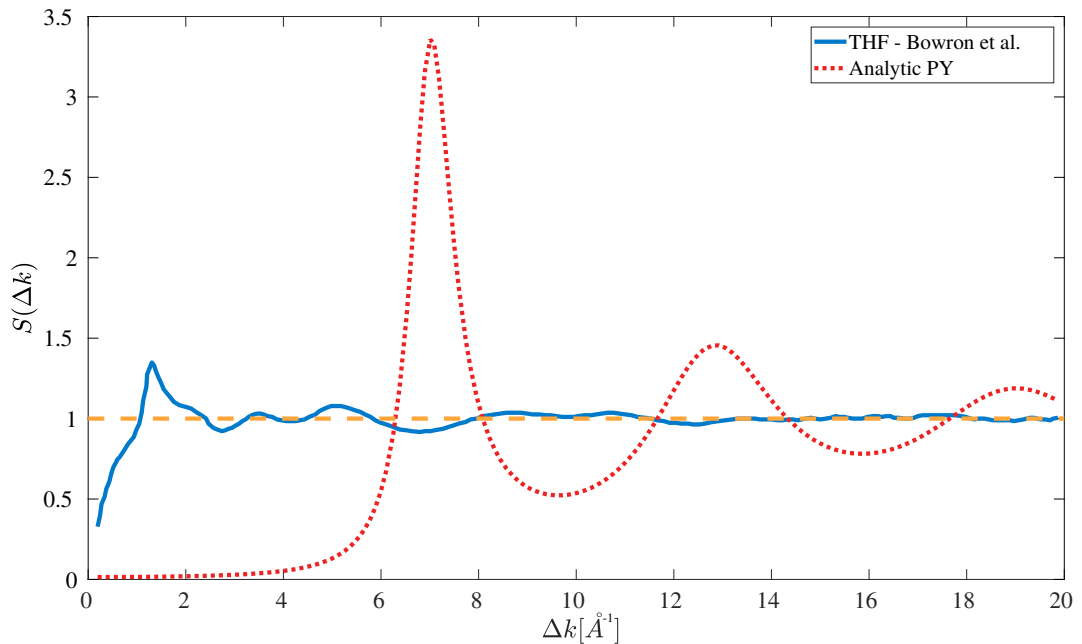


Figure 5.14: Static structure factor of liquid THF at atmospheric conditions measured by Bowron *et al.* [32] compared to an analytic structure factor computed via (3.18) assuming an ideal atomic liquid. The ideal gas value of  $S(\Delta k) = 1$  is plotted as a reference.

Clearly the structure factor of liquid THF is not at all like that of a simple analytic form for an ideal atomic liquid and reaffirms the importance of accurate liquid phase input data to the electron modeling framework proposed in this study. The experimental structure factor was used to modify the total momentum transfer cross section for

electron scattering in THF [48] in an attempt to capture the effects of coherent elastic scattering that occurs with low electron energies and high liquid densities.

In the previous Chapter, a modification was presented for the ionisation threshold energy of liquid argon to account for changes to the electron polarisation potential,  $P_+$ , and the delocalised electron energy level,  $V_0$ , that occurs as argon is condensed. As knowledge of  $V_0$  for electrons in liquid THF is currently limited, modification of the ionisation threshold energy was performed by lowering the threshold energy by a known polarisation potential of approximately 1.8 eV. This modification results in a lower ionisation potential of 7.75 eV from the gas phase value of 9.55 eV.

As per the modifications for liquid argon in the previous Chapter, any inelastic excitation processes with a threshold energy greater than the new liquid ionisation threshold were negated to form a final cross section set. This modification resulted in the three highest electronic excitation cross sections being negated. Finally, one should note that the final cross section set produced via these modifications merely offers an approximation of some electron transport effects in liquid, and may not be a complete and accurate representation of a complete set for electron transport in liquid THF.

Input transport data for the electron fluid modeling framework developed in this study is presented in Figures 5.15 - 5.17 for gaseous and approximate liquid THF transport. Input data values were computed from steady-state distribution functions calculated by a multi-term Boltzmann equation solution of the JCU group [193]. This input data takes into account the most recent advancements in electron-THF scattering cross sections [193]. These cross sections were refined through discriminating swarm experiments and calculations to test the accuracy and completeness of the THF cross section set presented in this Chapter.

## 5.5 Modeling of electron ionisation fronts in gaseous and structured THF

Using the input data presented in Figures 5.15 - 5.17, this Section models streamer formation and propagation in liquid THF. Ambient conditions were assumed [32] to yield a liquid THF density of  $n_0 = 7.4 \times 10^{27} \text{ m}^{-3}$  at 293 K. An applied reduced electric field of  $-300 \text{ Td}$  was used. As per the simulations of Chapter 4, an initial narrow Gaussian pulse of electron/positive ion pairs, formed by an ionisation event prior to the simulation start, was used as the initial condition where initial velocities, energies, and energy fluxes were specified as the steady-state values corresponding to the applied reduced field in the modified liquid data set. Streamer formation in the homogeneous liquid was considered for these simulations, as opposed to a full interfacial simulation as done in Chapter 4, because there is little information available on interfacial properties of THF, such as equilibrium gas-liquid density ratios, and interface widths. Results were obtained from four different models of liquid streamer transport:

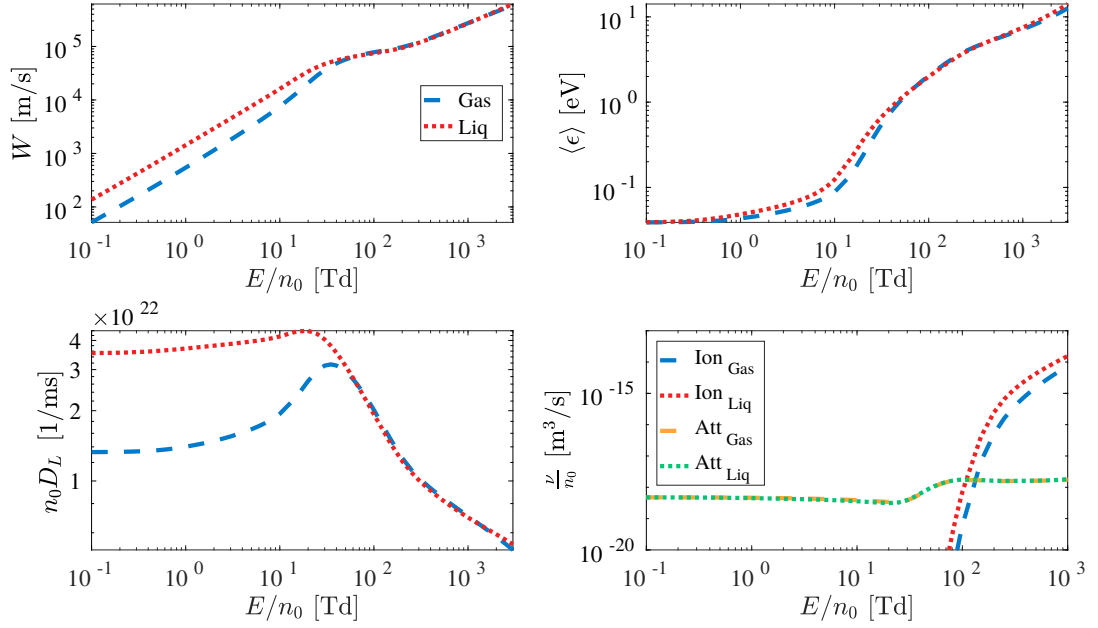


Figure 5.15: Input transport data of electrons in THF for local-field dependent electron fluid models. (Top-left) Drift velocity versus reduced field. (Top-right) Electron mean energy versus reduced field. (Bottom-left) Longitudinal reduced diffusion coefficient versus reduced field. (Bottom-right) Reduced ionisation and attachment collision rates versus reduced field.

- 4MM higher order, energy dependent model using approximate electron-liquid THF transport data,
- LFA drift-diffusion, field dependent model using approximate electron-liquid THF transport data,
- 4MM higher order, energy dependent model using gas phase electron-THF data scaled to liquid densities, and
- LFA drift-diffusion, field dependent model using gas phase electron-THF data scaled to liquid densities.

Results presented in Figures 5.18 - 5.21 demonstrate the transient formation, and in some cases eventual propagation, of an electron ionisation front in simulated liquid THF at three times of 0.25 ps, 1.5 ps, and 3.5 ps. These sample times were chosen to help demonstrate the variations between results of different model assumptions.

Application of the modeling framework, yielding the results presented in Figures 5.18 - 5.21, indicates clear, significant differences between the streamer formation and propagation using approximate liquid data, as compared to simply scaling gas phase data. The primary influence of these differences come via the lower ionisation threshold energy, which acts to accelerate the electric field screening. It was observed that these approximate liquid modifications allowed a streamer front to form within the liquid approximately three times quicker than the scaled gas data result. Effects due to coherent scattering are observable at the back of the propagating streamer tip, where small, screened values of  $E/n_0$  are experienced. This allows sampling of low-field input

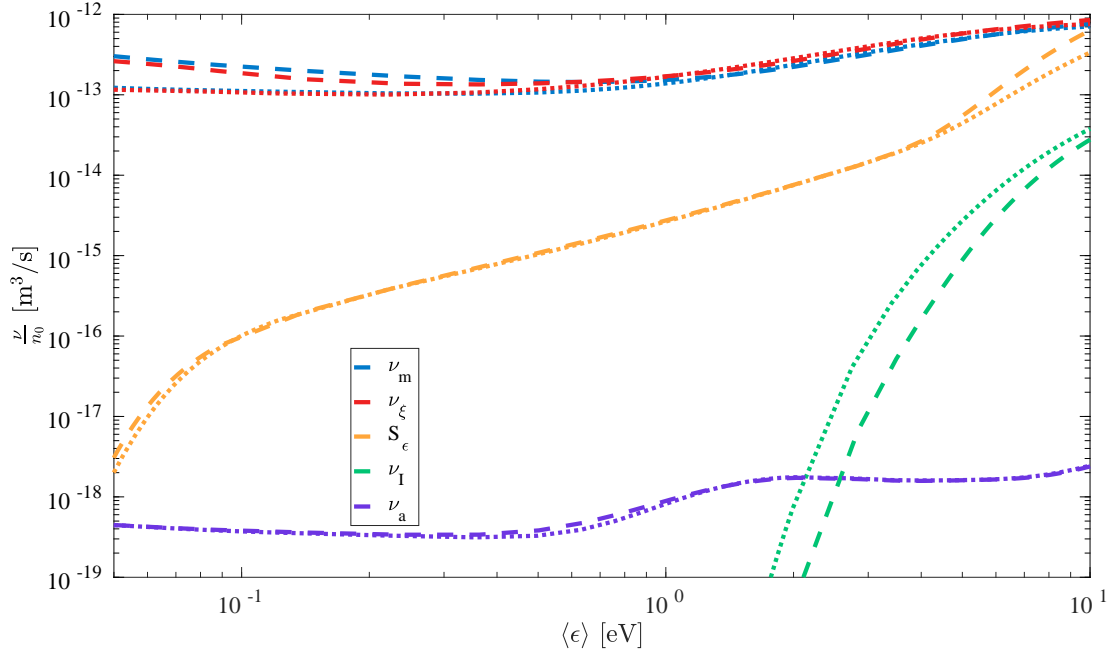


Figure 5.16: Input collision rates of electrons in THF for mean energy dependent higher order fluid model. Dashed lines denote gas transport, dotted lines denote liquid transport.

data that is more sensitive to the effects of coherent elastic scattering than high-field electron transport.

The presence of DEA reactions makes the behaviour of electron transport in THF fundamentally different to that of argon, which was considered in the previous chapter. Figure 5.19 demonstrates the formation of negative ions via DEA reactions in THF. As the collision rate for electron attachment in THF is considerably less than for ionisation, at high fields and energies found near the front of the streamer, one observes greater numbers of positive ions, compared to negative ions, preferentially created by the propagating electron front. As the reduced electric field is screened behind the front, the LFA model, using modified liquid data, demonstrates slightly lower negative ion densities compared to the energy dependent 4MM model. This result is an indicator of non-local electron transport, which can be resolved in the energy-dependent 4MM model, owing to the longer relaxation time for electron energy compared to that of electric field screening.

Finally, Figures 5.18 - 5.21 indicate relatively small variations between results of the 4MM and LFA models when using the approximate liquid input data set described in Section 5.4. Generally, the models appear to agree on the initial formation of the electron ionisation front but then deviate slightly as the front propagates through space. Energy dependent transport, using the 4MM, predicts a faster propagation than the local reduced field dependent LFA model. This observation is a consequence of the 4MM result resolving non-local electron transport by using electron mean energy, rather than the rapidly screened reduced electric field, to inform input data values.

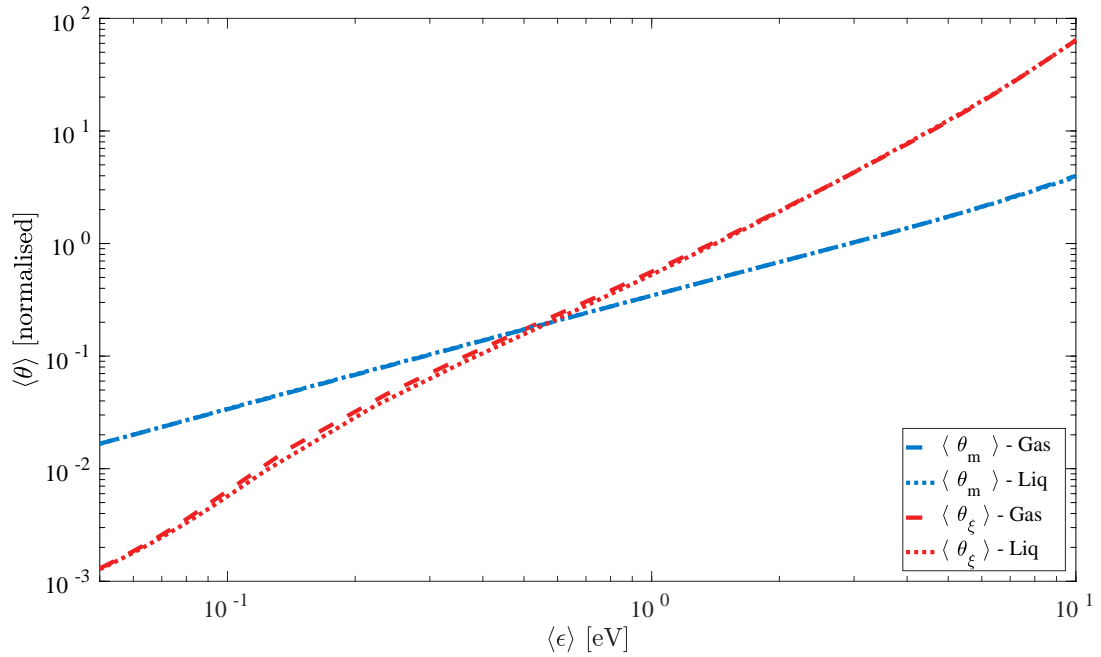


Figure 5.17: Input closure terms for mean energy dependent higher order fluid model for electrons in THF. Momentum balance closure term  $\theta_m = \langle v_z v_z \rangle$ . Energy flux balance closure term  $\theta_\xi = \langle v^2 v_z v_z \rangle$ . Dashed lines denote gas transport, dotted lines denote liquid transport.

## 5.6 Chapter Summary

This Chapter has conducted a critical analysis of existing experimental and theoretical cross sections for electron scattering in THF, to propose a largely complete set of cross sections in the energy range 0.01-300 eV. This has included the development of a set of rotational and neutral dissociation cross sections, for which no experimental measurements currently exist. This complete set of cross sections was then used to study the transport properties of electron swarms in THF, for a range of reduced electric fields from 0.01 - 10000 Td. The impact of the relevant cross sections on the transport properties has been discussed. The analysis also outlined issues associated with swarm measurements in THF, using current pulsed Townsend techniques, including a proposal for addressing them.

Using the formulated set of electron-THF cross sections, and appropriate modifications to approximate liquid transport, the differences between gaseous and an approximate liquid THF were presented and discussed. Simulation of streamer formation and propagation in liquid THF was then performed using this input data, in conjunction with the proposed modeling framework formulated during this research project. Clear variations between using approximate liquid data and simply scaling gas phase THF data were shown, reaffirming the need for accurate input data and careful formulation of electron transport modeling methods in liquids.

It is hoped that this study serves to motivate further theoretical and experimental studies of scattering, swarm transport, and interface dynamics of electrons in water and

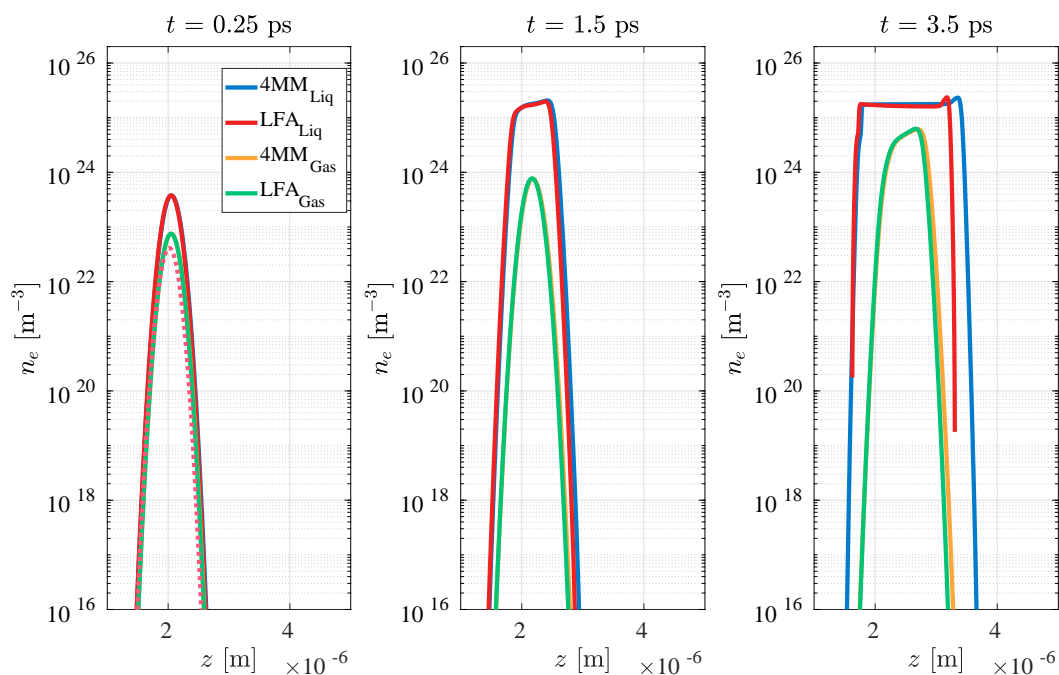


Figure 5.18: Electron density propagation within liquid THF. Pink dotted series denotes the initial condition. Evolution over time denotes major differences when using liquid data, compared to simply scaling gas phase data.

complex biomolecules to facilitate further understanding of emerging plasma medicine technologies.

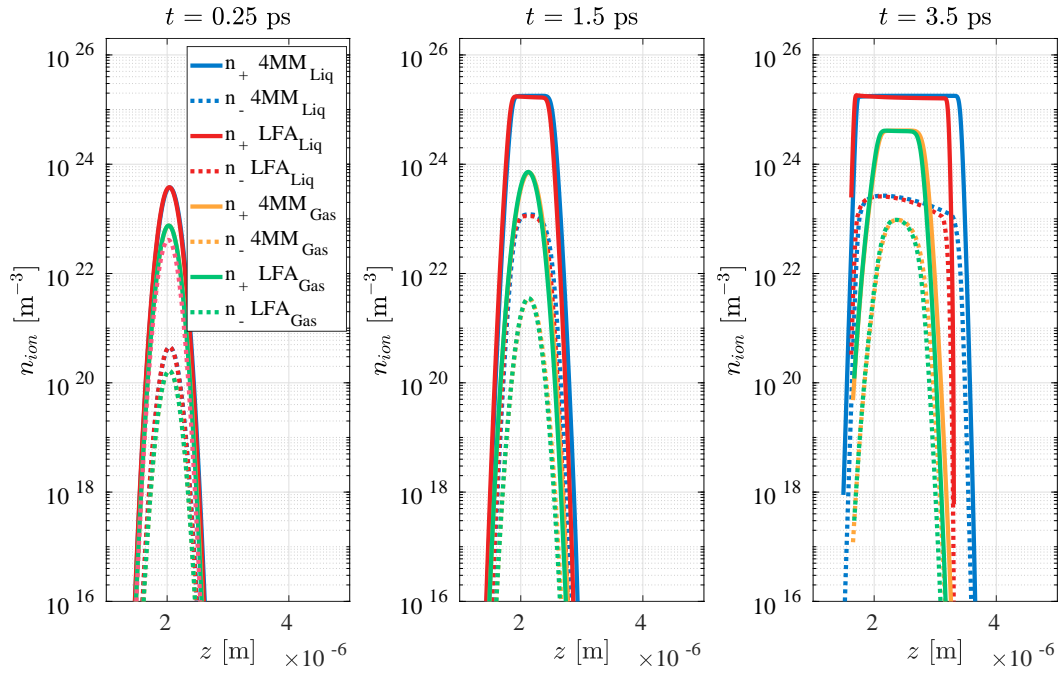


Figure 5.19: Ion density created within liquid THF. Solid lines denote  $n_+$  produced via electron impact ionisation. Dashed lines denote  $n_-$  produced via electron attachment. Pink dotted series denotes the initial  $n_+$  condition. Evolution over time denotes major differences when using liquid data, compared to simply scaling gas phase data.

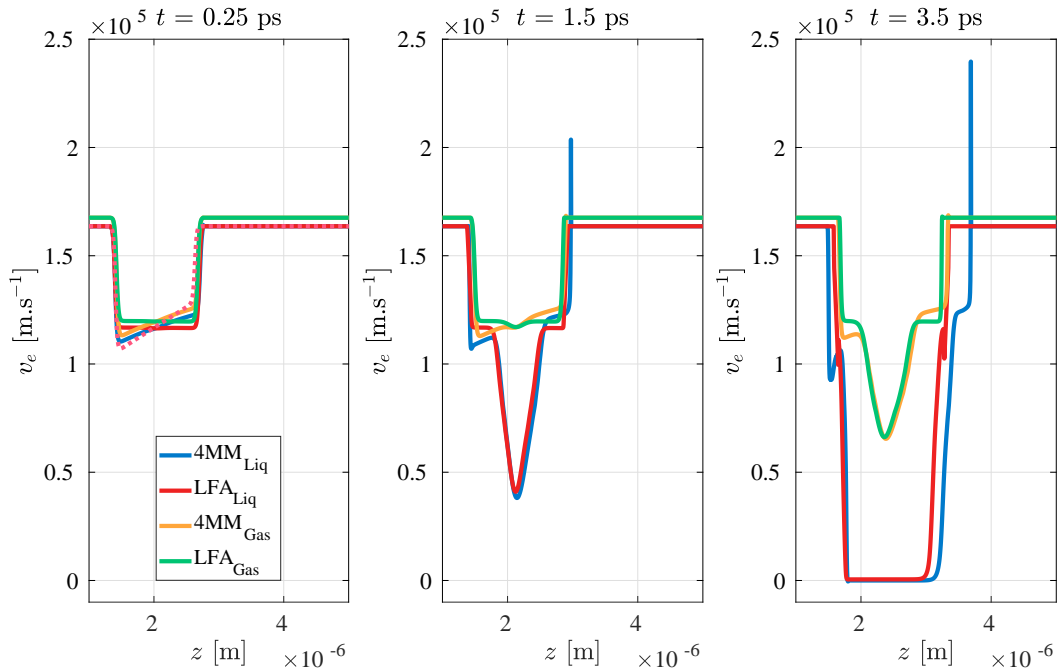


Figure 5.20: Evolution of the electron mean velocity experienced by a streamer front within liquid THF. Pink dotted series denotes the initial condition. Evolution over time denotes major differences when using liquid data, compared to simply scaling gas phase data.

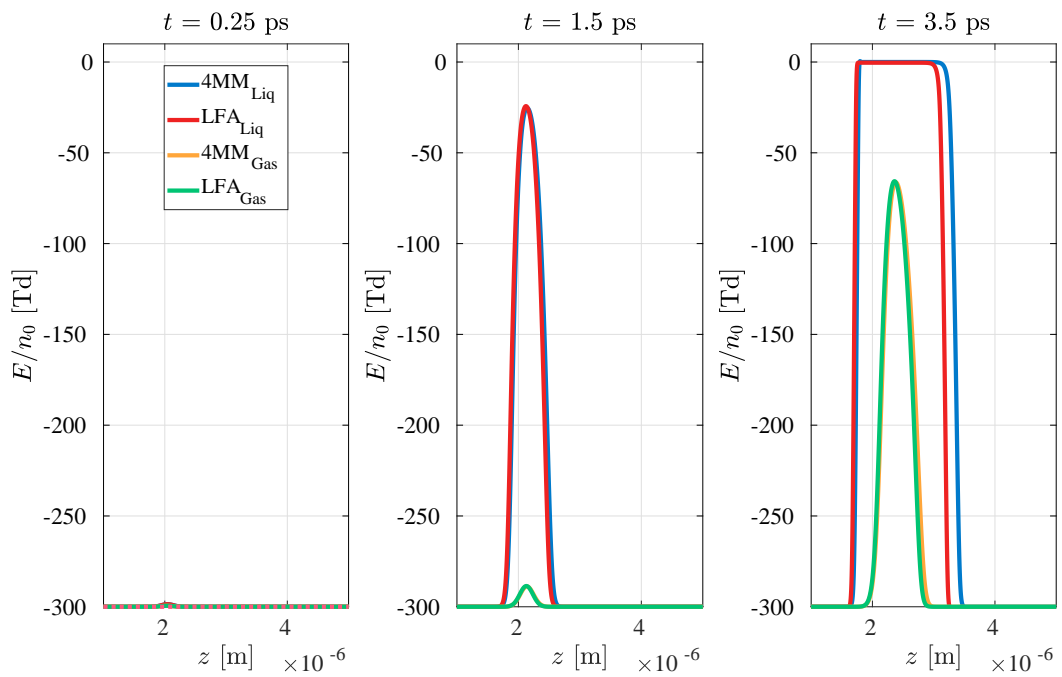


Figure 5.21: Evolution of the reduced electric field experienced by a streamer front within liquid THF. Pink dotted series denotes the initial condition. Evolution over time denotes major differences when using liquid data, compared to simply scaling gas phase data.

# 6

## Conclusion

### 6.1 Summary of results

---

Emerging plasma technologies, such as plasma medicine and plasma-water treatment, are reliant on the transfer of charged species from a gas phase plasma discharge, through an interfacial layer, to a soft-condensed liquid phase, such as tissue or water itself. The transport of electrons has been identified as a critical component to these applications, as electron-induced chemistry at the interface is a major source of ions and metastable reactive species that are delivered to the liquid. While the importance of electron transport near the interface has been identified, understanding of the physical transport mechanisms of electrons through the gas-liquid interface has received little attention. This research offers a first step to address this by proposing a simulation framework to model electron transport in, and between, gas and liquid discharge media.

To allow benchmarking and immediate application of the methods proposed in this study, a secondary application of dual phase gas-liquid particle detectors was identified. As liquid data is available for electron transport in simple atomic liquids, such as argon and xenon, the process of electron extraction from a detector's condensed liquid phase to gas phase can be modeled using the developed framework. Doing so allows demonstration of the applicability of the proposed framework, in order to facilitate future application to complex, polar liquids, such as water, found in plasma medicine applications.

The basis of the simulation framework was a non-local, four moment, fluid model for electron transport in both gas and liquid discharges. Proposals for parameter free, physical closure approximations and application of density-dependent liquid phase electron input data were outlined and validated against kinetic solutions of an analytic

simple liquid model. By assessing the assumptions employed in the four moment fluid model, the limitations of describing rapidly varying electron energy distribution functions through a moment model were also highlighted.

To bridge the gap between input data for gas and liquid phases, the non-linear dependence of electron transport on the background neutral density,  $n_0$ , was studied. To allow modeling of electron transport as a continuum across the interfacial layer, an approximation rule was proposed. The approximation method was validated against experimental data, and demonstrated the ability to resolve complex transport phenomena, particularly in liquid xenon. Implementing this approximation allowed computation of electron transport data at intermediate  $n_0$  values between gas and liquid density extrema. Modifications of gas phase cross sections were outlined in order to account for elastic coherent scattering, polarisation potential screening, and variation of the ionisation cross section threshold.

Application of the proposed fluid model, and input data approximation, was then made to simulate streamer transport from gas to liquid cryogenic argon phases. Additionally, extraction of electrons from condensed liquid into a gas layer was simulated to demonstrate applicability to electron transport in dual-phase liquid particle detectors. The effects of using scaled gas or accurate liquid input data, as well as assumption of a smooth or stepped interface transition, were studied for local reduced field dependent and mean energy dependent fluid models. It was demonstrated that the most reliable fluid modeling method was the proposed mean energy dependent four moment model. Application of this model was demonstrated to allow the option to simply assume a sheer step-function interface instead of a more complex tanh interfacial profile.

Finally, using available experimental and theoretical scattering cross sections for electrons in gaseous tetrahydrofuran (THF), the first complete cross section set for electron transport in THF was proposed. Using the available set of gas phase electron-THF cross sections, and an experimental static structure factor for liquid THF, a set of modified cross sections for electron transport in liquid THF were proposed to account for elastic coherent scattering and ionisation potential variation that arise at condensed phase densities. Electron transport data for gas and liquid phase THF was computed, and applied as input data to the simulation framework formulated in this study. Application of the modeling methods to streamer formation and propagation in liquid THF was demonstrated. As a result, clear differences were demonstrated between simply scaling gas phase data to liquid densities and using approximate liquid data accounting for elastic coherent scattering and ionisation threshold energy variation.

## 6.2 Future research directions

From the preceding research outcomes, a novel framework for simulating electron transport at gas-liquid interfaces has been demonstrated. While this outcome is a positive one, there are many remaining questions that need to be probed in future

research. Some possible directions that logically follow from this present research include:

**Expanding numerical implementation to two dimensional geometries** Transport simulations in two dimensions will allow important effects such as charge accumulation on the surface of a gas-liquid interface and anisotropic diffusion of species to be incorporated.

**Simulation of heavy particle transport** For the current research project, rapid electron dynamics were the primary focus however ion and neutral transport was not considered. In reality, the transport of ion and excited neutral species transport is very important for applications like plasma medicine, because much of the beneficial chemistry is delivered by interactions of these species with tissue.

**Inclusion of further scattering processes** In addition to the electron scattering processes considered in this study, further processes such as electron-ion recombination, ion-ion recombination, and electron-electron scattering should be factored into the collision data of the proposed model. Additionally, electron capture processes in polar liquids, such as solvation, should be accounted for by incorporating cross sections being developed in present theoretical studies.

**Incorporation of structured water transport data** As often mentioned in this research study, the big-picture goal of plasma-tissue interaction research is to achieve a better model of charged particle transport in human tissue by expanding upon the standard water vapour assumption. To achieve this, future research should endeavour to apply the developed framework to electron transport in structured water, and mixtures of water with biologically relevant molecules to achieve a more representative tissue analogue.

**Experimental studies of transport at the gas-liquid interface** To supplement theoretical studies, experimental studies of plasma interactions with liquid surfaces should be further developed. Diagnostic measurements of species transport at the interface, as well as deformation of the interface itself, are key areas of focus that could better inform models, such as that proposed in this present study.

# References

- [1] N. A. Garland, M. J. Brunger, G. Garcia, J. de Urquijo, and R. D. White. Transport properties of electron swarms in tetrahydrofuran under the influence of an applied electric field. *Physical Review A*, **88**, 062712 (2013).
- [2] N. A. Garland, D. G. Cocks, G. J. Boyle, S. Dujko, and R. D. White. Unified fluid model analysis and benchmark study for electron transport in gas and liquid analogs. *Plasma Sources Science and Technology*, **26**, 075003 (2017).
- [3] N. A. Garland, G. J. Boyle, D. G. Cocks, and R. D. White. Approximating the nonlinear density dependence of electron transport coefficients and scattering rates across the gas–liquid interface. *Plasma Sources Science and Technology*, **27**, 024002 (2018).
- [4] R. D. White, M. J. Brunger, N. A. Garland, R. E. Robson, K. F. Ness, G. Garcia, J. de Urquijo, S. Dujko, and Z. L. Petrović. Electron swarm transport in THF and water mixtures. *The European Physical Journal D*, **68**, 125 (2014).
- [5] R. D. White, D. Cocks, G. Boyle, M. Casey, N. Garland, D. Konovalov, B. Philippa, P. Stokes, J. de Urquijo, O. González-Magaña, R. P. McEachran, S. J. Buckman, M. J. Brunger, G. Garcia, S. Dujko, and Z. L. Petrovic. Electron transport in biomolecular gaseous and liquid systems: theory, experiment and self-consistent cross-sections. *Plasma Sources Science and Technology*, **27**, 053001 (2018).
- [6] M. Hoentsch, T. von Woedtke, K.-D. Weltmann, and J. Barbara Nebe. Time-dependent effects of low-temperature atmospheric-pressure argon plasma on epithelial cell attachment, viability and tight junction formation in vitro. *Journal of Physics D: Applied Physics*, **45**, 025206 (2012).
- [7] D. J. Lee, M. M. Da Gama, and K. E. Gubbins. The vapour-liquid interface for a lennard-jones model of argon-krypton mixtures. *Molecular Physics*, **53**, 1113 (1984).
- [8] A. Trokhymchuk and J. Alejandre. Computer simulations of liquid/vapor interface in Lennard-Jones fluids: Some questions and answers. *Journal of Chemical Physics*, **111**, 8510 (1999).

- [9] G. A. Chapela, G. Saville, S. M. Thompson, and J. S. Rowlinson. Computer simulation of a gas–liquid surface. Part 1. *J. Chem. Soc., Faraday Trans. 2*, **73**, 1133 (1977).
- [10] G. J. Boyle, W. J. Tattersall, D. G. Cocks, R. P. McEachran, and R. D. White. A multi-term solution of the space–time Boltzmann equation for electrons in gases and liquids. *Plasma Sources Science and Technology*, **26**, 024007 (2017).
- [11] E. Gushchin, A. Kruglov, and I. Obodovskii. Electron dynamics in condensed argon and xenon. *Sov. Phys. JETP*, **55**, 650 (1982).
- [12] G. J. Boyle, R. P. McEachran, D. G. Cocks, and R. D. White. Electron scattering and transport in liquid argon. *The Journal of Chemical Physics*, **142**, 154507 (2015).
- [13] L. S. Miller, S. Howe, and W. E. Spear. Charge Transport in Solid and Liquid Ar, Kr, and Xe. *Phys. Rev.*, **166**, 871 (1968).
- [14] J. L. Pack, R. E. Voshall, A. V. Phelps, and L. E. Kline. Longitudinal electron diffusion coefficients in gases: Noble gases. *Journal of Applied Physics*, **71**, 5363 (1992).
- [15] G. J. Boyle, R. P. McEachran, D. G. Cocks, M. J. Brunger, S. J. Buckman, S. Dujko, and R. D. White. Ab initio electron scattering cross-sections and transport in liquid xenon. *Journal of Physics D: Applied Physics*, **49**, 355201 (2016).
- [16] S. Huang and G. R. Freeman. Electron mobilities in gaseous, critical, and liquid xenon: Density, electric field, and temperature effects: Quasilocalization. *The Journal of Chemical Physics*, **68**, 1355 (1978).
- [17] M. Hayashi. *Bibliography of electron and photon cross sections with atoms and molecules published in the 20th century - Argon*. NIFS-DATA-72 (2003).
- [18] P. Mozejko, E. Ptasińska-Denga, A. Domaracka, and C. Szmytkowski. Absolute total cross-section measurements for electron collisions with tetrahydrofuran. *Physical Review A*, **74**, 012708 (2006).
- [19] M. C. Fuss, R. Colmenares, A. G. Sanz, A. Muñoz, J. C. Oller, F. Blanco, T. P. T. Do, M. J. Brunger, D. Almeida, P. Limão-Vieira, and G. García. Electron interactions with tetrahydrofuran. *Journal of Physics: Conference Series*, **373**, 012010 (2012).
- [20] A. Zecca, C. Perazzolli, and M. J. Brunger. Positron and electron scattering from tetrahydrofuran. *Journal of Physics B: Atomic, Molecular and Optical Physics*, **38**, 2079 (2005).

- [21] L. Chiari, E. Anderson, W. Tattersall, J. R. Machacek, P. Palihawadana, C. Makochekanwa, J. P. Sullivan, G. García, F. Blanco, R. P. McEachran, M. J. Brunger, and S. J. Buckman. Total, elastic, and inelastic cross sections for positron and electron collisions with tetrahydrofuran. *The Journal of Chemical Physics*, **138**, 074301 (2013).
- [22] W. Y. Baek, M. Bug, H. Rabus, E. Gargioni, and B. Grosswendt. Differential elastic and total electron scattering cross sections of tetrahydrofuran. *Physical Review A*, **86**, 032702 (2012).
- [23] M. Fuss, A. Muñoz, J. C. Oller, F. Blanco, D. Almeida, P. Limão-Vieira, T. P. D. Do, M. J. Brunger, and G. García. Electron-scattering cross sections for collisions with tetrahydrofuran from 50 to 5000 eV. *Physical Review A*, **80**, 052709 (2009).
- [24] C. J. Colyer, V. Vizcaino, J. P. Sullivan, M. J. Brunger, and S. J. Buckman. Absolute elastic cross-sections for low-energy electron scattering from tetrahydrofuran. *New Journal of Physics*, **9**, 41 (2007).
- [25] A. Gauf, L. R. Hargreaves, A. Jo, J. Tanner, M. A. Khakoo, T. Walls, C. Winstead, and V. McKoy. Low-energy electron scattering by tetrahydrofuran. *Physical Review A*, **85**, 052717 (2012).
- [26] M. Dampc, A. R. Milosavljević, I. Linert, B. P. Marinković, and M. Zubek. Differential cross sections for low-energy elastic electron scattering from tetrahydrofuran in the angular range 20°–180°. *Physical Review A*, **75**, 042710 (2007).
- [27] M. Allan. Absolute angle-differential elastic and vibrational excitation cross sections for electron collisions with tetrahydrofuran. *Journal of Physics B: Atomic, Molecular and Optical Physics*, **40**, 3531 (2007).
- [28] M. A. Khakoo, D. Orton, L. R. Hargreaves, and N. Meyer. Electron-impact vibrational excitation of tetrahydrofuran. *Physical Review A*, **88**, 012705 (2013).
- [29] P. Mozejko and L. Sanche. Cross sections for electron scattering from selected components of DNA and RNA. *Radiation Physics and Chemistry*, **73**, 77 (2005).
- [30] M. Dampc, E. Szymańska, B. Mielewska, and M. Zubek. Ionization and ionic fragmentation of tetrahydrofuran molecules by electron collisions. *Journal of Physics B: Atomic, Molecular and Optical Physics*, **44**, 055206 (2011).
- [31] T. P. T. Do, M. Leung, M. Fuss, G. Garcia, F. Blanco, K. Ratnavelu, and M. J. Brunger. Excitation of electronic states in tetrahydrofuran by electron impact. *The Journal of Chemical Physics*, **134**, 144302 (2011).
- [32] D. T. Bowron, J. L. Finney, and A. K. Soper. The Structure of Liquid Tetrahydrofuran. *Journal of the American Chemical Society*, **128**, 5119 (2006).
- [33] M. A. Lieberman and A. J. Lichtenberg. *Principles of Plasma Discharges and Materials Processing*, 2nd Edition. Wiley-Interscience (2005). ISBN 0471720011.

- [34] I. Adamovich, S. D. Baalrud, A. Bogaerts, P. J. Bruggeman, M. Cappelli, V. Colombo, U. Czarnetzki, U. Ebert, J. G. Eden, P. Favia, D. B. Graves, S. Hamaguchi, G. Hieftje, M. Hori, I. D. Kaganovich, U. Kortshagen, M. J. Kushner, N. J. Mason, S. Mazouffre, S. M. Thagard, H.-R. Metelmann, A. Mizuno, E. Moreau, A. B. Murphy, B. A. Niemira, G. S. Oehrlein, Z. L. Petrovic, L. C. Pitchford, Y.-K. Pu, S. Rauf, O. Sakai, S. Samukawa, S. Starikovskaia, J. Tennyson, K. Terashima, M. M. Turner, M. C. M. van de Sanden, and A. Vardelle. The 2017 Plasma Roadmap: Low temperature plasma science and technology. *Journal of Physics D: Applied Physics*, **50**, 323001 (2017).
- [35] F. Taccogna and F. Pellegrini. Kinetics of a plasma streamer ionization front. *Journal of Physics D: Applied Physics*, **51**, 064001 (2018).
- [36] P. K. Papadopoulos, P. Vafeas, P. Svarnas, K. Gazeli, P. M. Hatzikonstantinou, A. Gkelios, and F. Clément. Interpretation of the gas flow field modification induced by guided streamer (‘plasma bullet’) propagation. *Journal of Physics D: Applied Physics*, **47**, 425203 (2014).
- [37] J.-P. Boeuf, L. L. Yang, and L. C. Pitchford. Dynamics of a guided streamer (plasma bullet) in a helium jet in air at atmospheric pressure. *Journal of Physics D: Applied Physics*, **46**, 015201 (2013).
- [38] R. Brunetti, E. Calligarich, M. Cambiaghi, F. Carbonara, A. Cocco, C. De Vecchi, R. Dolfini, A. Ereditato, G. Fiorillo, L. Grandi, G. Mangano, A. Menegolli, C. Montanari, M. Prata, A. Rappoldi, G. L. Raselli, M. Roncadelli, M. Rossella, C. Rubbia, R. Santorelli, and C. Vignoli. WARP liquid argon detector for dark matter survey. *New Astronomy Reviews*, **49**, 265 (2005).
- [39] A. Bondar, A. Buzulutskov, A. Grebenuk, D. Pavlyuchenko, R. Snopkov, and Y. Tikhonov. Two-phase argon and xenon avalanche detectors based on Gas Electron Multipliers. *Nuclear Instruments and Methods in Physics Research, Section A: Accelerators, Spectrometers, Detectors and Associated Equipment*, **556**, 273 (2006).
- [40] C. Regenfus. The argon dark matter experiment (ArDM). *Journal of Physics: Conference Series*, **203**, 99 (2010).
- [41] S. Sangiorgio, T. Joshi, A. Bernstein, J. Coleman, M. Foxe, C. Hagmann, I. Jovanovic, K. Kazkaz, K. Mavrokoridis, V. Mozin, S. Pereverzev, and P. Sorensen. First demonstration of a sub-keV electron recoil energy threshold in a liquid argon ionization chamber. *Nuclear Instruments and Methods in Physics Research Section A: Accelerators, Spectrometers, Detectors and Associated Equipment*, **728**, 69 (2013).
- [42] T. Von Woedtke, H. R. Metelmann, and K. D. Weltmann. Clinical Plasma Medicine: State and Perspectives of in Vivo Application of Cold Atmospheric Plasma. *Contributions to Plasma Physics*, **54**, 104 (2014).

- [43] E. Stoffels, Y. Sakiyama, and D. B. Graves. Cold atmospheric plasma: Charged species and their interactions with cells and tissues. *IEEE Transactions on Plasma Science*, **36**, 1441 (2008).
- [44] M. G. Kong, G. Kroesen, G. Morfill, T. Nosenko, T. Shimizu, J. Van Dijk, and J. L. Zimmermann. Plasma medicine: An introductory review. *New Journal of Physics*, **11** (2009).
- [45] J. Heinlin, G. Morfill, M. Landthaler, W. Stolz, G. Isbary, J. L. Zimmermann, T. Shimizu, and S. Karrer. Plasma-Medizin: Anwendungsmöglichkeiten in der Dermatologie. *JDDG - Journal of the German Society of Dermatology*, **8**, 968 (2010).
- [46] S. Bekeschus, A. Schmidt, K. D. Weltmann, and T. von Woedtke. The plasma jet kINPen – A powerful tool for wound healing. *Clinical Plasma Medicine*, **4**, 19 (2016).
- [47] C. Chen, D. X. Liu, Z. C. Liu, A. J. Yang, H. L. Chen, G. Shama, and M. G. Kong. *A model of plasma-biofilm and plasma-tissue interactions at ambient pressure*, volume 34 (2014). ISBN 1109001495.
- [48] R. D. White and R. E. Robson. Multiterm solution of a generalized Boltzmann kinetic equation for electron and positron transport in structured and soft condensed matter. *Physical Review E*, **84**, 031125 (2011).
- [49] W. Tian and M. J. Kushner. Atmospheric pressure dielectric barrier discharges interacting with liquid covered tissue. *Journal of Physics D: Applied Physics*, **47**, 165201 (2014).
- [50] N. Y. Babaeva, W. Tian, and M. J. Kushner. The interaction between plasma filaments in dielectric barrier discharges and liquid covered wounds: electric fields delivered to model platelets and cells. *Journal of Physics D: Applied Physics*, **47**, 235201 (2014).
- [51] P. J. Bruggeman, M. J. Kushner, B. R. Locke, J. G. E. Gardeniers, W. G. Graham, D. B. Graves, R. C. H. M. Hofman-Caris, D. Maric, J. P. Reid, E. Ceriani, D. Fernandez Rivas, J. E. Foster, S. C. Garrick, Y. Gorbanev, S. Hamaguchi, F. Iza, H. Jablonowski, E. Klimova, J. Kolb, F. Krcma, P. Lukes, Z. Machala, I. Marinov, D. Mariotti, S. Mededovic Thagard, D. Minakata, E. C. Neyts, J. Pawlat, Z. L. Petrovic, R. Pflieger, S. Reuter, D. C. Schram, S. Schröter, M. Shiraiwa, B. Tarabová, P. A. Tsai, J. R. R. Verlet, T. von Woedtke, K. R. Wilson, K. Yasui, and G. Zvereva. Plasma–liquid interactions: a review and roadmap. *Plasma Sources Science and Technology*, **25**, 053002 (2016).
- [52] A. M. Lietz and M. J. Kushner. Air plasma treatment of liquid covered tissue: long timescale chemistry. *Journal of Physics D: Applied Physics*, **49**, 425204 (2016).

- [53] R. Gopalakrishnan, E. Kawamura, A. J. Lichtenberg, M. A. Lieberman, and D. B. Graves. Solvated electrons at the atmospheric pressure plasma-water anodic interface. *Journal of Physics D: Applied Physics*, **49**, 295205 (2016).
- [54] W. Schmidt. Electronic Conduction Processes in Dielectric Liquids. *IEEE Transactions on Electrical Insulation*, **EI-19**, 389 (1984).
- [55] Y. Sakai, S. Nakamura, and H. Tagashira. Drift Velocity of Hot Electrons in Liquid Ar, Kr, and Xe. *IEEE Transactions on Electrical Insulation*, **EI-20**, 133 (1985).
- [56] Y. Sakai, K. Sukegawa, S. Nakamura, and H. Tagashira. Monte Carlo simulation of electron transport behavior in liquid argon. *IEEE Transactions on Electrical Insulation*, **23**, 609 (1988).
- [57] J. Lekner. Motion of electrons in liquid argon. *Physical Review*, **158**, 130 (1967).
- [58] V. M. Atrazhev and I. T. Iakubov. Hot electrons in non-polar liquids. *Journal of Physics C: Solid State Physics*, **14**, 5139 (1981).
- [59] V. M. Atrazhev and I. T. Iakubov. The electron drift velocity in dense gases. *Journal of Physics D: Applied Physics*, **10**, 2155 (1977).
- [60] V. M. Atrazhev and E. G. Dmitriev. Hot electrons in atomic non-polar liquids with molecular impurities. *Journal of Physics C: Solid State Physics*, **19**, 4329 (1986).
- [61] V. Atrazhev and I. Timoshkin. Electron scattering by a cut-off atomic potential: Application to electron properties in atomic liquids. *Physical Review B - Condensed Matter and Materials Physics*, **54**, 11252 (1996).
- [62] W. F. Schmidt and E. Illenberger. Low energy electrons in non-polar liquids. *Nukleonika*, **48**, 75 (2003).
- [63] A. F. Borghesani, D. Iannuzzi, and G. Carugno. Excess electron mobility in liquid Ar-Kr and Ar-Xe mixtures. *Journal of Physics Condensed Matter*, **9**, 5057 (1997).
- [64] A. F. Borghesani. Electron and ion transport in dense rare gases. *IEEE Transactions on Dielectrics and Electrical Insulation*, **13**, 492 (2006).
- [65] W. J. Tattersall, D. G. Cocks, G. J. Boyle, S. J. Buckman, and R. D. White. Monte Carlo study of coherent scattering effects of low-energy charged particle transport in Percus-Yevick liquids. *Physical Review E*, **91**, 043304 (2015).
- [66] L. Boltzmann. *Lectures on Gas Theory translated by Stephen G Brush*. University of California Press, Berkeley (1872).

- [67] R. White, W. Tattersall, G. Boyle, R. Robson, S. Dujko, Z. Petrovic, A. Bankovic, M. Brunger, J. Sullivan, S. Buckman, and G. Garcia. Low-energy electron and positron transport in gases and soft-condensed systems of biological relevance. *Applied Radiation and Isotopes*, **83**, 77 (2014).
- [68] R. White, K. Ness, and R. Robson. Development of swarm transport theory in radio-frequency electric and crossed electric and magnetic fields. *Applied Surface Science*, **192**, 26 (2002).
- [69] G. J. Hagelaar and L. C. Pitchford. Solving the Boltzmann equation to obtain electron transport coefficients and rate coefficients for fluid models. *Plasma Sources Science and Technology*, **14**, 722 (2005).
- [70] R. E. Robson and K. F. Ness. Velocity distribution function and transport coefficients of electron swarms in gases: Spherical-harmonics decomposition of Boltzmann's equation. *Physical Review A*, **33**, 2068 (1986).
- [71] M. J. Brunger and S. J. Buckman. Electron-molecule scattering cross-sections. I. Experimental techniques and data for diatomic molecules. *Physics Reports*, **357**, 215 (2002).
- [72] S. J. Buckman and M. J. Brunger. A Critical Comparison of Electron Scattering Cross Sections measured by Single Collision and Swarm Techniques. *Australian Journal of Physics*, **50**, 483 (1997).
- [73] G. Ruíz-Vargas, M. Yousfi, and J. de Urquijo. Electron transport coefficients in the mixtures of H<sub>2</sub>O with N<sub>2</sub>, O<sub>2</sub>, CO<sub>2</sub> and dry air for the optimization of non-thermal atmospheric pressure plasmas. *Journal of Physics D: Applied Physics*, **43**, 455201 (2010).
- [74] C. Champion. Quantum-mechanical predictions of electron-induced ionization cross sections of DNA components. *The Journal of Chemical Physics*, **138**, 184306 (2013).
- [75] R. W. Crompton and M. A. Morrison. Analyses of Recent Experimental and Theoretical Determinations of e<sup>-</sup>-H<sub>2</sub> Vibrational Excitation Cross Sections: Assessing a Long-Standing Controversy. *Australian Journal of Physics*, **46**, 203 (1993).
- [76] R. Robson, R. White, and M. Hildebrandt. *Fundamentals of Charged Particle Transport in Gases and Condensed Matter (Monograph Series in Physical Sciences)*. CRC Press (2017). ISBN 9781498736367.
- [77] G. U. C.S. Wang-Chang and J. de Boer. *Studies in Statistical Mechanics II*. Wiley, New York (1964).
- [78] R. E. Robson and K. F. Ness. Physics of reacting particle swarms. III. Effects of ionization upon transport coefficients. *The Journal of Chemical Physics*, **89**, 4815 (1988).

- [79] A. M. Nolan, M. J. Brennan, K. F. Ness, and A. B. Wedding. A benchmark model for analysis of electron transport in non-conservative gases. *Journal of Physics D: Applied Physics*, **30**, 2865 (1997).
- [80] J. A. Bittencourt. *Fundamentals of plasma physics*. Springer, New York (2004). ISBN 0387209751.
- [81] M. Cohen and J. Lekner. Theory of Hot Electrons in Gases, Liquids, and Solids. *Physical Review*, **158**, 305 (1967).
- [82] L. Van Hove. Correlations in Space and Time and Born Approximation Scattering in Systems of Interacting Particles. *Physical Review*, **95**, 249 (1954).
- [83] L. Verlet and J.-J. Weis. Equilibrium Theory of Simple Liquids. *Physical Review A*, **5**, 939 (1972).
- [84] N. W. Ashcroft and D. C. Langreth. Structure of binary liquid mixtures. I. *Physical Review*, **156**, 685 (1967).
- [85] J. L. Yarnell, M. J. Katz, R. G. Wenzel, and S. H. Koenig. Structure Factor and Radial Distribution Function for Liquid Argon at 85 °K. *Physical Review A*, **7**, 2130 (1973).
- [86] N. Baguer, A. Bogaerts, and R. Gijbels. Hollow cathode glow discharge in He: Monte Carlo-fluid model combined with a transport model for the metastable atoms. *Journal of Applied Physics*, **93**, 47 (2003).
- [87] S. Dujko, R. D. White, and Z. L. Petrović. Monte Carlo studies of non-conservative electron transport in the steady-state Townsend experiment. *Journal of Physics D: Applied Physics*, **41**, 245205 (2008).
- [88] D. P. Lymberopoulos and D. J. Economou. Two-Dimensional Self-Consistent Radio-Frequency Plasma Simulations Relevant to the Gaseous Electronics Conference Rf Reference Cell. *Journal of Research of the National Institute of Standards and Technology*, **100**, 473 (1995).
- [89] M. M. Becker, H. Kählert, A. Sun, M. Bonitz, and D. Loffhagen. Advanced fluid modeling and PIC/MCC simulations of low-pressure ccrf discharges. *Plasma Sources Science and Technology*, **26**, 044001 (2017).
- [90] M. M. Turner, A. Derzsi, Z. Donkó, D. Eremin, S. J. Kelly, T. Lafleur, and T. Mussenbrock. Simulation benchmarks for low-pressure plasmas: Capacitive discharges. *Physics of Plasmas*, **20**, 013507 (2013).
- [91] A. L. Ward. Effect of Space Charge in Cold-Cathode Gas Discharges. *Phys. Rev.*, **112**, 1852 (1958).
- [92] J. P. Boeuf. Numerical model of rf glow discharges. *Physical Review A*, **36**, 2782 (1987).

- [93] G. Hagelaar and G. Kroesen. Speeding Up Fluid Models for Gas Discharges by Implicit Treatment of the Electron Energy Source Term. *Journal of Computational Physics*, **159**, 1 (2000).
- [94] M. M. Becker and D. Loffhagen. Derivation of Moment Equations for the Theoretical Description of Electrons in Nonthermal Plasmas. *Advances in Pure Mathematics*, **03**, 343 (2013).
- [95] S. Dujko, A. H. Markosyan, R. D. White, and U. Ebert. High-order fluid model for streamer discharges: I. Derivation of model and transport data. *Journal of Physics D: Applied Physics*, **46**, 475202 (2013).
- [96] R. E. Robson, R. D. White, and Z. L. Petrović. Colloquium : Physically based fluid modeling of collisionally dominated low-temperature plasmas. *Reviews of Modern Physics*, **77**, 1303 (2005).
- [97] P. Nicoletopoulos, R. E. Robson, and R. D. White. Fluid-model analysis of electron swarms in a space-varying field: Nonlocality and resonance phenomena. *Physical Review E*, **85**, 046404 (2012).
- [98] P. Nicoletopoulos and R. E. Robson. Periodic Electron Structures in Gases: A Fluid Model of the “Window” Phenomenon. *Physical Review Letters*, **100**, 124502 (2008).
- [99] P. W. Stokes, I. Simonović, B. Philippa, D. Cocks, S. Dujko, and R. D. White. Third-order transport coefficients for localised and delocalised charged-particle transport. *Scientific Reports*, **8**, 2226 (2018).
- [100] J. P. Boeuf and L. C. Pitchford. Two-dimensional model of a capacitively coupled rf discharge and comparisons with experiments in the Gaseous Electronics Conference reference reactor. *Physical Review E*, **51**, 1376 (1995).
- [101] G. K. Grubert, M. M. Becker, and D. Loffhagen. Why the local-mean-energy approximation should be used in hydrodynamic plasma descriptions instead of the local-field approximation. *Physical Review E*, **80**, 036405 (2009).
- [102] S. Dujko, R. D. White, Z. L. Petrović, and R. E. Robson. A multi-term solution of the nonconservative Boltzmann equation for the analysis of temporal and spatial non-local effects in charged-particle swarms in electric and magnetic fields. *Plasma Sources Science and Technology*, **20**, 024013 (2011).
- [103] M. M. Becker and D. Loffhagen. Enhanced reliability of drift-diffusion approximation for electrons in fluid models for nonthermal plasmas. *AIP Advances*, **3**, 012108 (2013).
- [104] A. H. Markosyan, J. Teunissen, S. Dujko, and U. Ebert. Comparing plasma fluid models of different order for 1D streamer ionization fronts. *Plasma Sources Science and Technology*, **24**, 065002 (2015).

- [105] R. E. Robson, P. Nicoletopoulos, M. Hildebrandt, and R. D. White. Fundamental issues in fluid modeling: Direct substitution and aliasing methods. *The Journal of Chemical Physics*, **137**, 214112 (2012).
- [106] R. Robson, R. White, and T. Makabe. Charged Particle Transport in Harmonically Varying Electric Fields: Foundations and Phenomenology. *Annals of Physics*, **261**, 74 (1997).
- [107] T. Govindan and M. Meyyappan. One-Dimensional Modeling Studies of the Gaseous Electronics Conference Rf Reference Cell. *Journal of Research of the National Institute of Standards and Technology*, **100**, 463 (1995).
- [108] J. D. P. Passchier and W. J. Goedheer. A two-dimensional fluid model for an argon rf discharge. *Journal of Applied Physics*, **74**, 3744 (1993).
- [109] T. K. Senega and R. P. Brinkmann. A multi-component transport model for non-equilibrium low-temperature low-pressure plasmas. *Journal of Physics D: Applied Physics*, **39**, 1606 (2006).
- [110] M. Surendra. Radiofrequency discharge benchmark model comparison. *Plasma Sources Science and Technology*, **4**, 56 (1995).
- [111] A. D. Lindsay, D. B. Graves, and S. C. Shannon. Fully coupled simulation of the plasma liquid interface and interfacial coefficient effects. *Journal of Physics D: Applied Physics*, **49**, 235204 (2016).
- [112] S. COMSOL AB. Comsol multiphysics®.
- [113] A. Venkatraman and A. K. Verma. plasmaFoam: An OpenFOAM framework for computational plasma physics and chemistry. In *APS Meeting Abstracts*, DT2.007 (2016).
- [114] OpenCFD. *OpenFOAM - The Open Source CFD Toolbox - User's Guide*. OpenCFD Ltd., United Kingdom.
- [115] J. van Dijk, K. Peerenboom, M. Jimenez, D. Mihailova, and J. van der Mullen. The plasma modelling toolkit Plasimo. *Journal of Physics D: Applied Physics*, **42**, 194012 (2009).
- [116] J. Golda, J. Held, B. Redeker, M. Konkowski, P. Beijer, A. Sobota, G. Kroesen, N. S. J. Braithwaite, S. Reuter, M. M. Turner, T. Gans, D. O'Connell, and V. Schulz-von der Gathen. Concepts and characteristics of the 'COST Reference Microplasma Jet'. *Journal of Physics D: Applied Physics*, **49**, 084003 (2016).
- [117] J. Lucas and H. T. Saelee. A comparison of a Monte Carlo simulation and the Boltzmann solution for electron swarm motion in gases. *Journal of Physics D: Applied Physics*, **8**, 640 (1975).

- [118] R. E. Robson. *Introductory Transport Theory for Charged Particles in Gases*. World Scientific Pub Co Inc (2006). ISBN 9812700110.
- [119] J. de Urquijo, A. Mitrani, G. Ruíz-Vargas, and E. Basurto. Limiting field strength and electron swarm coefficients of the CF 3 I–SF 6 gas mixture. *Journal of Physics D: Applied Physics*, **44**, 342001 (2011).
- [120] Z. L. Petrović, A. Banković, S. Dujko, S. Marjanović, M. Šuvakov, G. Malović, J. P. Marler, S. J. Buckman, R. D. White, and R. E. Robson. On new developments in the physics of positron swarms. *Journal of Physics: Conference Series*, **199**, 012016 (2010).
- [121] Z. L. Petrović, S. Dujko, D. Marić, G. Malović, Ž. Nikitović, O. Šašić, J. Jovanović, V. Stojanović, and M. Radmilović-Radenović. Measurement and interpretation of swarm parameters and their application in plasma modelling. *Journal of Physics D: Applied Physics*, **42**, 194002 (2009).
- [122] Z. L. Petrovic and R. W. Crompton. A Swarm Experiment in He–H<sub>2</sub> Mixtures to Examine Vibrational Excitation of H<sub>2</sub> by Electron Impact. *Australian Journal of Physics*, **40**, 347 (1987).
- [123] V. M. Atrazhev, I. V. Chernysheva, N. Bonifaci, and A. Denat. Time-of-flight method for determination of concentration of molecular impurity in atomic liquids. *IEEE International Conference on Dielectric Liquids, 2005. ICDL 2005.*, 45–48 (2005).
- [124] A. Bekstein, J. De Urquijo, O. Ducasse, J. C. Rodríguez-Luna, and A. M. Juárez. Determination of transport and reaction swarm coefficients from the analysis of complex transient pulses from the pulsed Townsend experiment. *Journal of Physics: Conference Series*, **370**, 012006 (2012).
- [125] A. Banković, J. Marler, M. Šuvakov, G. Malović, and Z. Petrović. Transport coefficients for positron swarms in nitrogen. *Nuclear Instruments and Methods in Physics Research Section B: Beam Interactions with Materials and Atoms*, **266**, 462 (2008).
- [126] R. D. White, K. F. Ness, and R. E. Robson. Velocity distribution functions for electron swarms in methane in electric and magnetic fields. *Journal of Physics D: Applied Physics*, **32**, 1842 (1999).
- [127] E. Shibamura, T. Takahashi, S. Kubota, and T. Doke. Ratio of diffusion coefficient to mobility for electrons in liquid argon. *Physical Review A*, **20**, 2547 (1979).
- [128] K. F. Ness, R. E. Robson, M. J. Brunger, and R. D. White. Transport coefficients and cross sections for electrons in water vapour: Comparison of cross section sets using an improved Boltzmann equation solution. *The Journal of Chemical Physics*, **136**, 024318 (2012).

- [129] Y. Itikawa and N. Mason. Cross Sections for Electron Collisions with Water Molecules. *Journal of Physical and Chemical Reference Data*, **34**, 1 (2005).
- [130] B. Boudaïffa, P. Cloutier, D. Hunting, M. A. Huels, and L. Sanche. Resonant formation of DNA strand breaks by low-energy (3 to 20 eV) electrons. *Science*, **287**, 1658 (2000).
- [131] B. Boudaïffa, D. Hunting, P. Cloutier,. Induction of single- and double-strand breaks in plasmid DNA by 100–1500 eV electrons. *International Journal of Radiation Biology*, **76**, 1209 (2000).
- [132] R. D. White, R. E. Robson, S. Dujko, P. Nicoletopoulos, and B. Li. Recent advances in the application of Boltzmann equation and fluid equation methods to charged particle transport in non-equilibrium plasmas. *Journal of Physics D: Applied Physics*, **42**, 194001 (2009).
- [133] M. G. P. Homem, R. T. Sugohara, I. P. Sanches, M. T. Lee, and I. Iga. Cross sections for elastic electron collisions with tetrahydrofuran. *Physical Review A*, **80**, 032705 (2009).
- [134] M. Dampe, I. Linert, A. R. Milosavljević, and M. Zubek. Vibrational excitation of tetrahydrofuran by electron impact in the low energy range. *Chemical Physics Letters*, **443**, 17 (2007).
- [135] M. Zubek, M. Dampe, I. Linert, and T. Neumann. Electronic states of tetrahydrofuran molecules studied by electron collisions. *The Journal of Chemical Physics*, **135**, 134317 (2011).
- [136] D. Bouchiha, J. D. Gorfinkiel, L. G. Caron, and L. Sanche. Low-energy electron collisions with tetrahydrofuran. *Journal of Physics B: Atomic, Molecular and Optical Physics*, **39**, 975 (2006).
- [137] C. Winstead and V. McKoy. Low-energy electron scattering by deoxyribose and related molecules. *The Journal of Chemical Physics*, **125**, 074302 (2006).
- [138] C. S. Trevisan, A. E. Orel, and T. N. Rescigno. Elastic scattering of low-energy electrons by tetrahydrofuran. *Journal of Physics B: Atomic, Molecular and Optical Physics*, **39**, L255 (2006).
- [139] C. Richmonds, M. Witzke, B. Bartling, S. W. Lee, J. Wainright, C. C. Liu, and R. M. Sankaran. Electron-transfer reactions at the plasma-liquid interface. *Journal of the American Chemical Society*, **133**, 17582 (2011).
- [140] D. Mariotti, J. Patel, V. Švrček, and P. Maguire. Plasma-liquid interactions at atmospheric pressure for nanomaterials synthesis and surface engineering. *Plasma Processes and Polymers*, **9**, 1074 (2012).

- [141] Y. Sakai. Quasifree electron transport under electric field in nonpolar simple-structured condensed matters. *Journal of Physics D: Applied Physics*, **40**, R441 (2007).
- [142] K. F. Ness and R. E. Robson. Velocity distribution function and transport coefficients of electron swarms in gases. II. Moment equations and applications. *Physical Review A*, **34**, 2185 (1986).
- [143] M. J. Kushner. Modeling of microdischarge devices: Pyramidal structures. *Journal of Applied Physics*, **95**, 846 (2004).
- [144] M. M. Becker and D. Loffhagen. Consistent description of electron transport in fluid models for nonthermal plasmas. *Icpig Xxxi*, 2–5 (2013).
- [145] F. Sigeneger and D. Loffhagen. Fluid model of a single striated filament in an RF plasma jet at atmospheric pressure. *Plasma Sources Science and Technology*, **25**, 35020 (2016).
- [146] A. H. Markosyan, S. Dujko, and U. Ebert. High-order fluid model for streamer discharges: II. Numerical solution and investigation of planar fronts. *Journal of Physics D: Applied Physics*, **46**, 475203 (2013).
- [147] B. Ramamurthi, D. J. Economou, and I. D. Kaganovich. Effect of non-local electron conductivity on power absorption and plasma density profiles in low pressure inductively coupled discharges. *Plasma Sources Science and Technology*, **12**, 170 (2003).
- [148] L. D. Tsendin. Nonlocal electron kinetics in gas-discharge plasma. *Physics-Uspokhi*, **53**, 133 (2010).
- [149] F. Sigeneger and R. Winkler. Nonlocal transport and dissipation properties of electrons in inhomogeneous plasmas. *IEEE Transactions on Plasma Science*, **27**, 1254 (1999).
- [150] J. P. Boris and D. L. Book. Flux-corrected transport. I. SHASTA, a fluid transport algorithm that works. *Journal of Computational Physics*, **11**, 38 (1973).
- [151] S. T. Zalesak. Fully multidimensional flux-corrected transport algorithms for fluids. *Journal of Computational Physics*, **31**, 335 (1979).
- [152] S. T. Zalesak. The Design of Flux-Corrected Transport (FCT) Algorithms for Structured Grids. In *Flux-Corrected Transport*, edited by D. Kuzmin, R. Löhner, and S. Turek, Scientific Computation., 23–65. Springer, Dordrecht (2012). ISBN 978-94-007-4037-2.
- [153] R. E. Robson, B. Li, and R. D. White. Spatially periodic structures in electron swarms and the Franck-Hertz experiment. *Journal of Physics B: Atomic, Molecular and Optical Physics*, **33**, 507 (2000).

- [154] L. Verlet and J.-J. Weis. Equilibrium Theory of Simple Liquids. *Physical Review A*, **5**, 939 (1972).
- [155] M. H. Kalos, J. K. Percus, and M. Rao. Structure of a liquid-vapor interface. *Journal of Statistical Physics*, **17**, 111 (1977).
- [156] P. Yi, D. Poulikakos, J. Walther, and G. Yadigaroglu. Molecular dynamics simulation of vaporization of an ultra-thin liquid argon layer on a surface. *International Journal of Heat and Mass Transfer*, **45**, 2087 (2002).
- [157] A. Blanc. Recherches sur les mobilités des ions dans les gaz. *Journal de Physique Théorique et Appliquée*, **7**, 825 (1908).
- [158] J. V. Jovanović, S. B. Vrhovac, and Z. L. Petrović. Application of Blanc's law at arbitrary electric field to gas density ratios. *European Physical Journal D*, **28**, 91 (2004).
- [159] R. V. Chiffikian. The analog of Blanc's law for drift velocities of electrons in gas mixtures in weakly ionized plasma. *Physics of Plasmas*, **2**, 3902 (1995).
- [160] R. D. White, K. F. Ness, R. E. Robson, and B. Li. Charged-particle transport in gases in electric and magnetic fields crossed at arbitrary angles: Multiterm solution of Boltzmann's equation. *Physical Review E*, **60**, 2231 (1999).
- [161] G. J. Boyle, R. D. White, R. E. Robson, S. Dujko, and Z. Lj Petrović. On the approximation of transport properties in structured materials using momentum-transfer theory. *New Journal of Physics*, **14**, 045011 (2012).
- [162] V. Atrazhev, A. Berezhnov, D. Dunikov, I. Chernysheva, V. Dmitrenko, and G. Kapralova. Electron transport coefficients in liquid xenon. *IEEE International Conference on Dielectric Liquids, 2005. ICDL 2005.*, 1–4 (2005).
- [163] O. Sifner and J. Klomfar. Thermodynamic Properties of Xenon from the Triple Point to 800 K with Pressures up to 350 MPa. *Journal of Physical and Chemical Reference Data*, **23**, 63 (1994).
- [164] R. B. Stewart and R. T. Jacobsen. Thermodynamic Properties of Argon from the Triple Point to 1200 K with Pressures to 1000 MPa. *Journal of Physical and Chemical Reference Data*, **18**, 639 (1989).
- [165] S. I. Sandler and E. A. Mason. Kinetic-Theory Deviations from Blanc's Law of Ion Mobilities. *The Journal of Chemical Physics*, **48**, 2873 (1968).
- [166] H. B. Milloy and R. E. Robson. The mobility of potassium ions in gas mixtures. *Journal of Physics B: Atomic and Molecular Physics*, **6**, 1139 (1973).
- [167] M. A. Biondi and L. M. Chanin. Blanc's law-ion mobilities in helium-neon mixtures. *Physical Review*, **122**, 843 (1961).

- [168] O. Šašić, J. Jovanović, Z. L. Petrović, J. de Urquijo, J. R. Castrejón-Pita, J. L. Hernández-Ávila, and E. Basurto. Electron drift velocities in mixtures of helium and xenon and experimental verification of corrections to Blanc's law. *Physical Review E*, **71**, 046408 (2005).
- [169] U. Ebert, F. Brau, G. Derks, W. Hundsdorfer, C.-Y. Kao, C. Li, A. Luque, B. Meulenbroek, S. Nijdam, V. Ratushnaya, L. Schäfer, and S. Tanveer. Multiple scales in streamer discharges, with an emphasis on moving boundary approximations. *Nonlinearity*, **24**, C1 (2011).
- [170] J. Meunier, P. Belenguer, and J. P. Boeuf. Numerical-Model of an Ac Plasma Display Panel Cell in Neon-Xenon Mixtures. *Journal of Applied Physics*, **78**, 731 (1995).
- [171] S. Dujko, R. D. White, Z. L. Petrović, and R. E. Robson. Benchmark calculations of nonconservative charged-particle swarms in dc electric and magnetic fields crossed at arbitrary angles. *Physical Review E*, **81**, 046403 (2010).
- [172] C. K. Birdsall and L. Fellow. Particle-in-Cell charged-particle simulations, Plus Monte Carlo collision with neutral atom, PIC-MCC. *IEEE Transactions on Plasma Science*, **19**, 65 (1991).
- [173] S. Dujko, I. Simonovic, G. Boyle, R. White, D. Bosnjakovic, and Z. Petrovic. Transport properties of electrons and transition of an electron avalanche into a streamer in atomic liquids. In *APS Gaseous Electronics Conference 2016 Abstracts*, MW6.036 (2016).
- [174] I. Simonović, Z. L. Petrović, and S. Dujko. Simulation of electron transport and negative planar streamer fronts in liquid argon and liquid xenon. In *Proc. 21st Symposium on Application of Plasma Processes (SAPP XXI)*, 226–230 (2017).
- [175] C. M. Evans and G. L. Findley. Energy of the Conduction Band in Near Critical Point Fluids. *Physics Research International*, **2010**, 1 (2010).
- [176] U. Asaf and I. T. Steinberger. Photoconductivity and electron transport parameters in liquid and solid xenon. *Physical Review B*, **10**, 4464 (1974).
- [177] M. Miyajima, T. Takahashi, S. Konno, T. Hamada, S. Kubota, H. Shibamura, and T. Doke. Average energy expended per ion pair in liquid argon. *Physical Review A*, **9**, 1438 (1974).
- [178] B. Halpern, J. Lekner, S. Rice, and R. Gomer. Drift Velocity and Energy of Electrons in Liquid Argon. *Physical Review*, **156**, 351 (1967).
- [179] M. Foxe, C. Hagmann, I. Jovanovic, A. Bernstein, K. Kazkaz, V. Mozin, S. Pereverzev, S. Sangiorgio, and P. Sorensen. Low-energy (<10 keV) electron ionization and recombination model for a liquid argon detector. *Nuclear Instruments and Methods in Physics Research Section A: Accelerators, Spectrometers, Detectors and Associated Equipment*, **771**, 88 (2015).

- [180] T. Ishiyama, T. Yano, and S. Fujikawa. Molecular dynamics study of kinetic boundary condition at an interface between argon vapor and its condensed phase. *Physics of Fluids*, **16**, 2899 (2004).
- [181] R. L. Amey and R. H. Cole. Dielectric Constants of Liquefied Noble Gases and Methane. *The Journal of Chemical Physics*, **40**, 146 (1964).
- [182] R. Swanson and E. Turkel. On central-difference and upwind schemes. *Journal of Computational Physics*, **101**, 292 (1992).
- [183] H. Lippold. Isothermal Compressibility and Density of Liquid Argon and Neon Up To Pressures of 1000 kg/cm<sup>2</sup>. *Cryogenics*, **April**, 112 (1969).
- [184] B. Abel, U. Buck, A. L. Sobolewski, and W. Domcke. On the nature and signatures of the solvated electron in water. *Phys. Chem. Chem. Phys.*, **14**, 22 (2012).
- [185] R. Robson. Generalized Einstein Relation and Negative Differential Conductivity in Gases. *Australian Journal of Physics*, **37**, 35 (1984).
- [186] K. Anzai, H. Kato, M. Hoshino, H. Tanaka, Y. Itikawa, L. Campbell, M. J. Brunger, S. J. Buckman, H. Cho, F. Blanco, G. Garcia, P. Limão-Vieira, and O. Ingólfsson. Cross section data sets for electron collisions with H<sub>2</sub>, O<sub>2</sub>, CO, CO<sub>2</sub>, N<sub>2</sub>O and H<sub>2</sub>O. *The European Physical Journal D*, **66**, 36 (2012).
- [187] Y. Itikawa. Cross Sections for Electron Collisions With Carbon Dioxide. *Journal of Physical and Chemical Reference Data*, **31**, 749 (2002).
- [188] Y. Itikawa. Cross Sections for Electron Collisions with Oxygen Molecules. *Journal of Physical and Chemical Reference Data*, **38**, 1 (2009).
- [189] A. Zecca, G. P. Karwasz, and R. S. Brusa. Total-cross-section measurements for electron scattering by NH<sub>3</sub>, SiH<sub>4</sub>, and H<sub>2</sub>S in the intermediate-energy range. *Physical Review A*, **45**, 2777 (1992).
- [190] R. C. L.G.H. Huxley. *The diffusion and drift of electrons in gases*. Wiley, New York (1974).
- [191] K. Kumar, H. Skullerud, and R. Robson. Kinetic Theory of Charged Particle Swarms in Neutral Gases. *Australian Journal of Physics*, **33**, 343 (1980).
- [192] S. Dupljanin, J. de Urquijo, O. Šašić, E. Basurto, A. M. Juárez, J. L. Hernández-Ávila, S. Dujko, and Z. L. Petrović. Transport coefficients and cross sections for electrons in N<sub>2</sub>O and N<sub>2</sub>O/N<sub>2</sub> mixtures. *Plasma Sources Science and Technology*, **19**, 025005 (2010).
- [193] M. J. E. Casey, J. de Urquijo, L. N. Serkovic Loli, D. G. Cocks, G. J. Boyle, D. B. Jones, M. J. Brunger, and R. D. White. Self-consistency of electron-THF cross sections using electron swarm techniques. *The Journal of Chemical Physics*, **147**, 195103 (2017).

- [194] I. B. Martini, E. R. Barthel, and B. J. Schwartz. Mechanisms of the ultrafast production and recombination of solvated electrons in weakly polar fluids: Comparison of multiphoton ionization and detachment via the charge-transfer-to-solvent transition of Na<sup>-</sup> in THF. *The Journal of Chemical Physics*, **113**, 11245 (2000).
- [195] B. M. Schulze, D. L. Watkins, J. Zhang, I. Ghiviriga, and R. K. Castellano. Estimating the shape and size of supramolecular assemblies by variable temperature diffusion ordered spectroscopy. *Org. Biomol. Chem.*, **12**, 7932 (2014).
- [196] P. D. Lax. Weak solutions of nonlinear hyperbolic equations and their numerical computation. *Communications on Pure and Applied Mathematics*, **7**, 159 (1954).
- [197] P. Lax and B. Wendroff. Systems of conservation laws. *Communications on Pure and Applied Mathematics*, **13**, 217 (1960).
- [198] S. Godunov. A difference method for the calculation of shock waves. *Amer. Math. Soc. Transl*, **16**, 389 (1960).
- [199] B. Fornberg. Generation of finite difference formulas on arbitrarily spaced grids. *Mathematics of Computation*, **51**, 699 (1988).
- [200] C.-w. Shu. Essentially Non-Oscillatory and Weighted Essentially Non-Oscillatory Schemes for Hyperbolic Conservation Laws Operated by Universities Space Research Association. *ICASE Report*, 1–78 (1997).
- [201] A. Harten and H. Tal-Ezer. On a fourth order accurate implicit finite difference scheme for hyperbolic conservation laws. II. Five-point schemes. *Journal of Computational Physics*, **41**, 329 (1981).
- [202] P. Wesseling. *Principles of Computational Fluid Dynamics*, volume 29 of *Springer Series in Computational Mathematics*. Springer Berlin Heidelberg, Berlin, Heidelberg (2001). ISBN 978-3-642-05145-6.



# Flux-corrected transport methods for hyperbolic PDEs

## A.1 Introduction

---

In order to solve the electron fluid models used throughout this research an accurate numerical method was required. Whether a solution is required for a simple continuity equation for electron density, or a four moment model (for electron density, flux, energy density, and energy density flux) the systems of equations used in this research can be generalised as the following transport equation

$$\frac{\partial \mathbf{u}}{\partial t} + \nabla \cdot \mathbf{F} = \mathbf{S}, \quad (\text{A.1})$$

where  $\mathbf{u} = [u_1, u_2, \dots, u_n]$  is a state vector of conserved quantities in space and time,  $\mathbf{F}$  is the transported flux of each state variable, and  $\mathbf{S}$  is a source term for each state variable.

In practical cases, where an analytic solution cannot be obtained due to complex geometries, non-linear fluxes or non-trivial source terms, the generic transport equation (A.1) must be solved numerically. To ensure that a numerical scheme produces physically realistic solutions and to avoid unintentional introduction of numerical artefacts into solution of (A.1), it was therefore pertinent to have complete control over numerical solutions used in this project. The choice to develop a custom numerical scheme was informed by the following requirements for the transport problems being studied in this research project.

**Conservation** As charged particle densities explicitly inform the self-consistent electric field computed via Maxwell’s equations, a numerical scheme must be written to guarantee conservation of particles (in the absence of non-conservative collisional processes such as ionisation or attachment). To ensure this is the case, conservation unit-testing must be performed on any proposed numerical scheme to ensure particles are not gained or lost through numerical error.

**Resolution of sharp gradients** It has been noted in the literature that when simulating ionisation front formation and propagation there are inherently high gradients at the front of the streamer [95, 104]. In order to accurately resolve real transport, and not conflate numerical diffusion effects as real transport phenomena, a proposed numerical scheme must be able to resolve sharp gradients without: (i) excessive diffusion or smearing of the solution, and (ii) introducing numerical oscillations to the solution.

**Positivity** Quantities such as density or energy require positivity in their solution, as any negative value predicted in a numerical solution is non-physical. Therefore any proposed solution scheme must ensure that, when required by the physics of the transported variable, a guaranteed positive solution is produced.

### A.1.1 Finite difference methods

The method of finite differences (FD) is often the simplest discretisation to implement when solving one, or many, differential equations like the generic transport equation (A.1). FD is based on local Taylor series approximations about fixed grid points. FD methods have gained popularity for their relative simplicity and practically, pioneered in the computational fluid dynamics community largely due to the seminal works of Lax & Wendroff [196, 197] and Godunov [198]. Since then, much work has been done on refining the accuracy and efficiency of FD techniques, resulting in concise guides on how to construct a discretising scheme and compute grid point weights for approximate derivatives [199].

Although a popular approach, there are some difficulties in implementing FD methods for certain problems where discontinuities exist in solutions, conservation of quantities at the discrete level is vital, and accurate representation of fluxes, particularly at boundaries when implementing boundary conditions, is of importance. In order to combat the disadvantages of the FD method, while still leveraging the theoretical simplicity of the discretisation scheme, the method of flux-corrected transport (FCT) was employed.

## A.2 Flux-Corrected Transport schemes

First define a one-dimensional discrete form of the general transport equation (A.1),

$$\frac{u_j^{n+1} - u_j^n}{\Delta t} + \frac{1}{\Delta x_j} \left( \tilde{F}_{j+\frac{1}{2}} - \tilde{F}_{j-\frac{1}{2}} \right) = S_j, \quad (\text{A.2})$$

where the temporal derivative has been discretised by a first order forward difference, spatial divergence operator has been discretised using the difference of conservative fluxes,  $\tilde{F}_{j\pm\frac{1}{2}}$ , taken at interface points between discretisation points,  $x_j$ , as per Figure A.1.

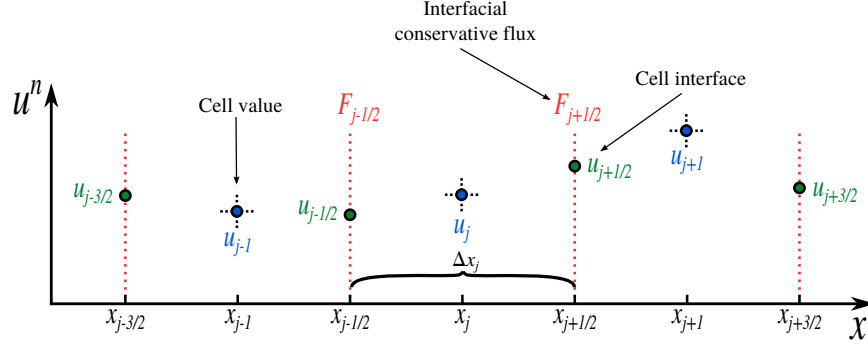


Figure A.1: Spatial discretisation scheme employed for FCT

Broadly speaking, FCT schemes are among a family of numerical methods that aim to use a high order approximations to the spatial flux  $\tilde{F}_{j\pm\frac{1}{2}}$  where possible, but in regions where a high order approximation may introduce errors or noise, due to discontinuities or oscillations, a lower order approximation is used as a fail-safe. In addition to FCT, weighted essentially non-oscillatory (WENO) methods [200] are often used in solution of hyperbolic systems of equations. Where these numerical methods deviate are in the way the conservative flux approximations,  $\tilde{F}_{j\pm\frac{1}{2}}$ , are made.

### A.2.1 FCT algorithm

The authors of the original FCT algorithm [150] designed the method to have the following properties:

- linearly stable in all cases of interest,
- mirror conservation properties of the physics,
- ensure positivity when needed,
- be reasonably accurate,
- be computationally efficient, and
- be independent of specific properties of one problem area.

The algorithm for FCT can be broken down as follows:

1. Compute the low order solution  $u^L$ ,
2. Compute the low order numerical fluxes  $\tilde{F}_{j+\frac{1}{2}}^L$  and  $\tilde{F}_{j-\frac{1}{2}}^L$ ,
3. Compute higher order numerical fluxes  $\tilde{F}_{j+\frac{1}{2}}^H$  and  $\tilde{F}_{j-\frac{1}{2}}^H$ ,

4. Compute the anti-diffusive fluxes

$$A_{j\pm\frac{1}{2}} = F_{j\pm\frac{1}{2}}^H - F_{j\pm\frac{1}{2}}^L, \quad (\text{A.3})$$

5. Limit the anti-diffusive flux to avoid amplifying existing extrema in the lower order solution or adding new extrema via the higher order solution

$$A_{j\pm\frac{1}{2}}^C = C_{j\pm\frac{1}{2}} A_{j\pm\frac{1}{2}}, \quad (\text{A.4})$$

6. Apply the limited anti-diffusive fluxes to find the new solution

$$u_j^{n+1} = u_j^L - \frac{\Delta t}{\Delta x_j} \left[ A_{j+\frac{1}{2}}^C - A_{j-\frac{1}{2}}^C \right] + \Delta t S_j.$$

At the flux limiting stage of the FCT algorithm, described in equation (A.4), each grid point is assigned a weight to dictate how much of the high and lower order methods that contribute to the final approximation to the flux. If  $C_{j\pm\frac{1}{2}} = 0$  then effectively the lower order solution is taken, while if  $C_{j\pm\frac{1}{2}} = 1$  then the full higher order solution is taken. Practically, in order to limit artificial numerical diffusion introduced in a lower order solution, or limit oscillations introduced by higher order solutions, a non-linear series of values for  $C_{j\pm\frac{1}{2}}$  are computed at the flux-limiting stage. The original flux-limiter of Boris and Book is implemented in this work

$$A_{j+\frac{1}{2}}^C = s_{j+\frac{1}{2}} \max \left\{ 0, \min \left[ |A_{j+\frac{1}{2}}|, s_{j+\frac{1}{2}} (u_{j+2}^L - u_{j+1}^L) \Delta x_{j+\frac{3}{2}}, s_{j+\frac{1}{2}} (u_j^L - u_{j-1}^L) \Delta x_{j-\frac{1}{2}} \right] \right\} \quad (\text{A.5})$$

$$\text{where } s_{j+\frac{1}{2}} = \begin{cases} +1 & \text{if } A_{j+\frac{1}{2}} \geq 0 \\ -1 & \text{if } A_{j+\frac{1}{2}} < 0 \end{cases}.$$

This limiter was designed to (i) avoid introducing oscillations that are not present in the lower order solution, and (ii) avoid amplifying extrema that present in the lower order solution. To do this, the flux-limiting process compares the sign of adjacent lower order fluxes to that of the proposed antidiffusive flux (A.3). If adjacent gradients are permissible according to the limiter (A.5), then the anti-diffusive flux is taken, otherwise the higher order flux is cancelled and the lower-order solution is taken. Some examples of applying the Boris-Book limiter are shown in Figure A.2.

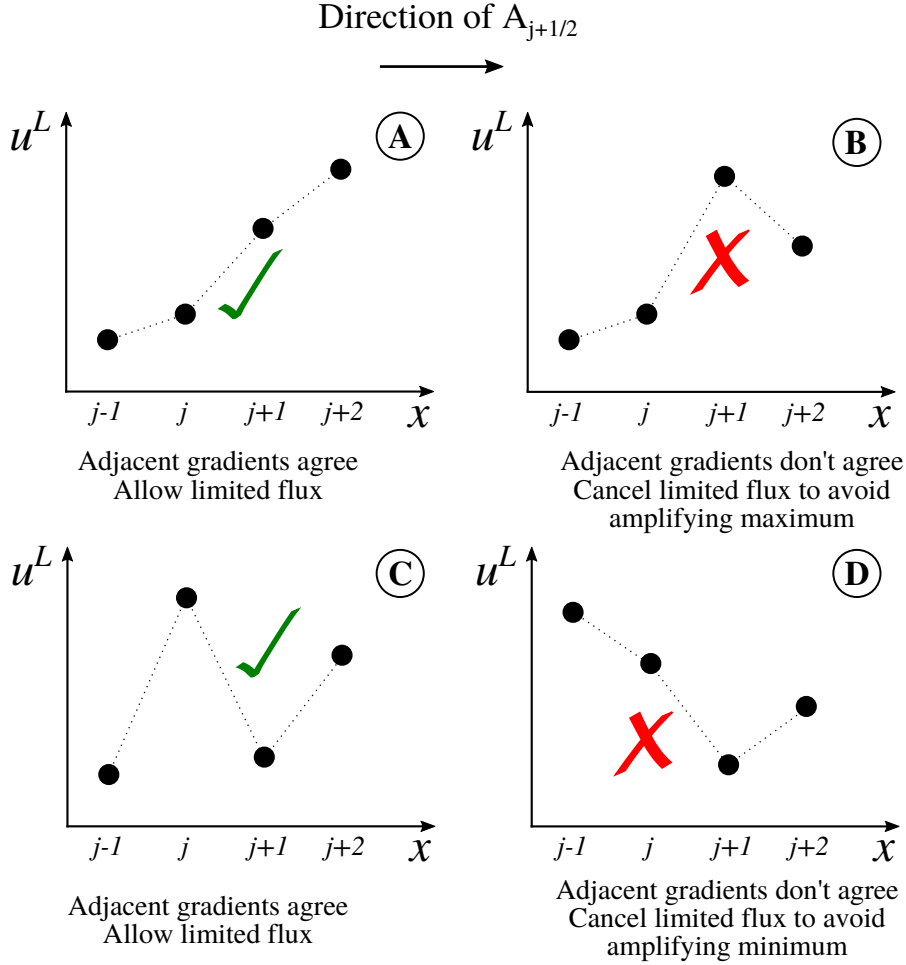


Figure A.2: Examples of flux limiting outcomes as per the Boris-Book limiter. Evaluating cases A and C with (A.5) allows a limited flux to be applied, as non-zero values are produced by the min-max operator. Cases B and D produce a cancelled zero flux as the signs of adjacent gradients do not agree.

### A.2.2 Explicit versus implicit discretisation

Before lower and higher order flux approximations are chosen and implemented, the choice of implicit or explicit FD approximations should be made. Often, this choice is dictated by the physics of the problems at hand. For the work described in this thesis, the ability to accurately resolve sharp-gradient, transient ionisation fronts was important. Within these problems, there are also distinctly different physical timescales at play, for example between collisional momentum and energy relaxation. To accommodate these physical constraints, the option of using implicit FD approximations was avoided as it was noted in literature that when multiple timescales are present in a non-linear transport problem, information transfer can occur faster than physically possible [150–152]. Furthermore, it was noted that when employing implicit schemes shock front resolution can be excessively diffusive, and error introduced via boundary conditions can propagate very quickly compared to explicit schemes [150–152, 200, 201]. In conclusion, the choice to employ simpler explicit discretisation schemes was made as a conservative decision.

### A.2.3 Spatial discretisation

#### Lower order flux

In this work a first order upwind scheme was used to approximate lower order solution,  $u^L$ , and fluxes,  $\tilde{F}_{j\pm\frac{1}{2}}^L$ . The approximation for low order fluxes are given by

$$\tilde{F}_{j+\frac{1}{2}}^L = 0.5(1 + w_j)F_j + 0.5(1 - w_j)F_{j+1} - \frac{1}{8} \frac{\Delta x_{j+\frac{1}{2}}}{\Delta t} (u_{j+1} - u_j), \quad (\text{A.6})$$

$$\tilde{F}_{j-\frac{1}{2}}^L = 0.5(1 + w_j)F_{j-1} + 0.5(1 - w_j)F_j - \frac{1}{8} \frac{\Delta x_{j-\frac{1}{2}}}{\Delta t} (u_j - u_{j-1}), \quad (\text{A.7})$$

where  $w_j$  is the sign of the local instantaneous variable 'velocity'.

For the simulations implemented in this work, a naive Roe type scheme [152] has been used to approximate the local instantaneous variable velocities, and thus  $w_j$ , when evaluating (A.6)-(A.7). Ideally, a Jacobian matrix for the system would be computed to diagonalise the system into a linear system of characteristic variables. Through this transformation, local advection velocities for the characteristic variables can be obtained via the eigenvalues of the Jacobian. However, given that the system of transport equations being solved in this work are highly non-linear and stiff, the process of computing Jacobians at each time step and transforming the system of equations would be excessively slow. To circumvent any inaccuracies or instabilities introduced by the simple Roe scheme, conservatively small time steps were implemented.

To ensure positivity in the solution, diffusive correction terms

$$\frac{1}{8} \frac{\Delta x_{j+\frac{1}{2}}}{\Delta t} (u_{j+1} - u_j), \quad \frac{1}{8} \frac{\Delta x_{j-\frac{1}{2}}}{\Delta t} (u_j - u_{j-1}),$$

are used as per the recommendation of Boris and Book [150, 152].

#### Higher order flux - Uniform grid

For solution domains that employ a uniformly spaced spatial grid, a fourth order, conservative, biased flux was used. The FD stencil was borrowed from the work of Zalesak [151, 152]

$$\tilde{F}_{j+\frac{1}{2}}^H = \frac{7}{12} (F_{j+1} + F_j) - \frac{1}{12} (F_{j+2} + F_{j-1}) - \frac{1}{8} \frac{\Delta x_{j+\frac{1}{2}}}{\Delta t} \left[ \frac{3}{16} (u_{j+1} - u_j) - \frac{1}{16} (u_{j+2} - u_{j-1}) \right], \quad (\text{A.8})$$

$$\tilde{F}_{j-\frac{1}{2}}^H = \frac{7}{12} (F_{j-1} + F_j) - \frac{1}{12} (F_{j-2} + F_{j+1}) - \frac{1}{8} \frac{\Delta x_{j-\frac{1}{2}}}{\Delta t} \left[ \frac{3}{16} (u_j - u_{j-1}) - \frac{1}{16} (u_{j+1} - u_{j-2}) \right], \quad (\text{A.9})$$

where the same form of diffusive correction terms of Boris and Book [150, 152] have been employed.

#### Higher order flux - Non-uniform grid

For a homogenous gas or liquid simulation, a uniformly spaced grid is quite adequate. However, when considering electron transport between either extreme, across an interface layer, variably sized spatial steps were required. Such a discretisation is

demonstrated in Figure A.3, where fine grid points were employed at the interfacial region.

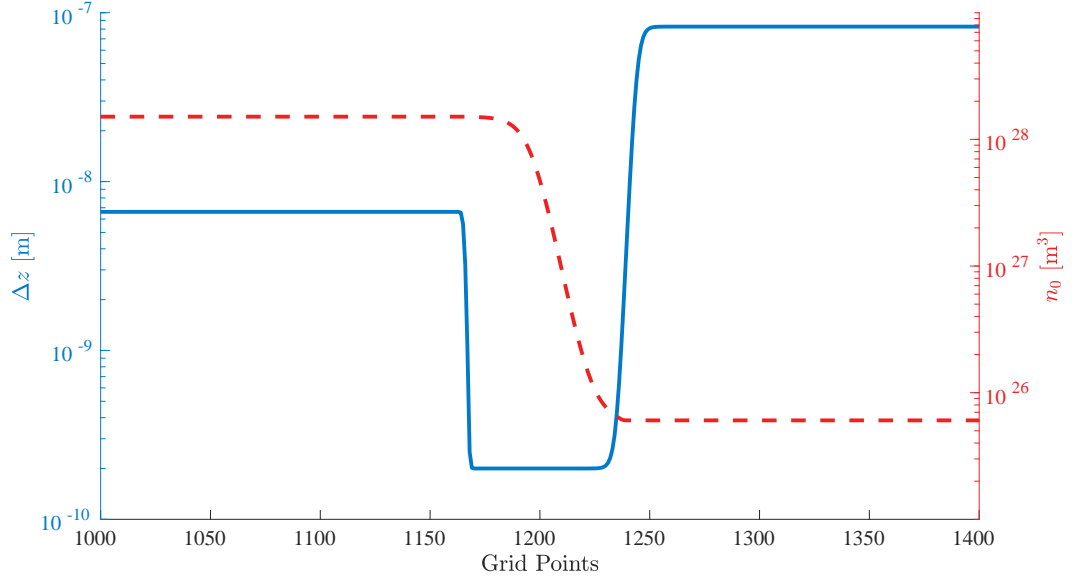


Figure A.3: Variable spatial grid implemented for a typical liquid to gas electron transport simulation

Given a solution domain with non-uniformly spaced grid points

$$x_{\frac{1}{2}} < x_{\frac{3}{2}} < x_{\frac{5}{2}} < \dots < x_{N-\frac{1}{2}} < x_{N+\frac{1}{2}},$$

representing interface points between adjacent cells, one can define cell centers as

$$I_i = \left[ x_{i-\frac{1}{2}}, x_{i+\frac{1}{2}} \right],$$

centered at the positions

$$x_i = \frac{1}{2} \left( x_{i-\frac{1}{2}} + x_{i+\frac{1}{2}} \right),$$

with variably spaced

$$\Delta x_i = x_{i+\frac{1}{2}} - x_{i-\frac{1}{2}}$$

Using the formulation of Shu [200], higher order numerical fluxes at interface points can be computed

$$\tilde{F}_{i+\frac{1}{2}} = \sum_{j=0}^{k-1} c_{rj} \tilde{F}_{i-r+j},$$

$$\tilde{F}_{i-\frac{1}{2}} = \sum_{j=0}^{k-1} c_{rj} \tilde{F}_{i+r-j}$$

where the weights are computed as

$$c_{rj} = \left( \frac{\sum_{m=j+1}^k \frac{\sum_{l=0}^k \prod_{q=0}^k (x_{i+\frac{1}{2}} - x_{i-r+q-\frac{1}{2}})}{l \neq m \quad q \neq m, l}}{\prod_{l=0}^k (x_{i-r+m-\frac{1}{2}} - x_{i-r+l-\frac{1}{2}})} \right) \Delta x_{i-r+j}$$

given a variably spaced grid.

If uniform grid spacing is used the weights can be computed analytically, up to arbitrary order and still maintain conservation. If variable grid spacing is used, it can be shown [200] that only 2nd order accuracy can be obtained while maintaining conservation.

### Boundary conditions

For the bulk of the simulations performed in this study open boundary conditions were implemented. This was done to allow information originating in the model domain to leave the domain without impacting the interior of the solution. Practically this was done via absorbing boundary conditions for each of the state variables for density, particle flux, energy density, and energy density flux [182, 201].

#### A.2.4 Time discretisation

For the current treatment, particular care has been taken with the spatial discretisation methods. Having taken care to treat spatial discretisation with FCT methods, any standard textbook time-integration routine can be used to discretise and then solve the system of hyperbolic transport equations. For this research both Euler's method,  $\mathcal{O}(\Delta t)$ , and a fourth order Runge-Kutta method,  $\mathcal{O}(\Delta t^4)$ , were employed. For development simulations, Euler's method was often used, and for generation of final figures and results for publication the Runge-Kutta method was used for higher accuracy. To ensure the approximations employed in this method do not excessively impact the numerical solutions, a conservative CFL condition was used through this work. Often, a value of 0.05 was used to ensure small time steps were used and stability of the solution was preserved.

## A.3 Unit testing and validation

### A.3.1 Square wave advection and advection-diffusion of a Gaussian pulse

Square wave and Gaussian pulse transport are typical benchmark simulations performed for numerical schemes. These two problems offer validation of a scheme's ability to resolve discontinuities and limit numerical diffusion introduced by low-order methods.

Square wave advection was simulated by solving

$$\frac{\partial u}{\partial t} + c \frac{\partial u}{\partial x} = 0 \quad (\text{A.10})$$

where  $u$  is a particle density and  $c$  is the speed of advection. An initial condition of a square wave was imposed, and as advection is the only transport phenomena present in equation (A.10) the analytic solution can be found by simply transporting the initial condition in space as per the constant advection speed.

Similarly, the advection-diffusion of a Gaussian pulse was simulated by solving

$$\frac{\partial u}{\partial t} + c \frac{\partial u}{\partial x} + D \frac{\partial^2 u}{\partial x^2} = 0, \quad (\text{A.11})$$

where  $D$  is an arbitrary diffusion coefficient. This model can be applied to electron transport in the time of flight experiment, schematically described in Figure A.4. Here, a point flux of  $N$  particles leaves one electrode and travels into a neutral gas of infinite spatial extent under the influence of a constant electric field.

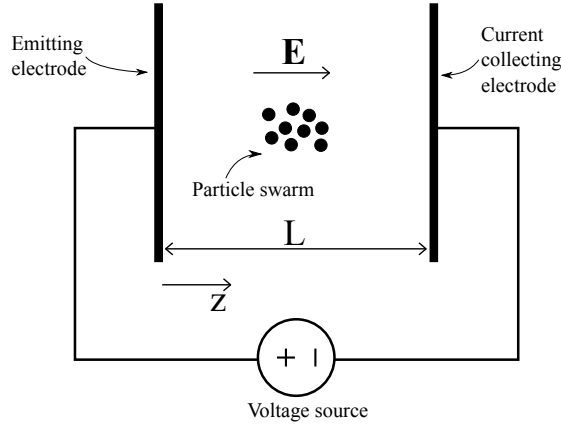


Figure A.4: Simplified schematic of a time of flight experiment

The solution of this partial differential equation can be computed analytically [118] and is given by

$$n(z, t) = \frac{N}{\sqrt{4\pi D_L t}} \exp\left(-\frac{(z - W_z t)^2}{4D_L t}\right). \quad (\text{A.12})$$

Although limited in practical plasma modeling, the simplified geometry and physics of this problem offers a useful benchmark for numerical routines. Practically, this means comparing the output of a numerical solver to that of (A.12) in order to determine if the implemented numerical scheme is accurate and captures the necessary physics for the time of flight problem.

Benchmark simulations were performed by advancing numerical solutions of (A.10) and (A.11) in dimensionless space-time. Advection speed,  $c$ , and diffusion rate,  $D$ , were assumed to be unity.

The benefit of FCT compared to a simple first order upwind scheme is demonstrated in Figure A.5, where resolution of discontinuities and reduction in numerical diffusion

are immediately apparent between the top and bottom solutions.

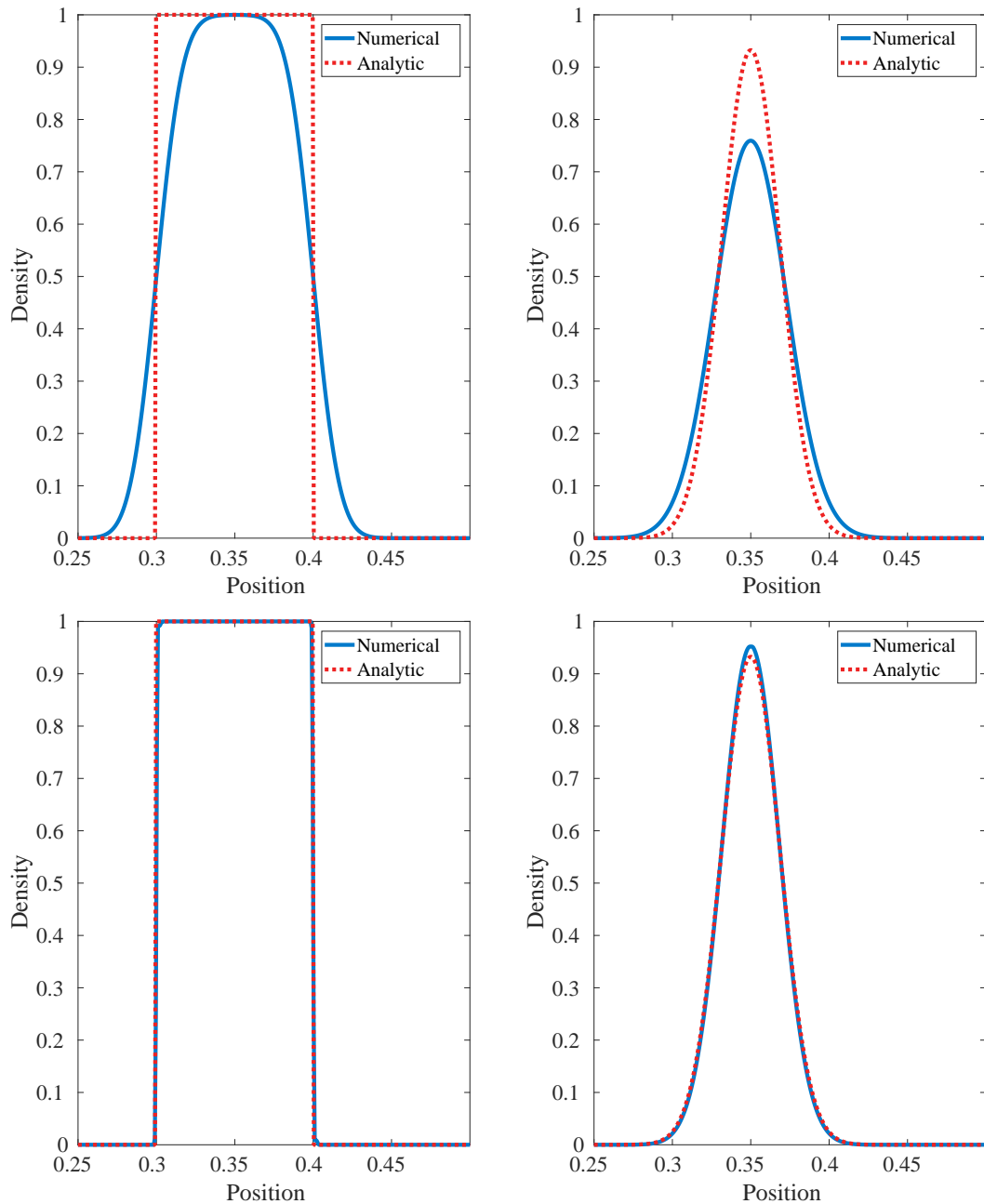


Figure A.5: Example unit test results for: (top) a 1st order upwind spatial discretisation, (bottom) a FCT solution where 4th order central differences are limited by a 1st order upwind scheme.

In these benchmark simulations, the evolution of numerical error was monitored, and the conservation of the scheme was recorded at each time step. The error propagation and conservative properties of the Gaussian pulse solutions presented in Figure A.5 are shown in Figure A.6. From this one can see the reduction in error propagation due to FCT, and for both schemes the loss of particle density is minimal to working numerical accuracy.

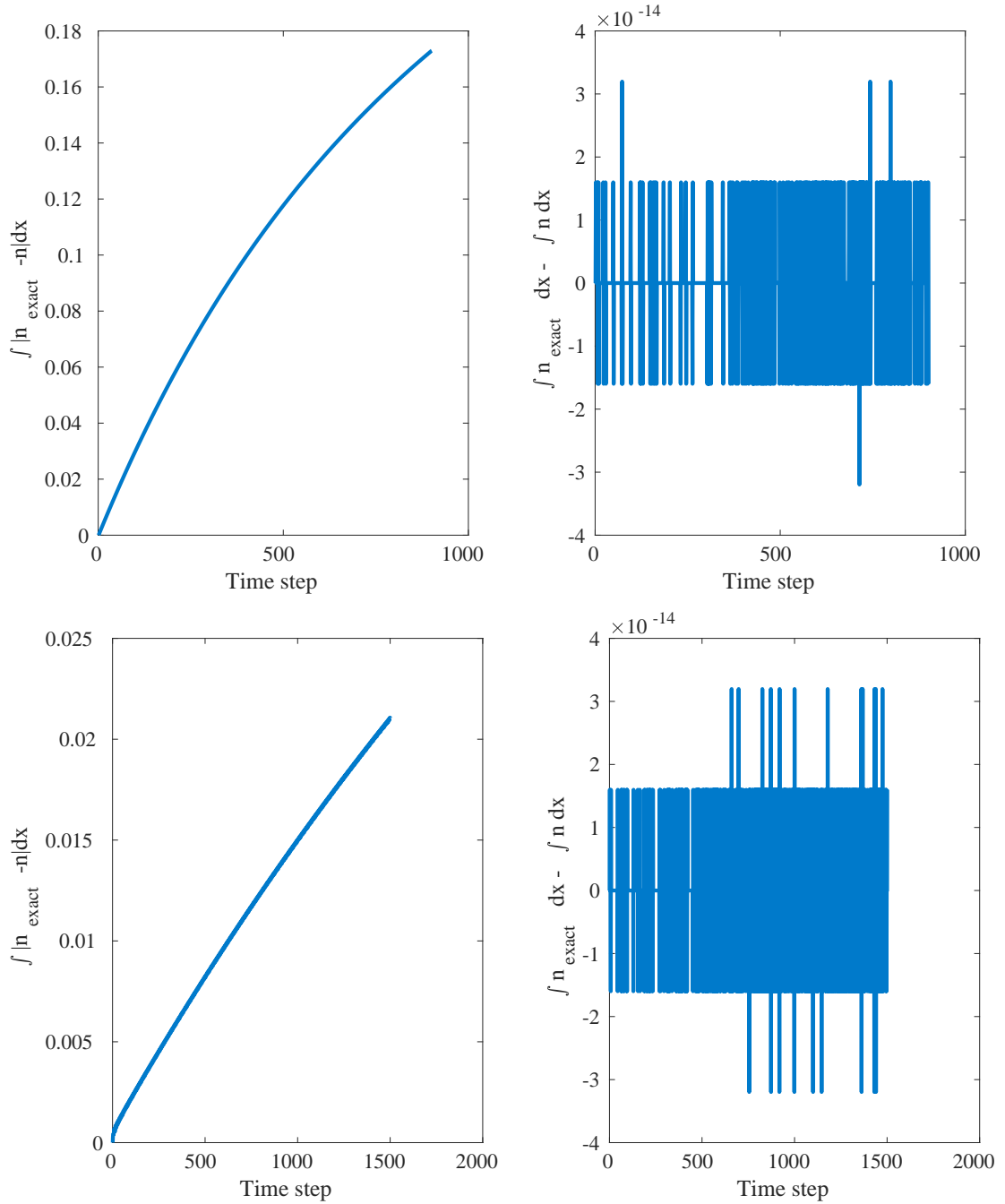


Figure A.6: Numerical error and conservation count of (top) a 1st order upwind spatial discretisation, (bottom) a FCT solution where 4th order central differences are limited by a 1st order upwind scheme.

### A.3.2 Sod's shock tube

To test the application of the developed numerical scheme to a system of transport equations, Euler's equations were solved for a well known benchmark problem, Sod's shock tube. In this test problem, a one dimensional domain is given a discontinuous initial condition for particle density,  $\rho$ , and pressure,  $P$ . To the left of the half-way point, the density and pressure are unity and the right-hand-side of the domain is zero. The initial particle velocity,  $u$ , was zero.

To simulate the evolution of this system Euler's equations are solved for particle density, flux,  $\rho u$ , and energy density,  $\rho E$

$$\frac{\partial}{\partial t} \begin{pmatrix} \rho \\ \rho u \\ \rho E \end{pmatrix} + \nabla \cdot \begin{pmatrix} \rho u \\ \rho u u + P \\ \rho E u + P u \end{pmatrix} = 0, \quad (\text{A.13})$$

along with the state equation

$$P = (\gamma - 1) \left( \rho E - \frac{1}{2} \rho u^2 \right), \quad (\text{A.14})$$

where  $\gamma = 1.4$ .

To validate the numerical solution of the system of equations A.13, time was evolved to  $t = 0.17$  and solutions were compared to an established solution provided by a Roe MUSCL scheme [202]. Results for this system are shown in Figure A.7 for both a first order upwind method, and the final FCT method employed in this work.

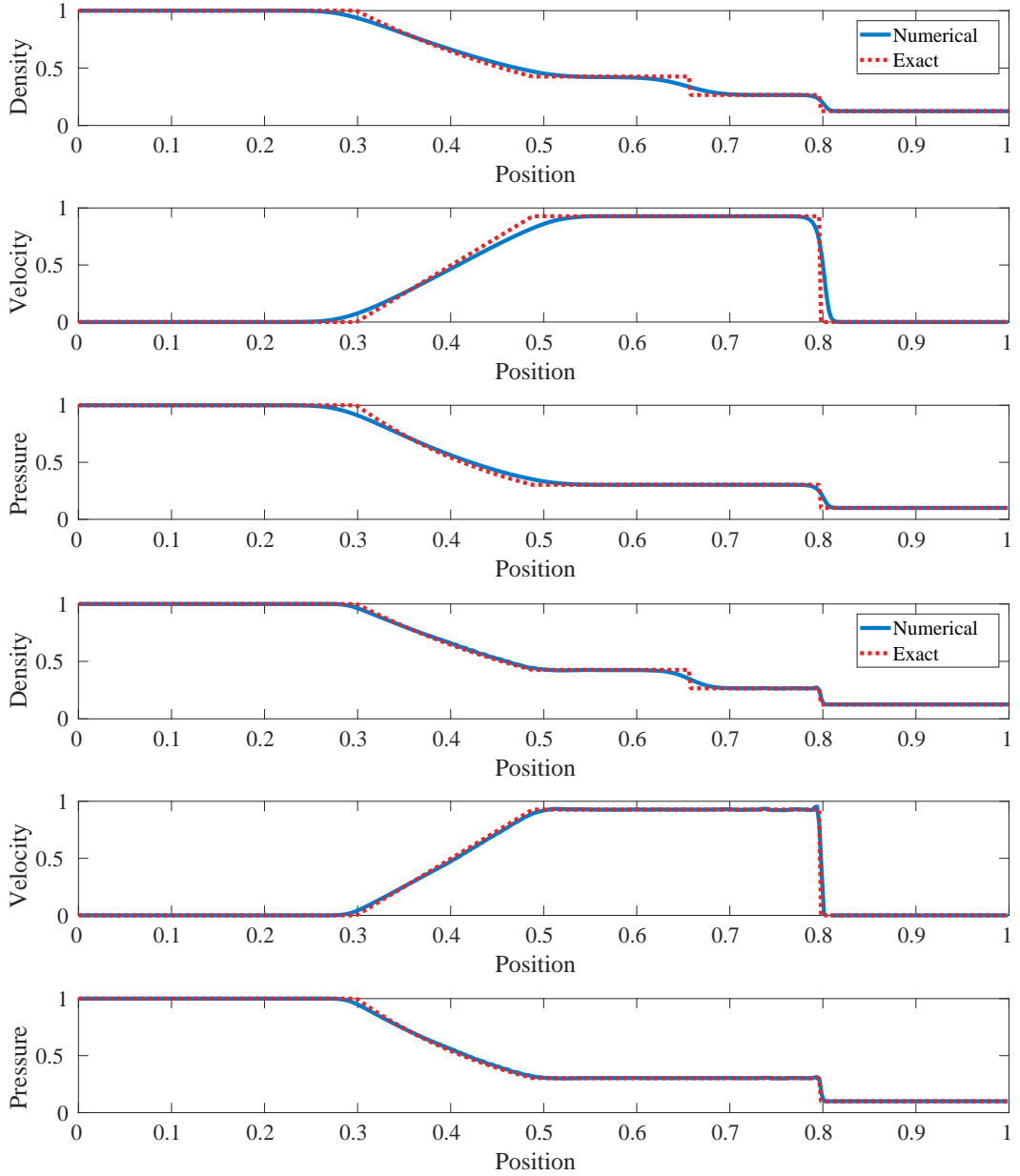


Figure A.7: Sod's shock tube solutions for: (top) a 1st order upwind spatial discretisation, (bottom) a FCT solution where 4th order central differences are limited by a 1st order upwind scheme.

The results of Figure A.7 indicate the low order method produces significant smearing of the solution near discontinuities of the known solution. In contrast, the FCT method, using a fourth order flux approximation, is able to resolve sharp gradients with greater success.

## A.4 Poisson equation solution

Considering a three-point grid centered on  $x_i$  with points to the left,  $x_{i-1}$ , and right,  $x_{i+1}$ , such that  $x_{i-1} < x_i < x_{i+1}$ , the variably sized steps between adjacent grid points to the left and right are given by  $h_L = x_i - x_{i-1}$  and  $h_R = x_{i+1} - x_i$  respectively. For

this grid, one must seek to construct FD stencils, for the necessary spatial derivatives, as a function of the arbitrarily sized spatial steps. Using these FD stencils, the continuous Poisson equation for electric potential can be discretized and subsequently solved as a system of linear equations

$$\begin{aligned}\frac{d^2V}{dx^2} &= f(x), \\ &\Downarrow \\ \mathbf{D}_2V &= f,\end{aligned}$$

where the difference matrix,  $\mathbf{D}_2$ , is a discretized second derivative operator.

Using the method of undetermined coefficients and introducing Taylor series expansions, one can eliminate zeroth and second derivatives to obtain an expression of approximately second order accuracy,  $\mathcal{O}(h_L h_R)$ ,

$$u''(x_i) \approx \frac{2}{h_L(h_L + h_R)}u(x_{i-1}) - \left[ \frac{2}{h_L(h_L + h_R)} + \frac{2}{h_R(h_L + h_R)} \right]u(x_i) + \frac{2}{h_R(h_L + h_R)}u(x_{i+1}) + \mathcal{O}(h_R - h_L),$$

where the error term is  $\mathcal{O}(h_R - h_L) = \frac{h_R - h_L}{3}u'''(x_i)$ .

## A.5 Treating zero density regions

When an electron ionisation front is propagating into free-space, regions of very small electron density will be approached by the traveling front. These regions of space can pose an issue when computing intensive variables from extensive computational variables. A prime example of this is the computation of mean electron energy, used to interpolate input data at each time-step,

$$\langle \epsilon \rangle = \frac{n_\epsilon}{n}.$$

To remedy this situation when computing an arbitrary intensive variable,  $\langle \psi \rangle$ , from the extensive, density scaled quantity,  $n_\psi = n \langle \psi \rangle$ , the following regularisation [95, 146] was used in this work

$$\langle \psi \rangle = \frac{n_\psi + \eta_0 \tilde{\psi}}{n + \eta_0},$$

where  $\eta_0$  is a small number chosen to denote the minimum electron density at which to revert to the value  $\tilde{\psi}$ , which is a representative value that zero density regions may revert to. In this study, values of  $\tilde{\psi}$  were assigned to be the steady-state values evaluated at the background reduced field experienced in the low-density region.

## A.6 Scaling variables

To assist the computational implementation of numerical solutions needed for this work, all variables were scaled by appropriate physical scales. One benefit of scaling SI variables, to ones of smaller magnitude, is to reduce the opportunity for numerical

errors to be introduced due to the limitations of double precision arithmetic limitations. Furthermore, it is beneficial to introduce the background neutral particle density,  $n_0$ , via scaling to form “reduced” versions of variables that appear in the systems of equations. Reduced quantities are either multiplied by  $n_0$ , e.g. reduced diffusion coefficient  $n_0 D$ , or divided by  $n_0$ , e.g. reduced collision frequency  $\nu/n_0$ , in order to obtain quantities normalised by the density of the system.

An arbitrary scattering mean free path is defined as the length scale. For the mean free path, scattering is assumed in a neutral gas of density  $n_0$  with a representative scattering cross section of  $\sigma_0 = 1 \text{ \AA}^2$ .

$$\tilde{L} = \frac{1}{\sigma_0 n_0},$$

$$z = \tilde{L} \tilde{z}.$$

The electron mass is chosen as the mass scale

$$\tilde{M} = m_e,$$

$$m = \tilde{M} \tilde{m}.$$

An energy of 1 eV is simply chosen as the energy scale

$$\tilde{\epsilon} = q_e,$$

$$\epsilon = \tilde{\epsilon} \tilde{\epsilon}.$$

A time scale can be computed via the chosen mass, length, and energy scales

$$\begin{aligned} \tilde{T} &= \frac{1}{\sigma_0 n_0} \sqrt{\frac{\tilde{M}}{2\tilde{\epsilon}}}, \\ t &= \tilde{T} \tilde{t}. \end{aligned}$$